Manufacturing of metal-free carbon-based catalysts for styrene production

Housseinou Ba

UNIVERSITÉ DE STRASBOURG

EDSC
Ecole Doctorale des Sciences Chimiques

ÉCOLE DOCTORALE DES SCIENCES CHIMIQUES

ICPEES, UMR 7515 CNRS

UCCS, UMR 8181 CNRS

THÈSE

présentée par

Housseinou BA

soutenue le **24 Juillet 2015**

pour obtenir le grade de

Docteur de l'Université de Strasbourg

Discipline/ Spécialité: Chimie /Chimie Matériaux

Développement des catalyseurs sans métaux à base de carbone pour la production de styrène

Manufacturing of metal-free carbon-based catalysts for styrene production

Membres du jury

Directeur de thèse :	**Dr. Cuong PHAM-HUU**	Directeur de recherche, UDS, Strasbourg
Co-Directeur de thèse :	**Prof. Pascal GRANGER**	Professeur, UDL1, Lille
Rapporteur externe :	**Prof. De CHEN**	Professeur, NTNU, Trondheim (NO)
Rapporteur externe	**Prof. Alexei LAPKIN**	Professeur, UC, Cambridge (UK)
Examinateur :	**Prof. Ovidu ERSEN**	Professeur, IPCMS, Strasbourg

To my parents

To my wife

Acknowledgement

I would never have made this exciting experience without the help of a lot of people around me. I would like to give many thanks to all of them.

The researchs which are the subject of this thesis was performed at the Institut de Chimie et Procédés pour l'Energie, l'Environnement et la Santé (ICPEES UMR 7515 CNRS and the University of Strasbourg) in Strasbourg.

First of all, I would like to give my sincere thanks to my supervisor, Dr. Cuong PHAM-HUU for accepting me in his laboratory, for his guidance, patience, and encouragement during my research. He is always ready to help me and guide me in the right scientific direction. I extend to him my warm and heartfelt thanks for the quality of his leadership and support. He is the funniest advisor and one of the smartest people I know. I am deeply grateful to him for making me benefit from his experience and expertise throughout the work. I have learned a lot from him, and without his help I could not have finished this dissertation successfully.

I would like to thank also my co-supervisor Prof. Pascal GRANGER, who accepted me as his Ph.D. student without any hesitation when Dr. Cuong PHAM-HUU presented him my research proposal. It was only due to his valuable guidance, cheerful enthusiasm and ever-friendly nature that I was able to complete my research work in a respectable manner.

I also want to thank Prof. Alexei LAPKIN from the Department of Chemical Engineering and Biotechnology at the University of Cambridge (UC) and Prof. De CHEN from the Chemical Engineering Department of the Norwegian University of Science and Technology (NTNU) for coming from a long way for serving as the advisory committee members. I would like also to express my thanks to Prof. Ovidiu ERSEN from the Institut de Physique et Chimie des Matériaux de Strasbourg (UMR CNRS 7504) at the University of Strasbourg who helped me for the TEM analysis and for accepting to be a member of the jury.

Special thanks are also given to Dr. Jean-Mario NHUT, Dr. Yuefeng LIU and Dr. Lai TRUONG-PHUOC, who also actively monitored the progress of my research. I would like to thank for their help, advice availability, and encouragement, which made me feel confident to fulfill my research and overcome every difficulty I encountered. At the last stage of my dissertation, they helped me to correct grammar mistakes in the dissertation text, and suggested possible improvements. It is not sufficient to express my gratitude with only a few words. I am also indebted to Drs. Dominique BEGIN, and Izabela JANOWSKA and Ioana FECHETTE for their valuable guidance and encouragement.

I warmly thank Mr. Cuong DUONG-VIET for his valuable support, availability, human values and attention he has shown to me throughout this work.

I would like to thank my friends in the ICPEES for their friendship, help and discussions: Fabrice VIGNERON, Drs. Tri TRUONG-HUU, Walid BAAZIZ, Seetharamoulou PODILA, and Xiaojie LIU.

I extend great thanks to all the administrative team (Véronique VERKRUYSSE, Agnès ORB, Nathalie WEBER and Francine JACKY) and the technical staff (Pierre BERNHARDT, Won-Hui DOH, Spyridon ZAFEIRATOS, Thierry ROMERO, Sécou SALL, Alain RACH, Thierry DINTZER, Christophe MELART, Christophe SUTTER…) of the ICPEES and the Faculty of Chemistry of Strasbourg for the help they have often brought me in my various approaches.

My sympathy also goes to trainees, Yann UBERSHLACH, Mathilde ILTIS, Camille HELLEU and Duo ZHANG, for their sympathy and friendship, encouraged me and helped me to carry out this work in excellent conditions.

I want to express my deep gratitude and thanks to my friends, who have shown me unwavering support in accomplishing this work. Their assistance is greatly acknowledged.

I have a special thought for my family of the sacrifices that they made on my behalf. Their prayers and support throughout the years for me was what sustained me thus far.

At the end I would like to express appreciation to my beloved wife Fatou TOURE who spent sleepless nights with me and was always my support in the moments when there was no one to answer my queries.

Table Contents

Acknowledgement.....i
Table Contents.....iii
Résumé 7
Références bibliographiques 19
CHAPTER 1 21
1. Generalities about styrene 23
1.1. Physical properties of ethylbenzene 27
1.2. Physical properties of styrene 27
2. Industrial process for styrene production 28
2.1. The limitations of current industrial processes 33
3. Carbon-based composites as metal-free catalysts 34
3.1. Oxidative Dehydrogenation (ODH) process 37
3.2. Direct dehydrogenation (DH) process 42
4. Objectives of the work 49
Reference 51
CHAPTER 2 57
Supports and characterization techniques 57
1. Materials synthesis 59
1.1. Nanodiamonds 59
1.2. Graphene based-materials 61
1.3. Carbone nanotubes / nanofibers 63
1.4. Silicon Carbide 66
2. Catalytic Reactions 69
2.1. Selective dehydrogenation of ethylbenzene to styrene 69
2.2. Oxygen Reduction Reaction (ORR) 70
3. Characterization techniques 71
References 74
CHAPTER 3 77
Nanodiamond decorated few-layer graphene composite as an efficient metal-free dehydrogenation catalyst for styrene production 79
Graphical abstract 80
Abstract 80
Keywords: 80

1. Introduction 81
2. Experimental 82
2.1 Nanodiamonds and few-layer graphene characteristics 82
2.2 Synthesis of the ND/FLG catalyst 83
3. Results and discussion 83
3.1 ND/FLG Characteristics 83
3.2 Steam-free selective dehydrogenation of ethylbenzene to styrene 87
3.3. The surface and structure analysis after dehydrogenation reaction 91
4. Conclusion 97
Acknowledgements 97
References 98
Few-layer graphene-graphene oxide composite containing nanodiamonds as metal-free catalyst in the dehydrogenation of ethylbenzene 101
Abstract 102
1. Introduction 103
2. Experimental 105
2.1. Exfoliation of expanded graphite in aqueous medium using graphene oxide as a surfactant 105
2.2. Self-organized decoration of nanodiamonds on the FLG-GO sheets 105
3. Results and discussion 105
4. Conclusion 116
Acknowledgements 116
References 117
Supporting Information 120
1. Synthesis of graphene oxide (GO) and GO-mediated exfoliation of expanded graphite (EG) in water 120
2. Self-organized decoration of nanodiamonds on the surface of GO-FLG 122
Reference 127
CHAPTER 4 129
Nanodiamonds decorated graphene-carbon nanofibers 3D architecture as a metal-Free catalyst for styrene production 131
Graphical abstract 132
Abstract 132
1. Introduction 133
2. Experimental 134

2.1 Few-layer graphene synthesis and characterization 134
2.2 Synthesis of FLG supported Ni nanoparticles 135
2.3 Synthesis of a 3D CNF/FLG composite 135
2.4 Deposition of nanodiamonds onto a CNF-FLG composite 135
3. Results and discussion 136
3.1 FLG supported Ni nanoparticles characteristics 136
3.2 CNF/FLG composite characteristics 137
3.3 ND/FLG-CNFs composite 138
3.4 Dehydrogenation of ethylbenzene into styrene 143
4. Conclusion 146
Acknowledgements 147
References 148
Supporting Information 151
CHAPTER 5 155
Nanodiamonds/β-SiC Composite as an Efficient Metal-Free Catalyst for the Steam-Free Dehydrogenation of Ethylbenzene to Styrene 157
Graphical abstract 158
Abstract 158
1. Introduction 159
2. Experimental Section 160
2.1 Metal-free catalysts preparation 160
2.2 Characterization techniques 161
2.3 Catalytic activity measurements 162
3. Results and discussion 163
4. Conclusions 179
Acknowledgements 179
References 180
Supporting Information 182
CHAPTER 6 185
Green chemical route to produce hierarchical carbon nanotubes coated with nitrogen-doped porous carbon as metal-free catalyst 187
Graphical abstract 188
Abstract 188
1. Introduction 189

2. Results and discussion 190
2.1. Oxygen reduction reaction (ORR) 194
2.2. Steam-Free Dehydrogenation of Ethylbenzene into Styrene. 196
3. Conclusions 198
Acknowledgment 199
References 200
Supporting information 203
Synthesis of nitrogen-doped carbon foam composite 203
A Highly N-Doped Carbon Phase "Dressing" of Macroscopic Supports for Catalytic Applications 213
Graphical and textual abstract 214
Abstract 214
1. Introduction 215
2. Results and discussion 218
3. Conclusions 219
Acknowledgments 220
References 220
Supporting information 222
Methods 222
References 229
Nitrogen-enriched carbon nanospheres decorated silicon carbide as a superior metal-free catalyst for styrene production 230
Abstract 231
1. Introduction 232
2. Experimental 234
2.1 Catalyst preparation 234
3. Results and discussion 235
3.1Morphology analyses of typical nitrogen-enriched carbon nanospheres 235
3.3 Physicochemical analyses of ND and ND@NMC composites 238
3.4 Catalytic performance on ND and ND@NMC composites 240
3.5 Characterization and catalytic reaction of macroscopic shaped ND@NMC/SiC composite. 242
3.6 Macroscopic ND@NMC/SiC catalyst under severe dehydrogenation conditions 246
4. Conclusion 249
Acknowledgements 249

References 250
Supporting Information 252
CHAPTER 7 255
Summary 256
General conclusions 256
Perspectives 259
References 261
Annex 264

Résumé

A l'heure actuelle, la catalyse est présente dans plus de 90 % des procédés chimiques industriels et 13 des 20 produits chimiques les plus importants sont fabriqués par voie catalytique: la vente de catalyseurs représente 3 milliards d'euros par an et celle des produits qui en sont issus 300 milliards d'euros par an, soit 100 fois plus.[1] Cette expansion sera poursuivie compte tenu de la forte demande dans les pays industriels mais aussi dans les pays émergents tels que la Chine, l'Inde et le Brésil, sans parler des pays du Sud-est asiatique où de fortes croissances sont à prévoir dans les années à venir.

La production de styrène a connu une croissance exponentielle depuis le premier procédé industriel dans les années 30[2,3], avec une estimation avoisinant les 25 millions de tonnes par an.[4] Le styrène est principalement utilisé dans la fabrication du polystyrène, des résines acrylonitrile-butadiène-styrène (ABS) mais aussi dans la formulation de divers autres polymères, et représente aujourd'hui le ciment de la révolution des matières plastiques. L'industrie du styrène est très diversifiée, allant des produits d'emballage et de construction, jusqu'à la filière automobile. Elle capitalise ainsi un chiffre d'affaire estimé à 60 milliards de dollars par an.

Le styrène est essentiellement fabriqué par la réaction de déshydrogénation catalytique de l'éthylbenzène en styrène, procédé de fabrication faisant partie des dix procédés catalytiques les plus importants au monde.[5] Les catalyseurs actuellement utilisés sont constitués d'oxyde de fer promu au potassium et stabilisé avec de l'alumine (K-Al-Fe).[6] Cependant, ils sont peu actifs et sélectifs et se désactivent rapidement au cours de la réaction par dépôt de résidus carbonés (ou coke, formé par polymérisation des intermédiaires réactionnels et notamment le styrène). Afin de réduire ce dépôt, une grande quantité de vapeur d'eau (5-15 %) est co-injectée dans le réacteur avec l'éthylbenzène, mais la génération de cette vapeur d'eau est un procédé très coûteux énergétiquement (1.5×10^9 cal/ tonne de styrène).[7] De plus, de grandes quantités d'eau polluée post-réaction doivent être traitées, ce qui représente également un coût énergétique et environnemental non négligeable pour le procédé. Il s'avère dès lors intéressant de trouver d'autres types de catalyseurs plus robustes et plus performants permettant de réaliser la transformation de l'éthylbenzène en styrène avec une conversion et une sélectivité élevée, et une meilleure stabilité en fonction du temps sous flux en l'absence de vapeur d'eau.

De nombreux travaux reportés dans la littérature ont montré que les matériaux carbonés tels que graphène, nanotubes ou nanofibres de carbone, et nanodiamants[8,9,10,11] occupent un intérêt particulier dans le milieu de la recherche et de l'industrie, en raison de leurs propriétés physiques et chimiques exceptionnelles à savoir, surface spécifique élevée et porosité ouverte, ainsi qu'une excellente inertie chimique. Ces atouts leur confèrent une place privilégiée dans plusieurs domaines d'applications tels que l'électronique,[12] la conversion et le stockage

d'énergie,[13] la nanomédecine,[14] le traitement des eaux usées,[15] et surtout dans les procédés de la catalyse moderne où ils peuvent être utilisés directement comme catalyseurs ou supports de catalyseurs.[16] De plus, leur dopage par d'autres éléments chimiques (N, B,...) permet de modifier leurs propriétés intrinsèques, et par conséquent, d'améliorer leurs performances en termes d'activité et de sélectivité dans les procédés catalytiques allant de l'oxydation à l'hydrogénation, en passant par la déshydrogénation sélective. De nombreux travaux ont ainsi reportés des performances catalytiques souvent supérieures de ces catalyseurs « sans métaux » à base de nanomatériaux carbonés comparés à celles obtenues sur les catalyseurs traditionnels supportés à base de métaux ou d'oxydes de métaux, et ce, avec une très grande stabilité.[17] C'est pourquoi ces catalyseurs "sans métaux" à base de carbone se présentaient comme des candidats incontournables pour remplacer le catalyseur traditionnel à base de fer dans le procédé de déshydrogénation directe de l'éthylbenzène en styrène.

D'autre part il s'avère que les catalyseurs carbonés sans métaux à base de nanodiamants présentaient de loin les meilleures performances catalytiques, en termes de conversion et sélectivité dans la réaction de déshydrogénation (DH) de l'éthylbenzène en styrène. La forte activité catalytique des nanodiamants a été attribuée à la présence de deux états d'hybridation de carbone, sp^2 et sp^3, sur la surface du matériau et qui lui confère des propriétés d'adsorption remarquables, bases de la catalyse hétérogène.

L'objectif de la thèse porte sur l'élaboration de catalyseurs "sans métaux" à base de carbone, et plus essentiellement à base de nanodiamants, pour le procédé de déshydrogénation directe (DH) de l'éthylbenzène (EB) en styrène (ST) en absence de vapeur d'eau.

Nous avons dans un premier temps, développer puis utiliser des matériaux à base de carbone tels que les nanotubes (CNTs) ou nanofibres de carbones (CNFs), le graphène multi-feuillets (FLG), ou les nanodiamants (NDs), et les tests catalytiques ainsi réalisés ont révélés une nette supériorité des performances catalytiques du catalyseur à base de nanodiamants comparé aux autres allotropies de carbone et au catalyseur industriel à base de fer (Figure 1). Ces performances sont essentiellement dues à la concentration des défauts de structures présentes en surface de ce matériau et au rapport surface/volume très élevé. De plus, comme on peut le constater, en l'absence d'eau dans la charge, le catalyseur industriel se désactive très rapidement pour atteindre un palier plus bas. Le catalyseur à base de nanodiamants présente également une sélectivité en styrène légèrement supérieure à celle du catalyseur industriel.

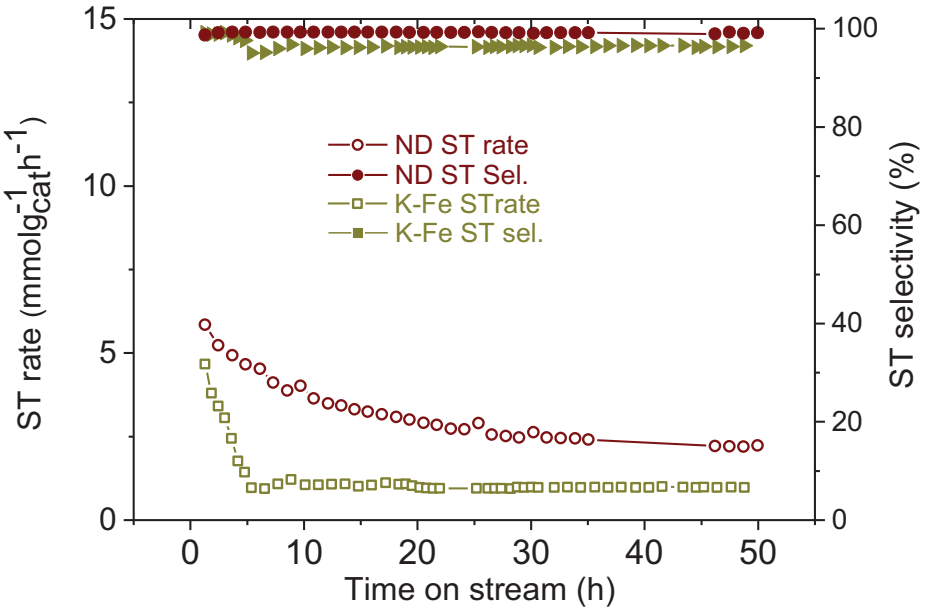

Figure 1 : Comparaison des performances catalytiques obtenues sur nanodiamants et sur catalyseur industriel à base de fer promus au potassium (Conditions de test: T = 600°C, P = atmosphérique, [EB] = 2,8 vol. %).

Néanmoins les investigations en microscopie réalisées sur les nanodiamants ont montré une distribution de taille de particules comprise entre 3-10 nm, et une forte tendance à s'agglomérer, ce qui en catalyse pourrait se traduire par une diminution de la densité des sites actifs et une activité qui pourrait être largement sous-estimée. Dans l'optique d'améliorer l'activité catalytique des nanodiamants, nous avons mis en œuvre un protocole permettant de synthétiser des matériaux hybrides consistant à disperser des particules de nanodiamants sur des supports à base de graphène (FLG) et graphène oxyde (GO). Les particules de diamant ont aussi été dispersées sur des matériaux hybrides carbonés avec une structure hiérarchisée constituée par une couche de nanofibres de carbone (CNFs) sur la surface du graphène. L'ajout de cette troisième dimension permet de mieux ancrer les nanodiamants, grâce à la présence de plans prismatiques sur la surface des nanofibres de carbone (ND/CNF-FLG), et de disperser des nanodiamants générant ainsi des sites actifs avec une meilleure accessibilité aux réactifs, ce qui permet l'obtention d'une excellente activité et une meilleure évacuation des produits de réaction hors de la zone catalytique, favorisant ainsi une bonne sélectivité et une formation plus faible de coke. Ces matériaux hybrides ainsi synthétisés ont accusé des performances catalytiques relativement élevées avec une meilleure activité spécifique du catalyseur 3D ND/CNF-FLG équivalent à 11,5 $mmol_{ST}\ g_{ND}^{-1}\ h^{-1}$ soit plus de quatre fois supérieure à celle des nanodiamants non supportés, et dix fois supérieure à celle du catalyseur

industriel à base de fer. Le principal avantage du catalyseur 3D ND/CNF-FLG comparé au catalyseur 2D ND/FLG réside dans sa très grande stabilité obtenue dans des conditions de test extrêmes reproduisant celles utilisées dans les unités industrielles (Figure 2), à savoir, hautes températures, pression partielle de l'éthylbenzène élevée, test longue durée.

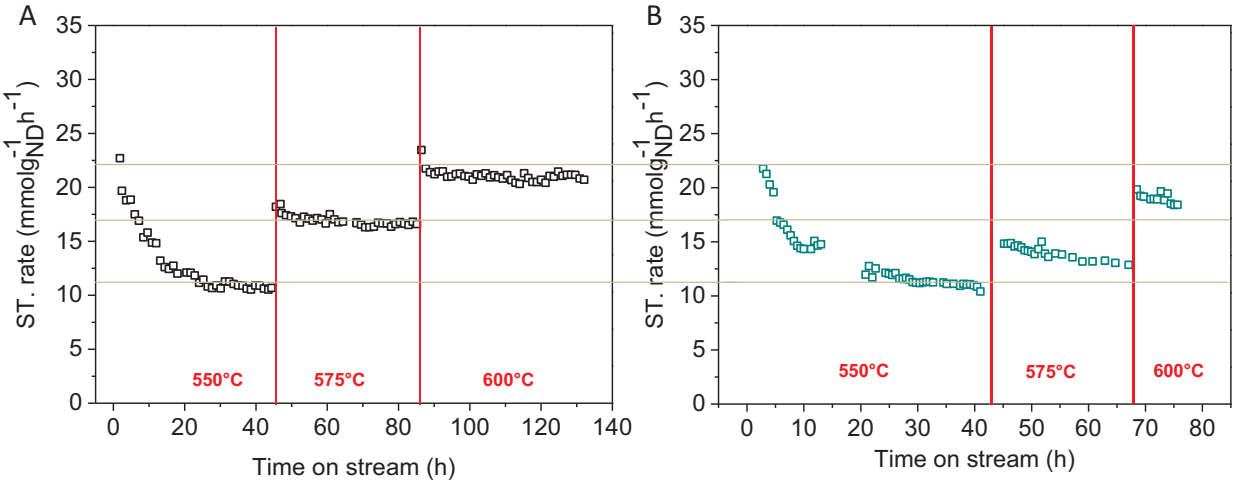

Figure 2. Influence de la température de réaction sur les performances catalytiques obtenues sur catalyseurs (A) ND/CNF-FLG et (B) 2D ND/FLG. (conditions opératoires: masse de catalyseur = 300 mg, 2.8 % d'EB dans l'hélium, flux total de gaz = 30 mL·min^{-1}).

Cependant, il est à noter que les nano-carbones sont généralement obtenus sous forme d'une fine poudre nanoscopique qui rend leur manipulation et leur transport difficiles. Dans le domaine de la catalyse hétérogène, leur utilisation est fortement entravé dans certaines applications fonctionnant avec des réacteurs a lit fixe, car limitées par des phénomènes liés à la perte de charge[18] à travers le lit catalytique, et dans le cas des lit agités, la récupération du catalyseur après réaction est souvent très difficile. Face à ces contraintes il était nécessaire de développer une nouvelle génération de catalyseurs avec une structure macroscopique permettant ainsi de répondre aux nouvelles exigences des procédés industriels modernes de catalyse, à savoir haute pression partielle et vitesse de gaz élevée. Nos recherches se sont donc orientées sur l'utilisation de supports de catalyseurs tels que l'alumine ou la silice couramment utilisés dans les procédés de catalyse hétérogène. Néanmoins, les performances catalytiques ne sont pas à la hauteur de notre attente. Un nouveau support de catalyseurs, le carbure de silicium (β-SiC), a été également choisi pour disperser les nanodiamants en raison de sa bonne conductivité thermique, sa résistance mécanique élevée, son inertie chimique et son excellente résistance à l'oxydation et à la corrosion.

La fabrication du SiC sous sa forme β est actuellement développée et industrialisée par la société SICAT Sarl (www.sicatcatalyst.com), et plusieurs mises en forme (grains, extrudés, pellets, mousse alvéolaire) sont disponibles selon le type d'applications visées (Figure 3).

Figure 3. Différentes formes à base de carbure de silicium de structure β utilisées pour la dispersion des nanodiamants.

Nous avons réussi à synthétiser en une seule étape des catalyseurs hybrides sous forme macroscopique, à base de nanoparticules de NDs décorées sur différentes formes de carbure de silicium, e.g. poudre (40 μm), grains (250-425 μm) et mousse alvéolaire (plusieurs centimètres de dimension), afin de voir l'influence de la morphologie du support sur l'activité du catalyseur. Les tests catalytiques ont montré une meilleure activité du catalyseur à base de NDs supportés sur mousse alvéolaire (ND/SiC foam) par rapport aux grains ou à la poudre (Figure 4), ce qui est en parfaite corrélation avec les données de la Figure 2B, illustrant les mesures de perte de charge réalisées sur différentes formes de SiC données. Le catalyseur ND/SiC(foam) possède aussi une grande surface et une porosité ouverte constituée essentiellement d'un vaste réseau mésoporeux et macroporeux. La présence de ponts reliant la structure permet de créer des microturbulences au sein du mélange réactionnel favorisant ainsi le contact effectif entre les réactifs et les sites actifs et par conséquent une meilleure réactivité. L'activité spécifique du ND/SiC(foam) est de 12,86 $mmol_{ST}\ g_{ND}^{-1}h^{-1}$, soit quatre fois supérieure à celle des NDs non supportés ,et 12 fois celle du catalyseur traditionnel K-Fe.

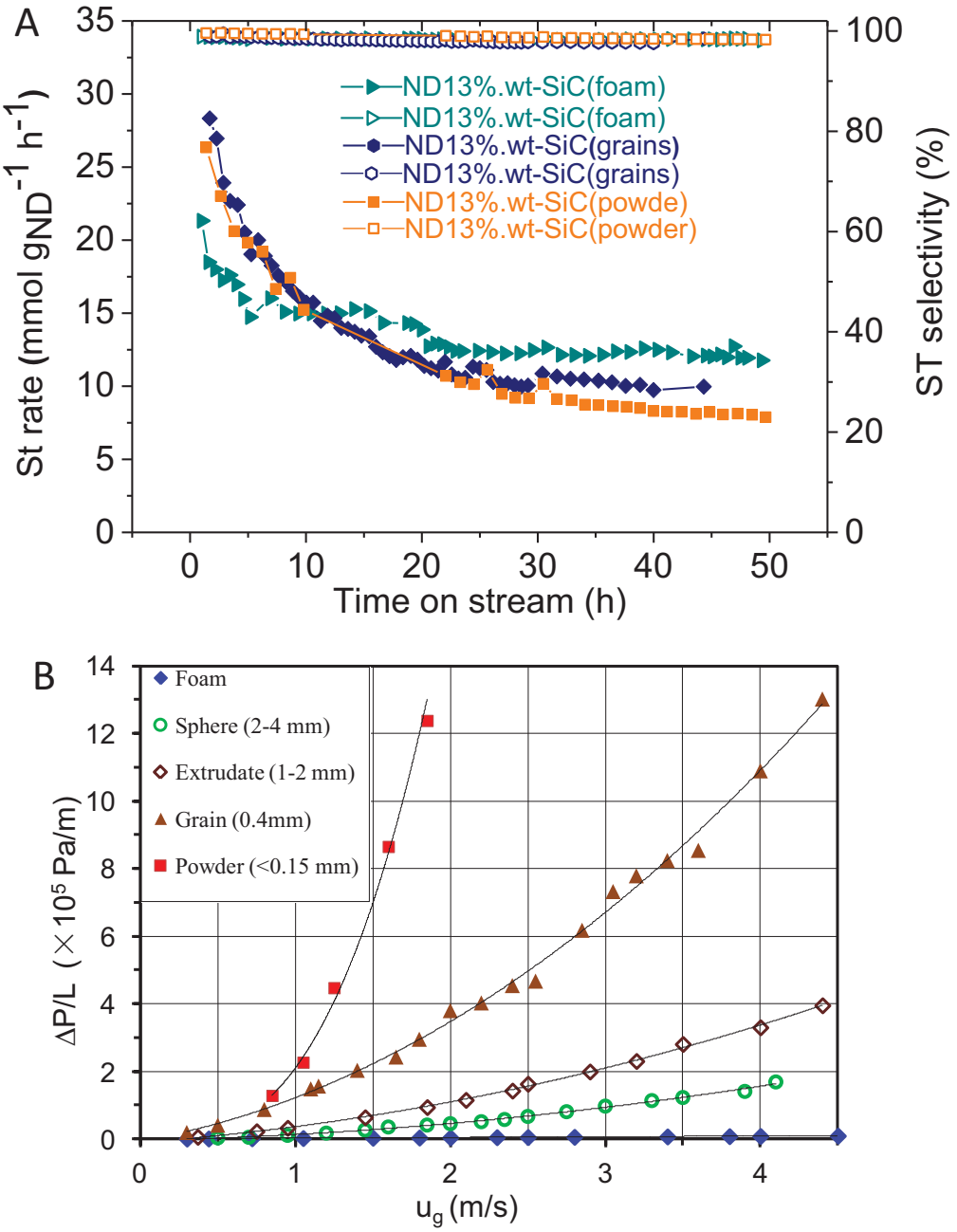

Figure 4. (A) Comparaison des performances catalytiques de catalyseurs à base de nanodiamants supporté sur différentes formes de SiC. (B) Mesures des chutes de pression obtenues sur différentes morphologies de SiC

La Figure 5 illustre les différentes grandes étapes (dispersion, macronisation, dopage) pour synthétiser les différents matériaux carbonés qui seront utilisés ensuite comme catalyseurs sans métaux dans la réaction de déshydrogénation directe de l'éthylbenzène en styrène.

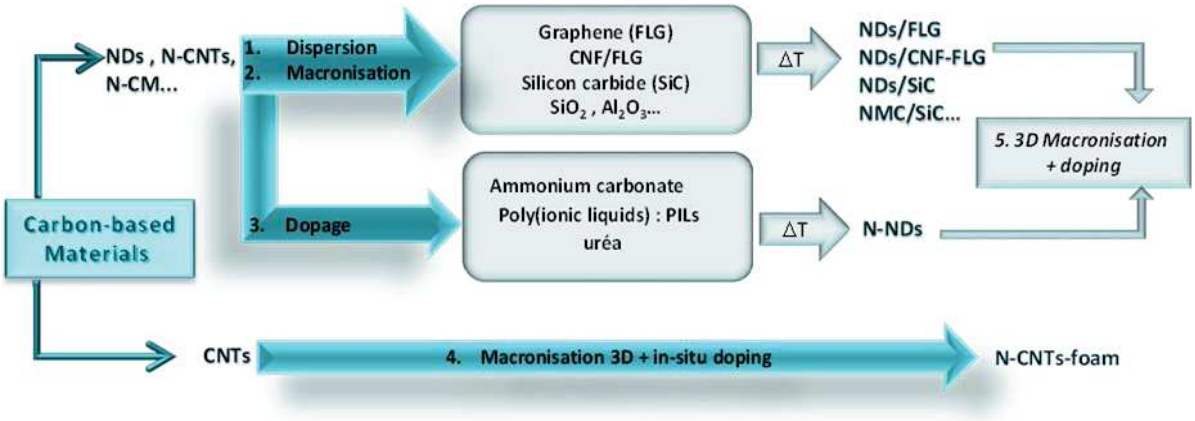

Figure 5. Illustration d'une série de matériaux carbonés synthétisés durant la thése, utilisés comme catalyseurs sans métaux dans la réaction de déshydrogénation de l'éthylbenzène en styrène.

Quelques images représentatives obtenues par microscopie électronique à balayage et en transmission sont présentées sur la Figure 6 pour illustrer les résultats discutés ci-dessus. Nous pouvons observer sur les clichés B, C, F et G une nette amélioration de la dispersion des nanodiamants supportés sur FLG ou sur SiC.

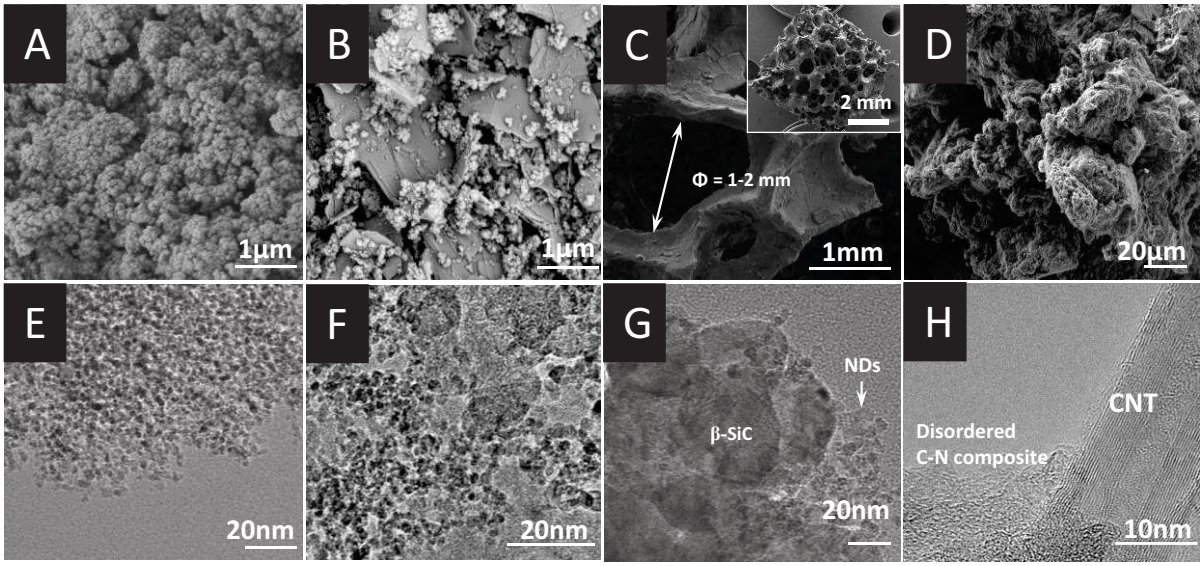

Figure 6 : Images obtenues par MEB et MET des catalyseurs sans métaux à base de nanodiamants (A, E) Nanodiamants, (B, F), Nanodiamants sur FLG, (C, H) Nanodiamants sur mousse de SiC et (E, I) Mousse de CNTs recouverte par une couche de carbone mésoporeux dopé avec de l'azote.

Différentes méthodes plus ou moins simples de synthèse de ces matériaux ont été utilisées (Figure 7): la technique de dépôt chimique en phase gaz (CVD)[19] notamment pour la synthèse des CNTs et CNFs et consistant à envoyer un mélange gazeux contenant la source de carbone (exemple C_2H_6/H_2) sur un catalyseur de croissance à base de Fer ou Nickel, le broyage mécanique dans le cas des mousses de CNTs, l'imprégnation directe et la sonication pour disperser les phases actives comme les nanodiamants.

Les matériaux ainsi synthétisés ont été soumis à différents traitements thermiques afin d'éliminer les éventuelles impuretés et de contrôler des paramètres physico-chimiques tels que la porosité et les espèces azotés présents à la surface (dans le cas du dopage à l'azote), ou le degré de graphitisation du matériau carboné, permettant ainsi d'obtenir une meilleure stabilité du catalyseur selon le type de test catalytique souhaité.

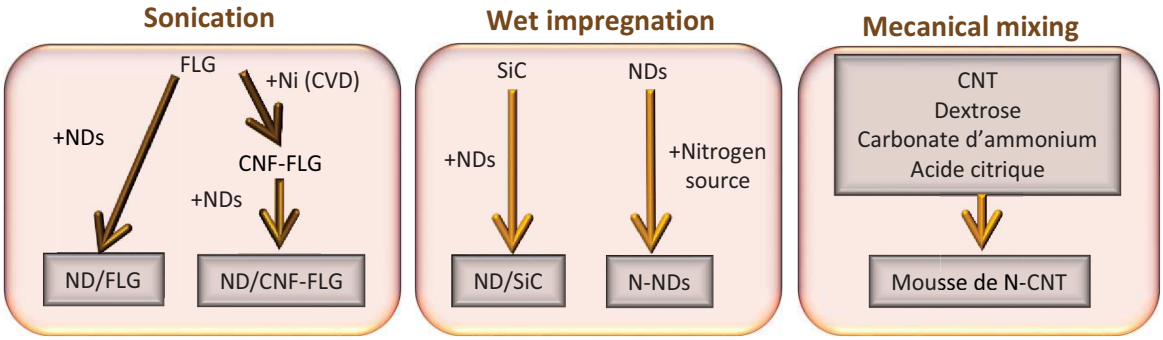

Figure 7 : Méthodes de synthèse des matériaux carbonés développés au cours de la thèse : dépôt par sonication, dépôt par imprégnation et dépôt par mélange mécanique.

Les résultats catalytiques obtenus sur ces catalyseurs sans métaux ont permis de montrer des performances catalytiques largement supérieures à celles du catalyseur industriel à base d'oxyde de fer (Figure 5), et s'avèrent être d'une très grande stabilité en fonction du temps de réaction, ce qui laisse entrevoir un possible développement de l'application à l'échelle industrielle.

Toujours dans cette même optique de développer un catalyseur performant sous une forme macroscopique, d'autres paramètres tels que le dopage ont aussi été étudiés durant cette thèse. Durant cette dernière décennie les matériaux à base de carbone 1D et 2D dopés ont suscité un intérêt croissant tant dans le milieu de la recherche que dans celui de l'industrie, en raison de leur capacité à promouvoir plusieurs procédés catalytiques très demandés, e.g. la réaction électrochimique de réduction de l'oxygène,[20,21] ou l'oxydation sélective d'impuretés pour la purification des gaz.[22]

Le dopage a l'azote est souvent réalisé dans des conditions de températures très élevées (650-800°C), ce qui rend le procédé peut rentable et les précurseurs d'azote utilisés sont souvent très toxiques, i.e. pyridine,[23] aniline,[24] melamine,[25] polypyrrole,[26] ou ammoniac[27,28]. Il est à noter également que pour les précurseurs de carbone on fait appel à des hydrocarbures qui présentent des problèmes d'inflammabilité non négligeables.

Face à ces contraintes nous avons développé un composite à base de nanotubes de carbone dopés par une méthode simple et à moindre coût. De plus, elle présente l'avantage d'utiliser des produits alimentaires donc plus écologiques et économiques, à savoir le dextrose (source de carbone), l'acide citrique (agent polymérisant) et le carbonate d'ammonium (source d'azote et agent porogène). Ce composite (mousse de N@CNT), synthétisé à basse température (170°C) et formé d'un enchevêtrement très dense de nanotubes de carbone, synthétisés par voie CVD, est constitué de méso et macrospores (Figure 8). Les mousses de N@CNT se présentent sous forme de mousse de dimension allant de 1 mm à plusieurs centimètres, et donc plus intéressants pour d'éventuelles applications industrielles. Les mousses de N@CNT présentent aussi des avantages non négligeables pour des applications en catalyse: grande surface effective, meilleure accessibilité aux réactifs, mise en forme contrôlée et une porosité ouverte adaptable en fonction des réactions visées, propriétés mécaniques intéressantes et enfin, une récupération facile du catalyseur dans les réactions en phase liquide.

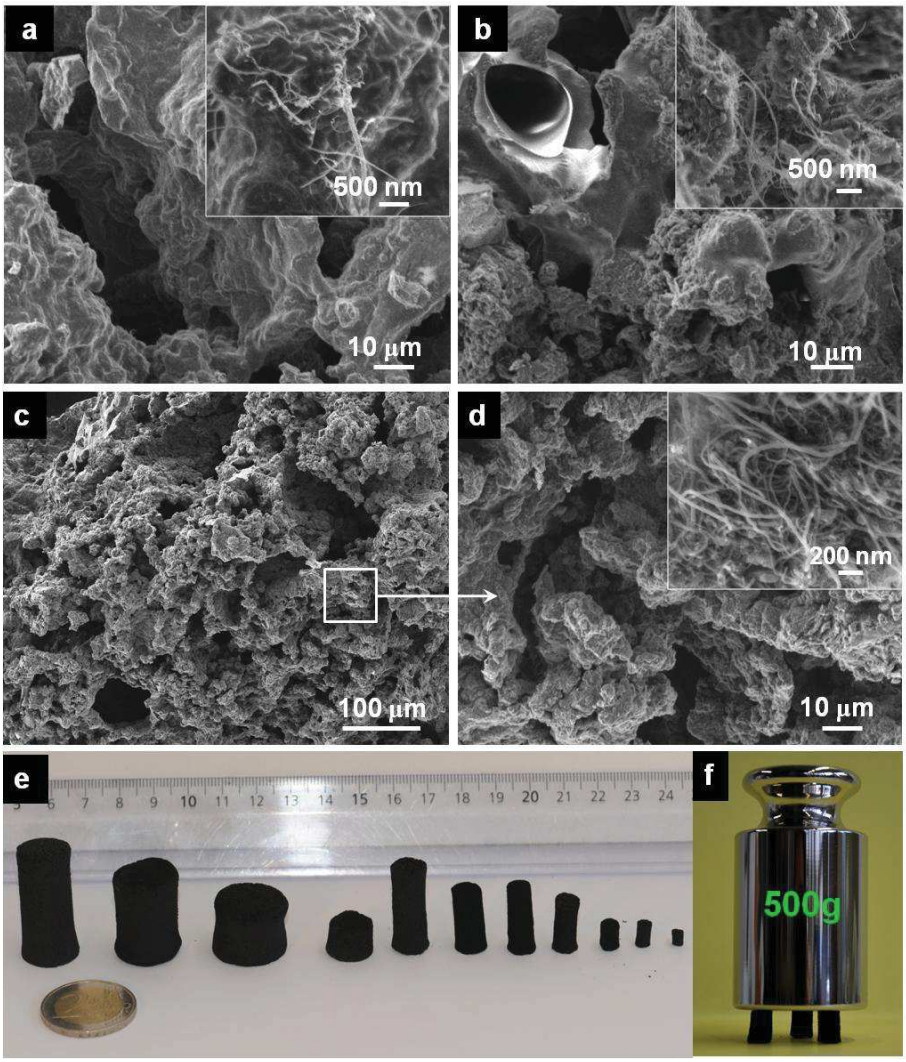

Figure 8. Image MEB (a,b) N@CNT foam après synthèse a basse température, (c,d) N@CNT obtenu après traitement thermique à 450°C sous air et (d,e) illustration des mises en forme possibles et de la résistance mécanique du composite

Ce type de catalyseur a montré des performances très prometteuses dans le domaine des piles à combustible où il témoigne d'une activité très similaire à celle du catalyseur commercial à base de platine supporté sur carbone (Pt-20 %/C), mais avec une désactivation moindre pour des tests longue durée. Dans la réaction de déshydrogénation de l'éthylbenzène en styrène la mousse de N@CNT présente une meilleure activité et stabilité comparée non seulement au catalyseur industriel mais aussi aux nanodiamants supportés.

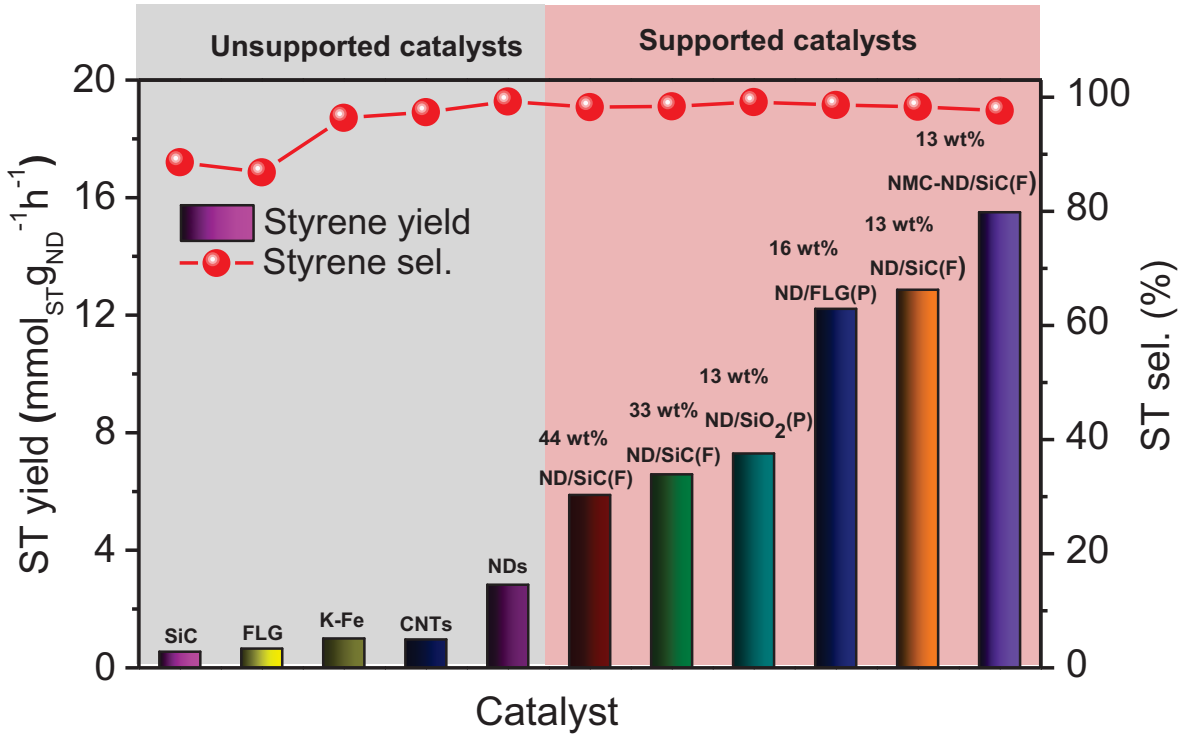

Figure 9. Comparaison des catalyseurs synthétisés à base de carbone (supportés ou non) avec le catalyseur industriel K-Fe. (Température de réaction 550°C, P = atm, [EB] = 2,8 vol.%)

La Figure 9 regroupe les performances catalytiques des divers catalyseurs « sans métaux » testés dans le cadre de cette thèse ainsi que celles des supports seuls et aussi du catalyseur industriel à base de fer. Mais le fait le plus marquant de la thèse est que nous avons réussi à développer un catalyseur carboné sans métaux (NMC-ND/SiC) et extrêmement actif à partir de produits alimentaires, à savoir le sucre, le citron et la levure (dextrose, acide citrique et carbonate d'ammonium respectivement). Ce matériau facile à synthétiser et à coût très modéré, innovant et révolutionnaire s'est avéré non seulement plus performant dans la réaction de déshydrogénation directe de l'éthylbenzène en styrène que le catalyseur industriel à base de fer, mais aussi plus performant que ses homologues à base de carbone. De plus, ce catalyseur présente aussi de meilleures performances que les catalyseurs traditionnels dans d'autres domaines d'applications très demandés, tels que le traitement des eaux, la détection de pesticides, la réduction de l'oxygène dans les piles combustibles ou l'oxydation partielle des traces d'H_2S en soufre élémentaire.

En conclusion, nous avons développé dans le cadre de la thèse une nouvelle famille de catalyseurs sans métaux à base de carbone supportés sur diverses structures hôtes macroscopiques pour le procédé de déshydrogénation sélective de l'éthylbenzène en styrène en absence de la vapeur d'eau. Les catalyseurs ainsi développés sont extrêmement stables

pour le procédé visé, permettant ainsi de réduire d'une manière significative les coûts énergétiques du procédé traditionnel où de larges quantités de vapeur sont co-injectées avec le réactif, mais aussi son impact sur l'environnement. Dans la suite de la thèse un nouveau procédé de synthèse des composites carbonés dopés avec de l'azote a également permis de synthétiser de nouveaux catalyseurs sans métaux extrêmement actifs et sélectifs pour le procédé testé dans la thèse, mais aussi dans plusieurs autres procédés tels que le traitement des eaux, la réduction de l'oxygène dans les piles à combustibles, l'oxydation sélective du sulfure d'hydrogène en soufre élémentaire, la détection des pesticides où des tests à grande échelle ont déjà été réalisés sur plusieurs localités en Alsace.

Références bibliographiques

(1) Bartholomew, C. H.; Farrauto, R. J. *Fundamentals of Industrial Catalytic Processes*; John Wiley & Sons, 2011.

(2) Geisst, C. R. *Encyclopedia of American Business History*; Infobase Publishing, 2009.

(3) Scheirs, J.; Priddy, D. *Modern Styrenic Polymers: Polystyrenes and Styrenic Copolymers*; John Wiley & Sons, 2003.

(4) Atanda, L. A.; Balasamy, R. J.; Khurshid, A.; Al-Ali, A. A. S.; Sagata, K.; Asamoto, M.; Yahiro, H.; Nomura, K.; Sano, T.; Takehira, K.; *et al.* Ethylbenzene Dehydrogenation over Mg3Fe0.5−xCoxAl0.5 Catalysts Derived from Hydrotalcites: Comparison with Mg3Fe0.5−yNiyAl0.5 Catalysts. *Appl. Catal. Gen.***2011**, *396*, 107–115.

(5) Shekhah, O.; Ranke, W.; Schlögl, R. Styrene Synthesis: In Situ Characterization and Reactivity Studies of Unpromoted and Potassium-Promoted Iron Oxide Model Catalysts. *J. Catal.***2004**, *225*, 56–68.

(6) Tope, B. B.; Balasamy, R. J.; Khurshid, A.; Atanda, L. A.; Yahiro, H.; Shishido, T.; Takehira, K.; Al-Khattaf, S. S. Catalytic Mechanism of the Dehydrogenation of Ethylbenzene over Fe–Co/Mg(Al)O Derived from Hydrotalcites. *Appl. Catal. Gen.***2011**, *407*, 118–126.

(7) Mimura, N.; Takahara, I.; Saito, M.; Hattori, T.; Ohkuma, K.; Ando, M. Dehydrogenation of Ethylbenzene over Iron Oxide-Based Catalyst in the Presence of Carbon Dioxide. *Catal. Today***1998**, *45*, 61–64.

(8) Janowska, I.; Vigneron, F.; Bégin, D.; Ersen, O.; Bernhardt, P.; Romero, T.; Ledoux, M. J.; Pham-Huu, C. Mechanical Thinning to Make Few-Layer Graphene from Pencil Lead. *Carbon***2012**, *50*, 3106–3110.

(9) Ayala, P.; Arenal, R.; Rümmeli, M.; Rubio, A.; Pichler, T. The Doping of Carbon Nanotubes with Nitrogen and Their Potential Applications. *Carbon***2010**, *48*, 575–586.

(10) Delgado, J. J.; Chen, X.-W.; Frank, B.; Su, D. S.; Schlögl, R. Activation Processes of Highly Ordered Carbon Nanofibers in the Oxidative Dehydrogenation of Ethylbenzene. *Catal. Today***2012**, *186*, 93–98.

(11) Belobrov, P. I.; Bursill, L. A.; Maslakov, K. I.; Dementjev, A. P. Electron Spectroscopy of Nanodiamond Surface States. *Appl. Surf. Sci.***2003**, *215*, 169–177.

(12) Miao, M. 3 - Carbon Nanotube Yarns for Electronic Textiles. In *Electronic Textiles*; Dias, T., Ed.; Woodhead Publishing: Oxford, 2015; pp. 55–72.

(13) Deng, J.-H.; Wang, F.-J.; Cheng, L.; Yu, B.; Li, G.-Z.; Hou, X.-G.; Li, D.-J.; Cheng, G.-A. Improved Field Emission of Few-Layer Graphene–carbon Nanotube Composites by High-Temperature Processing. *Mater. Lett.***2014**, *124*, 15–17.

(14) Man, H. B.; Zhang, K.; Robinson, E.; Chow, E. K.; Ho, D. Chapter 15 - Engineering Nanoparticulate Diamond for Applications in Nanomedicine and Biology. In *Ultananocrystalline Diamond (Second Edition)*; Gruen, O. A. S. M., Ed.; William Andrew Publishing: Oxford, 2012; pp. 493–518.

(15) Choi, J.; Chung, J. Evaluation of Potential for Reuse of Industrial Wastewater Using Metal-Immobilized Catalysts and Reverse Osmosis. *Chemosphere***2015**, *125*, 139–146.

(16) Schlögl, R. Chapter Two - Carbon in Catalysis. In *Advances in Catalysis*; Jentoft, B. C. G. and F. C., Ed.; Academic Press, 2013; Vol. 56, pp. 103–185.

(17) Zhang, J.; Su, D. S.; Blume, R.; Schlögl, R.; Wang, R.; Yang, X.; Gajović, A. Surface Chemistry and Catalytic Reactivity of a Nanodiamond in the Steam-Free Dehydrogenation of Ethylbenzene. *Angew. Chem. Int. Ed.***2010**, *49*, 8640–8644.

(18) Akhavan-Behabadi, M. A.; Shahidi, M.; Aligoodarz, M. R. An Experimental Study on Heat Transfer and Pressure Drop of MWCNT–water Nano-Fluid inside Horizontal Coiled Wire Inserted Tube. *Int. Commun. Heat Mass Transf.***2015**, *63*, 62–72.
(19) Gulino, G.; Vieira, R.; Amadou, J.; Nguyen, P.; Ledoux, M. J.; Galvagno, S.; Centi, G.; Pham-Huu, C. C2H6 as an Active Carbon Source for a Large Scale Synthesis of Carbon Nanotubes by Chemical Vapour Deposition. *Appl. Catal. Gen.***2005**, *279*, 89–97.
(20) Li, H.; Liu, H.; Jong, Z.; Qu, W.; Geng, D.; Sun, X.; Wang, H. Nitrogen-Doped Carbon Nanotubes with High Activity for Oxygen Reduction in Alkaline Media. *Int. J. Hydrog. Energy***2011**, *36*, 2258–2265.
(21) Hibino, T.; Kobayashi, K.; Heo, P. Oxygen Reduction Reaction over Nitrogen-Doped Graphene Oxide Cathodes in Acid and Alkaline Fuel Cells at Intermediate Temperatures. *Electrochimica Acta***2013**, *112*, 82–89.
(22) Chizari, K.; Deneuve, A.; Ersen, O.; Florea, I.; Liu, Y.; Edouard, D.; Janowska, I.; Begin, D.; Pham-Huu, C. Nitrogen-Doped Carbon Nanotubes as a Highly Active Metal-Free Catalyst for Selective Oxidation. *ChemSusChem***2012**, *5*, 102–108.
(23) Sharifi, T.; Nitze, F.; Barzegar, H. R.; Tai, C.-W.; Mazurkiewicz, M.; Malolepszy, A.; Stobinski, L.; Wågberg, T. Nitrogen Doped Multi Walled Carbon Nanotubes Produced by CVD-Correlating XPS and Raman Spectroscopy for the Study of Nitrogen Inclusion. *Carbon***2012**, *50*, 3535–3541.
(24) Nxumalo, E. N.; Nyamori, V. O.; Coville, N. J. CVD Synthesis of Nitrogen Doped Carbon Nanotubes Using Ferrocene/aniline Mixtures. *J. Organomet. Chem.***2008**, *693*, 2942–2948.
(25) Zhong, Y.; Jaidann, M.; Zhang, Y.; Zhang, G.; Liu, H.; Ioan Ionescu, M.; Li, R.; Sun, X.; Abou-Rachid, H.; Lussier, L.-S. Synthesis of High Nitrogen Doping of Carbon Nanotubes and Modeling the Stabilization of Filled DAATO@CNTs (10,10) for Nanoenergetic Materials. *J. Phys. Chem. Solids***2010**, *71*, 134–139.
(26) Xu, G.; Ding, B.; Nie, P.; Shen, L.; Wang, J.; Zhang, X. Porous Nitrogen-Doped Carbon Nanotubes Derived from Tubular Polypyrrole for Energy-Storage Applications. *Chem. Weinh. Bergstr. Ger.***2013**, *19*, 12306–12312.
(27) Yu, D.; Zhang, Q.; Dai, L. Highly Efficient Metal-Free Growth of Nitrogen-Doped Single-Walled Carbon Nanotubes on Plasma-Etched Substrates for Oxygen Reduction. *J. Am. Chem. Soc.***2010**, *132*, 15127–15129.
(28) Maldonado, S.; Morin, S.; Stevenson, K. J. Structure, Composition, and Chemical Reactivity of Carbon Nanotubes by Selective Nitrogen Doping. *Carbon***2006**, *44*, 1429–1437.

Chapter 1

Introduction

1. Generalities about styrene

World population is facing an unprecedented growth since the last decades and alongside with this phenomenon, goods demand also following the same trend and even more for the future. On the same time, the amount of energy required for producing goods should be reduced as much as possible in order to cope with the general policy regarding the problems linked with the greenhouse gas.[1]

Catalysis is contributed to more than 80 % of the whole chemical processes for producing day life products.[2] Catalysts allow one to reduce the energy and waste products in each chemical conversion step which is in line with the more stringent legislation dealing with the global climate change linked to an increasing energy demand worldwide. Nowadays, most of the catalytic systems are constituted by an active phase, i.e. metals, oxides, alloys, sulfides, carbides, etc,[3,4,5,6,7] deposited on an appropriate support. The support provides a high surface area to efficiently disperse the active phase in order to maximize the catalytic effective surface area for the reaction.[8] The support porosity is also finely tuned in order to avoid as much as possible micropores as this later will lead to an apparent higher residence time of the intermediate product, and thus, favoring the formation of by-products which contribute to the lowering of the overall selectivity of the process. The support also prevents catalytic activity lost during the course of the reaction through the active phase sintering or encapsulation by side-products. However, deactivation through sintering and catalytic surface poisoning or encapsulation always occur leading to a gradual catalytic deactivation. In order to maintain the catalytic performance the spent catalyst is submitted to a periodical oxidative regeneration which allows the removal of deposit residues on the active phase surface or in the catalyst pore size.[9] The repeated regeneration could induce slow deterioration of the catalyst performance which calls for complete replacement of the catalyst. Therefore, it is of interest to develop new catalytic systems which exhibit higher resistance towards sintering and encapsulation through carbonaceous residue deposit which allow one to avoid frequent oxidative regeneration which is cost incentive for the process.

Styrene (ST), also known as phenylethylene, vinylbenzene, styrol, or cinnamene, C_6H_5–$CH{=}CH_2$, is one of the most important unsaturated aromatic monomers in modern petrochemical industry. It occurs naturally in small quantities in some plants and foods. In the nineteenth century, styrene was isolated by distillation of the natural balsam storax.[10] It has been identified in cinnamon, coffee beans, peanuts, and it is also found in coal tar.

The world production of styrene monomer is significantly increased since the last decade to reach about 26 Mt per annum in 2012 and continue to face a high growing rate in the future (Fig. 10).[11] The main licensors of styrene production processes are Badger, Lummus, LyondellBasell, Shell, DOW and BASF. The annual production of styrene in the U.S.A. already exceeds 6 Mt and continuous growing.[78]

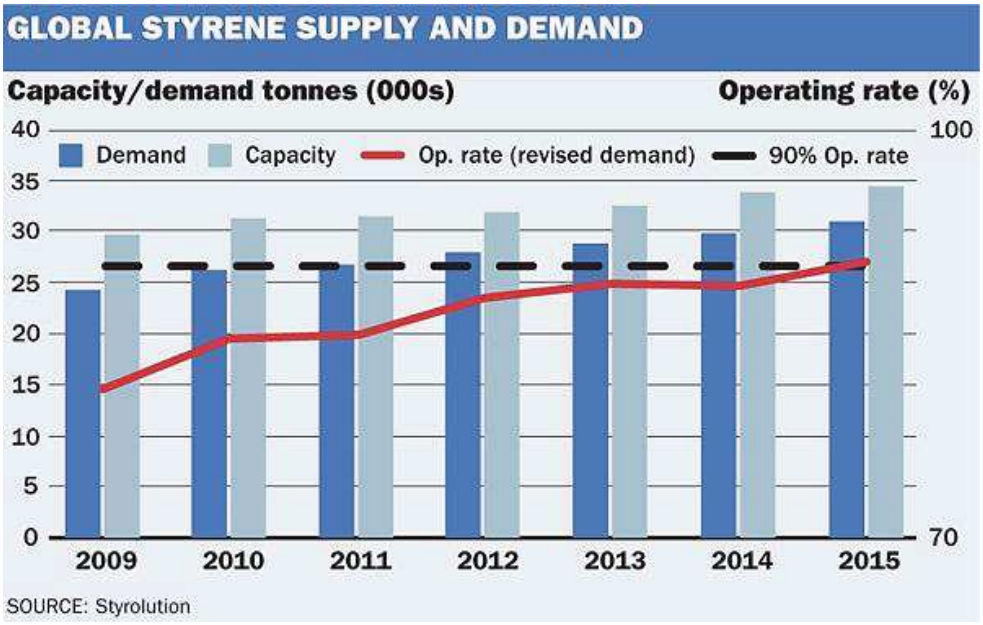

Figure 10. World styrene supply and demand during the last few years.[11]

The styrene commercial processes were developed in the 1930s independently and simultaneously by BASF in Germany (Figs. 12 and 13) and by DOW Chemical in the USA.[12,13] The need for synthetic styrene – butadiene rubber (Styrene – Butadiene Rubber (SBR)) during World War II provided the impetus for large-scale production.

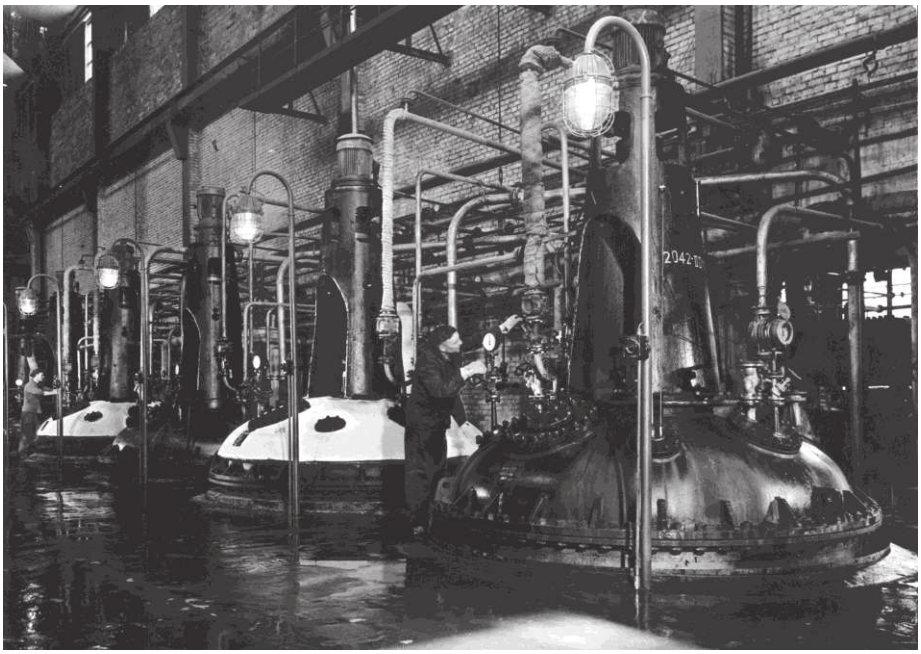

Figure 12. Reaction kettles in the BASF polystyrene production plant.[13]

Styrene is the raw material involving in the production of various polymeric materials, the most important being polystyrene, synthetic rubbers, plastics, acrylonitrile–butadiene–

styrene (ABS) and styrene-acrylonitrile (SAN) resins, latex (SBL). The international styrene industry is a diversified capitalizing approximately USD 60 billion (annually) comprising thousands of companies, facilities, and employees throughout the world. Styrene owns its popularity to the easily reacting double bond that can undergo polymerization reactions with themselves or with other monomers.

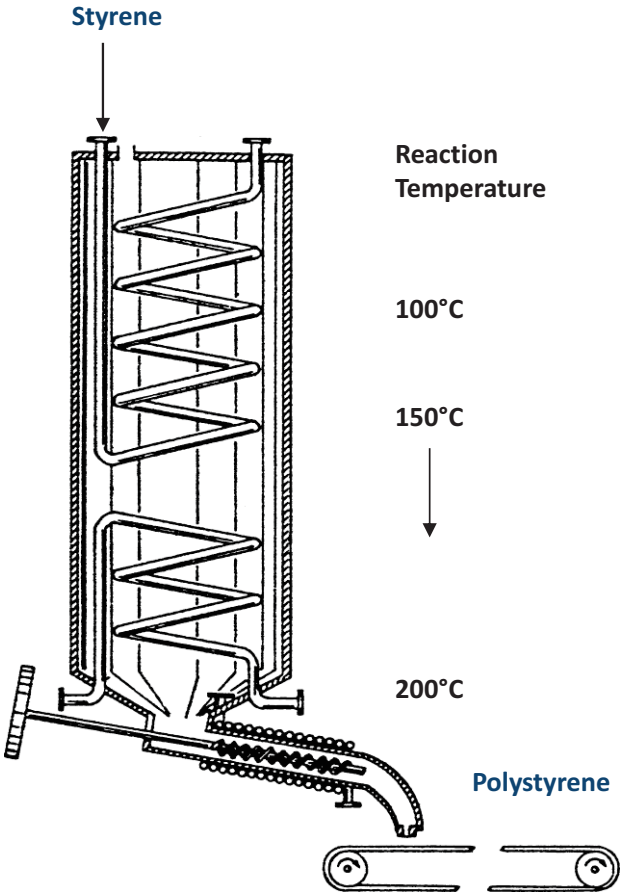

Figure 13. Schematic of BASF's early tower process for the continuous polymerization of styrene. This configuration was designed by Wulff and Dorrer in the early 1930s. Polymerization was thermally initiated and the exothermicity was controlled by heat transfer tubes.[13]

Manufacturers use styrene-based resins to produce a wide variety of everyday goods ranging from cups and utensils to furniture, bathroom, and kitchen appliances, hospital and school supplies, boats, sports and recreational equipment, consumer electronics, automobile parts, and durable lightweight packaging of all kinds (Fig. 14A). It provides essential raw materials and products for nearly all major European, American, and Asian industries, from automobiles and construction to electronics and packaging (Fig. 14B), just to cite a few.

A

B

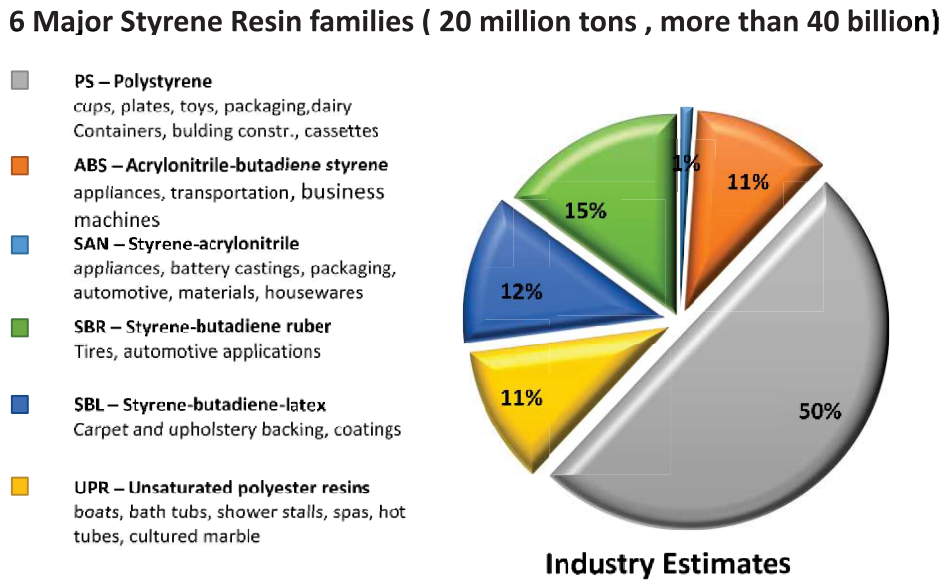

Figure. 14. Examples of day-life products produced from styrene.

Currently styrene is industrially produced mainly by two catalytic processes. In the first one, which is a modification of the Halcon process, styrene is obtained as a by-product in the epoxidation of propene with ethylbenzene hydroperoxide over Mo complex-based catalysts. This process is commercialized by ARCO Chemical (formerly Oxirane) and by Shell. About 2.5 kg styrene is obtained per kilogram of propylene oxide. Approximately 1.2×10^6 t/year of styrene are currently produced with this technology.[11] The second one and also the most

important manufacturing route to styrene is the direct dehydrogenation (DH) of ethylbenzene (EB), which accounts for more than 90% of the worldwide capacity production.[14]

1.1. Physical properties of ethylbenzene

Under ordinary conditions, ethylbenzene is a clear, colorless liquid with a characteristic aromatic odor. Ethylbenzene is an irritant to the skin and eyes and is moderately toxic by ingestion, inhalation, and skin adsorption. The main physical characteristics of ethylbenzene are summarized in Table 1.

Table 1. Physical characteristics of ethylbenzene.

M(C_6H_5-CH_2-CH_3)	106.17	Flash point, Tag Closed Cup	15°C
Boiling point (101 kPa)	136.19°C	Autoignition point	460°C
mp	-94.9°C	Refractive index, n_D (20°C)	1.49588
Heat of vaporization (ΔH_y)	335 J/g	Density, g/mL (20°C)	0.8669

1.2. Physical properties of styrene

Styrene is a colorless liquid with a distinctive, sweetish odor. Styrene is miscible with most organic solvents in any ratio. It is a good solvent for synthetic rubber, polystyrene, and other non- cross-linked high polymers. Styrene and water are sparingly soluble in each other. Some physical properties of styrene are summarized in Table 2. Vapor pressure is a key property in the design of styrene distillation equipment.

Table 2. Physical characteristics of styrene.

M(C_6H_5-CH_2=CH_2)	145.15	Flash point, Tag Closed Cup	31.1°C
Boiling point (101 kPa)	145.15°C	Autoignition point	490°C
mp	-30.6°C	Refractive index, n_D (20°C)	1.5468
Heat of vaporization (ΔH_y)	421.7 J/g	Density, g/mL (20°C)	0.9050
Flammable limits in air	1.1-6.1 %	Heat of polymerization (ΔH_p) (20°C)	-69.8 kJ/mol

2. Industrial process for styrene production

The industrial catalyst is the iron-based catalyst promoted with potassium and different foreign elements, in order to increase the lifetime of the catalysts, has been extensively used for styrene production.[15] The iron promoted potassium catalyst was constituted by about 84 wt. % of iron oxide Fe_2O_3 (hematite) and at least 13 wt. % of potassium oxide, small amounts of alumina (Al_2O_3) and chromium (Cr_2O_3) which acting as structural promoters to increase the lifetime of the catalysts. Oxides such as MgO, Cr_2O_3, CeO_3 and MoO_3 have also been incorporated inside the iron-based catalyst to improve the dehydrogenation selectivity, but have virtually no effect toward the dehydrogenation activity. The role of the promoter, i.e. potassium, is to increase the DH activity by more than one order of magnitude compared to the DH activity of iron oxide, and also to increases the selectivity to styrene as well as the stability of the catalyst under operation.

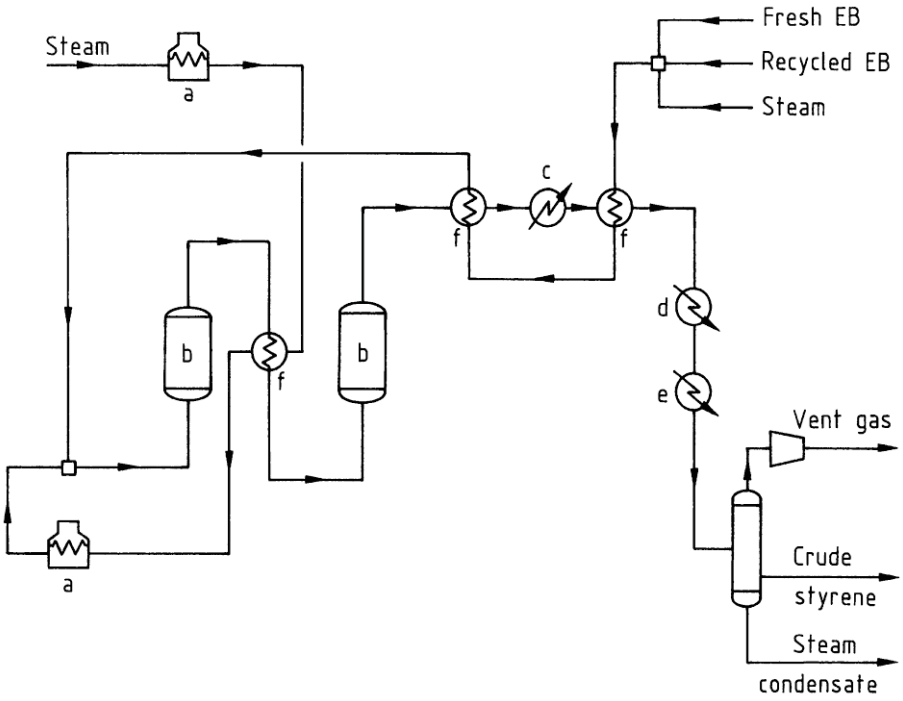

Figure 15. Adiabatic dehydrogenation of ethylbenzene (EB). a) Steam superheater, b) Reactor, c) High-pressure Steam, d) Low-pressure Steam, e) Condenser, f) Heat exchanger.[16]

The process can be run industrially either adiabatically or isothermally over a fixed bed reactor in which the reactants are passed over the catalyst bed employing radial or axial flow. Over 75 % of all operating styrene plants carry out the dehydrogenation reaction adiabatically[17] in multiple reactors or reactor beds operated in series (Fig. 15).The heat

necessary to the reaction is provided at the inlet to each stage, either by injection of super-heated steam or by indirect heat transfer. The inlet temperature of the feed is about 910 K and the molar ratio of steam to EB is varies from 7 to 12, depending on the catalyst formulation and type of the used process. EB conversion in the first reactor is about 35 mol% to give a total conversion of 65 mol% for the process. This process is licensed by Badger, ARCO and Shell etc.

Isothermal dehydrogenation process (Fig. 16) was pioneered by BASF and has been used by them for many years. The reactor is built like a shell-and-tube heat exchanger, heated indirectly by the hot flue gas. Vaporized ethylbenzene is mixed with steam (steam/EB molar ratio of 3 - 6) and passed into the tubular reactor (600°C) filled with suitable catalyst.

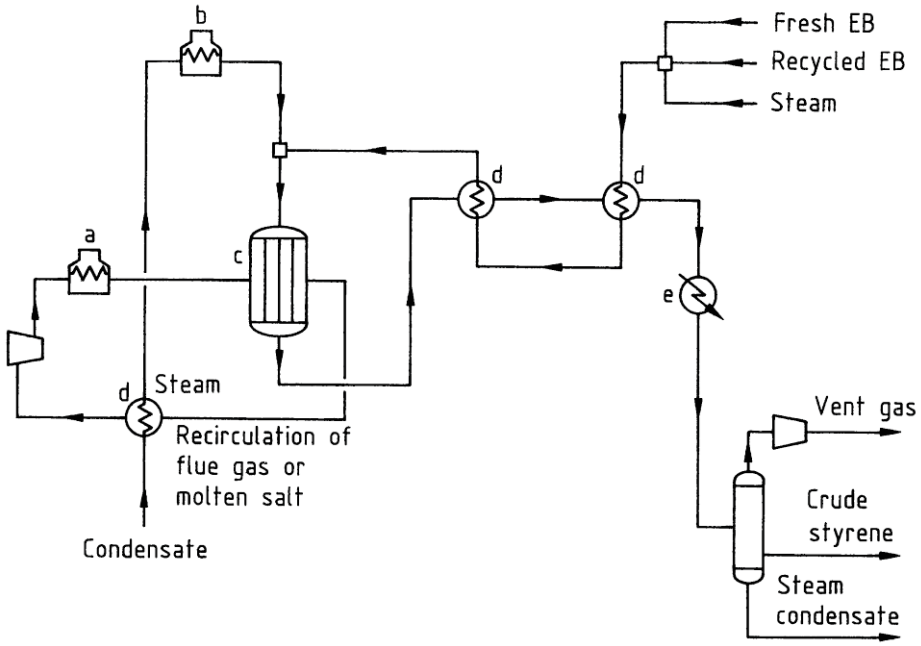

Figure 16. Isothermal dehydrogenation of ethylbenzene (EB). a) Heater, b) Steam superheater, c) Reactor, d) Heat exchanger, e) Condenser.[16]

This reaction proceeds thermally with low yield and catalytically with high yield. As it is a reversible gas- phase reaction producing 2 mol of product from 1 mol of starting material, low pressure favors the forward reaction. It is mostly established that one of the most important role of potassium promoter consist of selectively turn the catalyst toward the formation of an active phase $KFeO_2$.[18,19,20] Hirano[14,21] was the first who identified by XRD and XPS analysis that the $KFeO_2$ are the active phase, and then work developed by Muhler[22] demonstrated by a revolutionary model that the active state is resulted from an equilibrium between $KFeO_2$ and $K_2Fe_{22}O_{32}$. The active phase can be reduced by hydrogen to KOH and Fe_3O_4 (magnetite), leading to an irreversible deactivation. The schematic life cycle of the traditional potassium-promoted iron-based catalyst is illustrated in Figure 17.

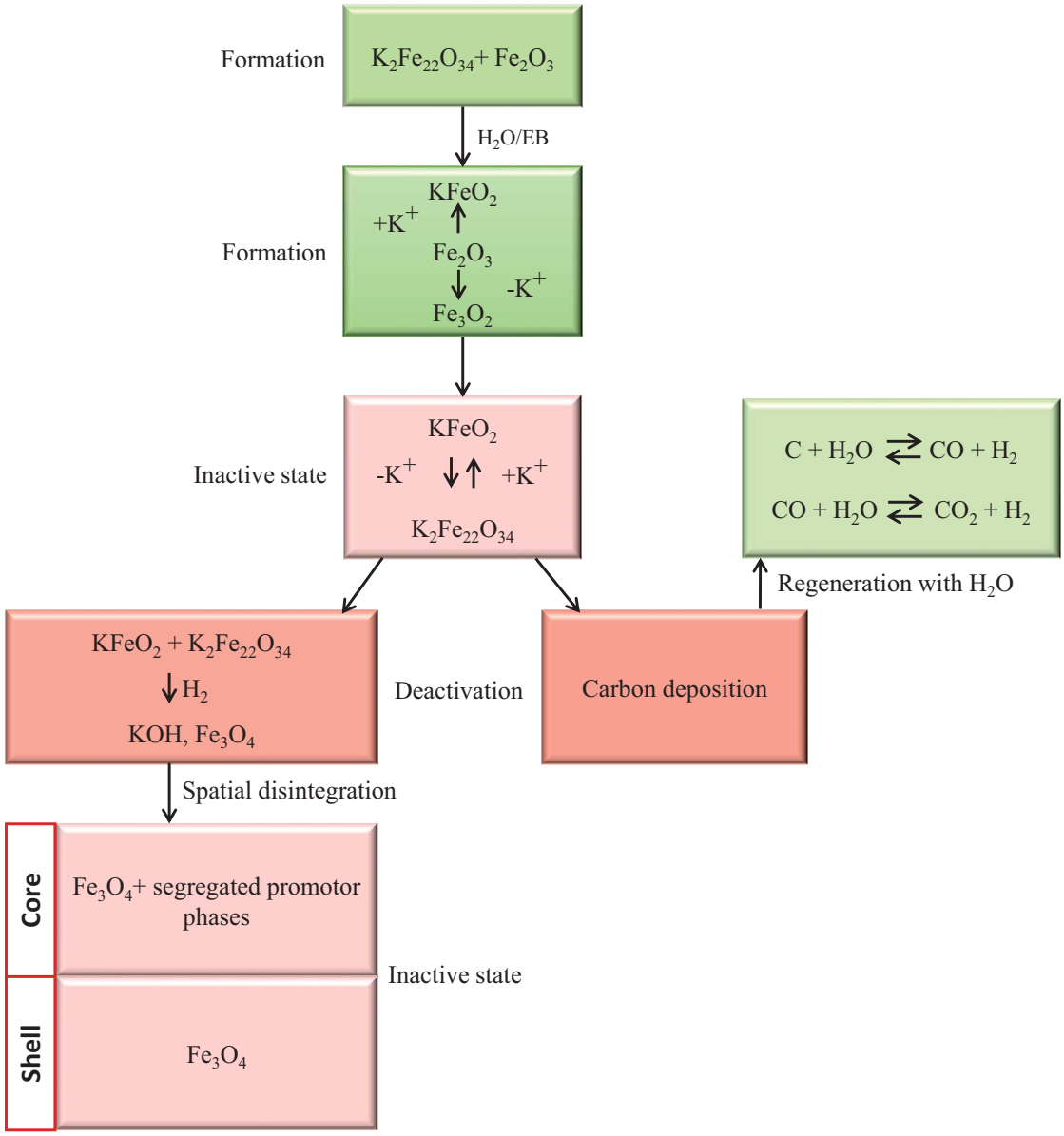

Figure 17. Schematic life cycle of the iron-based catalyst with potassium without any promotor additives.[22]

The C-H groups of the EB-ethyl group get deprotonation at basic oxygen sites and two hydroxyl groups are formed at the surface of the catalyst.[23] The active state of the Fe–K catalyst was analyzed by transient response experiments and it has been reported that initially high activity was correlated with Fe^{3+} state and the reduction from Fe^{3+} to Fe^{2+} state caused deactivation of the catalytic activity.[24] Simultaneously or subsequently an electron transfer to acidic Fe^{3+} sites is required before the styrene molecule can desorbs from the catalyst surface. Finally, the hydrogen atoms forming the two hydroxyl groups recombine to form hydrogen molecule which further desorb from the catalyst surface, the reduced Fe^{2+} species get re-

oxidation to Fe^{3+}, and the basic oxygen sites are reestablished for the next turnover cycle. In the proposed active $KFeO_2$ surface phase, potassium saturated Fe-O bonds increase the basicity of the oxygen sites. They also must be located in an adequate geometry with respect to the acidic Fe^{3+} sites, so that an effective deprotonation of the EB molecule becomes possible.

The EB dehydrogenation is an endothermic and reversible reaction with an increase in the number of molecules in agreement with the reaction mechanism. The dehydrogenation reaction was conducted at temperature at 600-700°C,[25,26,27,28] high equilibrium conversion can be achieved by a high temperature and a low EB partial pressure. The main reaction product is hydrogen and styrene (Equation 1). The selectivity of the process is extremely high (> 95%) and the main reaction products are hydrogen and styrene. However, it is worthy to note that the conversion per pass is not complete and the exit product also contains residual ethylbenzene and steam which calls for recycling. The typical by-products of the EB dehydrogenation are benzene (~1%) and toluene (~2%) (Equations 2 and 3). Benzene can be recycled to the alkylation process to make EB and toluene can be sold for a by-product credit. Hydrogen can also be removed from the product stream and sold, if it can be used in the nearby area. Otherwise, its heating value can be used for the process itself. The unreacted EB was recycled in the DH process.

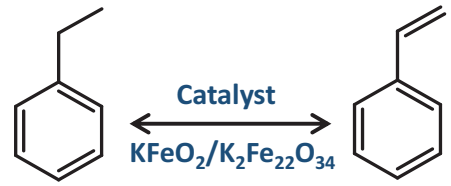

+ H_2 ΔH= 124.9 KJ.mol^{-1} (1)

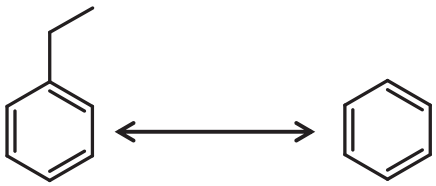

+ $H_2C=CH_2$ ΔH= 101.8 KJ.mol^{-1} (2)

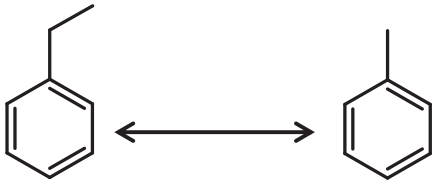

+ CH_4 ΔH= -64.5 KJ.mol^{-1} (3)

During the course of the reaction the iron active sites were gradually deactivated by carbonaceous residues generated by the reaction leading to a drastic decrease of the DH activity. In order to maintain the active sites from these carbonaceous residues an excess of steam was co-feeded with the reactant onto the catalyst,[18] which could block the most surface sites resulting the sharply deactivation (Equation 4). When potassium is incorporated into the

iron oxide catalyst, the catalyst becomes self-cleaning (through enhancement of the reaction of carbon with steam to give carbon dioxide, which is removed in the reactor vent gas). The overall effect of the increase of the steam-to-hydrocarbon ratio is to increase the activity, the selectivity at the same level of conversion (or the conversion at the same value of selectivity), the lifetime and stability of the catalyst. It is believed that water vapor does not participate in the reaction itself, i.e. not involved in the rate determining step of the reaction mechanism, but acts purely as an oxidant agent to prevent active site encapsulation by carbonaceous residue (Equation 5) and also as inert dilution agent to lower the partial pressure of ethylbenzene, shifting the equilibrium toward styrene and minimizing the loss to thermal cracking. The steam also supplies the necessary heat to the reaction according to the endothermic character of the process. Indeed, for such endothermic reaction the catalyst temperature decreases as increasing the dehydrogenation activity, i.e. the ethylbenzene conversion per unit time, which will further lead to a decrease of the catalyst performance. Steam presence allows one to reduce such catalyst temperature lost during the course of the reaction.

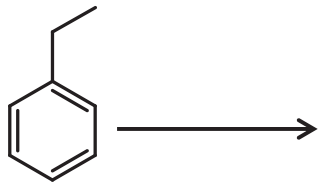

$$\rightarrow \quad 8C + 5H_2 \qquad \Delta H = 1.72\ KJ.mol^{-1} \tag{4}$$

$$C + 2H_2O \longrightarrow CO_2 + 2H_2 \qquad \Delta H = -64.5\ KJ.mol^{-1} \tag{5}$$

The general accepted reactions and side reactions taking place during the EB dehydrogenation other than the dehydrogenation of ethylbenzene to styrene are mentioned above (some of these reactions are thermodynamically favored at low temperature, while others are at higher temperatures),[29] and phenomena which generates these processes are listed in Figure 18.

Direct reactions

Ethylbenzene ⟷ styrene + H_2	(dehydrogenation)
Ethylbenzene ⟶ benzene + C_2H_4	(cracking)
Ethylbenzene + H_2 ⟶ toluene + CH_4	(hyrogenolysis/hydrocracking)
Ethylbenzene + CO_2 ⟶ CO + H_2	(dry reforming)

Consecutive reactions

H_2 + CO_2 ⟷ H_2O + CO	(reverse water-gas-shift)
Styrene ⟶ precursors of coke	(oligomrisation, polymerization, condensation)
Precursors of coke ⟶ coke + H_2	(dehydrogenation)
(Precursor of) coke + CO_2 ⟷ CO	(reverse Boudouard)

Figure 18. Nature of the reactions taking place during the dehydrogenation of ethylbenzene to styrene

2.1. The limitations of current industrial processes

The problems encountered in the current ethylbenzene dehydrogenation process are summarized below:

1) The dehydrogenation of EB to styrene is equilibrium limited and highly endothermic ($\Delta H°_{298}$ =28.1 kcal/mol). The reversibility of the dehydrogenation process thermodynamically hinders maximum yields of styrene. The technical EB conversion is limited below 60%, to keep an acceptable high selectivity to styrene. The limited styrene yields and the low EB conversions achieved per pass through the reactor lead to the necessity of a reactant recycle. Indeed, for styrene polymerization applications, styrene has to be purified to more than 99.8%. The separation of un-reacted EB and co-products from styrene is costly due to the close boiling points, especially for EB (136°C) and styrene (145°C).

2) The high sensitive of the iron-based catalyst towards coke formation and encapsulation along with the high energy consumption due to the use of excess steam for preventing DH activity loss during the process. Indeed, the high amount of steam leads to a huge energy consumption of the process which can be estimated to be 1.5×10^9 cal/ ton of styrene[30] and also to a large amount of wastewater containing trace amount of hydrocarbons which needs to be recycled downstream. The use of steam causes also other serious limitations, namely, (i) consumption of ethylbenzene and of styrene by steam-reforming, (ii) chemical reaction of

steam with K_2CO_3 forming free KOH leading to the gradual loss of the promoter and finally, to the irreversible catalyst deactivation.
3) The K-Fe catalyst slowly deactivates due to surface encapsulation by coke, despite in the presence of steam, with operation and typically needs to be replaced every 1 - 2 year. In view of the scale of the reactors used, this is an expensive operation.

The number of problems that are encountered in the current commercial process for styrene production is the driving force to develop alternative technologies. It is therefore of high interest to find new catalysts which could be operated under a more environmental conditions, i.e. higher stability against deactivation by carbonaceous residue in order to reduce or eventually phase-out the need of steam in the process, while keeping similar catalytic performance. The catalyst should also display a high catalytic stability as a function of time on stream in order to reduce as much as possible replacement and solid waste generation. The catalyst needs to be robust in terms of oxidative resistance in order to withstand periodical oxidative regeneration. The catalyst production price should be also low enough for being competitive with that of the iron-based catalyst operated nowadays in the industrial process. Last but not least the catalyst should also be easy to produce in macroscopic shape for coping with the industrial parameters of operation.

3. Carbon-based composites as metal-free catalysts

Carbon-based materials, i.e. carbon black, carbon nanotubes/nanofibres, graphene and nanodiamonds[31,32,33,34,35] have received an ever increasing scientific and industrial interest during the last decade[36] for several potential fields of application such as electronic,[37] energy conversion and storage,[38] medicine,[39] wastewater treatment[40] and catalysis.[41]

Carbon materials, and especially nanocarbon consisting of carbon nanotubes/nanofibers, graphene and nanodiamonds (Figure 19), just to cite a few, play currently a privileged role and interest in the research and industrial environments, due to their numerous attracting properties such as high surface area and high open porosity, that can also be tailored depending to the downstream application, mechanical stiffness, chemical inertness, large ability to be chemically functionalized.[42,43,44] The surface hydrophobicity/hydrophilicity of these carbon-based materials can be also tuned as well in order to adapt the catalyst to the reaction needs. These noticeable features make carbon-based materials as a potential candidate in the field of catalysis in numerous processes, either as catalyst support or directly as catalytic material itself .[45,46,47] Carbon-based materials have witnessed a large scientific and industrial interest since the last few years thanks to the growing knowledge on the controlled

synthesis and in-depth characterization, involving both experimental and theoretical studies, which allow one to set rational bases for their subsequence development. The large possibility of doping the carbon-based materials with numerous foreign elements also opens a new area for potential catalytic applications reaching far beyond the fields under development today. Taken into account the large number of catalytic processes that involve nanocarbons, we will restrict the discussion here to the field of oxidative dehydrogenation and direct dehydrogenation processes. For the synthesis and other applications one can find several update reviews devoted to such area.[48,49,50,51,52]

The recent reports published by different research groups have evidenced that nanocarbon-based materials can be efficiently employed as metal-free catalysts with high performance and stability in both oxidative and direct dehydrogenation processes for the styrene production in place of the industrial iron-based ones.

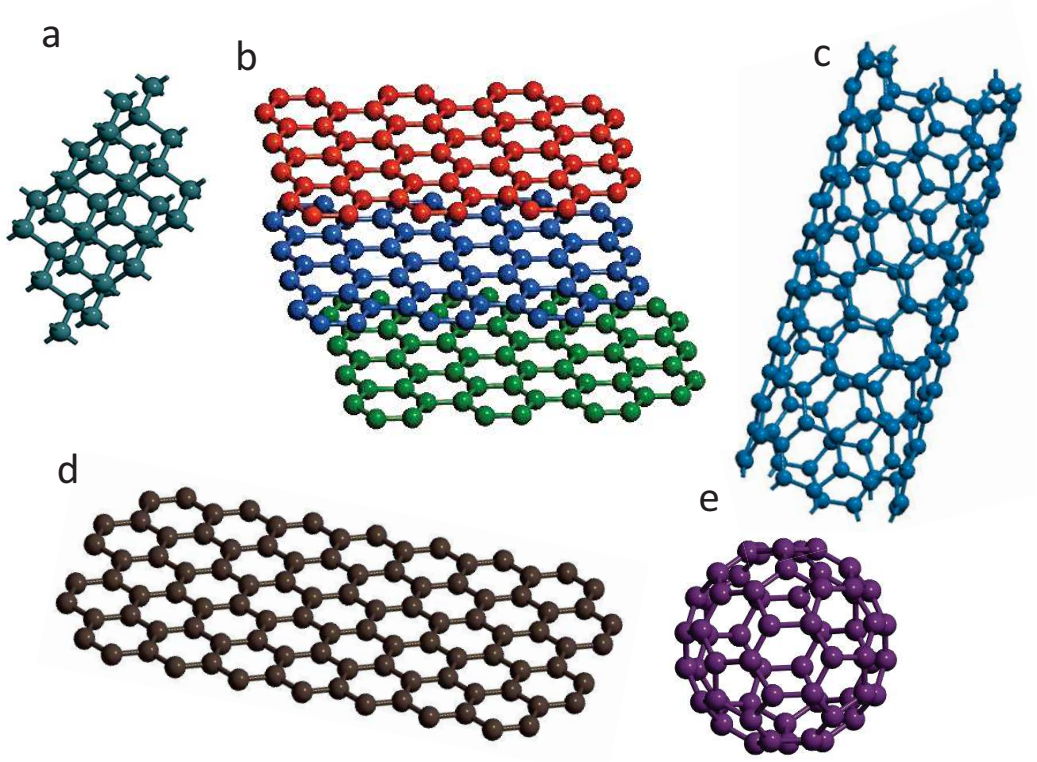

Figure 19. Crystal structures of different allotropes of carbon. (a) nanodiamond (0D), (b) graphite (3D), (c) graphene (2D), (d) nanotubes (1D), and (e) buckyballs (0D)

Indeed, alternative catalytic routes involved carbon-based metal-free catalysts have been extensively studied during the last decades deal with the direct dehydrogenation (DH) or oxidative dehydrogenation (ODH) processes.[53,54] Numerous articles have pointed out that the oxidative dehydrogenation (ODH), using carbon allotropes (Fig. 19), is an elegant and very promising alternative to conventional dehydrogenation process where deactivation represents

the main drawback. The metal-free carbon-based catalysts exhibit a relatively high DH or ODH performance compared to the traditional catalysts along with an extremely high stability as a function of time on stream thanks to their high resistance towards coke encapsulation. The high catalytic performance could be directly attributed to the high effective surface area of these nanocarbon-based catalysts which providing higher contact surface between the active sites and the reactant. The nanoscopic dispersion of the active phase present on such carbon-based catalysts also plays a vital role for the catalytic process as well.

However, aside from the fundamental point of view these nanocarbons should be produced in a macroscopic shape in view of the future industrial development. Indeed, nanocarbons are present in a powder form and thus, generate a large pressure drop across the catalyst bed which could significantly modify the activity and selectivity of the process (Figure 20). The macronization can be performed either by self-assembly of the carbon materials itself or by decorating them on macrocopic support such as alumina or silicon carbide, examples of these materials are presented in Figure 21.

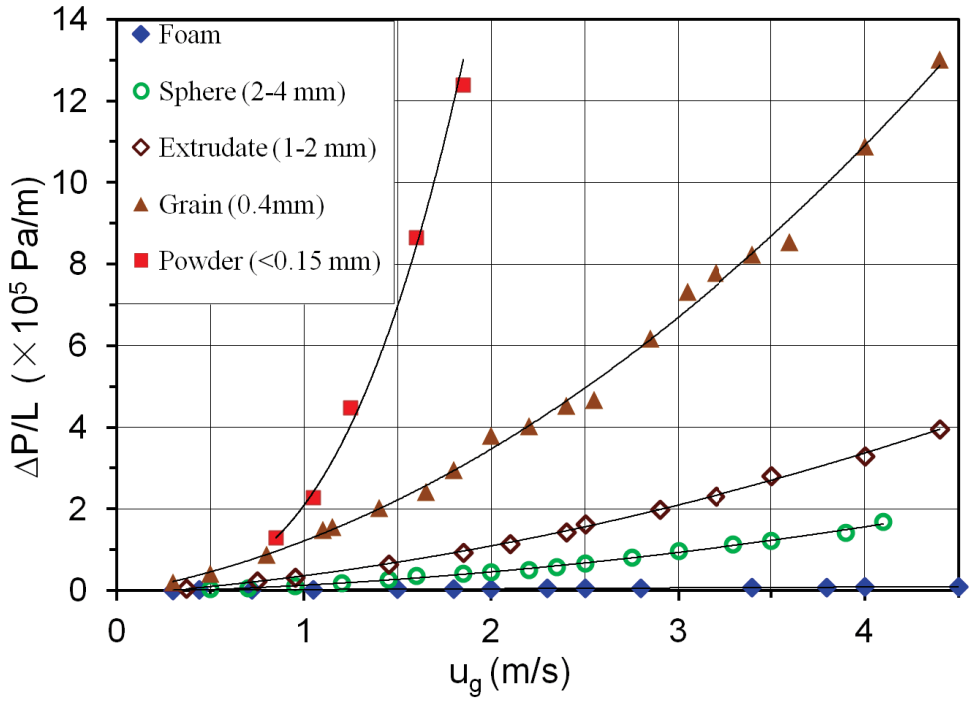

Figure 20. Pressure drop measurements on the various macroscopic composites with different shapes.

The nanoscopic shape also generates problems linked with the handling and transport as well as those linked with the charging and discharging of the catalyst bed as well. Figure 21 summarizes the different dimensions of these nanocarbons including the supported form for

industrial applications. It is worthy to note that the macroscopic shaping not only reduce the problem of pressure drop and the dispersion of the active phase, but also allows one to control the problem of heat and mass transfer during the reaction by adapting the macroscopic shape to the reaction conditions. Previous works on the silicon carbide containing cobalt catalysts have shown that the use of a thermal conductive support greatly improve the liquid hydrocarbons selectivity in the Fischer-Tropsch synthesis process by favoring the heat transfer within the catalyst body.[55] Similar results have also been reported on the beneficial effect of the thermal conductive SiC support on the endothermic dehydrogenation of n-butane reaction.[56]

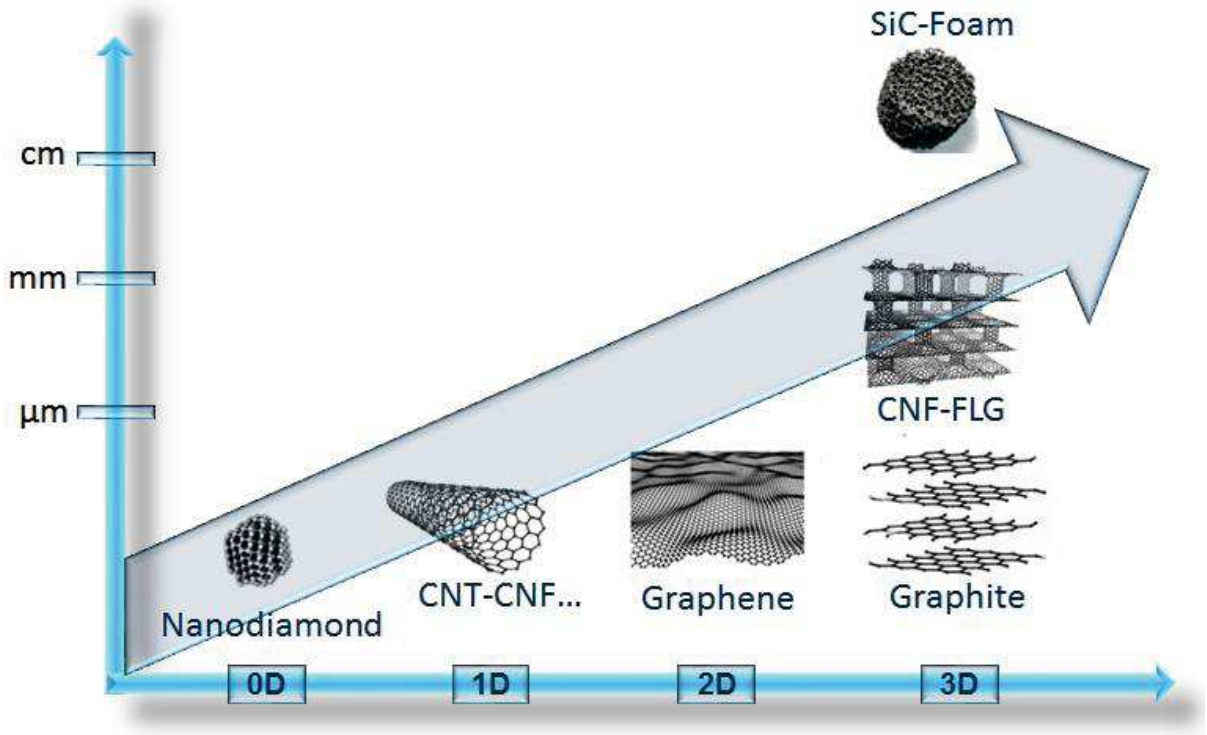

Figure 21. Various carbon-based materials, from nanoscopique to 3D macroscopic shape.

3.1. Oxidative Dehydrogenation (ODH) process

The exothermic ODH process to convert ethylbenzene (EB) to styrene (ST) operates in the presence of oxygen to allow the removal of the formed hydrogen as steam. On the other hand, the strongly exothermic ODH of hydrocarbons also reduces the problem linked with the catalyst temperature lost as encountered with the endothermic DH process. The presence of oxygen also allows operating the process at lower reaction temperature, 400-500°C, compared

to that operated in the DH process. The presence of oxygen and steam (generated in-situ during the course of the reaction) also contribute to the reducing of the amount of cracking products and also the coke formation and thus, the use of extra steam can be avoided which leads to a significant energy saving for the process. In addition, the ODH process also eliminates most limitations imposed by thermodynamic compared to the DH process and potentially higher yields (90%) can be obtained per pass. However, it is worthy to note that the ODH is an exothermic process and thus, reaction conditions need to be controlled in order to reduce as much as possible the direct oxidation of the starting compounds through CO/CO_2 formation which significantly lower the overall selectivity of the process. In addition, the process involves oxygen and hydrocarbons at a relatively high temperature and thus, the operating conditions need to be controlled in a strict way due to the explosive character of the mixture.

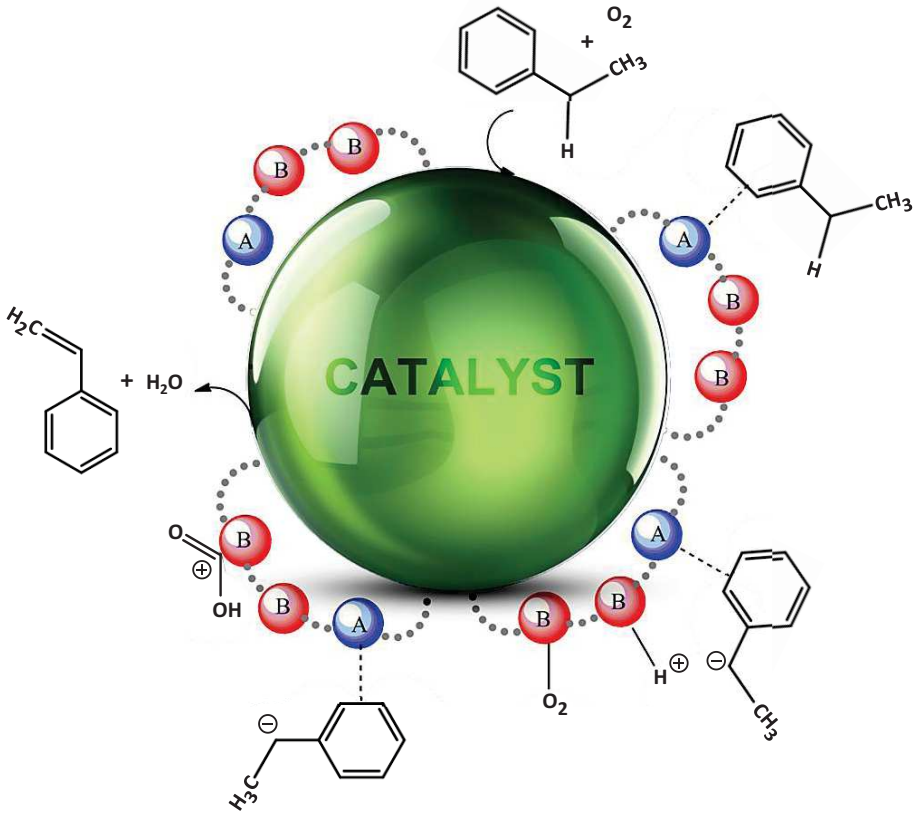

Figure 22. Schematic representation of the mechanistic model of the oxidative dehydrogenation of ethylbenzene to styrene, where A and B represent respectively acid and basic sites.

The numerous work realized by Figueiredo and co-workers,[57,58,59] have really helped to establish that carbonyl/quinone functional groups present on the carbon surface are the active sites for performing ODH (Figure 22). A redox mechanism of Mars van Krevelen type involving quinone/hydroquinone groups on the surface of the activated carbon is suggested for the reaction, where the quinone surface groups are reduced to hydroquinone by the

adsorbed ethylbenzene, and reoxidised back to quinone by oxygen.[60] However, the activated carbon (AC) catalysts displayed a low stability neighboring 60% as a function of time on stream in an oxidative atmosphere, hindering the potential use of it as metal-free catalyst in the presence of oxygen.[59] In addition, the presence of a large amount of micropores in the AC also significantly increases the problem of diffusion of the reactant to the active site localized inside the pore and the escaping of the product.

From these results new structured carbon-based catalyst such as carbon nanotubes and nanofibers, with higher graphitization degree, were developed to overcome the weakness of AC described above. Carbon nanotubes (CNTs) and nanofibres (CNFs) have shown significant progress in the field of catalysis due to their high specific surface areas, improved electronic and thermal properties, and easy surface modification by chemical functionalization or doping with foreign elements such as nitrogen, sulfur, boron and phosphorus.[61,62,63,64] In addition, these nanocarbon-based materials display mesoporous network which significantly improve the accessibility of the reactants toward the catalytic sites and also for the escaping of the intermediate products. Pereira and co-workers has reported the use of CNTs as catalyst for ODH reaction, the reaction test evidences a high stability of the CNT-based catalyst compared to the AC-based catalyst. However activated carbon gives the highest catalytic performance compare to the CNTs catalyst which could be attributed to the higher specific surface area of the catalyst compared to that of the CNTs (Figure 23).[46] However, on the AC catalyst deactivation occurs as a function of time on stream leading to the lower ODH activity after about 600 minutes of reaction whereas stable ODH activity are observed on the CNT-based catalyst owing to it high oxidative resistance in the presence of oxygen. The main drawback of the CNT-based catalyst is it nanoscopic shape which render difficult the handling and transport as well as the direct use in fixed-bed reactor where high pressure drop is prohibitive.

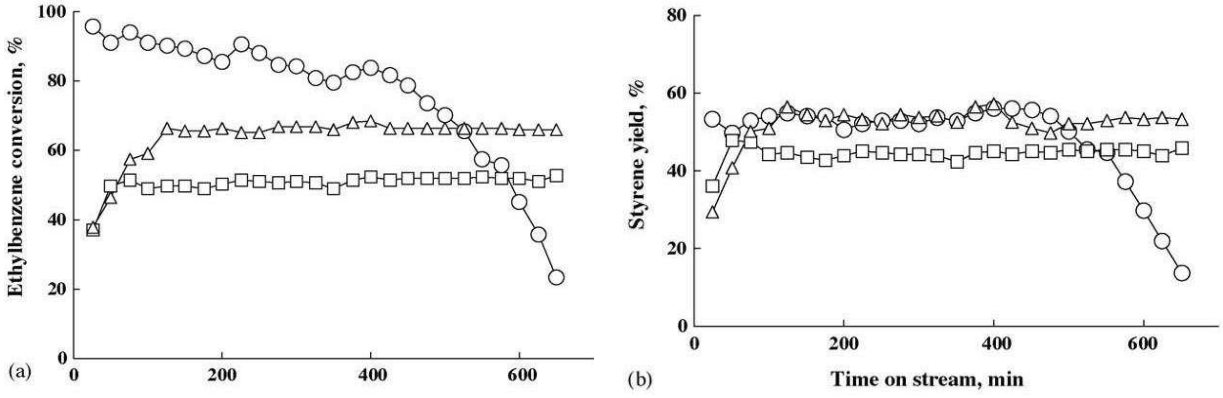

Figure 23. Dehydrogenation performance (a) EB bconversion and (b) styrene yield as a function of time on stream obtained at 823 K on carbon black (o), graphite (□) and CNTs (Δ) catalyst.[46]

Actually the "real" metal-free catalyst is the carbonaceous deposited (coke) on the surface of oxide having acid Lewis sites formed during the early stage of the reaction, and not the catalyst itself.[65] The coke was characterized as polyaromatic compounds having a relatively high oxygen content, i.e. O/C = 0.10 - 0.15 at.%. The catalytic sites on this coke are the surface quinone/hydroquinone groups that act as redox sites for hydrogen abstraction from EB (Figure 24).[65]

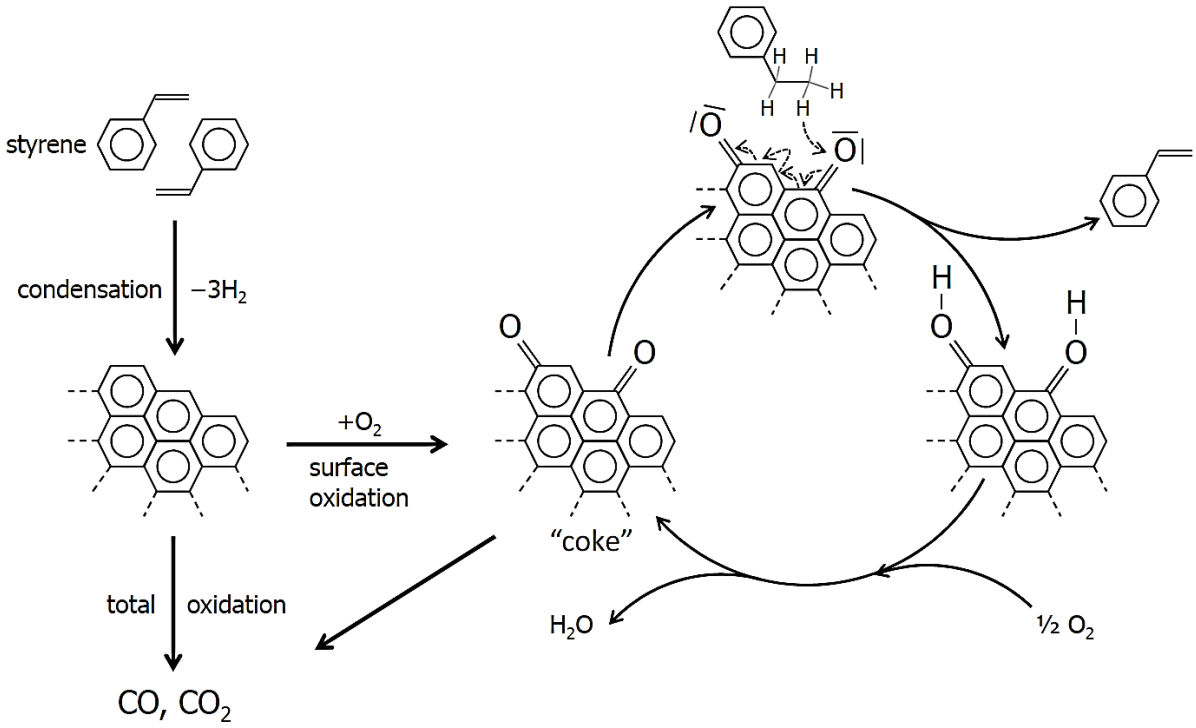

Figure 24. Simplified mechanism for the oxidative dehydrogenation reaction. [66]

The research groups of Schlögl and Su had extensively investigated the use of all kinds of structured carbon-based materials for the ODH reactions to convert EB to ST and butane to butenes.[46,67] Su et al. showed that partially oxidized CNTs efficiently catalyze the ODH of ethylbenzene to styrene with high efficiency.[53] Compared with metal oxide-based catalysts, CNTs have enhanced selectivity for alkenes. Other carbon-based materials have been also investigated to perform ODH of ethylbenzene, such as carbon nanofibers, carbon nanofilaments, nanodiamonds (ND), and also hierarchical composites consisting of carbon materials deposited on a macroscopic host support.[33,68,69,70] In the continuation of studies on carbon-nitride materials, Zhao et al.[71] updated hybrid catalysts made by pyrolysis process between melamine and nanodiamond particles at different temperature (i.e. 650, 700 and 750°C). The nanodiamond/carbon nitride (ND/CN_x) composite exhibits synergistically

enhanced catalytic performance for the direct oxidative dehydrogenation (ODH) of ethylbenzene to styrene under steam-free conditions. The developed ND/CN_x nano-architecture exhibited an enhancement of the catalytic performance of 1.5 and 4.2 times of the steady-state styrene rate of the established un-promoted ND and the industrially used K–Fe catalyst (Figure 25), respectively. It is worthy to note that the DH performance on these ND/CN_x catalysts is also significantly influenced by the pyrolysis temperature. High pyrolysis temperature significantly decreases the DH performance of the catalyst. In addition, the highest DH catalyst, ND/CN_x pyrolyzed at 750°C, still show a gradual deactivation as a function of time on stream which evidence the fact that active site blocking by carbonaceous residue is still occur.

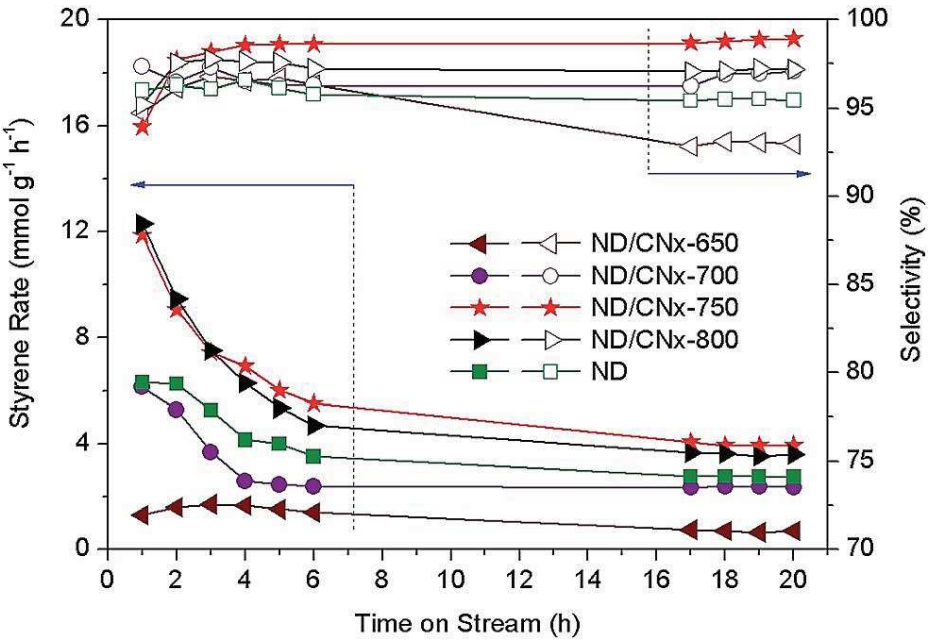

Figure 25. Schematic illustration for the fabrication of ND/CNx nanoarchitectures via a facile pyrolysis approach, and catalytic performance of the ND/CNx nanostructures prepared using divers pyrolysis temperatures as a function of time on stream for metal-free direct dehydrogenation of ethylbenzene to styrene under oxygen-and steam-free conditions.[72]

However, it is worthy to note that the direct comparison of the catalytic performance and stability of all the above cited metal-free catalysts is difficult, due to the fact that the reaction conditions often vary tremendously. In summarize, one can note that these carbon-based metal-free materials are active for ODH process, with selectivity generally ranged between 55 and 85%. Similarly to the results reported by Su[74] and Zhao,[73] Dai's group has reported that various nanocarbon materials can efficiently catalyze the ODH reaction of ethylbenzene to styrene.[75] In general, the catalytic performance of these nanostructured carbon based-catalysts exhibited comparable or even better activities than the industrial iron oxide

catalysts. The high ODH activity of these carbon-based metal-free catalysts can be attributed to several facts such as: (i) high effective surface area with low diffusion phenomenon, (ii) high stability of the materials towards oxidation in the presence of oxygen thanks to their high degree of graphitization, (iii) high stability of the active sites against coke encapsulation.

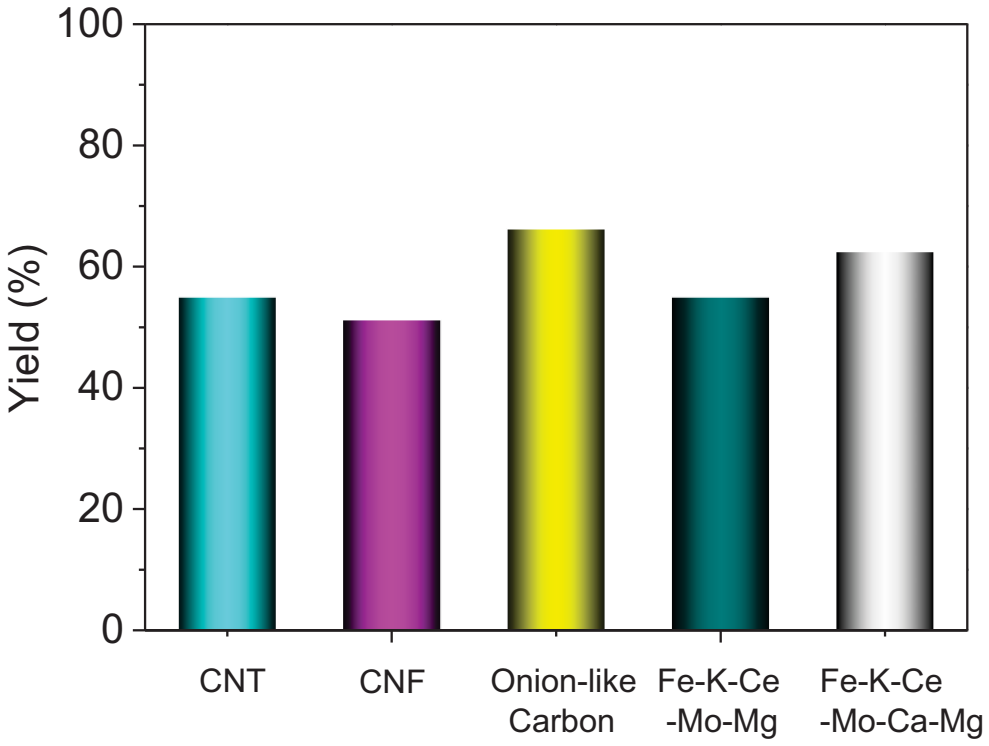

Figure 26. Styrene yield comparison over carbon based-materials and metal catalysts in oxidative dehydrogenation.[73]

3.2. Direct dehydrogenation (DH) process

The main drawback of the ODH process is due to the presence of oxygen in the processing feed which could directly reacted with the starting hydrocarbons to form CO and CO_2 and thus, leads to the lost of the overall selectivity of the process. The oxygen presents in the feed can also react with the carbon-based catalyst itself leading to a gradual lost of the catalyst as a function of time on stream. In addition this process has a potential risk of explosion due to the presence of oxygen and hydrocarbons at a relatively high temperature. According to the drawbacks cited above it is of interest to find new metal-free catalysts with

better coke resistance (under steam-free conditions) for performing the conversion of EB into ST under an oxygen-free medium, i.e. direct dehydrogenation (DH) process (Figure 27).

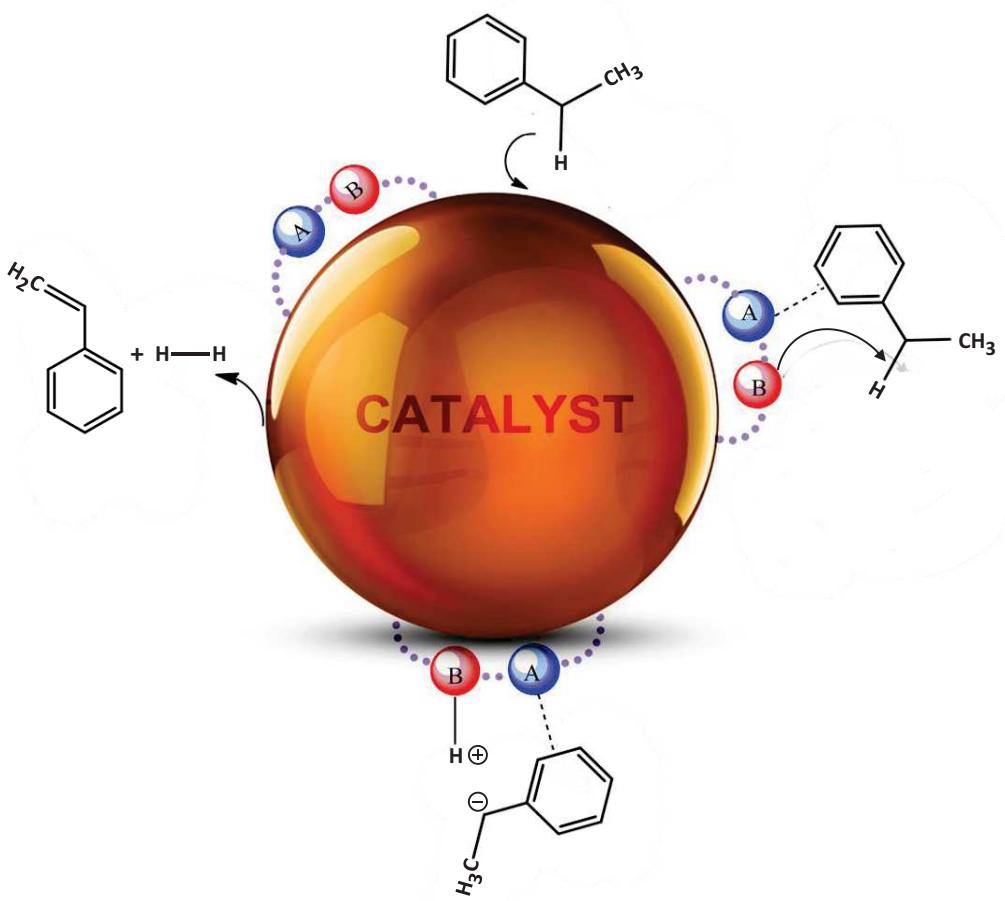

Figure 27. Schematic representation of the mechanistic model of the direct dehydrogenation of ethylbenzene to styrene, where A and B represent respectively acid and basic sites.

It is worthy to note that a large part of the literature results reported nowadays is deal with the use of these metal-free nanocarbon catalysts in the oxidative dehydrogenation process while the direct dehydrogenation (DH) is only scarcely reported despite its high advantages versus the ODH process. For the DH process only few reports have been published up to now in the literature and most of them are based on the use of nanodiamonds (ND) as metal-free catalyst.[54]

Synthetic nanodiamonds (ND) have an average size ranging 4-8 nm and their large surface-to-volume ratio endows them with higher surface reactivity than other form of carbon. The ND not only has all the characteristics of diamond, but also has all the characteristics of powders, such as large surface area, good chemical activity, large entropy and high structural defects. The NDs are used in several processes in the field of composite coating, grinding, polishing, lubrication, seals, photographic materials, high-strength resin and rubber, seeds, drugs delivery while their use in the field of catalysis had only recently reported. Aleksenskii

et al.[74] have reported that detonation ND particles consist of a diamond core coated with shells having an onion (onion-like) structure with graphite inclusions. The structure of nanodiamonds is explained within the model of icosahedral nanoparticles with a shell structure. The nearest environment of all the atoms involved in the structure of the outer shells becomes more and more different from the diamond structure and transforms gradually into a graphene structure. It is turn out that ND is consisted by a mixture of sp^2 and sp^3 carbon structure which confers to it's a different surface reactivity than diamond and/or related carbon-based materials.

Schlögl and co-workers[54] have reported the development of a highly active metal-free and steam-free DH catalyst based on the bulk nanodiamonds (NDs) catalyst. The NDs-based catalyst exhibits DH activity about three times higher than the one obtained with the iron-based industrial catalyst along with a high selectivity towards styrene formation. The ND-based catalyst also exhibits high catalytic performance stability as a function of time on stream which confers to it a high advantage for further development (Figure 28).

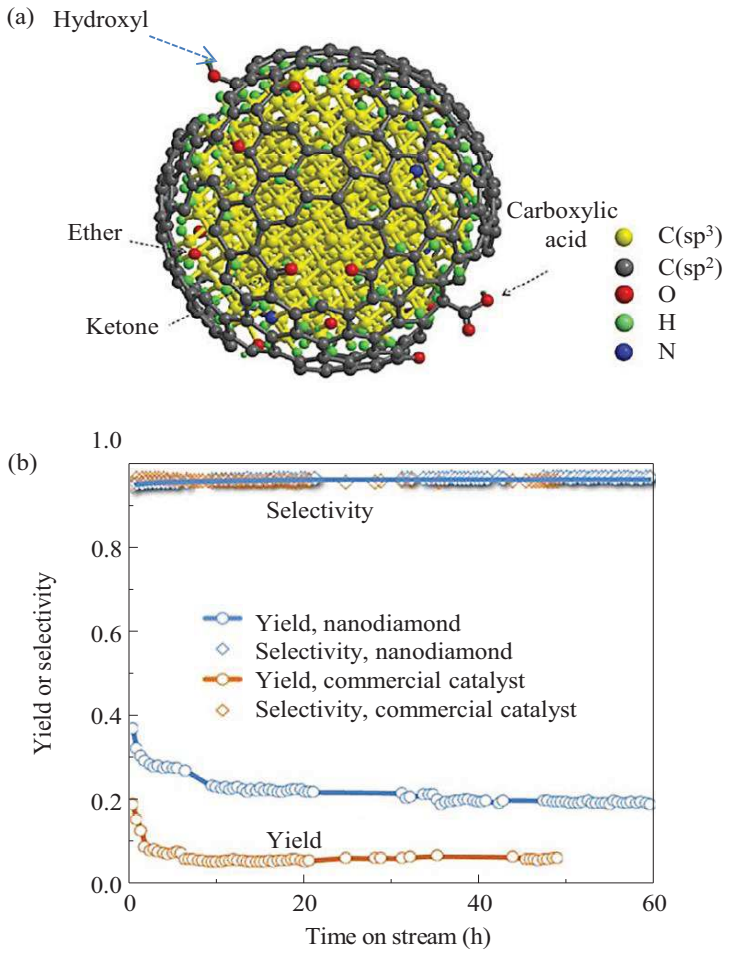

Figure 28. (a) Shematic representation of the diamond nanostructure. (b) Catalytic performance over nanodiamond compared to traditional iron-based catalyst. Reaction conditions: 0.05 g, 550°C, 2.8% EB in helium, 10 ml/min.[75]

However, commercial ND is presented in a powder form consisted with agglomerates (Figure 29) which significantly reduce the accessibility of the active site per weight unit and thus, it is expected that the reported DH catalytic performance could be significantly improved by appropriate better dispersion of the ND active phase onto an appropriate support. In addition, the nanoscopic dimension of these carbon based-materials also contributes to problems related to health, handling and transportation. In the field of catalysis their use in fixed-bed reactors is very constrained because of the issues related to a huge pressure drop across the catalyst bed which could modify both the catalytic activity and selectivity of the process.[76]

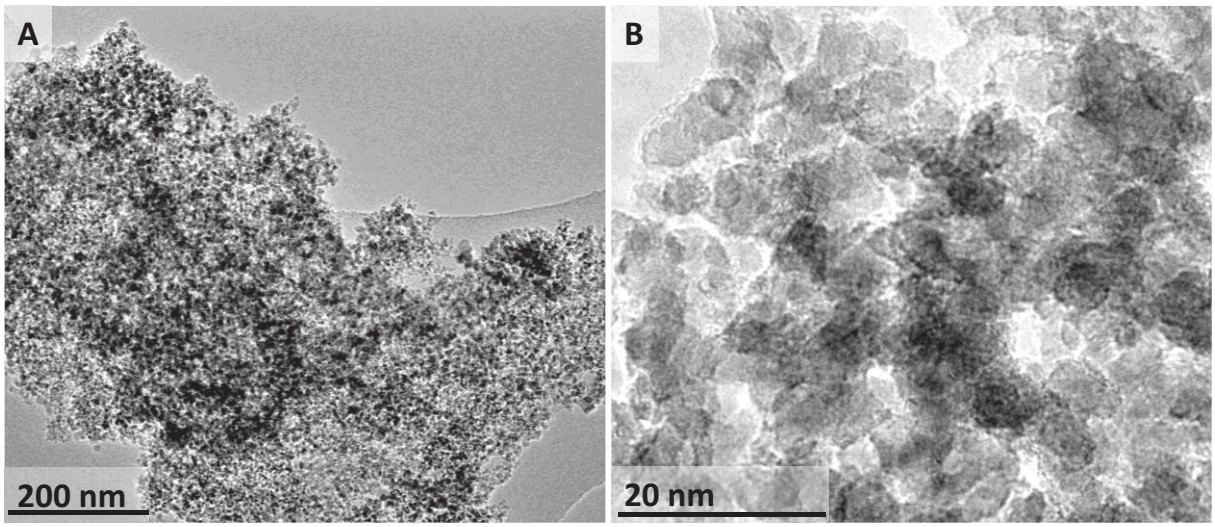

Figure 29. Representative TEM micrographs of the nanodiamonds showing the presence of aggregates with low accessibility.

In this regard it is necessary to develop new synthetic routes in order to overcome the drawbacks cited above. The first route consists in the dispersion of the nanodiamonds materials on an appropriate support which allow the reduction in size of the aggregates leading to a higher active site density per weight of the active phase and as a consequence, to improve its catalytic performance. The macroscopic shape of the support could also favor the escaping of the intermediate products and thus, contribute to the maintaining of the overall activity of the catalyst by lowering secondary reactions leading to coke formation.

Lately study based on changes in the intrinsic properties of carbon materials have attracted a lot of scientific interests worldwide, these changes were made by functionalizing or by doping. It has been demonstrated the doping with nitrogen is an effective approach to intrinsically regulate the electronic properties of carbon nanomaterials. The introduction of

foreign element, such as, nitrogen, boron, sulfur, inside the carbon matrix leads to a new class of catalyst with unexpected properties with improved electro-catalytic performance. The doping of N-donor atoms into the carbon lattice can significantly influence their optical properties and enhance greatly their chemical and physical properties.

Dai et al.[73] reported that vertically aligned nitrogen-doped carbon nanotube arrays can be used as an efficient metal catalyst for the demanding oxygen reduction reaction (ORR) in fuel cells. The authors have attributed the improved catalytic performance to the electron-accepting ability of the nitrogen atoms, which creates a net positive charge on the adjacent carbon atoms in the nanotube carbon plane of vertically aligned NCNTs (VA-NCNT). It has been also showed that the use of nitrogen doped nanodiamond as metal-free electrode exhibit superior electrochemical activity compared to other carbon allotropes.[73] Therefore, uncounted scientists work devoted to the synthesis, characterization of bulk mesoporous carbon nitride materials by using different strategies and precursors.

Carbone nitride-based materials have been used as metal-free catalyst in the oxidative dehydrogenation (ODH) and direct dehydrogenation (DH) of ethylbenzene into styrene.[72] Great interest has been aroused in the recently by the work realized by Zhao et al.[71] in the synthesis of highly-ordered mesoporous carbon nitride catalyst displaying a very high surface area ranged between 971 to 1124 m^2/g and high open porosity. The as-synthesized mesoporous carbon nitride catalyst exhibit a superior catalytic performance in DH of ethylbenzene to styrene compared to the other types of carbon-based metal-free catalysts, i.e. nanodiamonds, classical mesoporous carbon nitride (MCN-1) and mesoporous carbon (CMK-3) (Figure 30A). In addition, the mesoporous carbon nitride developed by the authors, i.e. DUT-1, also exhibits a higher stability as a function of time on stream compared to the other carbon-based catalysts. The authors have attributed such high DH activity to the ultrahigh surface area and ultralarge pore volume of the DUT-1. The authors have also reported the strong influence of the pyrolysis temperature on the DH performance of the developed mesoporous carbon nitride (Figure 30B). According to the results one can see that the DH performance of the DUT-based catalysts followed a volcano curve as a function of the pyrolysis temperature. Low pyrolysis temperature leads to a catalyst with medium DH performance where high pyrolysis temperature leads to a catalyst with a lowest DH performance. The catalyst after being pyrolyzed at 750°C seems to be the most active for performing the DH of ethylbenzene to styrene. However, this mesoporous carbon nitride is prepared in a powder form which renders it unlikely for future industrial development due to the problem linked with pressure drop across the fixed-bed.

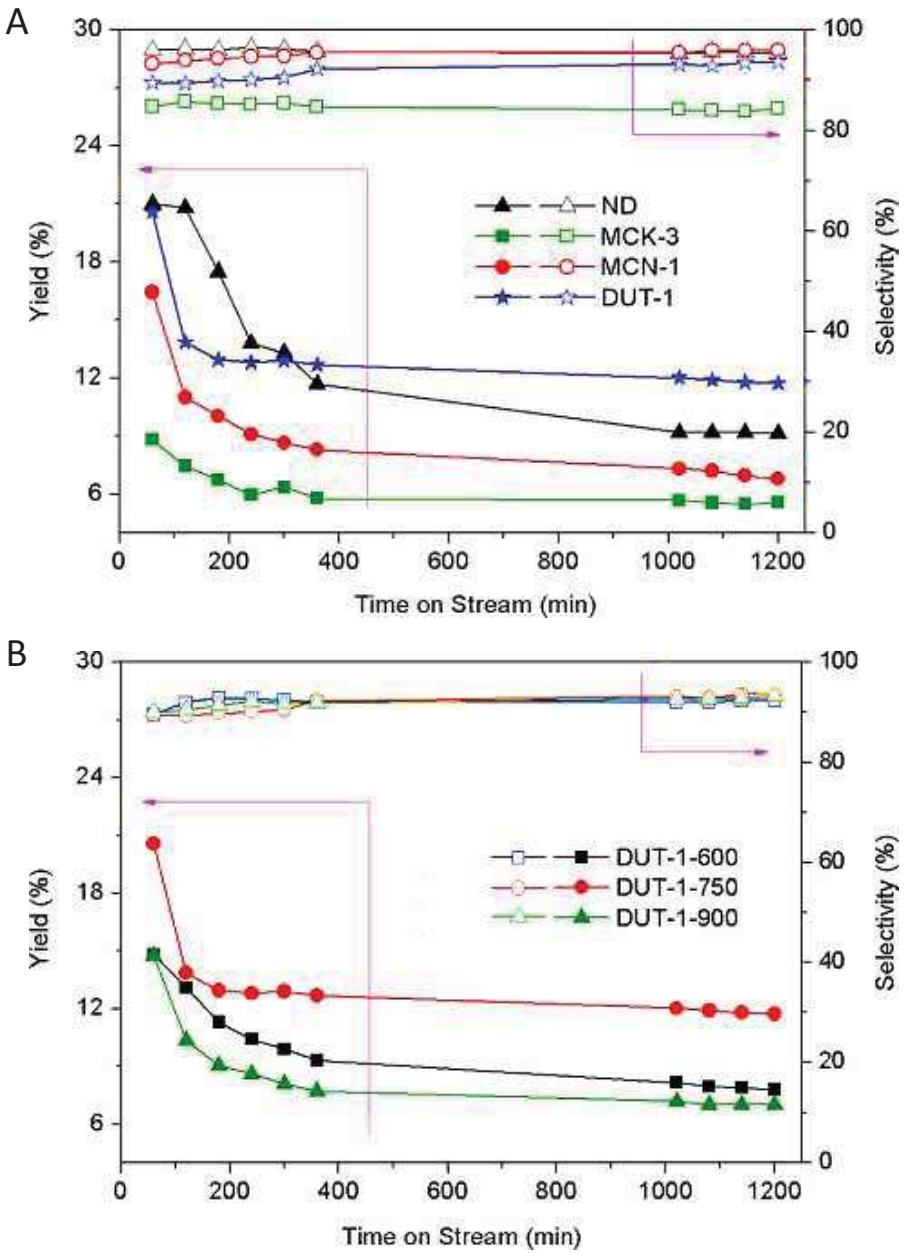

Figure 30. (A) Catalytic performance of the mesoporous carbon nitride DUT-1 in the direct dehydrogenation of ethylbenzene to styrene under oxygen-and steam-free conditions. The DH performance of the other carbon-based catalysts, i.e. nanodiamonds, classical mesoporous carbon nitride (MCN-1) and mesoporous carbon (CMK-3), has also been reported in the same figure for comparison. Reaction conditions: 0.025g catalyst, 550°C, 2.8% of ethylbenzene in argon, 10mL min^{-1}. (B) Catalytic performance of DUT-1-600, DUT-1-750, and DUT-1-900 for direct dehydrogenation of ethylbenzene to styrene under oxygen and steam-free conditions evidencing the strong influence of the pyrolysis temperature on the DH performance. Reaction conditions: 0.025g catalyst, 550°C, 2.8% of ethylbenzene in argon, 10 mL min^{-1}.[71]

Recently, Liu et al.[77] developed a two-step method to support NDs onto the carbon nanotubes (CNTs) network decorated a low surface area SiC macroscopic host structure. The SiC macroscopic host structure was synthesized by a slurry coating method of polyurethane foam followed by a thermal treatment leading to the formation of SiC foam. However, the synthesis method leads to the formation of SiC foam with a relatively low specific surface area and thus, cannot be directly used as a macroscopic support for NDs dispersion. In order to overcome such problem a layer of CNTs with high effective surface area is further deposited through a CVD synthesis method on the SiC surface.

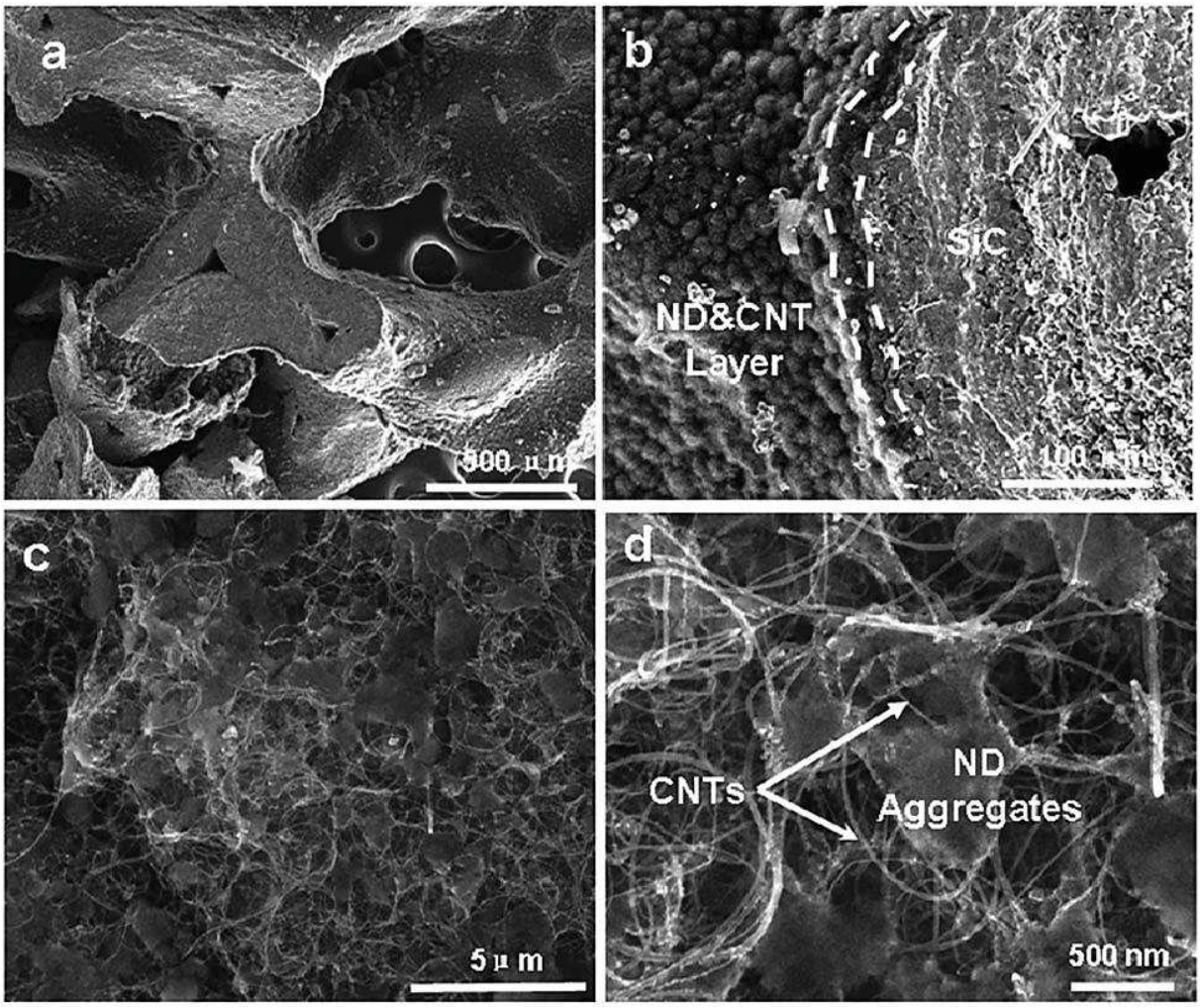

Figure 31. (a–d) SEM images of the CNT/SiC monolith with different magnifications. Inset is the photograph of the CNT/SiC monolith. [77]

The CNTs layer will play a role of support to disperse the NDs on the composite as shown by the SEM micrographs presented in Figure 31. The SEM analysis indicates that the main part of the NDs was directly anchored on the CNTs support which could be attributed to

the presence of surface defects which play a role of anchorage sites. The DH activity is similar to that of the pristine bulk NDs but in this study the powdered form of NDs has been replaced by a composite with macroscopic shape which could be efficiently used in industrial process. The ethylbenzene dehydrogenation (DH) into styrene test on the bulk NDs, CNT/SiC and ND/CNT-SiC catalysts was evaluated. According to the results the ND/CNT-Sic NDs shows a relatively higher DH activity compared to the industrial iron-based catalyst. The styrene selectivity is also extremely high.

In summary new developments in the field of direct dehydrogenation of aromatic and linear hydrocarbons on metal-free carbon-based catalysts have received an ever increasing scientific interest since the last decades and it is expected that such interest will continue to growth in the near future taken into account the great promises hold by these metal-free catalysts compared to the traditional supported oxide ones. Among these metal-free carbon-based catalysts nanodiamonds seem to be the most promising, especially in the direct dehydrogenation process, which allows one to have better reaction control and selectivity for the targeted product. However, despite the promising catalytic performance it is expected that optimization processes are still needed to improve the nanodiamonds dispersion and as a consequence, it intrinsic activity per weight of the active phase for future industrial developments. Finally, it is worthy to note that up to now no study deals with the catalytic evaluation of these nanodiamonds-based catalysts under relevant industrial conditions has been reported which render difficult the economical assessment for future industrial development.

4. Objectives of the work

According to the Introduction part presented above the work realized during this PhD will mainly focused on the development of the optimized nanodiamonds as metal-free catalyst for the steam-free selective direct dehydrogenation of ethylbenzene into styrene. The emphasis will be put on the preparation of supported nanodiamonds catalysts with higher exposed active sites per catalyst weight unit and the macroscopic shaping for further industrial development. The supports will be consisted by few-layer graphene (FLG), graphene oxide/few-layer graphene (GO/FLG), carbon nanofibers decorated few-layer graphene (CNFs/FLG), and macroscopic silicon carbide foam. The catalytic performance of the optimized catalyst will be also bench-marked with the iron-based industrial catalyst under relevant industrial reaction conditions. The main objective is the development of nanodiamonds metal-free catalyst with better catalytic performance and also with a macroscopic shape for future industrial development.

Chapter II will summarize the synthesis methods of the different supports and the characterization techniques used in the present work.

Chapter III will deal with the dispersion of nanodiamonds (ND) on the few-layer graphene-based (FLG) supports, either pure or modified with a layer of graphene oxide (GO), in order to improve the dispersion of nanodiamond particles with enhanced active site density. The results obtained allow us to get more insight about the different interactions between the ND and the carbon-based support for further optimization process.

Chapter IV will present the synthesis of 3D structure generated by in-situ growing of a layer of carbon nanofibers on few-layer graphene surface followed by an anchorage of NDs particles. It is expected that such 3D or hierarchical structure will provide the higher dispersion of NDs and also to a more opened structure with higher effective surface area for the reactant adsorption. The catalytic performance of this 3D hierarchical composite will be compared with that of the 2D catalyst consisting of ND deposited on few-layer graphene. The main aim of this Chapter is to unravel the influence of hierarchical structure on the dehydrogenation performance.

Chapter V will deal with the use of a macroscopic hierarchical structure consisted with silicon carbide (SiC), i.e. extrudates and cellular foam, for supporting ND active phase. The main aim is to combine on such macroscopic host structures the easy way to disperse the ND aggregates and also for facilitating the handling and industrial development of these metal-free catalysts. The influence of the reaction temperature and ethylbenzene concentration will be also evaluated and discussed. Finally, the optimized catalyst will be tested under relevant industrial reaction conditions, i.e. high reaction temperature, high ethylbenzene concentration and long-term evaluation, and the results will be compared with that of the industrial iron-based catalyst. The influence of the regeneration process on the catalytic activity and stability will also be carried out within this work.

Chapter VI will mainly focused on a new synthesis method which allows one to prepare nitrogen-doped carbon matrix, with high nitrogen loading, coated on a CNTs skeleton composites with various macroscopic shapes, ranged from millimeter to centimeters size, and high effective surface area, i.e. > 300 m^2/g, depending to the downstream applications. The nitrogen-doped carbon matrix with high nitrogen loading (N@MC) was synthesized from food stuffs raw materials, i.e. ammonium carbonate, glucose and citric acid. In the same chapter we will also investigate the use of ND as nucleation centers to synthesize the N@MC/ND composite with high dehydrogenation efficiency. The as-synthesized N@MC/ND composite will be also evaluated in a macroscopic shape under relevant industrial process.

Chapter VII will summarize all the main results obtained in the present study and to present some perspectives of the work.

Reference

(1) Grischkat, S.; Hunecke, M.; Böhler, S.; Haustein, S. Potential for the Reduction of Greenhouse Gas Emissions through the Use of Mobility Services. *Transp. Policy* **2014**, *35*, 295–303.

(2) Balasamy, R. J.; Khurshid, A.; Al-Ali, A. A. S.; Atanda, L. A.; Sagata, K.; Asamoto, M.; Yahiro, H.; Nomura, K.; Sano, T.; Takehira, K.; *et al.* Ethylbenzene Dehydrogenation over Binary FeOx–MeOy/Mg(Al)O Catalysts Derived from Hydrotalcites. *Appl. Catal. Gen.* **2010**, *390*, 225–234.

(3) Choi, J.; Chung, J. Evaluation of Potential for Reuse of Industrial Wastewater Using Metal-Immobilized Catalysts and Reverse Osmosis. *Chemosphere* **2015**, *125*, 139–146.

(4) Tang, X.; Gao, F.; Xiang, Y.; Yi, H.; Zhao, S. Low Temperature Catalytic Oxidation of Nitric Oxide over the Mn–CoOx Catalyst Modified by Nonthermal Plasma. *Catal. Commun.* **2015**, *64*, 12–17.

(5) Xie, H.; Ye, X.; Duan, K.; Xue, M.; Du, Y.; Ye, W.; Wang, C. CuAu–ZnO–graphene Nanocomposite: A Novel Graphene-Based Bimetallic Alloy-Semiconductor Catalyst with Its Enhanced Photocatalytic Degradation Performance. *J. Alloys Compd.* **2015**, *636*, 40–47.

(6) Majumder, A.; Gupta, R.; Mandal, M.; Babu, M.; Chakraborty, D. Air-Stable palladium(0) Phosphine Sulfide Catalysts for Ullmann-Type C–N and C–O Coupling Reactions. *J. Organomet. Chem.* **2015**, *781*, 23–34.

(7) Lausche, A. C.; Schaidle, J. A.; Schweitzer, N.; Thompson, L. T. 7.14 - Nanoscale Carbide and Nitride Catalysts. In *Comprehensive Inorganic Chemistry II (Second Edition)*; Poeppelmeier, J. R., Ed.; Elsevier: Amsterdam, 2013; pp. 371–404.

(8) Ivanova, S.; Louis, B.; Madani, B.; Tessonnier, J. P.; Ledoux, M. J.; Pham-Huu, C. ZSM-5 Coatings on B-SiC Monoliths: Possible New Structured Catalyst for the Methanol-to-Olefins Process. *J. Phys. Chem. C* **2007**, *111*, 4368–4374.

(9) Alejandro, S.; Valdés, H.; Manéro, M.-H.; Zaror, C. A. Oxidative Regeneration of Toluene-Saturated Natural Zeolite by Gaseous Ozone: The Influence of Zeolite Chemical Surface Characteristics. *J. Hazard. Mater.* **2014**, *274*, 212–220.

(10) TOSSAVAINEN, A. Styrene Use and Occupational Exposure in the Plastics Industry. *Scand. J. Work. Environ. Health* **1978**, *4*, 7–13.

(11) Atanda, L. A.; Balasamy, R. J.; Khurshid, A.; Al-Ali, A. A. S.; Sagata, K.; Asamoto, M.; Yahiro, H.; Nomura, K.; Sano, T.; Takehira, K.; *et al.* Ethylbenzene Dehydrogenation over Mg3Fe0.5−xCoxAl0.5 Catalysts Derived from Hydrotalcites: Comparison with Mg3Fe0.5−yNiyAl0.5 Catalysts. *Appl. Catal. Gen.* **2011**, *396*, 107–115.

(12) Geisst, C. R. *Encyclopedia of American Business History*; Infobase Publishing, 2009.

(13) Scheirs, J.; Priddy, D. *Modern Styrenic Polymers: Polystyrenes and Styrenic Copolymers*; John Wiley & Sons, 2003.

(14) Shekhah, O.; Ranke, W.; Schlögl, R. Styrene Synthesis: In Situ Characterization and Reactivity Studies of Unpromoted and Potassium-Promoted Iron Oxide Model Catalysts. *J. Catal.* **2004**, *225*, 56–68.

(15) Tope, B. B.; Balasamy, R. J.; Khurshid, A.; Atanda, L. A.; Yahiro, H.; Shishido, T.; Takehira, K.; Al-Khattaf, S. S. Catalytic Mechanism of the Dehydrogenation of Ethylbenzene over Fe–Co/Mg(Al)O Derived from Hydrotalcites. *Appl. Catal. Gen.* **2011**, *407*, 118–126.

(16) Behr, A. styrene production from ethylbenzene http://www.tc.bci.tu-dortmund.de/Downloads/Praktika/tc30_styrene_english.pdf (accessed Jun 4, 2015).
(17) Addiego, W. P.; Liu, W.; Boger, T. Iron Oxide-Based Honeycomb Catalysts for the Dehydrogenation of Ethylbenzene to Styrene. *Catal. Today* **2001**, *69*, 25–31.
(18) Coulter, K.; Goodman, D. W.; Moore, R. G. Kinetics of the Dehydrogenation of Ethylbenzene to Styrene over Unpromoted and K-Promoted Model Iron Oxide Catalysts. *Catal. Lett.* **1995**, *31*, 1–8.
(19) Stobbe, D. E.; van Buren, F. R.; van Dillen, A. J.; Geus, J. W. Potassium Promotion of Iron Oxide Dehydrogenation Catalysts Supported on Magnesium Oxide: 1. Preparation and Characterization. *J. Catal.* **1992**, *135*, 533–547.
(20) Hirano, T. Active Phase in Potassium-Promoted Iron Oxide Catalyst for Dehydrogenation of Ethylbenzene. *Appl. Catal.* **1986**, *26*, 81–90.
(21) Hirano, T. Dehydrogenation of Ethylbenzene over Potassium-Promoted Iron Oxide Containing Cerium and Molybdenum Oxides. *Appl. Catal.* **1986**, *28*, 119–132.
(22) Muhler, M.; Schütze, J.; Wesemann, M.; Rayment, T.; Dent, A.; Schlögl, R.; Ertl, G. The Nature of the Iron Oxide-Based Catalyst for Dehydrogenation of Ethylbenzene to Styrene: I. Solid-State Chemistry and Bulk Characterization. *J. Catal.* **1990**, *126*, 339–360.
(23) Weiss, W.; Schlögl, R. An Integrated Surface Science Approach towards Metal Oxide Catalysis. *Top. Catal.* **2000**, *13*, 75–90.
(24) Zhu, X. M.; Schön, M.; Bartmann, U.; van Veen, A. C.; Muhler, M. The Dehydrogenation of Ethylbenzene to Styrene over a Potassium-Promoted Iron Oxide-Based Catalyst: A Transient Kinetic Study. *Appl. Catal. Gen.* **2004**, *266*, 99–108.
(25) Mihajlova, A.; Andreev, A.; Shopov, D.; Dimitrova, R. Effect of the Precursor Properties on the Selectivity of Iron Based Catalysts in the Dehydrogenation of Ethylbenzene to Styrene. *Appl. Catal.* **1988**, *40*, 247–253.
(26) Process for Dehydrogenation of Ethylbenzene to Styrene.
(27) James E Gantt. Dehydrogenation of Ethylbenzene to Styrene.
(28) Weiss, W.; Zscherpel, D.; Schlögl, R. On the Nature of the Active Site for the Ethylbenzene Dehydrogenation over Iron Oxide Catalysts. *Catal. Lett.* **1998**, *52*, 215–220.
(29) Cavani, F.; Trifirò, F. Alternative Processes for the Production of Styrene. *Appl. Catal. Gen.* **1995**, *133*, 219–239.
(30) Mimura, N.; Takahara, I.; Saito, M.; Hattori, T.; Ohkuma, K.; Ando, M. Dehydrogenation of Ethylbenzene over Iron Oxide-Based Catalyst in the Presence of Carbon Dioxide. *Catal. Today* **1998**, *45*, 61–64.
(31) Kim, J.; Yeo, S.; Jeon, J.-D.; Kwak, S.-Y. Enhancement of Hydrogen Storage Capacity and Hydrostability of Metal–organic Frameworks (MOFs) with Surface-Loaded Platinum Nanoparticles and Carbon Black. *Microporous Mesoporous Mater.* **2015**, *202*, 8–15.
(32) Ayala, P.; Arenal, R.; Rümmeli, M.; Rubio, A.; Pichler, T. The Doping of Carbon Nanotubes with Nitrogen and Their Potential Applications. *Carbon* **2010**, *48*, 575–586.
(33) Delgado, J. J.; Chen, X.-W.; Frank, B.; Su, D. S.; Schlögl, R. Activation Processes of Highly Ordered Carbon Nanofibers in the Oxidative Dehydrogenation of Ethylbenzene. *Catal. Today* **2012**, *186*, 93–98.
(34) Janowska, I.; Vigneron, F.; Bégin, D.; Ersen, O.; Bernhardt, P.; Romero, T.; Ledoux, M. J.; Pham-Huu, C. Mechanical Thinning to Make Few-Layer Graphene from Pencil Lead. *Carbon* **2012**, *50*, 3106–3110.
(35) Belobrov, P. I.; Bursill, L. A.; Maslakov, K. I.; Dementjev, A. P. Electron Spectroscopy of Nanodiamond Surface States. *Appl. Surf. Sci.* **2003**, *215*, 169–177.

(36) Wang, X.; Jin, B.; Mulcahy, D. Impact of Carbon and Nitrogen Sources on Hydrogen Production by a Newly Isolated Clostridium Butyricum W5. *Int. J. Hydrog. Energy* **2008**, *33*, 4998–5005.
(37) Shyu, F.-L. Field-Enhanced Electronic Specific Heat of Carbon Nanotubes. *Phys. E Low-Dimens. Syst. Nanostructures* **2015**, *67*, 89–98.
(38) Shi, J.-L.; Peng, H.-J.; Zhu, L.; Zhu, W.; Zhang, Q. Template Growth of Porous Graphene Microspheres on Layered Double Oxide Catalysts and Their Applications in Lithium–sulfur Batteries. *Carbon* **2015**, *92*, 96–105.
(39) Tran, P. A.; Zhang, L.; Webster, T. J. Carbon Nanofibers and Carbon Nanotubes in Regenerative Medicine. *Adv. Drug Deliv. Rev.* **2009**, *61*, 1097–1114.
(40) Belmouden, M.; Assabbane, A.; Ait Ichou, Y. Removal of 2.4-Dichloro Phenoxyacetic Acid from Aqueous Solution by Adsorption on Activated Carbon. A Kinetic Study. *Ann. Chim. Sci. Matér.* **2001**, *26*, 79–85.
(41) Chen, D.; Holmen, A.; Sui, Z.; Zhou, X. Carbon Mediated Catalysis: A Review on Oxidative Dehydrogenation. *Chin. J. Catal.* **2014**, *35*, 824–841.
(42) Ghadyani, G.; Öchsner, A. On a Thickness Free Expression for the Stiffness of Carbon Nanotubes. *Solid State Commun.* **2015**, *209–210*, 38–44.
(43) Sharma, M.; Gao, S.; Mäder, E.; Sharma, H.; Wei, L. Y.; Bijwe, J. Carbon Fiber Surfaces and Composite Interphases. *Compos. Sci. Technol.* **2014**, *102*, 35–50.
(44) Yang, H.; Liu, W.; Ma, C.; Zhang, Y.; Wang, X.; Yu, J.; Song, X. Gold–silver Nanocomposite-Functionalized Graphene Based Electrochemiluminescence Immunosensor Using Graphene Quantum Dots Coated Porous PtPd Nanochains as Labels. *Electrochimica Acta* **2014**, *123*, 470–476.
(45) Schlögl, R. Chapter Two - Carbon in Catalysis. In *Advances in Catalysis*; Jentoft, B. C. G. and F. C., Ed.; Academic Press, 2013; Vol. 56, pp. 103–185.
(46) Su, D. S.; Maksimova, N.; Delgado, J. J.; Keller, N.; Mestl, G.; Ledoux, M. J.; Schlögl, R. Nanocarbons in Selective Oxidative Dehydrogenation Reaction. *Catal. Today* **2005**, *102–103*, 110–114.
(47) Polshettiwar, V. Nanomaterials in Catalysis . Edited by Philippe Serp and Karine Philippot. *Angew. Chem. Int. Ed.* **2013**, *52*, 11199–11199.
(48) Zhang, R.; Zhang, Y.; Wei, F. Chapter 4 - Synthesis and Properties of Ultralong Carbon Nanotubes. In *Nanotube Superfiber Materials*; Yin, M. J. S. N. S., Ed.; William Andrew Publishing: Boston, 2014; pp. 87–136.
(49) Fang, Q.; Shen, Y.; Chen, B. Synthesis, Decoration and Properties of Three-Dimensional Graphene-Based Macrostructures: A Review. *Chem. Eng. J.* **2015**, *264*, 753–771.
(50) Ray, S. C. Chapter 2 - Application and Uses of Graphene Oxide and Reduced Graphene Oxide. In *Applications of Graphene and Graphene-Oxide Based Nanomaterials*; Ray, S. C., Ed.; Micro and Nano Technologies; William Andrew Publishing: Oxford, 2015; pp. 39–55.
(51) Tiwari, J. N.; Tiwari, R. N.; Kim, K. S. Zero-Dimensional, One-Dimensional, Two-Dimensional and Three-Dimensional Nanostructured Materials for Advanced Electrochemical Energy Devices. *Prog. Mater. Sci.* **2012**, *57*, 724–803.
(52) Shenderova, O. A. 3.07 - Production of Nanodiamond Particles. In *Comprehensive Hard Materials*; Sarin, V. K., Ed.; Elsevier: Oxford, 2014; pp. 143–171.
(53) Zhang, J.; Liu, X.; Blume, R.; Zhang, A.; Schlögl, R.; Su, D. S. Surface-Modified Carbon Nanotubes Catalyze Oxidative Dehydrogenation of N-Butane. *Science* **2008**, *322*, 73–77.

(54) Zhang, J.; Su, D. S.; Blume, R.; Schlögl, R.; Wang, R.; Yang, X.; Gajović, A. Surface Chemistry and Catalytic Reactivity of a Nanodiamond in the Steam-Free Dehydrogenation of Ethylbenzene. *Angew. Chem. Int. Ed.* **2010**, *49*, 8640–8644.
(55) Liu, Y.; Edouard, D.; Nguyen, L. D.; Begin, D.; Nguyen, P.; Pham, C.; Pham-Huu, C. High Performance Structured Platelet Milli-Reactor Filled with Supported Cobalt Open Cell SiC Foam Catalyst for the Fischer–Tropsch Synthesis. *Chem. Eng. J.* **2013**, *222*, 265–273.
(56) Harlin, M. E.; Krause, A. O. I.; Heinrich, B.; Pham-Huu, C.; Ledoux, M. J. Part II. Dehydrogenation of N-Butane over Carbon Modified MoO3 Supported on SiC. *Appl. Catal. Gen.* **1999**, *185*, 311–322.
(57) Pereira, M. F. R.; Órfão, J. J. M.; Figueiredo, J. L. Oxidative Dehydrogenation of Ethylbenzene on Activated Carbon Catalysts. I. Influence of Surface Chemical Groups. *Appl. Catal. Gen.* **1999**, *184*, 153–160.
(58) Pereira, M. F. R.; Orfão, J. J. M.; Figueiredo, J. L. Oxidative Dehydrogenation of Ethylbenzene on Activated Carbon Catalysts: 2. Kinetic Modelling. *Appl. Catal. Gen.* **2000**, *196*, 43–54.
(59) Pereira, M. F. R.; Órfão, J. J. M.; Figueiredo, J. L. Oxidative Dehydrogenation of Ethylbenzene on Activated Carbon Catalysts: 3. Catalyst Deactivation. *Appl. Catal. Gen.* **2001**, *218*, 307–318.
(60) Mars, P.; van Krevelen, D. W. Oxidations Carried out by Means of Vanadium Oxide Catalysts. *Chem. Eng. Sci.* **1954**, *3, Supplement 1*, 41–59.
(61) He, C.; Shen, P. K. Synthesis of the Nitrogen-Doped Carbon Nanotube (NCNT) Bouquets and Their Electrochemical Properties. *Electrochem. Commun.* **2013**, *35*, 80–83.
(62) Li, Z.; Huang, Y.; Yuan, L.; Hao, Z.; Huang, Y. Status and Prospects in Sulfur–carbon Composites as Cathode Materials for Rechargeable Lithium–sulfur Batteries. *Carbon* **2015**, *92*, 41–63.
(63) Yu, Z.-Y.; Chen, L.-F.; Song, L.-T.; Zhu, Y.-W.; Ji, H.-X.; Yu, S.-H. Free-Standing Boron and Oxygen Co-Doped Carbon Nanofiber Films for Large Volumetric Capacitance and High Rate Capability Supercapacitors. *Nano Energy*.
(64) Tong, Y.; Zhang, X.; Wang, Q.; Xu, X. The Adsorption Mechanism of Platinum on Phosphorus-Doped Single Walled Carbon Nanotube. *Comput. Theor. Chem.* **2015**, *1059*, 1–6.
(65) McGregor, J.; Huang, Z.; Parrott, E. P. J.; Zeitler, J. A.; Nguyen, K. L.; Rawson, J. M.; Carley, A.; Hansen, T. W.; Tessonnier, J.-P.; Su, D. S.; *et al.* Active Coke: Carbonaceous Materials as Catalysts for Alkane Dehydrogenation. *J. Catal.* **2010**, *269*, 329–339.
(66) Emig, G.; Hofmann, H. Action of Zirconium Phosphate as a Catalyst for the Oxydehydrogenation of Ethylbenzene to Styrene. *J. Catal.* **1983**, *84*, 15–26.
(67) Liu, X.; Frank, B.; Zhang, W.; Cotter, T. P.; Schlögl, R.; Su, D. S. Carbon-Catalyzed Oxidative Dehydrogenation of N-Butane: Selective Site Formation during sp3-to-sp2 Lattice Rearrangement. *Angew. Chem. Int. Ed.* **2011**, *50*, 3318–3322.
(68) Mestl, G.; Maksimova, N. I.; Keller, N.; Roddatis, V. V.; Schlögl, R. Carbon Nanofilaments in Heterogeneous Catalysis: An Industrial Application for New Carbon Materials? *Angew. Chem. Int. Ed.* **2001**, *40*, 2066–2068.
(69) Su, D.; Maksimova, N. I.; Mestl, G.; Kuznetsov, V. L.; Keller, V.; Schlögl, R.; Keller, N. Oxidative Dehydrogenation of Ethylbenzene to Styrene over Ultra-Dispersed Diamond and Onion-like Carbon. *Carbon* **2007**, *45*, 2145–2151.

(70) Delgado, J. J.; Su, D. S.; Rebmann, G.; Keller, N.; Gajovic, A.; Schlögl, R. Immobilized Carbon Nanofibers as Industrial Catalyst for ODH Reactions. *J. Catal.* **2006**, *244*, 126–129.
(71) Zhao, Z.; Dai, Y.; Lin, J.; Wang, G. Highly-Ordered Mesoporous Carbon Nitride with Ultrahigh Surface Area and Pore Volume as a Superior Dehydrogenation Catalyst. *Chem. Mater.* **2014**, *26*, 3151–3161.
(72) Zhao, Z.; Dai, Y. Nanodiamond/carbon Nitride Hybrid Nanoarchitecture as an Efficient Metal-Free Catalyst for Oxidant- and Steam-Free Dehydrogenation. *J. Mater. Chem. A* **2014**, *2*, 13442.
(73) Yu, D.; Nagelli, E.; Du, F.; Dai, L. Metal-Free Carbon Nanomaterials Become More Active than Metal Catalysts and Last Longer. *J. Phys. Chem. Lett.* **2010**, *1*, 2165–2173.
(74) Kuznetsov, V.; Moseenkov, S.; Ischenko, A.; Romanenko, A.; Buryakov, T.; Anikeeva, O.; Maksimenko, S.; Kuzhir, P.; Bychanok, D.; Gusinski, A.; *et al.* Controllable Electromagnetic Response of Onion-like Carbon Based Materials. *Phys. Status Solidi B* **2008**, *245*, 2051–2054.
(75) SUN, X.; WANG, R.; SU, D. Research Progress in Metal-Free Carbon-Based Catalysts. *Chin. J. Catal.* **2013**, *34*, 508–523.
(76) Ba, H.; Liu, Y.; Mu, X.; Doh, W.-H.; Nhut, J.-M.; Granger, P.; Pham-Huu, C. Macroscopic Nanodiamonds/β-SiC Composite as Metal-Free Catalysts for the Steam-Free Dehydrogenation of Ethylbenzene to Styrene. *Appl. Catal. Gen.*
(77) Liu, H.; Diao, J.; Wang, Q.; Gu, S.; Chen, T.; Miao, C.; Yang, W.; Su, D. A nanodiamond/CNT–SiC Monolith as a Novel Metal Free Catalyst for Ethylbenzene Direct Dehydrogenation to Styrene. *Chem. Commun.* **2014**, *50*, 7810–7812.
(78) http://mcgroup.co.uk/researches/styrene, Styrene: 2015 World Market Outlook and up to 2019. **2015.**

Chapter 2

Supports and characterization techniques

1. Materials synthesis

1.1. Nanodiamonds

The unique nanodiamonds history could be summed up in 3 main Milestones in URSS. It was first discovered by a group of scientists at VNIITF (Snezhinsk) in 1963, but remains unknown to the rest of the world, and then rediscovered in 1982 by A.M. Staver and A.I. Lyamkin from the Academy of Sciences of the USSR (Novosibirsk), and by G.I. Savvakin at the Institute of Problems of Materials Science, Academy of Sciences of the UkSSR (Kiev).[1] Long-time unrecognized, thanks to a number of significant inroads these diamond particles has known greater interest in the late of 1990[s], especially in the field of electronic,[2] engineering and biomedical,[3] of composite coating, grinding,[4] polishing, lubrication, seals, photographic materials, high-strength resin and rubber, seeds, drugs.[5]

The nanodiamond can be obtain by different synthesis method, with negative oxygen detonation technique,[6,7] high-energy ball milling of high-pressure high-temperature (HPHT) diamond microcrystals,[8] chemical vapour deposition (CVD),[9] ion irradiation of graphite just to cite a few,[10] however the first method still the most used industrially.

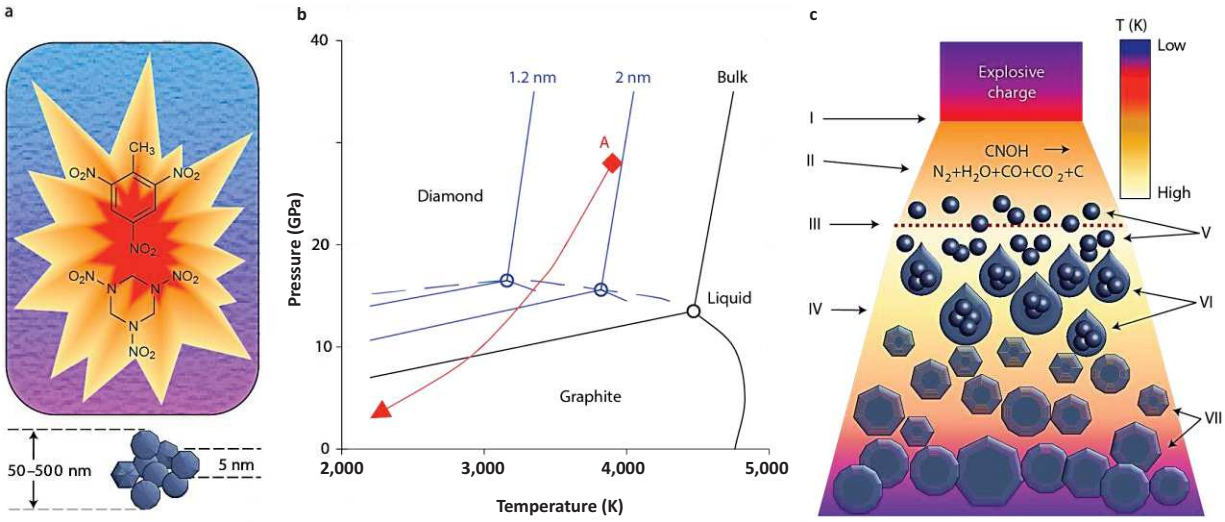

Figure 32. (a) Detonation diamond synthesis using TNT and hexogen as carbon and energy source, (b) Phase diagram of carbon and the detonation parameters showing the region of stability during the detonation process, and (c) Schematic of the detonation wave propagation.[11]

Detonation synthesis of nanodiamonds is summarized in figure. 32, typically a mixture of 60 wt% TNT ($C_6H_2(NO_2)_3CH_3$) and 40 wt% hexogen ($C_3H_6N_6O_6$))[12] are detonated in a closed metallic chamber in an atmosphere of N_2, CO_2 and liquid or solid H_2O.The technique

allows to makes the carbons transform into diamond under the conditions of high temperature (from 3000 K to 5000 K) and high pressure (from 20 GPa to 30 GPa) produced by a moment explosion. After detonation, diamond-containing soot is collected from the bottom and the walls of the chamber. b, Phase diagram showing that the most stable phase of carbon is graphite at low pressures, and diamond at high pressures, with both phases melting when at temperatures above 4,500 K (with the precise melting temperature for each phase depending on the pressure). Gogotsi et al. described well in figure1.c the schematic of the detonation wave propagation showing (I) the front of the shock wave caused by the explosion; (II) the zone of chemical reaction in which the explosive molecules decompose; (III) the Chapman–Jouguet plane (where P and T correspond to point A in Fig. 1b, indicating the conditions when reaction and energy release are essentially complete); (IV) the expanding detonation products; (V) the formation of carbon nanoclusters; (VI) the coagulation into liquid nanodroplets; and (VII) the crystallization, growth and agglomeration of nanodiamonds.[11]

Figure 1.b shows the phase diagram for carbon, showing that diamond is metastable at room temperature and pressure. However, the detonation of carbon-containing explosives at high temperature and pressure with a negative oxygen balance results in the condensation of the free atomic carbon products as diamond or liquid carbon. This is due to a fast decrease in pressure while the system is still at a high temperature, which favours a diamond-to-graphite transformation. Study based on theoretical calculation have shown that the conditions for diamond stability during the detonation are only maintained for few sub-microsecond and are closely followed by conditions where graphite is the more stable phase.[13]

To obtain diamond, it is therefore important to control the rate at which the system cools, the higher the cooling capacity, the larger the diamond yield. After synthesis diamond particles are subjected to a sieve to trap metals, plastics, and other pieces of impurities. After achieving the above step diamond particles submitted to different heat treatment and strong acidic treatment in order to remove respectively the non-diamond phase and the impurities such us metal and oxides originate from the detonation igniter and the steel wall of the detonation chamber.[14,15,16]

Commercial detonation ND powders contain up to 98% diamond in the form of 2–10nm particles with very small amounts of sp^2 impurity and has a high degree of structural defect.The nanodiamond in powder form used in this work purchased from the Carbodeon Ltd Oy (Finland) and were used without any further treatment. The NDs size, measured by TEM, was centered at around 5 ± 2 nm and is present in large aggregates (Fig. 33).

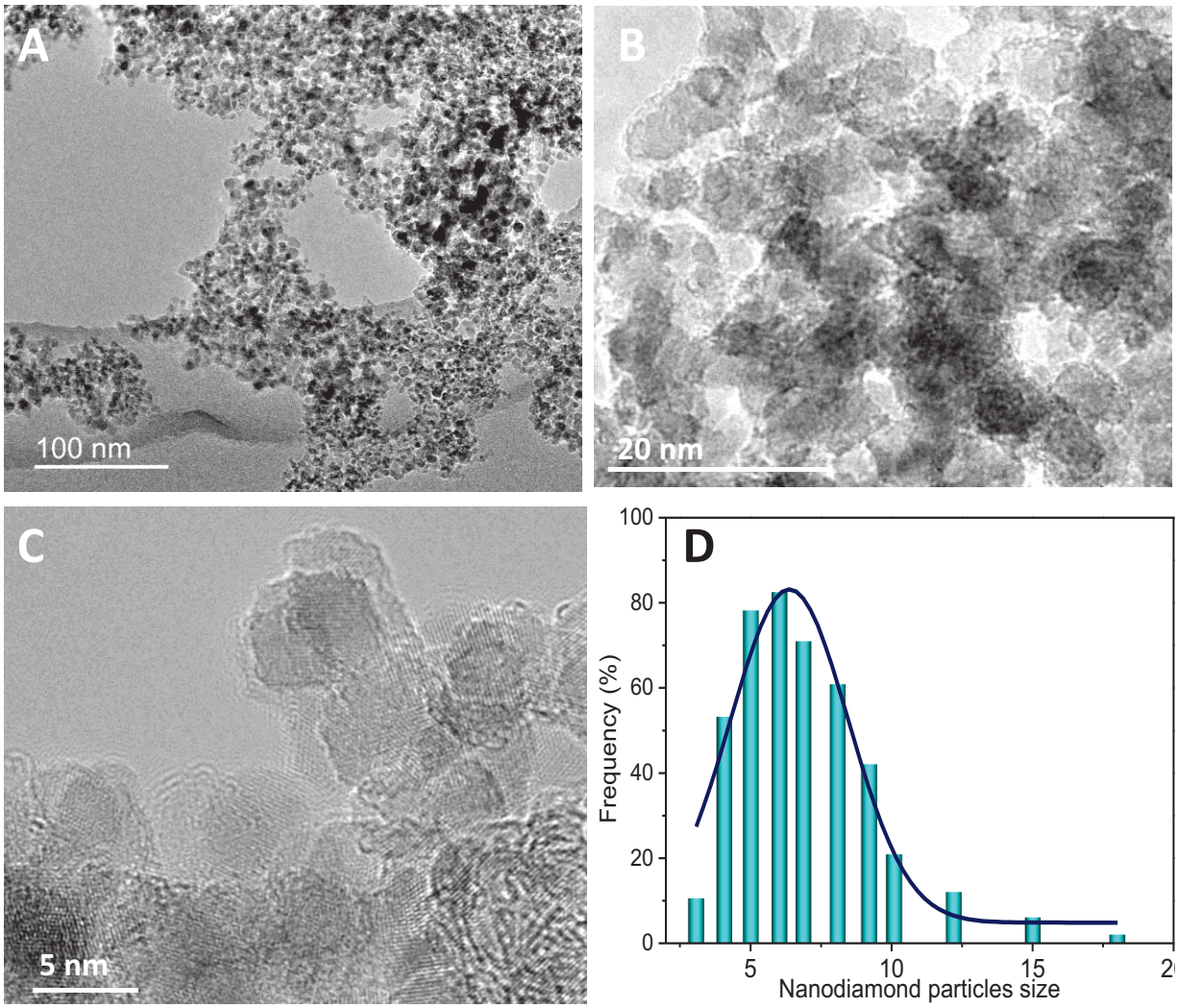

Figure 33. TEM micrographs of the pristine NDs powder and corresponding particle size distribution

1.2. Graphene based-materials

1.2.1. Few-layer graphene

The few-layer graphene (FLG) was synthesized by a mechanical ablation method using pencil lead as a starting raw material.[17] The process is based on the mechanical thinning of pencil lead on a solid surface with controlled roughness (glass, quartz or metal) combined with the ultra-sonication in an appropriate liquid media. Commercially available pencil leads consist of graphitic material embedded in an inorganic binder which maintains the macroscopic form of the lead. High hardness coefficients (scale of Mohs) for the minerals present in the binder (kaolin) and for quartz disk allow the ablation of the lead, and not only a

simple sliding of the graphene sheets. The mechanical thinning of the pencil lead is carried out on an automatically home-made setup where the pencil leads move with controlled pressure force onto the glass (quartz) and rotate (or not) in the opposite direction of the disk rotation (Fig. 34). By continuous rotating, the part of the disk which is covered by the ablated lead periodically passes through an ultra-sonication bath containing a solvent (ethanol, toluene, water) which permits to remove the graphene sheets from the disk surface.

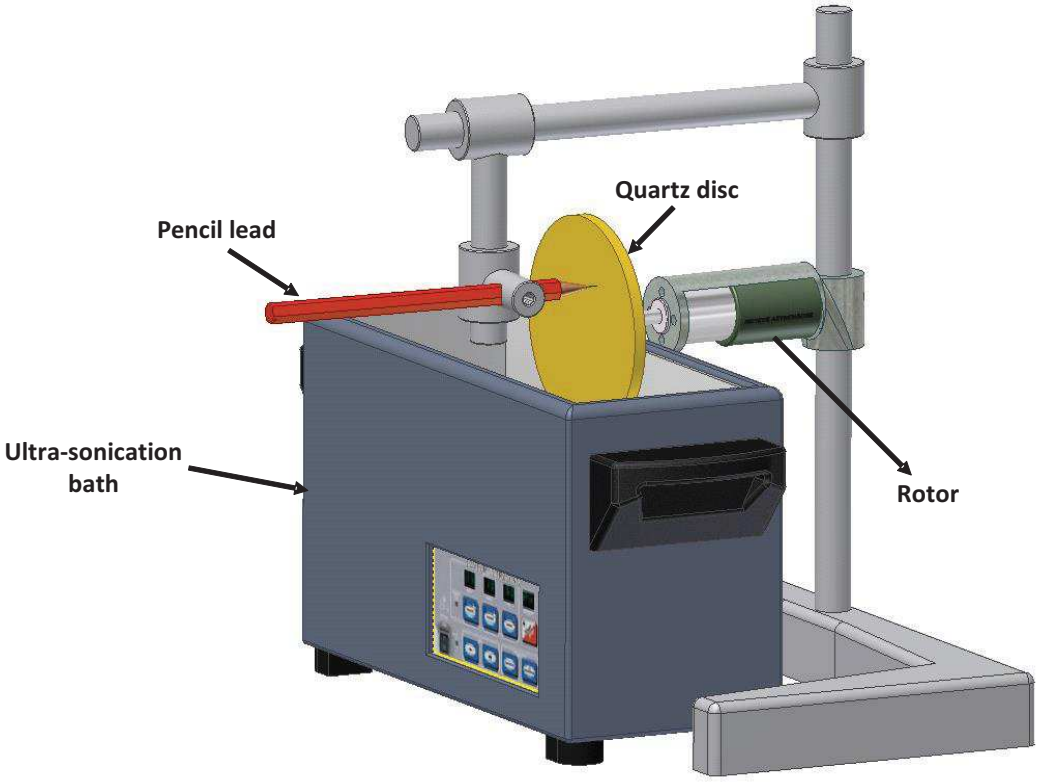

Figure 34. Illustration of the main part of the mechanical set-up to synthetize the FLG from the pencil lead by a mechanical ablation

The obtained suspension, containing the FLG and inorganic binders, is purify from the inorganic binder, which requires a filtration in the case of organic solvents, followed by a separated basic (NaOH, 20%wt., 3 h) and acid (HCl, 5 M, 1 h) treatments in reflux, washing, further filtration and drying.The product is then ultra-sonicated for 0.5 h in toluene, or ethanol and the suspension is then subjected to decantation, which allows the separation of the FLG from the heavier, thicker, not well ablated graphite core.

The TEM analysis indicates that the material synthesized by this method is consisted of FLG sheets with a dimension of about few μm and are consisted with FLG contain between two up to thirty graphene sheets (Figure 35).

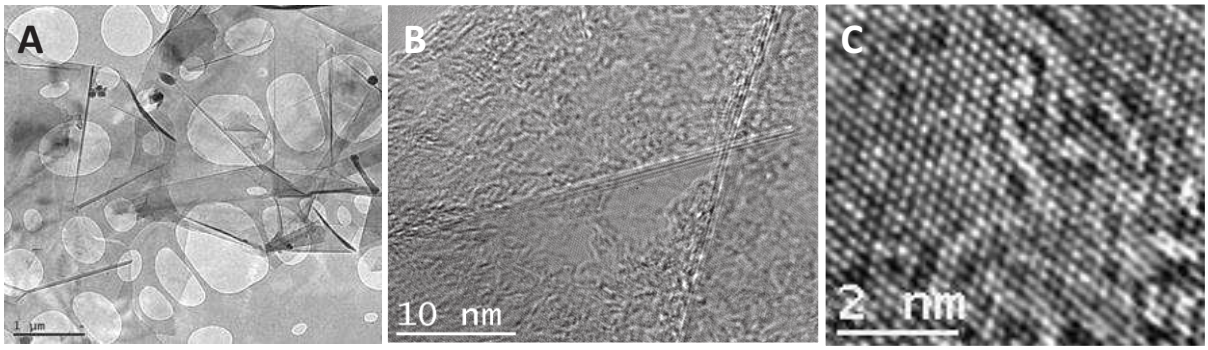

Figure 35. TEM micrographs with different magnifications of the FLG synthesized by a mechanical ablation method.

1.2.2. Graphene oxide

Graphene oxide (GO) powder was prepared from graphite flakes using modified Hummers method.[18,19] Briefly, 5 g of graphite (Sigma-Aldrich, cat # 332461, ~ 150 μm) and 3.75 g of $NaNO_3$ were placed in a flask. Then, 375 mL of H_2SO_4 (95%) was added drop-wise while the system was kept under stirring in an ice-water bath, and 25 g of $KMnO_4$ were slowly added during 1 h. Stirring was continued for 2 h in the ice-water bath. The ice bath was then removed and the mixture was stirred at room temperature until it became pasty brownish and then 250 mL deionized (DI) water was slowly added to the system. The reaction temperature was rapidly increased to 98°C, and the color changed to brown after 2 h. Finally, 15 mL of 30 wt% aqueous solution of H_2O_2 was added to complete the oxidation process. The ions of oxidant and other inorganic impurities were removed by repeating cycles of centrifugation, followed by the removal of the supernatant liquid, and the solid was redispersed using 3 wt % HCl aqueous solution. After filtration, the solid was dispersed again in water using ultrasonication for 2 h and centrifuged at 6000 rpm for 30 min to remove the multilayered- carbon species.

1.3. Carbone nanotubes / nanofibers

Chemical vapor deposition (CVD) is a most widely used method for synthesizing CNTs/CNFs.[20] The advantages of the CVD method are: (i) low synthesis temperatures compared to arc-discharge and laser ablation methods,[21,22] (ii) high selectivity towards CNTs thus allows one to avoid post-synthesis oxidative purification step, and (iii) the easy scaling up of the method for mass production of CNTs. A scheme of the CVD synthesis setup used for synthesis of carbon nanotubes or nanofibers is shown in Figure 36. Synthesis

of carbon nanotubes by CVD method was first done in 1993 by Jose-Yacaman et. al.[23] Since then, this method have been rapidly progressed for synthesis of CNTs in different ways i.e. fixed bed CVD, fluidized bed CVD and liquid or solid precursor CVD.

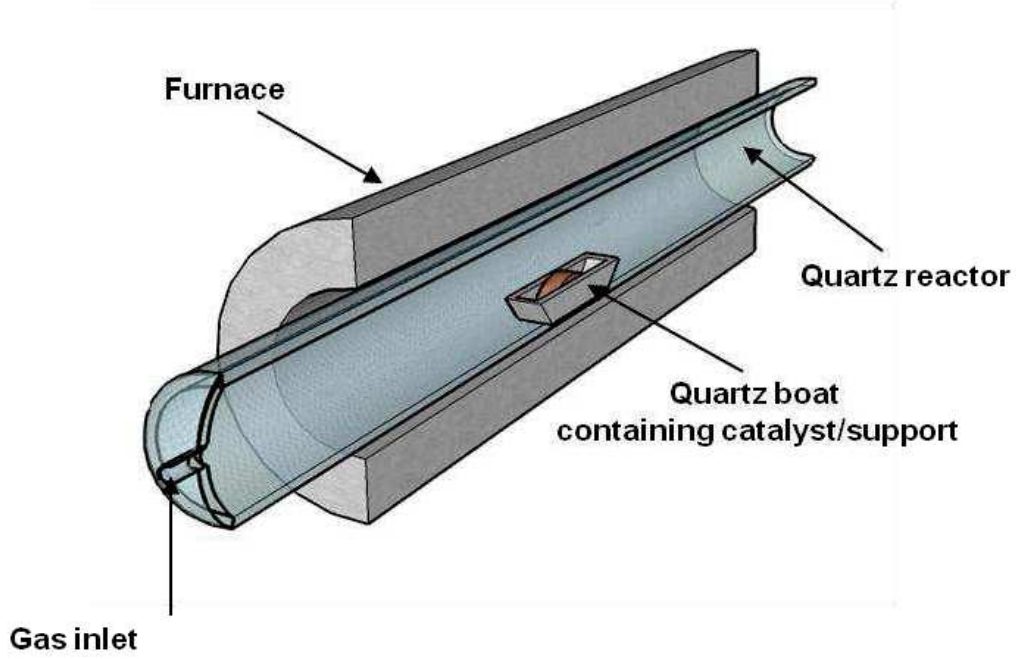

Figure 36. Scheme showing the setup for the synthesis of carbon nanotubes by CVD method.

The support used was a high surface area γ-Al_2O_3 (CK 300B Ketjen with a surface area of 220 m^2g^{-1}) which was mainly made up of a mesoporous network. The alumina support was crushed and sieved and a fraction of 80–150 μm was retained for catalyst preparation. The catalyst was prepared using an aqueous solution of Fe ($Fe(NO_3)_3.9H_2O$), with the Fe concentration fixed at 20 wt.%. The wet solid was dried at 100°C and then calcined in air at 450°C for 2 h in order to obtain the oxidic form of the catalyst precursor, and in the case of nanofibers synthesis nickel is used as growth catalyst.

The catalyst (1 g), in its oxidic form, was placed in a ceramic boat inside a quartz tube (diameter 30 mm, length 600 mm), located in an horizontal electrical furnace, and flushed for 30 min in flowing pure hydrogen at room temperature and finally reduced at 400°C for 2 h. After this treatment the hydrogen flow was replaced by a mixture of ethane and hydrogen (50 ml min^{-1}/50 ml min^{-1}) and the temperature of the furnace was rapidly increased (20°C min-1) to 650°C. The synthesis was carried out at 650°C for 2 h. After synthesis the raw products were treated with a solution of NaOH (1 M) at 110°C in order to remove the alumina support. The resulting material was washed several times with distilled water and then treated with a solution of aqua regia (HCl/HNO_3 3/1) in order to remove the remaining iron particles, it was

then washed with distilled water before being dried at 200°C. Figure 37 show the high yield carbone nanotubes obtained by CVD method, that allowing this process to be part of one of the most promising techniques for industrial application.
Carbon yields were calculated by weighing the sample after the reduction process and after the carbon nanotube synthesis according to the following formula:

$$\textbf{CNTs yield (wt.\%)} = (M_F - M_I)/M_I) \times 100$$

where MF is the total weight obtained after synthesis and MI is the weight of the catalyst after reduction.

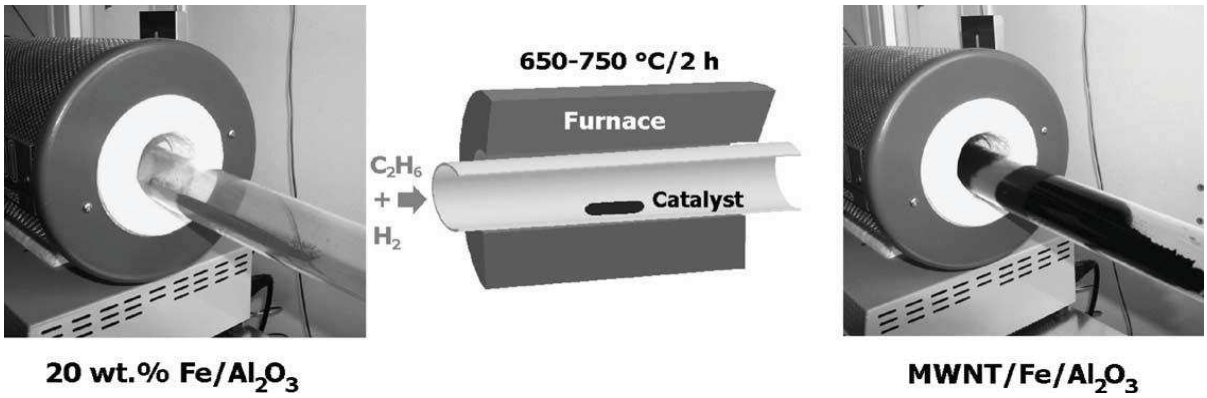

Figure 37. Illustration of the high yield of the synthesized carbone nanotubes bye chemical vapor deposition process

CVD is also one of the most used methods for synthesis of the N-doped CNTs material. The properties of these doped carbon nanotubes, closely depend on the conditions of the CVD method, i.e. the source of nitrogen and carbon, synthesis temperature and the type of CVD method used. Various kinds of nitrogen source have been used for N-CNTs synthesis, in our case Nitrogen source was provided by ammonia (Air liquide, 99.9996%) which was co-feeded into the reactant mixture. Ethane (Linde, 99.9995%) and argon (Linde, 99.99995%) were used as carbon source and carrier gas, respectively. The experimental design is based on a central composite design with the synthesis temperature ranging between 600 °C and 850°C and ethane/ammonia concentration (defined as a volume percentage of $C_2H_6/(C_2H_6 + NH_3)$) ranging between 20% and 100%. Figure 38 present the morphology of various carbon-based materials synthetized bye CVD method during my thesis.

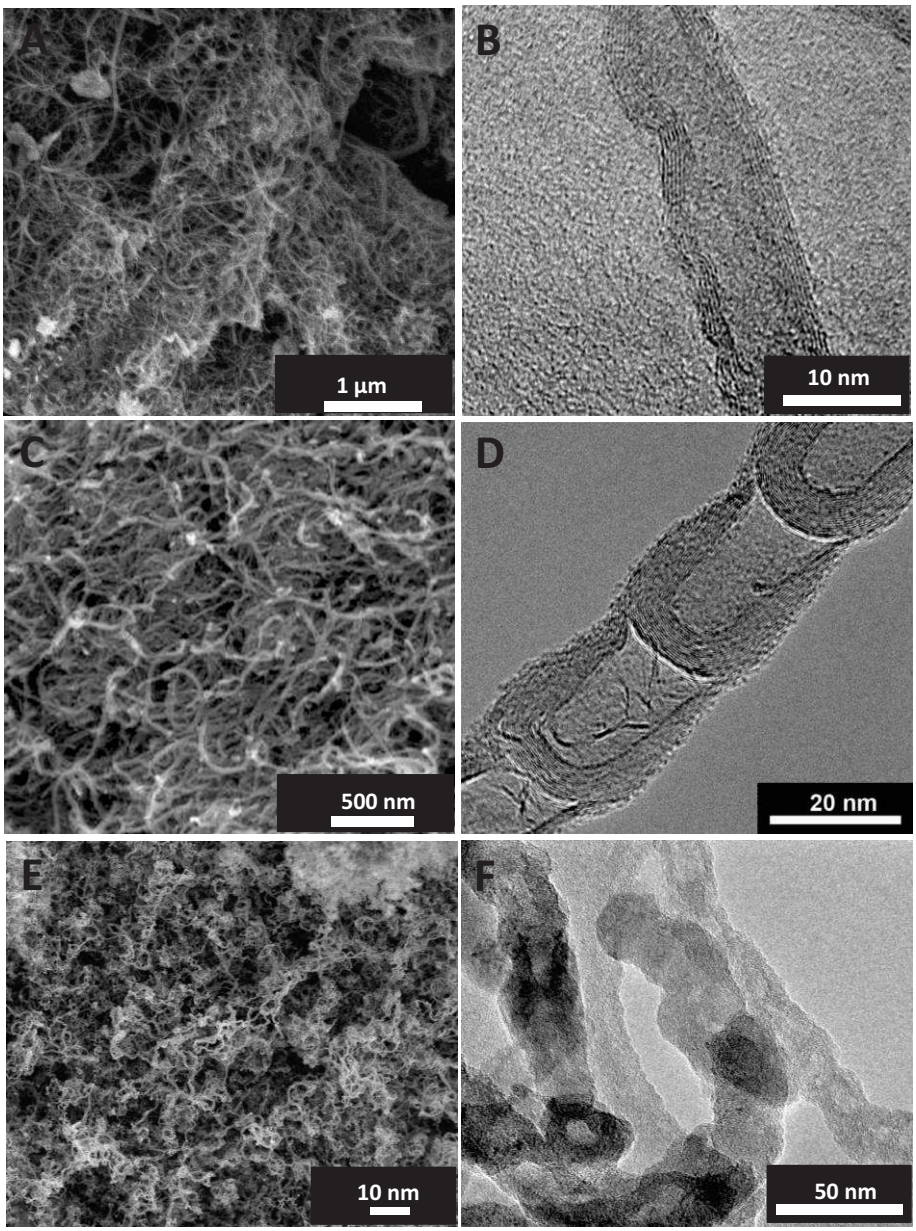

Figure 38. SEM and TEM images of (A, B) carbon nanotubes, (C, D) nitrogen-doped carbon nanotubes showing the presence of periodical bamboo-like structure along the tube axis and (E, F) carbone nanofibers with the prismatic planes.

1.4. Silicon Carbide

Silicon carbide (SiC) is a covalent material synthesized by a gas–solid reaction, exhibit a high thermal conductivity, mechanical strength, chemical inertness and excellent resistance to oxidation and corrosion.Since the last decades, SiC with medium to high surface area and different size and shape, i.e. extrudates, grains, beads, foam, etc., was expected to be an very promising catalyst support in the research and industrial environment.

Silicon carbide (β-SiC) in different shape was synthesized via a gas-solid reaction between SiO vapour and dispersed solid carbon. The detailed synthesis of the SiC-based materials is summarized in a recent review.[24] The β-SiC was using stoichiometric mixture of micronized (<20µm) metallic silicon and carbon (carbon black, Cabot and high carbon yield binder as carbon pre-cursor). Temporary binder, i.e. methyl cellulose, polyvinyl alcohol, polyethylene glycol, sodium silicate, SiO_2 sol, can be also added. Then the starting materials are mechanically mixed until obtaining a pasty mixture. The paste will be further shaped into desired shape, i.e. extrudates, grains, beads, etc, before carburization using standard technologies, like extrusion, spheronisation, granulation, pelletizing and etc. The carburization process was carried out under flowing argon at temperature around 1350°C during one hour in order to synthesize self-bonded porous silicon carbide materials. Above1000°C, the metallic silicon will then react with residual traces of oxygen to form SiO(g) which siliconize the carbon structure into SiC according to Eq.(1) and (2), whereas CO is allowed to carburize the metallic silicon, the crossed reactions being.

$$SiO_g + 2C_s \rightarrow SiC_s + CO_g \quad (1)$$

$$CO_g + 2Si_s \rightarrow SiO_s + SiC_s \quad (2)$$

For the synthesis of β-SiC in foam shape, the starting polyruethane foam (PU foam) was infiltrated with a mixture of phenolic resin containing micrometric Si and carbon black at room temperature. After drying, the obtained solid containing the resin, Si and carbon black was slowly heated up in flowing argon (1°C min^{-1}) from room-temperature to the carburization temperature (1350°C). During the heating from room-temperature to 700°C the resin underwent carbonization leaving behind a solid carbon skeleton containing oxygenated groups. At the carburization temperature, the oxygen issued from the resin reacted with Si to generate SiO vapour which further reacted with the carbon structure to form the SiC. The synthesis method allowed the complete conservation of the foam structure when passing from PU to carbon and finally SiC. furthermore, the foam structure displays a significant improvement of radial mixing of the flow passing through it porous matrix, due to the continuous impact between the flow and the support struts which generates turbulences within the flow pattern with favor the accessibility of reactant and the product evacuation.

The as-synthesized SiC was submitted to an oxidative treatment in air at 800°C for 2 h in order to remove the residual carbon. The resulted SiC material was thus partly covered with a thin layer of SiO_2 and SiO_xC_y (Fig. 39 A,B) which could play the role of anchorage site for dispersing metal nanoparticles on its surface.[25,26]

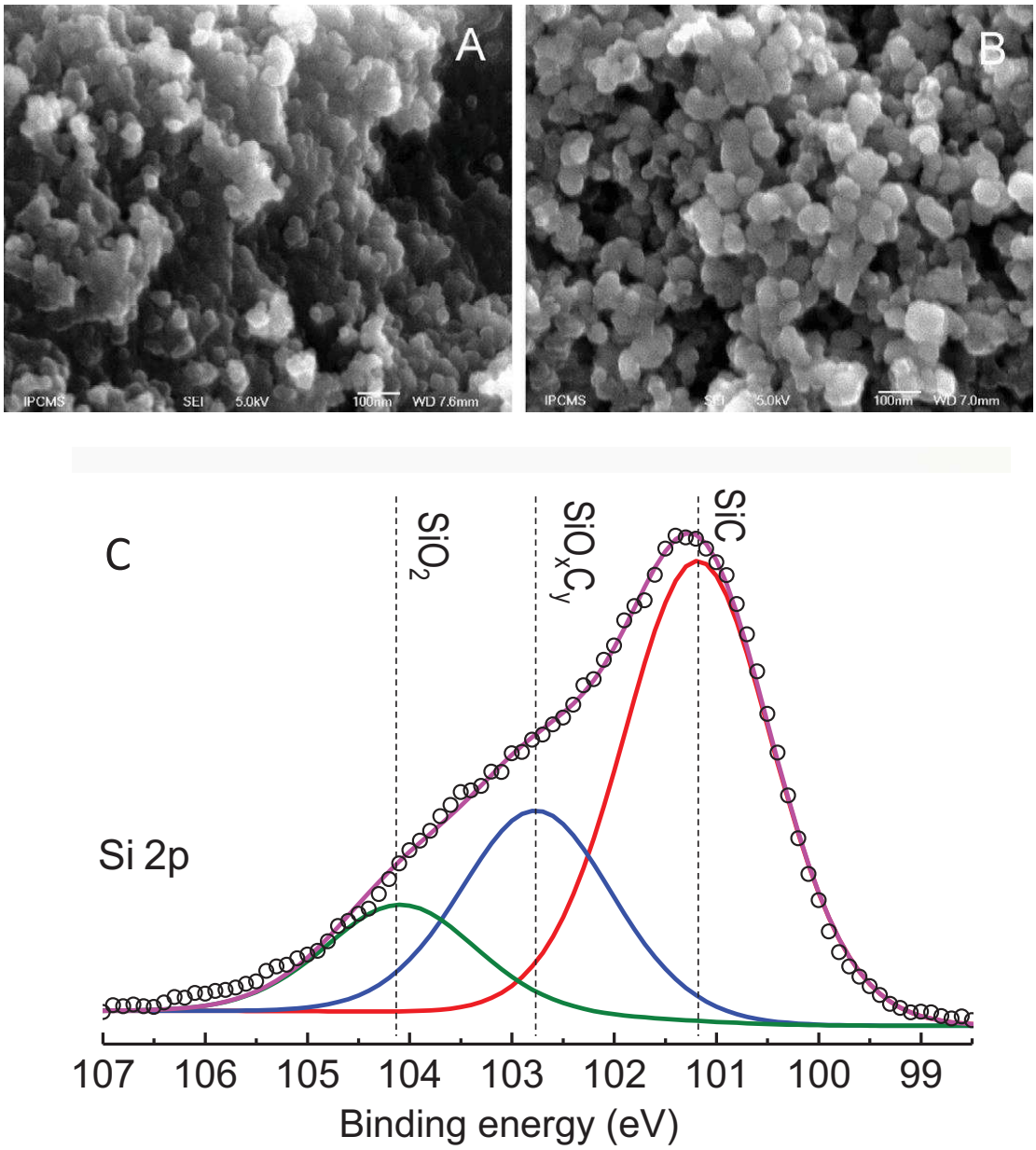

Figure 39. SEM micrographs of (A) carbon black, Cabot and (B) corresponding beta SiC material showing the complete morphological conservation of the material during the C-to-SiC transformation. (C) XPS Si *2p* of the SiC surface showing the presence of SiC, SiO_xC_y and SiO_2.

Currently the process is industrialized by SiCAT Sarl, and the company are able to produce a large panel of well controlled SiC materials with controlled size and shape with medium to high specific surface area and adaptable morphology regarding the downstream catalytic applications. Some examples of these SiC-based materials are presented in Figure 40.

Shape	Diameter (mm)	Length (mm)
Extrudates	1 - 5	2 - 10
Trilobes	1.6	2 - 10
Rings	OD 5 - 13 / ID 3 - 8	5 - 15
Spheres	2 - 8	-
	Cell size (PPI)	Size (mm)
Foams	8 - 30	10 - 300

Figure 40. Macroscopic shapes, i.e. grains, extrudates, foams, rings of silicon carbide synthesized by a gas-solid reaction (www.sicatcatalyst.com)

2. Catalytic Reactions

2.1. Selective dehydrogenation of ethylbenzene to styrene

The steam-free catalytic dehydrogenation of ethylbenzene to styrene is carried out in a fixed-bed continuous flow reactor under atmospheric pressure. The catalyst (300mg) is loaded onto a quartz fritted disk located inside a tubular quartz reactor (id x l: 8 mm x 800 mm). Helium gas was fed into the reactor at a flow rate of 30 mL min^{-1} through a mass flow controller (BROOKS MFC) and passed through a glass evaporator filled with liquid EB maintained at 40 °C (EB partial pressure of 2922 Pa) using a thermal regulated bath. The helium flow containing EB was passed downward through the catalyst bed.

The reaction system was heated to 550°C and kept for 2h under the He. The reactant flow (2.8 vol. % EB diluted in helium, total flow rate of 30 mL·min^{-1}) was then fed to the

reactor. The reactant and the products (styrene (ST), benzene (BZ) and toluene (TOL) exit from the reactor was analyzed on–line with a PERICHROM (PR 2100) gas chromatography equipped with a flame detector (FID) and CP WAX S2CB column which was previously calibrated. In order to avoid any possible condensation of the reactant or the products all the tube lines were wrapped with a heating wire kept maintaining 110°C.
The ethylbenzene conversion (X_{EB}), styrene selectivity (S_{ST}) and yield (Y_{ST}) were evaluated using the following equations:

$$X_{\mathrm{EB}} = \frac{F_0 C_{EB,inlet} - \mathrm{F} C_{EB,outlet}}{F_0 C_{EB,inlet}} \times 100\% \quad (1)$$

$$S_{\mathrm{ST}} = \frac{C_{ST,outlet}}{C_{ST,outlet} + C_{TOL,outlet} + C_{BZ,outlet}} \times 100\% \quad (2)$$

$$Y_{ST} = X_{EB} \times S_{ST} \quad (3)$$

Where F and F_0 are the flow rates of the outlet and inlet, respectively, and CEB, CST, CTOL and CBZ represent the concentration of ethylbenzene, styrene, toluene and benzene. The carbon balances amounted to ≥ 96% in all investigations. The specific rate is expressed as amount of styrene produced per gram catalysts per hour (mmolST.g-1.h-1). The results are obtained after 15h on stream with stable catalytic performance at testing conditions.

2.2. Oxygen Reduction Reaction (ORR)

Electrochemical studies were performed at 25 °C in a three-electrode cell in 0.1 M KOH supporting electrolyte, using an Autolab PGSTAT30 (Eco Chemie, The Netherlands) potentiostat equipped with an analogue linear sweep generator at a scan rate of 10 mV s^{-1}. Mercury oxide (Hg/HgO) electrode and Pt-wire electrode were used as reference and counter electrode, respectively. Unless otherwise stated, all potentials hereinafter are referred to the reversible hydrogen electrode (RHE). The electrochemical impedance spectroscopic (EIS) is used to determine the resistance of the electrolyte solution.
RRDE (rotating-ring disk electrode) measurements were performed on a Pine electrode (PINE AFE6R2GCPT, glassy carbon disk: 5.5 mm diameter and 0.2376 cm^2 geometrical area, Pt ring: 0.234 cm^2). 10.0 mg of catalyst, 5 mL isopropanol and 50 µL Nafion solution (5 wt.%) were ultrasonically mixed to form a homogenous catalyst ink that was drop-casted onto the

GC electrode and dried at room temperature. The reference Pt curve was recorded with a 20 wt.% Pt/VXC-72 (Sigma) catalyst with a loading of 25 μg_{Pt} cm^{-2}.

All aqueous solutions were prepared using ultrapure water (18MΩcm, < 3 ppb TOC) and supra-pure KOH (Sigma-Aldrich). In O_2-reduction experiments oxygen was constantly bubbled through the solution in order to maintain the saturation level and the ring potential was set at 1.2 V *vs*. RHE. Collection efficiency (N) was calculated from the experimental data obtained in 10 mM K_3FeCN_6 in 0.1 M NaOH at standard measurement conditions (potential sweep rate 10 mV s^{-1}, 25°C). The collection efficiency for the Pt(20%)/VXC-72 electrode was found to be 37 % which displays the same value as reported by Chlistunoff.[27]

The catalyst four-electron selectivity was evaluated on the basis of the H_2O_2 yield, calculated from the following equation (Eq. [1]):

$$H_2O_2(\%) = 200(J_R/N)/(J_R/N\text{-}J_D) \qquad [1]$$

Here, J_D and J_R are the disk and ring currents density, respectively, and *N* is the ring collection efficiency.

The electron transfer number can be calculated in two ways. The first is to use the ring current and the disk current (Eq. [2]):

$$n = -4J_D/(J_R/N\text{-}J_D) \qquad [2]$$

The second way to calculate n is by using the first-order Koutecky-Levich equation (Eq. [3]):

$$1/J_D = 1/j_k + 1/j_d \qquad [3]$$

where j_k is the kinetic current density and j_d *is* the diffusion-limited current density through the expression $j_d = Bf^{1/2} = 0.2nF\gamma^{-1/6}D_{O2}{}^{2/3}C_{O2}f^{1/2}$. Here *n* is the average electron transfer number; *F* is the Faraday constant; γ is the kinematic viscosity of the electrolyte; D_{O2} is the oxygen diffusion coefficient (1.95×10^{-5} cm^2/s); C_{O2} is the bulk oxygen concentration in the electrolyte (1.15×10^{-3} mol/dm^3); *f* is the angular velocity of the electrode. The kinetic current density (j_k) and the Koutecky-Levich slope (1/*B*) can be obtained from a plot of 1/*j* versus $1/f^{1/2}$.

3. Characterization techniques

X-ray diffraction (XRD) measurements were carried out in a Bruker D-8 Advance diffractometer equipped with a Vantec detector (Cu K_α radiation). The powdered sample was

packed onto a glass slide. The data sets were acquired in step-scan mode in a 2θ range 10-80º.

The X-ray photoelectron spectroscopy (XPS) measurements were carried out in an ultrahigh vacuum (UHV) spectrometer equipped with a VSW ClassWA hemispherical electron analyzer. A monochromated Al Kα X-ray source (1486.6 eV) was used as incident radiation and XP spectra were recorded using pass energy of 20 eV. Survey and high resolution spectra were recorded in constant pass energy mode (100 and 20 eV, respectively). The CASA XPS program with a Gaussian-Lorentzian mix function and Shirley background subtraction was employed to deconvolute the XP spectra.
UV-vis spectra were recorded using a spectrophotometer equipped with Peltier PTP1 system (PerkinElmer Lambda 35) at room temperature

Thermal gravimetry analysis (TGA) was performed on a Setaram apparatus with an air flow rate of 25 $mL \cdot min^{-1}$ and a heating rate of 10 $^{o}C \cdot min^{-1}$ from room temperature to 1000ºC.

The specific surface area of the support and the catalyst, after reduction, were determined in a Micromeritics sorptometer. The sample was outgassed at 250 °C under vacuum for 8 h in order to desorb moisture and adsorbed species on its surface. Physisorption measurements were carried out using N_2 as adsorbent at liquid N_2 temperature at relative pressures between 0.06 and 0.99.

Temperature programmed oxidation was determined in a Micromeritics ASAP-2100 setup equipped with a multi-channel mass spectrometer. The typical sample with 5 mg was loaded in the reactor and then flushed with 1% O_2/He mixture (25 ml/min) at room temperature (RT) for 30 min. The temperature was raised from RT to 900 ºC at a heating rate of 10 ºC/min. The evolved species were monitored with m/e intensities for 2(H_2), 18 (H_2O), 28 (CO) and 44 (CO_2), respectively.

Scanning electron microscopy (SEM) images were recorded using a JEOL 2600F instrument operating at an acceleration voltage of 15 kV and an emission current of 10 mA. The sample was covered by a thin layer of sputtered gold in order to avoid charging problem during the analysis.

Transmission electron microscope (TEM) was conducted on JEOL 2100F working at 200 kV accelerated voltage, equipped with a probe corrector for spherical aberrations, and a point-to-point resolution of 0.2 nm. The sample was dispersed in ethanol with the aid of mild sonication for 5 minutes and a drop of the suspension was deposited on a holey carbon grid for measurement.

The Raman spectra were recorded using LabRAM ARAMIS Horiba Raman spectrometer equipment. Spectra were recorded over the range of 500 - 4000 cm^{-1} at the laser excitation wavelength of 532 nm. The sample was deposited on glass substrate by spin-coating of its suspension and carefully dried before measurement.

References

(1) Danilenko, V. V. On the History of the Discovery of Nanodiamond Synthesis. *Phys. Solid State* **2004**, *46*, 595–599.

(2) He, D.; Shao, L.; Gong, W.; Xie, E.; Xu, K.; Chen, G. Electron Transport and Electron Field Emission of Nanodiamond Synthesized by Explosive Detonation. *Diam. Relat. Mater.* **2000**, *9*, 1600–1603.

(3) Khabashesku, V. N.; Margrave, J. L.; Barrera, E. V. Functionalized Carbon Nanotubes and Nanodiamonds for Engineering and Biomedical Applications. *Diam. Relat. Mater.* **2005**, *14*, 859–866.

(4) Chkhalov, N. I.; Fedorchenko, M. V.; Kruglyakov, E. P.; Volokhov, A. I.; Baraboshkin, K. S.; Komarov, V. F.; Kostyukov, S. I.; Petrov, E. A. Ultradispersed Diamond Powders of Detonation Nature for Polishing X-Ray Mirrors. *Nucl. Instrum. Methods Phys. Res. Sect. Accel. Spectrometers Detect. Assoc. Equip.* **1995**, *359*, 155–156.

(5) Kossovsky, N.; Gelman, A.; Hnatyszyn, H. J.; Rajguru, S.; Garrell, R. L.; Torbati, S.; Freitas, S. S.; Chow, G. M. Surface-Modified Diamond Nanoparticles as Antigen Delivery Vehicles. *Bioconjug. Chem.* **1995**, *6*, 507–511.

(6) Staver, A. M.; Gubareva, N. V.; Lyamkin, A. I.; Petrov, E. A. Ultrafine Diamond Powders Made by the Use of Explosion Energy. *Combust. Explos. Shock Waves* **1984**, *20*, 567–570.

(7) Kuznetsov, V. L.; Chuvilin, A. L.; Butenko, Y. V.; Mal'kov, I. Y.; Titov, V. M. Onion-like Carbon from Ultra-Disperse Diamond. *Chem. Phys. Lett.* **1994**, *222*, 343–348.

(8) Boudou, J.-P.; Curmi, P. A.; Jelezko, F.; Wrachtrup, J.; Aubert, P.; Sennour, M.; Balasubramanian, G.; Reuter, R.; Thorel, A.; Gaffet, E. High Yield Fabrication of Fluorescent Nanodiamonds. *Nanotechnology* **2009**, *20*, 235602.

(9) Frenklach, M.; Howard, W.; Huang, D.; Yuan, J.; Spear, K. E.; Koba, R. Induced Nucleation of Diamond Powder. *Appl. Phys. Lett.* **1991**, *59*, 546–548.

(10) Daulton, T. L.; Kirk, M. A.; Lewis, R. S.; Rehn, L. E. Production of Nanodiamonds by High-Energy Ion Irradiation of Graphite at Room Temperature. *Nucl. Instrum. Methods Phys. Res. Sect. B Beam Interact. Mater. At.* **2001**, *175–177*, 12–20.

(11) Mochalin, V. N.; Shenderova, O.; Ho, D.; Gogotsi, Y. The Properties and Applications of Nanodiamonds. *Nat. Nanotechnol.* **2012**, *7*, 11–23.

(12) *Conversion Concepts for Commercial Applications and Disposal Technologies of Energetic Systems*; Krause, H. H., Ed.; Springer Netherlands: Dordrecht, 1997.

(13) Dolmatov, V. Y.; Veretennikova, M. V.; Marchukov, V. A.; Sushchev, V. G. Currently Available Methods of Industrial Nanodiamond Synthesis. *Phys. Solid State* **2004**, *46*, 611–615.

(14) Jiang, T.; Xu, K. FTIR Study of Ultradispersed Diamond Powder Synthesized by Explosive Detonation. *Carbon* **1995**, *33*, 1663–1671.

(15) Gogotsi, Y.; Mochalin, V.; Osswald, S.; Yushin, G. Process of Purifying Nanodiamond Compositions and Applications Thereof. US20100028675 A1, 2010.

(16) Osswald, S. CHAPTER 4. In *CHAPTER 4:Nanodiamond Purification*; 2014.

(17) Janowska, I.; Vigneron, F.; Bégin, D.; Ersen, O.; Bernhardt, P.; Romero, T.; Ledoux, M. J.; Pham-Huu, C. Mechanical Thinning to Make Few-Layer Graphene from Pencil Lead. *Carbon* **2012**, *50*, 3106–3110.

(18) Hummers, W. S.; Offeman, R. E. Preparation of Graphitic Oxide. *J. Am. Chem. Soc.* **1958**, *80*, 1339–1339.

(19) Liang, Y. Y.; Wu, D. Q.; Feng, X. L.; Müllen, K. Dispersion of Graphene Sheets in Organic Solvent Supported by Ionic Interactions. *Adv. Mater.* **2009**, *21*, 1679–1683.

(20) Gulino, G.; Vieira, R.; Amadou, J.; Nguyen, P.; Ledoux, M. J.; Galvagno, S.; Centi, G.; Pham-Huu, C. C2H6 as an Active Carbon Source for a Large Scale Synthesis of Carbon Nanotubes by Chemical Vapour Deposition. *Appl. Catal. Gen.* **2005**, *279*, 89–97.
(21) Gamaly, E. G.; Ebbesen, T. W. Mechanism of Carbon Nanotube Formation in the Arc Discharge. *Phys. Rev. B* **1995**, *52*, 2083–2089.
(22) Journet, C.; Maser, W. K.; Bernier, P.; Loiseau, A.; de la Chapelle, M. L.; Lefrant, S.; Deniard, P.; Lee, R.; Fischer, J. E. Large-Scale Production of Single-Walled Carbon Nanotubes by the Electric-Arc Technique. *Nature* **1997**, *388*, 756–758.
(23) José-Yacamán, M.; Miki-Yoshida, M.; Rendón, L.; Santiesteban, J. G. Catalytic Growth of Carbon Microtubules with Fullerene Structure. *Appl. Phys. Lett.* **1993**, *62*, 202–204.
(24) Nguyen, P.; Pham, C. Innovative Porous SiC-Based Materials: From Nanoscopic Understandings to Tunable Carriers Serving Catalytic Needs. *Appl. Catal. Gen.* **2011**, *391*, 443–454.
(25) Deneuve, A.; Florea, I.; Ersen, O.; Nguyen, P.; Pham, C.; Bégin, D.; Edouard, D.; Ledoux, M.-J.; Pham-Huu, C. Catalytic Growth of Silicon Carbide Composite with Nanoscopic Properties and Enhanced Oxidative Resistance as Catalyst Support. *Appl. Catal. Gen.* **2010**, *385*, 52–61.
(26) Liu, Y.; Ersen, O.; Meny, C.; Luck, F.; Pham-Huu, C. Fischer–Tropsch Reaction on a Thermally Conductive and Reusable Silicon Carbide Support. *ChemSusChem* **2014**, *7*, 1218–1239.
(27) Chlistunoff, J.; Sansiñena, J.-M. Surface Confinement of Oxygen in Carbon Supported Oxygen Reduction Catalysts. *Meet. Abstr.* **2015**, *MA2015-01*, 1581–1581.

Chapter 3

Nanodiamonds supported on graphene-based materials as an efficient metal-free catalyst for styrene production

Nanodiamond decorated few-layer graphene composite as an efficient metal-free dehydrogenation catalyst for styrene production

Housseinou Ba [a,b], Seetharamulu Podila [a], Yuefeng Liu [a, *], Xiaoke Mu [a], Jean-Mario Nhut [a], Vasiliki Papaefthimiou [a], Spyridon Zafeiratos[a], Pascal Granger [b], Cuong Pham-Huu [a, *]

[a]*Institut de Chimie et Procédés pour l'Energie, l'Environnement et la Santé (ICPEES), ECPM, UMR 7515 du CNRS-Université de Strasbourg, 25 rue Becquerel, 67087 Strasbourg Cedex 02, France.*

[b]*Unité de Catalyse et Chimie du Solide (UCCS), UMR 8181 CNRS-Université de Lille1, Sciences et Technologies, 59655 - Villeneuve d'Ascq Cedex France.*

Article published in catalysis today DOI: 10.1016/j.cattod.2014.10.029

Graphical abstract

Abstract

Hybrid materials consisting of graphene and nanodiamonds (ND) can potentially display not only the individual properties of ND and graphene, but also those resulting from synergism when they closely interact. Herein, synergistic effects between ND and few-layer-graphene containing between 5 to 20 layers of graphene (FLG) are examined. The ND/FLG composite was prepared by mixing a suspension of FLG in ethanol with NDs. In this case, FLG plays the role of 2D support for dispersing ND clusters while NDs acting as a nano-spacer for partly preventing the re-stacking of the FLG sheets. The as-synthesized hybrid material was further used as metal-free catalyst for the steam-free direct dehydrogenation (DH) of ethylbenzene (EB) to styrene (ST). The DH activity obtained on the ND/FLG catalyst was benchmarked with other catalysts, i.e. commercial K-promoted Fe-based catalysts and carbon-based catalysts. The ND/FLG catalyst exhibits the highest DH activity among the tested catalysts with a dehydrogenation specific rate as high as 19 $mmol_{ST}g_{ND}^{-1}h^{-1}$ along with a selectivity towards styrene up to 95%. The catalyst displays a relatively high stability as a function of time on stream while the deactivated catalyst can be easily regenerated by an oxidative treatment in mild temperature conditions.

Keywords:

Nanodiamond – Few-Layer Graphene – Dehydrogenation – Ethylbenzene – Styrene – Metal-free catalyst

1. Introduction

Styrene is well recognized as one of the most important monomers for polymers and copolymers synthesis. Its production has known an exponential growth during the past century and will own this position for a long time to come. The industrial process for the catalytic dehydrogenation of ethylbenzene to styrene is one of the 10 most important organic catalytic processes.[1] Over 25×10^6 tons/year of styrene monomer is produced worldwide[2] which are further used in different types of application, including raw materials for the production of polystyrene, synthetic rubbers, plastics, acrylonitrile-butadiene-styrene (ABS) and styrene- acrylonitrile (SAN) resins.

Styrene is mostly produced by direct dehydrogenation of ethylbenzene on an iron-based catalyst, generally promoted with alkaline. Due to the endothermic character and equilibrium limitations of the dehydrogenation reaction, high temperatures are usually needed (i.e. 500-700°C). In such temperature conditions a large amount of carbonaceous is stepwise deposited on the iron surface during the reaction leading to a gradual encapsulation of the active phase and subsequent deactivation.[3] The presence of steam in large excess in the ethylbenzene dehydrogenation can partly remove the carbonaceous deposition by the gasification reaction and then preserve the catalyst activity. Steam also provides heat to maintain the reaction temperature within the catalyst bed in order to counter balance the endothermic character of the process. However, this process has a significant drawback since high energy consumption is required corresponding to 1.5×10^9 cal/ton of styrene.[4] In order to overcome this problem, oxidative dehydrogenation has been proposed as an alternative catalytic route.

Numerous studies have been focused on the low-temperature oxidative dehydrogenation (ODH) of ethylbenzene into styrene.[5-8] Indeed, during the last decade, metal-free catalysts based on nano-carbon materials, i.e. carbon nanotubes, either pure or doped, and carbon nanofibers, have been reported to be an alternative route for performing the oxidative dehydrogenation (ODH) of ethylbenzene to styrene.[9-11] The high degree of graphitization of these materials allows them to survive harsh operation conditions which would damage activated carbon due to its lower oxidative resistance.[10, 11] It is worthy to note that a large part of the literature data deals with the use of these metal-free nano-carbon catalysts in the oxidative dehydrogenation of alkanes in the presence of oxygen (ODH) while the direct dehydrogenation is only scarcely reported. In fact, the ODH reaction presents some important disadvantages compared to the oxygen-free dehydrogenation process namely the use of a mixture containing oxygen and hydrocarbon which leads to low selectivity towards styrene formation due to parallel side-reactions such as combustion. Recently, a report emphasized the use of nanodiamonds-based catalysts in the oxygen- and steam-free dehydrogenation of ethylbenezene to styrene.[12] It was found that nanodiamonds (NDs) catalyst exhibits a relatively high DH activity compared to that obtained on an iron-based commercial catalyst,

i.e. 20.5% of EB conversion instead of 7.1 %, and an almost exclusive selectivity towards styrene, i.e. 97 %, and a long-term stability up to several tenth of hours on stream.[12] The NDs also display an extremely high DH activity compared to other carbon-based catalysts as reported elsewhere.[12] The high DH activity of the NDs was attributed to the presence of a core-shell structured material, i.e. NDs wrapped with graphene layer with an unique sp^2-sp^3 hybrid structure, which provides high activity related to a partial delocalization of the electron density. The sp^2-sp^3 hybrid structure of NDs also actively contributes to the reduction of coke formation on the carbon surface.[13] However, commercial NDs in a powder form are composed of agglomerates which significantly reduce the accessibility of the active sites. Recently Su and co-workers[14] prepared NDs supported on a composite constituted by a silicon carbide host structure decorated with carbon nanotubes. The carbon nanotubes play the role of high effective surface support to anchor the NDs compared to the relatively low specific surface area of the SiC host structure which can hardly disperse the NDs.

The aim of the present study is to develop a highly active carbon-based catalyst consisting of dispersed nanodiamonds (NDs) decorated few-layer graphene (FLG) for the steam-free dehydrogenation (DH) of ethylbenzene (EB) to styrene (ST) in a fixed-bed reactor configuration. Few-layer graphene contains a large number of vacancies and defects which can promote the dispersion of NDs particles. Previous works has shown that the FLG is an efficient support for palladium in the liquid-phase hydrogenation of cinnamaldehyde.[15] In this present work, the dispersion of the NDs on the FLG surface leads to an increase of the density of active sites and, as a consequence, a significant improvement in the DH activity compared to bulk NDs while keeping the selectivity towards ST unchanged. The catalyst displays a higher DH performance compared to that obtained on the commercial iron-based catalyst which highlighted the advantage of using carbon-based catalysts to replace metal oxide catalysts for such a highly demanded reaction.[16] The as-synthesized catalyst also exhibits an extremely high stability as a function of the experiment duration.

2. Experimental

2.1 Nanodiamonds and few-layer graphene characteristics

The commercial nanodiamonds in powder form were supplied by the Hightech Co (Finland) and were used without any further purification. The NDs size, measured by TEM, was centered at around 5 ± 2 nm and is present in large aggregates (Fig. 41).

The FLG was synthesized by sonication of the expanded graphite (EG) at room temperature in an ethanol medium. The sonicated sample was allowed to settling for 30

minutes and the supernatant suspension containing thin few-layer graphene sheets was recovered for subsequent use. TEM analysis shows that the FLG is characterized by a large lateral size up to several micrometers and contains between two up to twenty graphene layers (Fig. 41 B and E). High-resolution TEM analysis indicates the presence of vacancies and defects on the FLG surface which provide anchorage sites for the active phase dispersion and stabilization. However, Raman analysis indicates that the FLG produced from the exfoliation of the expanded graphite used in this work is more graphitized and contains a lower number of defects than its counterpart synthesized by a mechanical ablation or sonication process of graphite-based materials.[17]

2.2 Synthesis of the ND/FLG catalyst

The suspension of FLG (typically from 5 to 20 layers) in ethanol was mixed with NDs through sonication process at room-temperature for 1h. The sonication allowed de-staking of the graphene sheets from each other because graphene has a high tendency to re-stake leading to a small exposed surface area. The formed mixture was then dried under agitation until the complete evaporation of solvent leading to the formation of the ND/FLG composite. The as-synthesized catalyst was further annealed in argon flow at 900°C for 2h before catalytic measurements in the direct dehydrogenation process. The NDs particles were anchored on both sides of the FLG sheet, according to our previous investigations of the Fe_3O_4/FLG system by TEM tomography[18,19] preventing further excessive re-stacking of the FLG sheets in the final composite.

3. Results and discussion

3.1 ND/FLG Characteristics

The representative SEM and TEM micrographs of the NDs, FLG and ND/FLG catalyst, are presented in Fig. 41. Comparing the unsupported NDs (Fig. 41 A and D) and then deposited on the FLG surface (Figs. 41C and F), we can clearly observe the higher dispersion of the NDs along with the significant reduction of aggregates within the NDs. It is expected that such dispersion should lead to significant improvements on the dehydrogenation activity per NDs weight over unsupported NDs compared to that of the unsupported NDs. However, it is worthy to note that the NDs dispersion on FLG surface is somewhat lower than that on GO

surface.[20] Such lower dispersion could be attributed to the presence of a lower density of defect on the FLG synthesized by the present method compared to the GO or FLG synthesized by mechanical ablation or microwaves assisted sonication process.[17, 21]

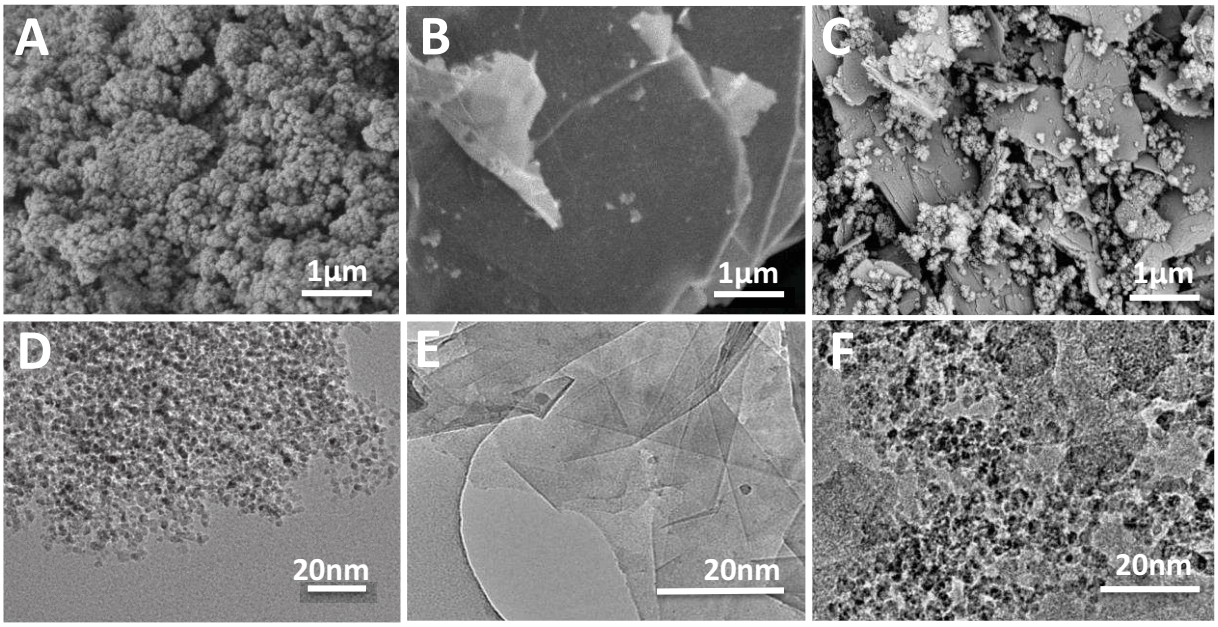

Figure 41. SEM and TEM micrographs of (A, D) bulk nanodiamond showing a highly dense structure, (B, E) few-layer graphene (FLG) with a relatively large lateral dimension. (C, F) the ND-FLG composite with 16 wt % NDs loading of displaying a noticeable dispersion of the NDs particles on the FLG surface.

The specific surface of different samples is presented in Table 3. Among the samples the FLG displays the lowest specific surface area, i.e. 30 m^2/g, which could be attributed to the high tendency of the FLG to restack upon drying through van der Waals forces. The NDs show the highest specific surface area, 330 m^2/g, which can be ascribed to the nanoscopic size of the material with a high density of surface defects. The ND/FLG samples display an intermediate specific surface area, ranging between 134 and 77 m^2/g, as a function of the NDs loading.

Table 3. Texture characteristics of nanodiamonds (ND), few-layer graphene (FLG) and different ND/FLG composites.

Sample	S_{BET} (m^2/g)	V_{total} (cm^3/g)	D_{BJH} (nm)
Commercial NDs[a]	283	1.27	15.8
NDs[b]	330	1.8	19.4
33 wt %ND/FLG	134	0.54	14.5
16 wt %ND/FLG	77	0.29	15.2
FLG	30	0.13	18.5

[a] The data is detected by using commercial NDs. [b] The commercial NDs were treated in helium at 550 ºC according to the EB reaction conditions.

As it can be found in Fig. 42, the C 1s photopeak from X-ray photoelectron spectroscopy (XPS) analysis for ND/FLG composite is observed, together with the spectra for NDs (treated in He at 550 ºC) and FLG as references. It is clearly observed that the presence of two C1s peaks at 284.5 eV and 286.5 eV can be respectively attributed to the carbon originated from typical sp^2-bonded and sp^3-bonded carbon (Fig. 42 A).[22,23] The shape of the ND/FLG composite is identical to the mixture of sp^2 and sp^3 bonded carbon. The C1s photopeaks that correspond to NDs appear to be broad and located at relatively high BEs, confirming the presence of several carbon species on the surface of NDs.[24,25] The ND/FLG intensity ratio calculated by analyzing the C 1s spectrum of ND and FLG related components is 0.4 and 1.0 for 13 wt. % and 33 wt. % NDs on the FLG, respectively.

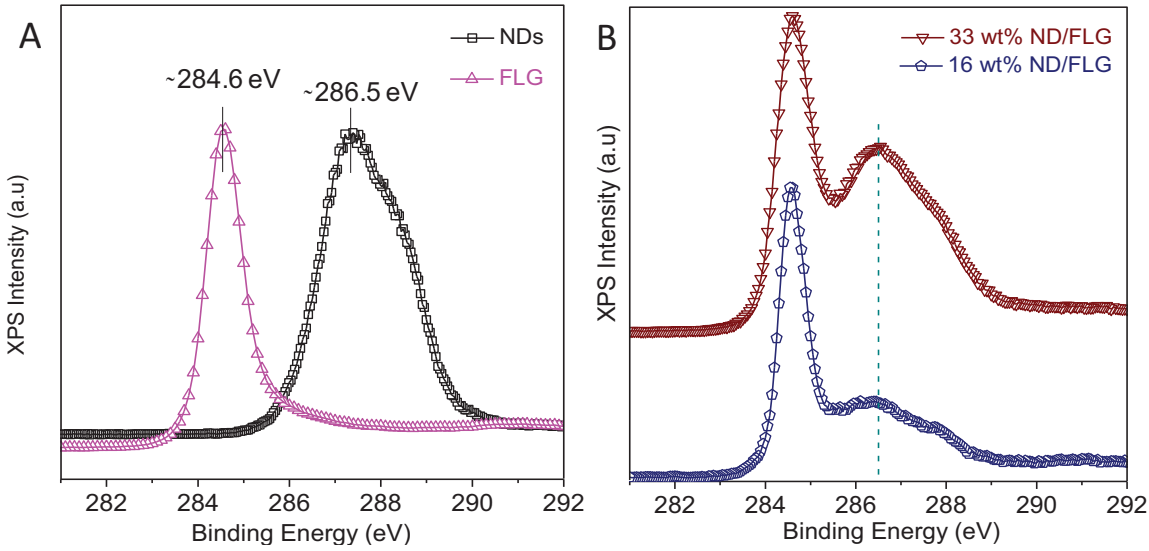

Figure 42. XPS C1s spectra of (A) Nanodiamond and FLG, and (B) ND/FLG with 16 wt. % and 33 wt. % nanodiamond particles loading.

High resolution TEM and the corresponding fast-Fourier transform (FFT) images are shown in Figs. 43 A-D, which display in-depth crystalline feature of such NDs decorated FLG composite. According to the HRTEM micrograph of ND/FLG catalyst with ND loading of 16 wt % in Fig. 43A, the NDs particles are well dispersed on the surface of the FLG. As previously discussed, such improvement of dispersion of the ND particles could be attributed to the presence of defects and vacancies on the FLG surface which play the role of anchorage sites for NDs. Similar results have also been observed with other metals and/or oxides nanoparticles.[18, 26, 27]

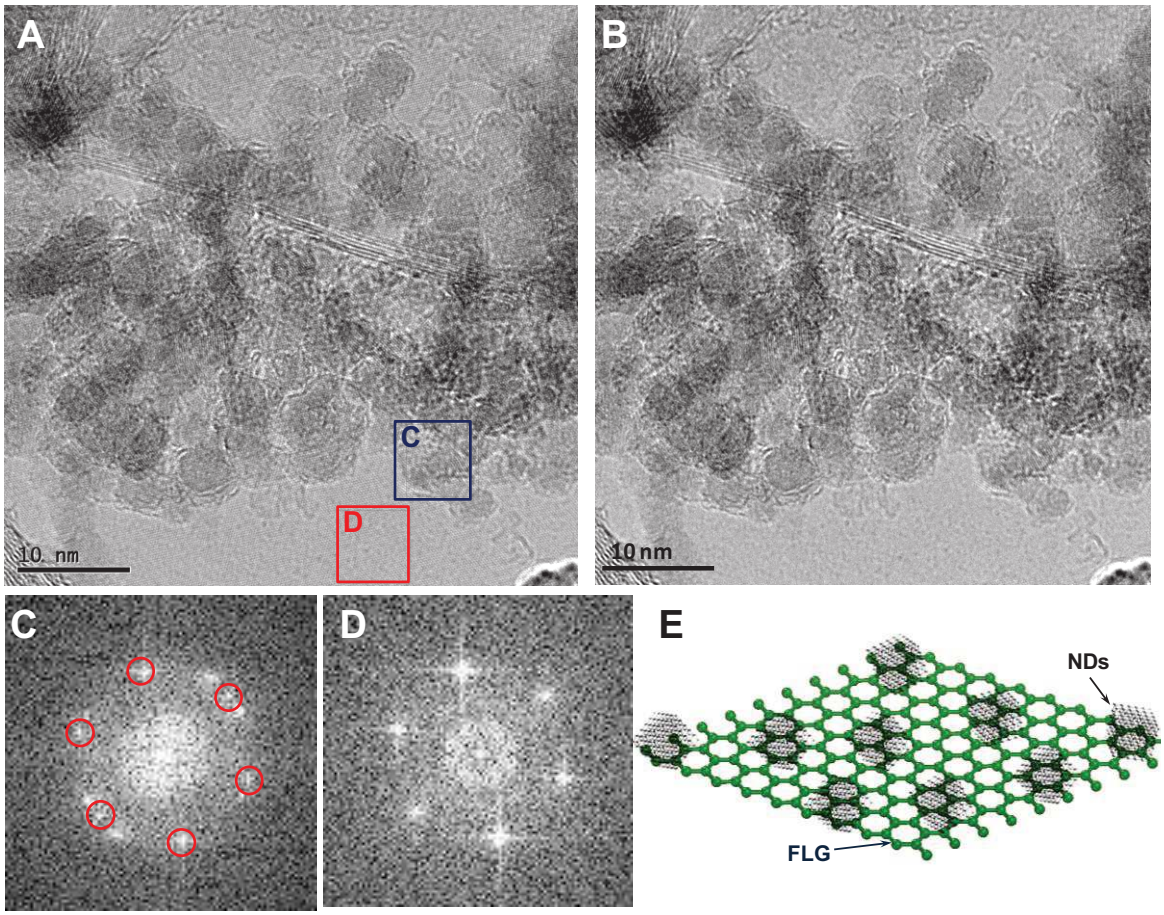

Figure 43. (A) High-resolution transmission electron microscopy (HRTEM) image of the ND/FLG (16 wt %) composite. (B) Fourier-filtered image of A shows the pure diamond lattices, where the contrast from graphene lattices is eliminated. (C) Fast-Fourier transform (FFT) of the area highlighted by the blue box in A. The red circles highlight the signals from the graphene lattices, which are removed in order to obtain the B. (D) FFT of the area highlighted by the red box in figure A. The hexagonal arranged bright spots represent the graphene lattices. (E) Schematic model illustrating the NDs anchored on the surface of graphene.

It is interesting to see that the average size of the NDs centered around 5 nm and is well anchored on both sides of the FLG surface. The presence of sp^2 layer on the topmost surface

of the ND particle is also clearly visible in the HR-TEM micrograph. The FFT of different area of Figure 3A are checked, where the NDs loaded on the FLG (blue box in Figure 43A) and blank FLG (red box in Figure 43A). The red circles highlight the signals from the graphene lattices, which are removed in order to obtain pure diamond lattices. The HRTEM image after fast-Fourier filtered (Figure 43B) of the ND/FLG composite indicates the pure diamond lattices, where the contrast from graphene lattices is eliminated. It is confirmed that the nano diamonds are highly dispersed on graphene surface through defects/vacancies anchorage (schematically presented in Fig. 43E), which could prevent the NDs agglomeration during the catalytic reaction.

3.2 Steam-free selective dehydrogenation of ethylbenzene to styrene

The DH activity and selectivity obtained over the different catalysts, i.e. ND, FLG, ND/FLG (33 wt %), as a function of time on stream are presented in Fig. 4A and Table 4. The FLG shows almost no DH activity. Indeed, the styrene yield per weight of catalyst per hour is only 0.54 $mmol_{STG_{catalyst}^{-1}h^{-1}}$ in the present reaction conditions whereas the DH activity on the pure NDs catalyst amounts to 2.89 $mmol_{STG_{catalyst}^{-1}h^{-1}}$, and remains stable up to 50 h on stream. Such results are in good agreement with those reported by Su and co-workers in their previous investigations.[12] The supported ND/FLG (33 wt %) shows a DH activity of 3.41 $mmol_{STG_{catalyst}^{-1}h^{-1}}$ and selectivity towards styrene is extremely high for all the tested catalysts reaching almost 97% (Fig. 44A).

The catalytic performance expressed in terms of styrene products per gram of nanodiomand per hours ($mmol_{STG_{ND}^{-1}h^{-1}}$) on 33 wt % ND/FLG composite is extremely high after 40 h on stream at steady state (Figure 4A). The styrene yield is about 11.01 $mmol_{STG_{ND}^{-1}h^{-1}}$ compared to 2.89 $mmol_{STG_{ND}^{-1}h^{-1}}$ for the unsupported NDs. For comparison, the commercial K-promoted iron catalyst (iron loading as high as 90 wt %) is also evaluated and the results are presented under the same reaction conditions, which are presented in Fig. 44B and Table 4. The commercial iron-based catalyst exhibits an extremely high DH activity at the beginning of the catalytic testing. A subsequent sharp deactivation takes place to reach a low steady state activity at 1.00 $mmol_{STG_{catalyst}^{-1}h^{-1}}$. The low DH activity obtained on the iron-based catalyst could be explained by the rapid saturation of the active sites by carbonaceous residue as the reaction was carried out under steam-free conditions (see next section). A long-term catalytic testing was also carried out on the ND/FLG (33 wt %) catalyst and the results are presented in Fig. 4C. According to the results the ND/FLG catalyst exhibits a relatively high DH activity even after more than 100 h of test.

Table 4. Dehydrogenation activities of NDs and ND/FLG composites.[a]

Catalyst	EB conversion (%)		Styrene selectivity (%)		Steady-state reaction rate ($mmol_{STG_{catalyst}}^{-1}h^{-1}$)	Steady-state reaction rate ($mmol_{STG_{ND}}^{-1}h^{-1}$)
	Initial	Steady-state	Initial	Steady-state		
NDs	60.0	19.3	99	97	2.89	2.89
33 wt% ND/FLG	59.8	23.0	98	97	3.41	11.01
16 wt% ND/FLG[b]	40.0	25.5	99	99	1.95	12.21
FLG	7.6	8.8	80	88	0.54	-
K-Fe_2O_3	26.5	6.65	99	96	1.00	-

[a] Reaction conditions: 150 mg of catalyst, 550 °C, 2.8 % EB in helium, 30 $mL \cdot min^{-1}$, atmospheric pressure. [b] Reaction conditions: 300 mg of catalyst, 2.8 % EB in helium, 30 $mL \cdot min^{-1}$, atmospheric pressure.

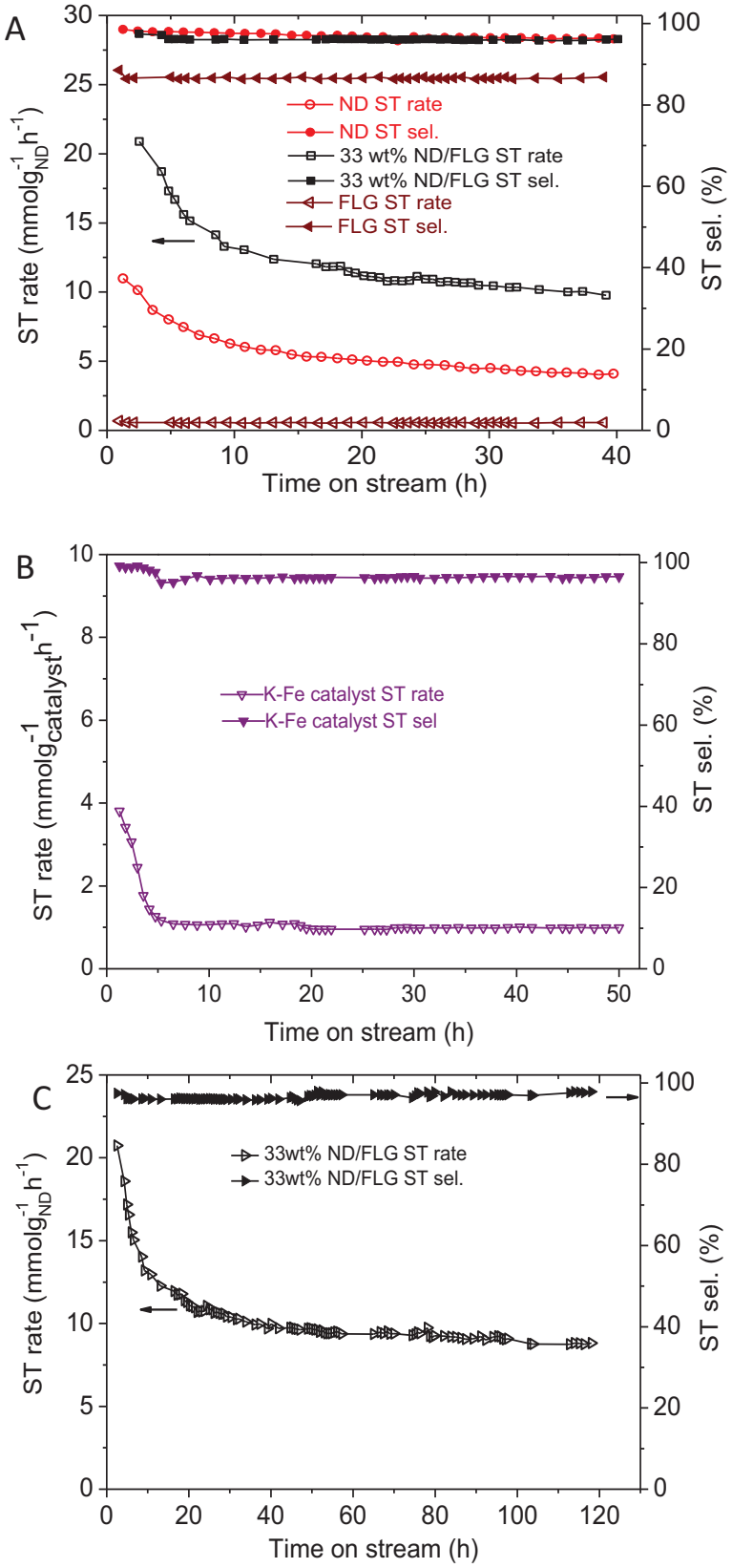

Figure 44. (A) Dehydrogenation activity and styrene selectivity on metal-free carbon-based catalysts: NDs, FLG and, and ND/FLG composite. (B) Catalytic activity of the industrial K-Fe catalyst. (C) Long-term test dehydrogenation activity of 33 wt%ND/FLG catalyst. Reaction conditions: 150 mg of

catalyst, 550 °C, 2.8 % EB in helium, total flow rate = 30 mL·min^{-1}, atmospheric pressure.

The DH activity expressed per weight of NDs obtained over the supported catalysts is significantly improved comparing to the bulk NDs. This can be attributed to the higher dispersion of the NDs on the FLG surface which provides a higher density of active sites for the reaction. Such dispersion was evidenced by means of the SEM and TEM analysis presented above. In addition, the NDs are well anchored on both sides of the FLG surface and thus, acting as nanoscopic spacers to prevent the re-stacking of the FLG sheets and providing a high effective surface area for the catalytic reaction. Similar improvement has also been reported for ND@GO-FLG catalyst.[20] However, the DH activity of the ND@GO-FLG is somewhat lower compared with that obtained on ND/FLG, i.e. 3.84 $mmol_{ST}g_{ND}^{-1}h^{-1}$ versus 11.01 $mmol_{ST}g_{ND}^{-1}h^{-1}$. The difference in terms of DH activity could be ascribed to the lower thermal conductivity of the ND@GO-FLG due to the insulator character of the GO layer which might influence the catalyst temperature due to the endothermic character of the reaction. As summarized in Fig. 45, the ND/FLG catalysts loaded with different ND weight ($mmol_{ST}g_{ND}^{-1}h^{-1}$), exhibit better DH activity compared to other carbon-based catalysts and also to the commercial iron-promoted catalyst as well.

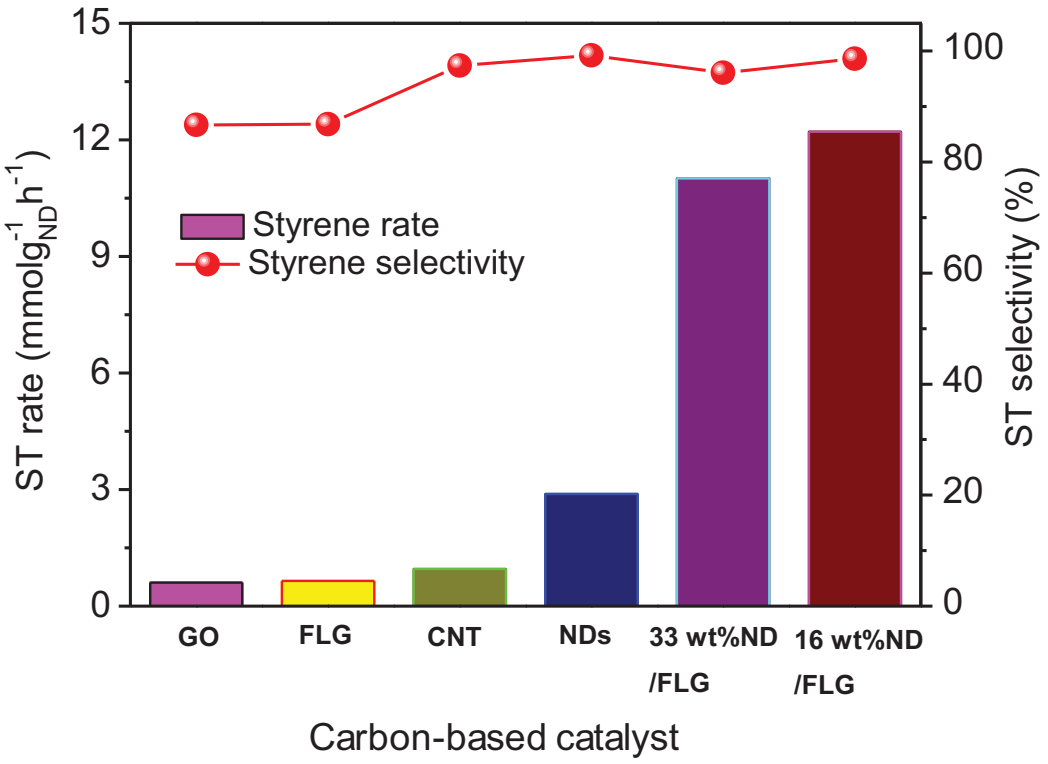

Figure 45. Dehydrogenation catalytic performance of various carbon-based catalysts under steady state. Reaction conditions: 550 °C, 2.8 % EB in helium, total flow rate = 30 mL·min^{-1}, atmospheric pressure.

The influence of the reaction temperature on the DH activity over the ND-FLG catalysts was also evaluated and the results are presented in Fig. 46. Increasing the reaction temperature leads to an increment of the DH activity, i.e. 19.23 $mmol_{ST}g_{ND}^{-1}h^{-1}$ at 600 °C versus 11.01 $mmol_{ST}g_{ND}^{-1}h^{-1}$ at 550 °C. To our best of knowledge, such catalytic activity is among the highest ones reported up to now in the field as far as the open literature is concerned. However, the selectivity towards styrene is slightly decreased slightly decreasing from almost 99% at 550°C to ~95% at 600 °C. The selectivity loss is likely due to the formation of cracking products in our operating conditions, at high temperature. The deactivation rate remains similar regardless the reaction temperature studied. Work is ongoing to evaluate the DH performance of such catalyst at higher ethylbenzene space velocity.

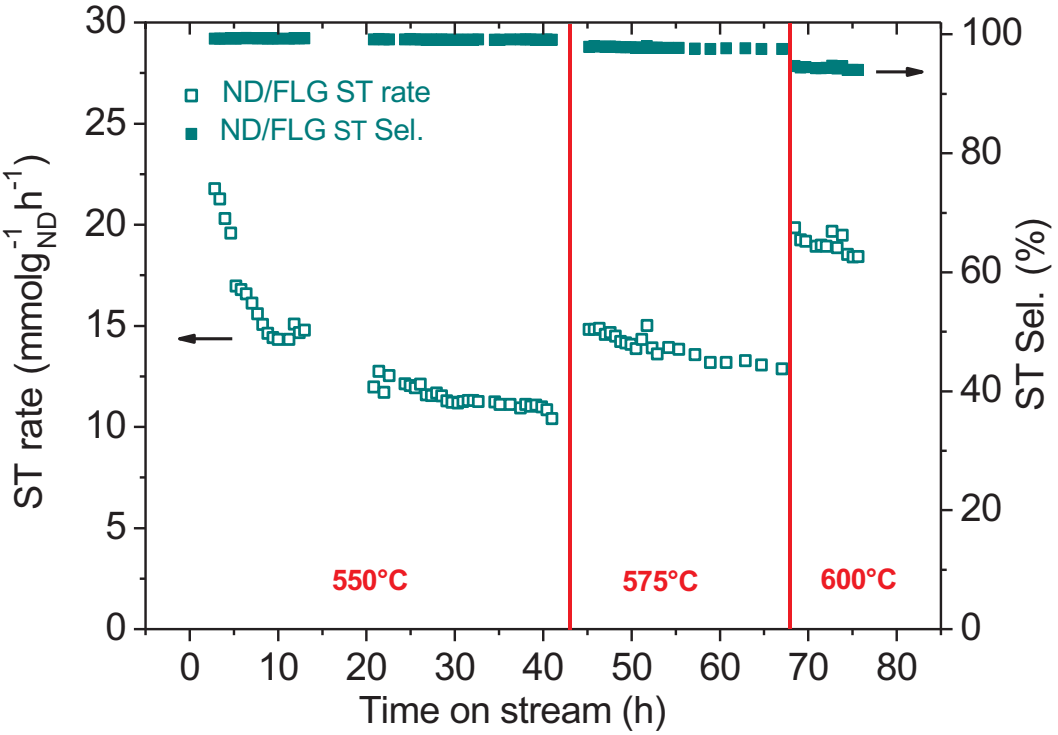

Figure 46. Influence of the reaction temperature on the dehydrogenation performance of the ND/FLG and commercial iron-based catalysts. Reaction conditions: 16 wt% of nanodiamonds, 300 mg, 550 - 600 °C, 2.8 % EB in helium, 30 mL·min^{-1}.

3.3. The surface and structure analysis after dehydrogenation reaction

In order to clarify the nature of active sites surface and structure after direct dehydrogenation reaction and to investigate further the deactivation effects on NDs localized on the FLG surface, the spent samples were analyzed by various physicochemical

techniques.[28,29] Fig. 47 shows the X-ray diffraction pattern of the pristine and pure and used nanodiamond samples. Broad peaks ascribed to pure nanodiamond appear at 2 θ =43.8° and 75.4 ° in Fig. 7A, corresponding respectively to (111) and (220) diffraction planes. Another broader peak in the 2θ range 18°- 27° would correspond to the (002) reflexion of graphite crystal plane. Fig. 47B shows the X-ray diffraction pattern of the spent NDs. As illustrated, the sharp graphite (002) peak at 2 θ = 25.1 intensifies. This graphite (002) broad peak comes from the onion-like nanographite.[30] The (002) graphitic peak is well identified on FLG sample as can be observed in the Fig. 47C. On the basis of this result, it can be concluded that a graphitization of the sample takes place during the catalytic testing.

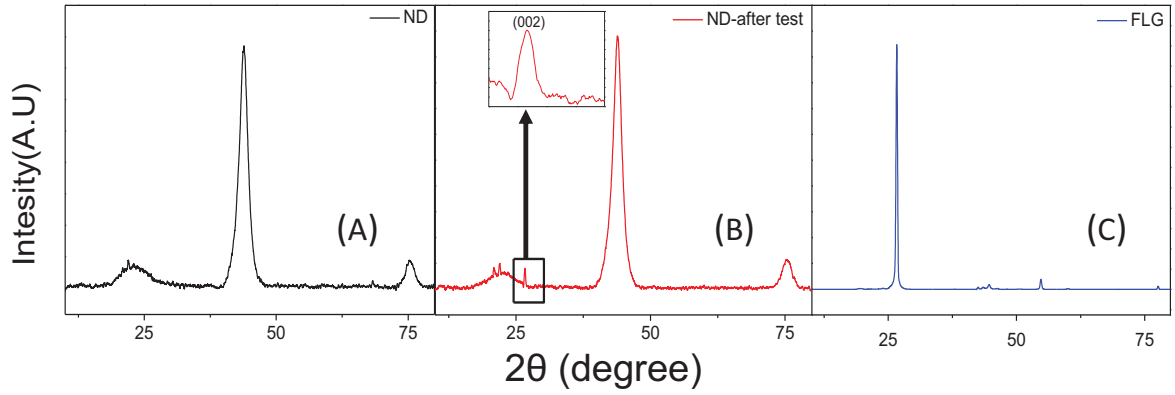

Figure 47. XRD patterns NDs before and after dehydrogenation test, and XRD pattern of few-layer graphene.

Temperature program oxidation coupled with mass spectrometry (TPO-MS) analysis (Fig. 48) carried out on the fresh and spent ND/FLG catalysts evidences a slight amount of low-temperature coke on the surface. In Fig. 48, in the temperature range 400-600ºC, one can observe an increase in CO_2 production on spent catalyst which could be attributed to the oxidation of adsorbed organic compounds and low temperature coke formation during the DH reaction. This observation would confirm that the deactivation taking place after few hours on stream is likely due to the coke deposited on the NDs active sites. However, the iron-based catalyst shows a heavy coke formation after DH test (not shown).[12] It is expected that the major reason for this sharp deactivation should be resulted from the large number of active sites blocked during the reaction. It is also worthy to note that the commercial iron-promoted catalyst exhibits an extremely high stability after the first deactivation period. During this first period the amounts of coke deposited from the gas phase and removed by reaction with H_2 reached equilibrium and then further deactivation is unlikely to occur. The CO_2 formation signal of the spent ND/FLG sample shows the difference shape at temperature ranging from 700 to 1000 ºC as compared to the fresh ND/FLG sample. The dehydrogenation reaction leads to a carbon species allotrope on the NDs surface.

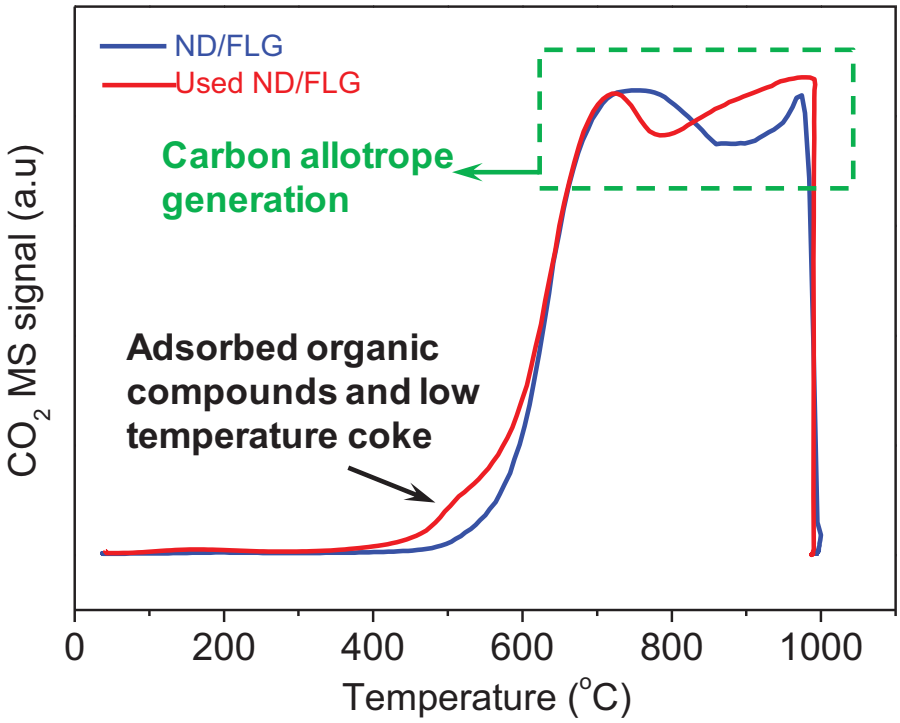

Figure 48. Temperature program oxidation-mass spectrograph analysis of the typical ND/FLG (16 wt % ND) before and after EB dehydrogenation.

The fresh and spent NDs and FLG as well as the ND/FLG catalysts were also characterized by XPS. After DH reaction the shape of C1s photopeak recorded on the spent FLGs remains unchanged (Fig. 49A) with a predominant contribution at around 284.6 eV, while the shape of the pristine-NDs C1s photopeak changes considerably with an additional contribution appearing at lower B.E. values around 283.7 eV inducing a shift from 286.5 to 287.5 eV to on the apparent maximum ascribed to sp^2 graphitic carbon (Fig. 9B). It has been reported that comparing with graphite, nanodiamond is a metastable phase under atmospheric pressure according to the thermodynamic equilibrium phase diagram of carbon [31, 32]. The formation of the first peak at 283.7 eV in Fig. 49A can be attributed to relaxation of the nanodiamond surface and graphitization effect on the amorphous carbon deposit during the catalytic reaction leading to a transition from sp^3 to sp^2 bonding; the second broad peak of used nanodiamond at 287.5 eV is due to the fact that nanodiamond is not completely transformed into graphite under the conditions of temperature and pressure of this study. XPS analysis carried out on the 33 wt % ND/FLG catalyst (Fig. 49C) also evidences a growth in intensity of the first C1s peak at 284.6 eV, which could be attributed to the formation of coke during the DH reaction or a new carbon allotrope generated by redistribution and graphitization effects on the surface of nanodiamonds. Comparison of the O 1s spectra of 33 wt% ND/FLG before and after reaction, it can be found that the shape of the oxygen peak is

almost identical in the two cases (Figure 49D). In addition the oxygen concentration (ca. 3 %) on the surface remained practically unaffected. We can conclude that the deactivation of the investigated catalyst is not related to the consumption of oxygen functionalities in such oxygen-free and stream-free dehydrogenation reaction. This result is not in contradiction with the findings of Zhang et al,[12] since as they indicated that the active C=O species were reactive and probably disappeared when the reaction stoped. Zhang et al,[12] performed the surface chemical property of a nanodiamond in the ethylbenzene dehydrogenation, which was studied *in-situ* by means of near ambient pressure XPS. They observed changes in the O 1s XPS spectra when heating in vacuum and in 0.25 mbar ethylbenzene. However, the XPS analysis performed in this work was done *ex-situ* on the catalysts, i.e. before and after the catalytic reaction, which are exposed in the air before analysis the oxygen functionalities.

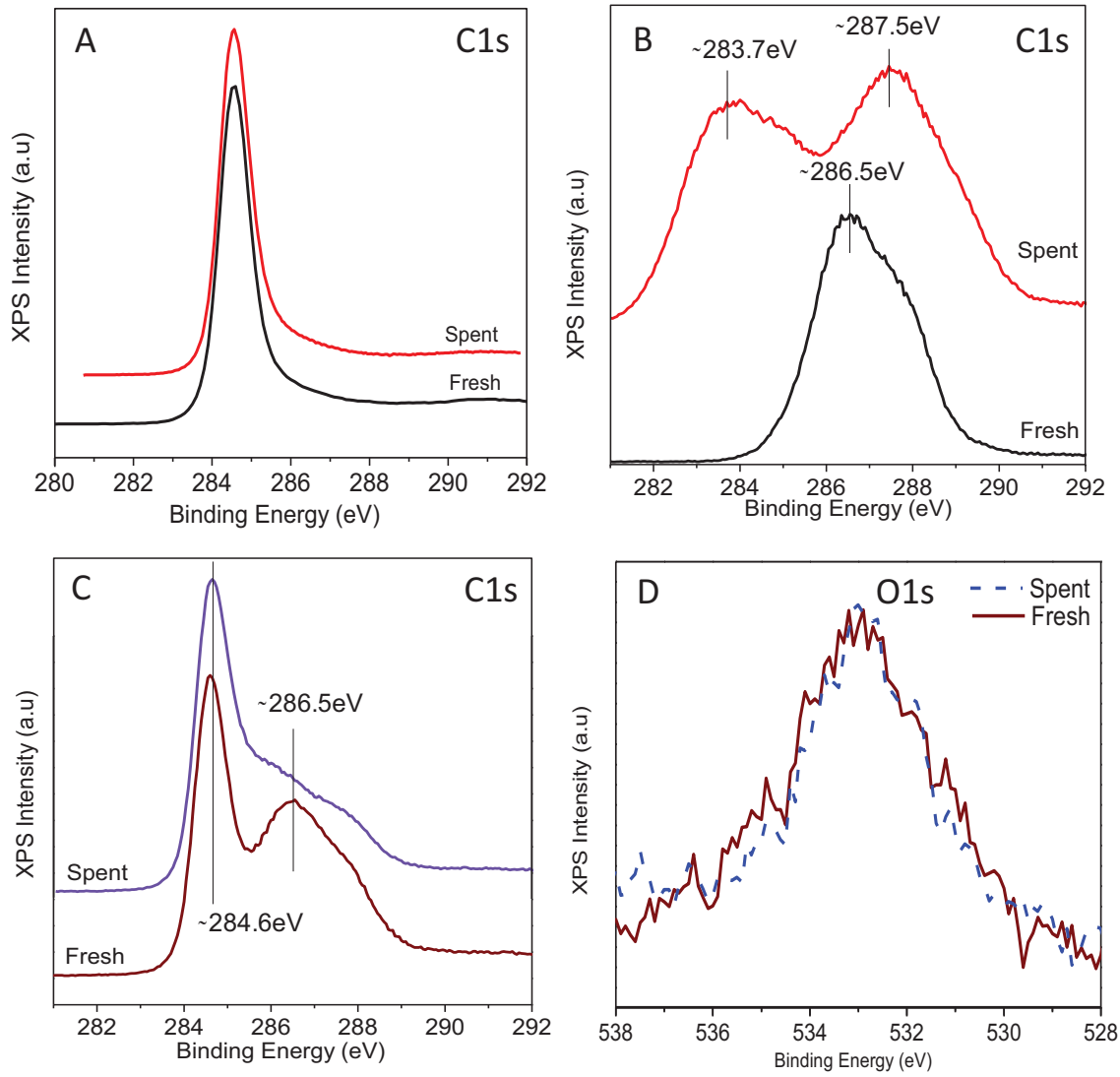

Figure 49. XPS C1s and O1s spectra of (A) FLG, (B) nanodiamonds and (C, D) 33 wt% ND/FLG catalyst before and after dehydrogenation test.

High-resolution TEM analysis fully supports the results of TPO-MS and XPS, showing the formation of graphitic ribbons, onions-like carbon, and concentric graphitic shells in ND/FLG catalyst after DH reaction.[13, 33] Fig. 50 presents representative HRTEM of spent ND/FLG sample revealing a diameter still around 4-8 nm without significant change in size for the spent nanodiamonds. Most of particles present the typical (111) planes of nanodiamonds with an interplanar distance of 0.206 nm.[34] The dramatic change in morphology after DH reaction is also demonstrated in Fig. 50A, part of the NDs transformation is forming during the catalytic test with the appearance of an external graphitic layers shell over the nanodiamond planes. This type of disordered carbon and graphitic sp^2-boned carbon on the NDs surface can be oxidized in air at around 425 ^oC as reported by Osswald et al.[33]

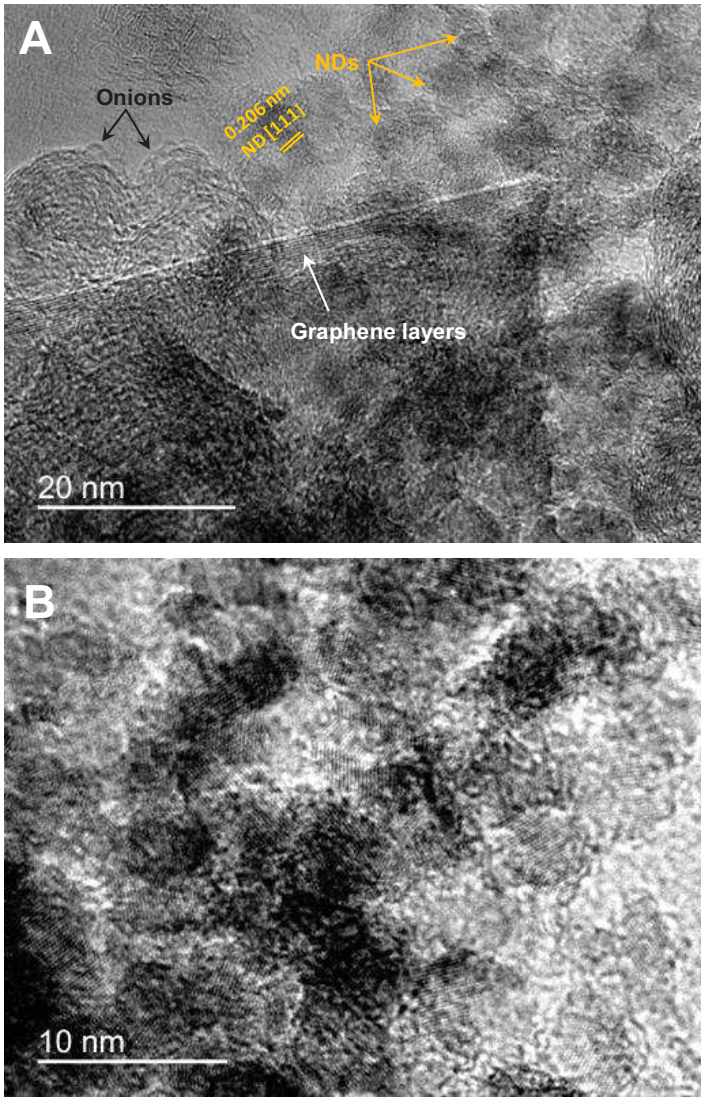

Figure 50. High-resolution TEM images of 16 wt% ND/FLG after dehydrogenation reaction showing the a part of nanodiamond surface is transformed to onion-like carbon

Fig. 44A, it can be observed that a slight deactivation still occurs on the ND/FLG catalyst as a function of the test duration. The deactivation can be due to the coke generated (onion-like carbon) within the layer of FLG which slowly hinders the access of the reactant to the catalytic sites. Oxidative regeneration step was carried out in order to study the DH performance of this hybrid catalyst as a function of the regeneration cycles. The oxidative regeneration is carried out at 450°C according to the TPO results reported above which show that the carbonaceous residue deposited on the catalyst surface was removed at temperature around 450°C. The results are presented in Fig. 51 and it can be clearly seen that the DH catalytic activity of the ND/FLG catalyst was completely recovered after an oxidative regeneration at 450 °C for 2h under air flow and confirms that the carbonaceous residue is mostly responsible for the DH activity lost observed. The regenerated catalyst also displays a higher stability as a function of time on stream. The DH stability improvement after an oxidative regeneration cycle could be attributed to the removal of some amorphous carbon species present on the ND surface.

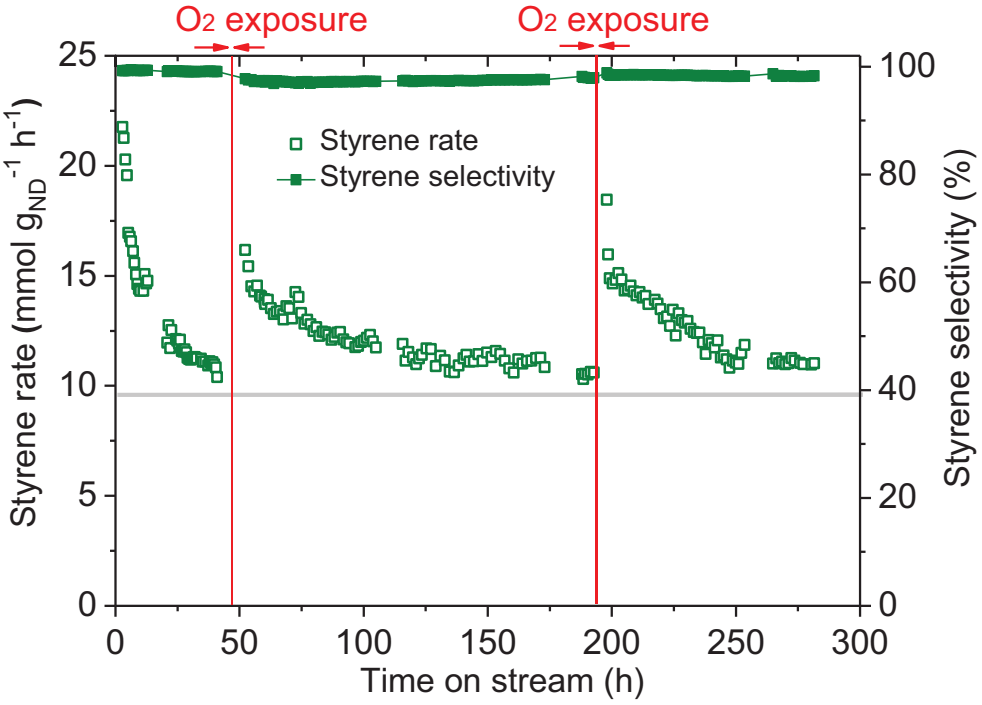

Figure 51. EB dehydrogenation results of regenerate ND/FLG catalysts by diluted air flow. Regenerated conditions: 450° C, 30 ml min^{-1} of diluted oxygen flow (20 vol. % O_2 in helium). Reaction conditions: 16 wt% of nanodiamonds, 300 mg, 550 °C, 2.8 % EB in helium, 30 mL·min^{-1}.

4. Conclusion

In conclusion we have demonstrated in the present work an easy and scalable method to synthesize a hybrid structured catalyst consisting of nanodiamond decorated few-layers graphene surface. The hybrid composite exhibits a high and relatively stable DH performance compared to the other carbon-based and doped iron industrial catalysts. The DH activity per weight unit of NDs was about four times higher than the one obtained on the unsupported ones. The DH activity can be significantly improved by performing the reaction at 600°C where DH activity around 19.2 $mmol_{ST}g_{ND}^{-1}h^{-1}$ is obtained. Taken into account such DH activity the catalyst weight of 130 kg (21 kg of NDs supported on the FLG) is needed to produce 1t/day of styrene. The DH performance improvement observed on the ND/FLG composite catalyst could be attributed to the dispersion of the ND particles on the FLG surface leading to a higher effective surface area, the graphitization of the surface composite during the DH reaction and the synergistic effects of the hybrid carbon nanostructured materials. Such DH activity is among the highest ones reported up to now in the literature. The selectivity towards styrene is extremely high reaching ~97% at 550°C and 95% at 600°C. The ND/FLG catalyst also exhibits an extremely high stability as a function of time on stream which indicates that deactivation by coke deposition is negligible. In addition, the catalyst can be easily regenerated by applying an oxidative treatment at low temperature. Additional investigation will be performed in order to check the influence of the ethylbenzene space velocity and the reaction pressure on the DH performance of the ND/FLG catalyst. Work will also be carried out on the hybrid catalyst consisting of ND decorated FLG/SiC with controlled macroscopic shape for future development.

Acknowledgements

The present work is financially supported by a European project (Freecats) under a contract number NMP3-SL-2012-280658. The SEM and TEM analysis were performed at the facilities of the IPCMS (UMR 7504 CNRS-University of Strasbourg) and T. Romero (ICPEES) is gratefully acknowledged for performing SEM analysis.

References

(1) O. Shekhah, W. Ranke, R. Schlogl, Styrene synthesis: in situ characterization and r eactivity studies of unpromoted and potassium-promoted iron oxide model catalysts, J Catal, 225 (**2004**) 56-68.

(2) S.J. Liao, T. Chen, C.X. Miao, W.M. Yang, Z.K. Xie, Q.L. Chen, Effect of TiO2 on the structure and catalytic behavior of iron-potassium oxide catalyst for dehydrogenation of ethylbenzene to styrene, Catal Commun, 9 (**2008**) 1817-1821.

(3) R.J. Balasamy, A. Khurshid, A.A.S. Al-Ali, L.A. Atanda, K. Sagata, M. Asamoto, H. Yahiro, K. Nomura, T. Sano, K. Takehira, S.S. Al-Khattaf, Ethylbenzene dehydrogenation over binary FeOx-MeOy/Mg(Al)O catalysts derived from hydrotalcites, Appl Catal A-Gen, 390 (**2010**) 225-234.

(4) N. Mimura, I. Takahara, M. Saito, T. Hattori, K. Ohkuma, M. Ando, Dehydrogenation of ethylbenzene over iron oxide-based catalyst in the presence of carbon dioxide, Catal Today, 45 (1998) 61-64.

(5) N.R. Shiju, M. Anilkumar, S.P. Mirajkar, C.S. Gopinath, B.S. Rao, C.V. Satyanarayana, Oxidative dehydrogenation of ethylbenzene over vanadia-alumina catalysts in the presence of nitrous oxide: structure-activity relationship, J Catal, 230 (**2005**) 484-492.

(6) V.M. Zhyznevskiy, R.D. Tsybukh, V.V. Gumenetskiy, V.V. Kochubeiy, Physico-chemical and catalytic properties of Fe2BiMo2Ox catalyst ultrasound treated and promoted with Al2O3 in the oxidative dehydrogenation of ethylbenzene to styrene, Appl Catal A-Gen, 238 (**2003**) 19-28.

(7) R. Rao, Q.Y. Zhang, H.D. Liu, H.X. Yang, Q. Ling, M. Yang, A.M. Zhang, W. Chen, Enhanced catalytic performance of CeO2 confined inside carbon nanotubes for dehydrogenation of ethylbenzene in the presence of CO2, J Mol Catal A-Chem, 363 (**2012**) 283-290.

(8) K. Nakagawa, C. Kajita, K. Okumura, N. Ikenaga, M. Nishitani-Gamo, T. Ando, T. Kobayashi, T. Suzuki, Role of carbon dioxide in the dehydrogenation of ethane over gallium-loaded catalysts, J Catal, 203 (**2001**) 87-93.

(9) D.S. Su, N.I. Maksimova, G. Mestl, V.L. Kuznetsov, V. Keller, R. Schlogl, N. Keller, Oxidative dehydrogenation of ethylbenzene to styrene over ultra-dispersed diamond and onion-like carbon, Carbon, 45 (**2007**) 2145-2151.

(10) A. Guerreroruiz, I. Rodriguezramos, Oxydehydrogenation of Ethylbenzene to Styrene Catalyzed by Graphites and Activated Carbons, Carbon, 32 (**1994**) 23-29.

(11) M.F.R. Pereira, J.J.M. Orfao, J.L. Figueiredo, Oxidative dehydrogenation of ethylbenzene on activated carbon catalysts. I. Influence of surface chemical groups, Appl Catal A-Gen, 184 (**1999**) 153-160.

(12) J. Zhang, D.S. Su, R. Blume, R. Schlogl, R. Wang, X.G. Yang, A. Gajovic, Surface Chemistry and Catalytic Reactivity of a Nanodiamond in the Steam-Free Dehydrogenation of Ethylbenzene, Angew Chem Int Ed, 49 (**2010**) 8640-8644.

(13) X. Liu, B. Frank, W. Zhang, T.P. Cotter, R. Schlogl, D.S. Su, Carbon-Catalyzed Oxidative Dehydrogenation of n-Butane: Selective Site Formation during sp(3)-to-sp(2) Lattice Rearrangement, Angew Chem Int Ed, 50 (**2011**) 3318-3322.

(14) H.Y. Liu, J.Y. Diao, Q. Wang, S.Y. Gu, T. Chen, C.X. Miao, W.M. Yang, D.S. Su, A nanodiamond/CNT-SiC monolith as a novel metal free catalyst for ethylbenzene direct dehydrogenation to styrene, Chem Commum, 50 (**2014**) 7810-7812.

(15) T.H. Tri, K. Chizari, I. Janowska, M.S. Moldovan, O. Ersen, L.D. Nguyen, M.J. Ledoux, P.H. Cuong, D. Begin, Few-layer graphene supporting palladium nanoparticles

with a fully accessible effective surface for liquid-phase hydrogenation reaction, Catal Today, 189 (**2012**) 77-82.
(16) C. Duong-Viet, H. Ba, Y. Liu, L. Truong-Phuoc, J.-M. Nhut, C. Pham-Huu, Nitrogen-doped carbon nanotubes on silicon carbide as a metal-free catalyst, Chinese J Catal, 35 (**2014**) 906-913.
(17) I. Janowska, F. Vigneron, D. Begin, O. Ersen, P. Bernhardt, T. Romero, M.J. Ledoux, C. Pham-Huu, Mechanical thinning to make few-layer graphene from pencil lead, Carbon, 50 (**2012**) 3106-3110.
(18) W. Baaziz, L. Truong-Phuoc, C. Duong-Viet, G. Melinte, I. Janowska, V. Papaefthimiou, O. Ersen, S. Zafeiratos, D. Begin, S. Begin-Colin, C. Pham-Huu, Few layer graphene decorated with homogeneous magnetic Fe3O4 nanoparticles with tunable covering densities, Journal of Materials Chemistry A, 2 (**2014**) 2690-2700.
(19) G. Melinte, I. Florea, S. Moldovan, I. Janowska, W. Baaziz, R. Arenal, A. Wisnet, C. Scheu, S. Begin-Colin, D. Begin, C. Pham-Huu, O. Ersen, A 3D insight on the catalytic nanostructuration of few-layer graphene, Nat Commun, 5 (**2014**).
(20) T. Tran Thanh, H. Ba, L. Truong-Phuoc, J.-M. Nhut, O. Ersen, D. Begin, I. Janowska, D.L. Nguyen, P. Granger, C. Pham-Huu, A few-layer graphene-graphene oxide composite containing nanodiamonds as metal-free catalysts, Journal of Materials Chemistry A, 2 (**2014**) 11349-11357.
(21) I. Janowska, K. Chizari, O. Ersen, S. Zafeiratos, D. Soubane, V. Da Costa, V. Speisser, C. Boeglin, M. Houlle, D. Begin, D. Plee, M.J. Ledoux, C. Pham-Huu, Microwave synthesis of large few-layer graphene sheets in aqueous solution of ammonia, Nano Res, 3 (**2010**) 126-137.
(22) P.I. Belobrov, L.A. Bursill, K.I. Maslakov, A.P. Dementjev, Electron spectroscopy of nanodiamond surface states, Appl Surf Sci, 215 (**2003**) 169-177.
(23) A. Siokou, F. Ravani, S. Karakalos, O. Frank, M. Kalbac, C. Galiotis, Surface refinement and electronic properties of graphene layers grown on copper substrate: An XPS, UPS and EELS study, Appl Surf Sci, 257 (**2011**) 9785-9790.
(24) J. Shalini, K.J. Sankaran, C.L. Dong, C.Y. Lee, N.H. Tai, I.N. Lin, In situ detection of dopamine using nitrogen incorporated diamond nanowire electrode, Nanoscale, 5 (**2013**) 1159-1167.
(25) T. Petit, J.C. Arnault, H.A. Girard, M. Sennour, P. Bergonzo, Early stages of surface graphitization on nanodiamond probed by x-ray photoelectron spectroscopy, Phys Rev B, 84 (**2011**).
(26) M.S. Moldovan, H. Bulou, Y.J. Dappe, I. Janowska, D. Begin, C. Pham-Huu, O. Ersen, On the Evolution of Pt Nanoparticles on Few-Layer Graphene Supports in the High-Temperature Range, J Phys Chem C, 116 (**2012**) 9274-9282.
(27) W. Baaziz, G. Melinte, O. Ersen, C. Pham-Huu, I. Janowska, Effect of nitriding/nanostructuration of few layer graphene supported iron-based particles; catalyst in graphene etching and carbon nanofilament growth, Phys Chem Chem Phys, 16 (2014) 15988-15993.
(28) O. Irún, S.A. Sadosche, J. Lasobras, J. Soler, E. Francés, J. Herguido, M. Menéndez, Catalysts for the production of styrene from ethylbenzene: Redox and deactivation study, Catal Today, 203 (**2013**) 53-59.
(29) T. Vazhnova, S.P. Rigby, D.B. Lukyanov, Benzene alkylation with ethane in ethylbenzene over a PtH-MFI catalyst: Kinetic and IR investigation of the catalyst deactivation, J Catal, 301 (**2013**) 125-133.
(30) J. Qian, C. Pantea, J. Huang, T.W. Zerda, Y. Zhao, Graphitization of diamond powders of different sizes at high pressure-high temperature, Carbon, 42 (**2004**) 2691-2697.

(31) N.S. Xu, J. Chen, S.Z. Deng, Effect of heat treatment on the properties of nano-diamond under oxygen and argon ambient, Diam Relat Mater, 11 (**2002**) 249-256.
(32) S. Prawer, J.L. Peng, J.O. Orwa, J.C. McCallum, D.N. Jamieson, L.A. Bursill, Size dependence of structural stability in nanocrystalline diamond, Phys Rev B, 62 (**2000**) R16360-R16363.
(33) S. Osswald, G. Yushin, V. Mochalin, S.O. Kucheyev, Y. Gogotsi, Control of sp(2)/sp(3) carbon ratio and surface chemistry of nanodiamond powders by selective oxidation in air, J Am Chem Soc, 128 (**2006**) 11635-11642.
(34) F. Banhart, P.M. Ajayan, Carbon onions as nanoscopic pressure cells for diamond formation, Nature, 382 (**1996**) 433-435.

Few-layer graphene-graphene oxide composite containing nanodiamonds as metal-free catalyst in the dehydrogenation of ethylbenzene

Tran Thanh Tung[a], Housseinou Ba[a], Lai Truong-Phuoc[a], Jean-Mario Nhut[a], Ovidiu Ersen[b], Dominique Begin[a], Izabela Janowska[a], Dinh Lam Nguyen[c], Pascal Granger[d], Cuong Pham-Huu[a*]

[a]*Institut de Chimie et Procédés pour l'Energie, l'Environnement et la Santé (ICPEES), ECPM, UMR 7515 du CNRS-Université de Strasbourg, 25 rue Becquerel, 67087 Strasbourg Cedex 02, France.*

[b]*Institut de Physique et de Chimie des Matériaux de Strasbourg (IPCMS), UMR 7504 du CNRS-Université de Strasbourg,23 rue du Lœss, BP 43, 67034 STRASBOURG Cedex 02, France*

[c]*The University of Da-Nang, University of Science and Tecnology, 54, Nguyen Luong Bang, Da-Nang, Viet-Nam*

[d]*Unité de Catalyse et Chimie du Solide (UCCS), UMR 8181 du CNRS-Université de Lille-1, Bâtiment C3, Université Lille 1, 59655 - Villeneuve d'Ascq Cedex, France*

Article published in Journal of Material Chemistry A DOI: 10.1039/C4TA01307G

Abstract

We report a high yield exfoliation of few-layer-graphene (FLG) with up to 17% yield from expanded graphite, under 5 h sonication time in water, using graphene oxide (GO) as a surfactant. The aqueous dispersion of GO attached FLG (FLG–GO), with less than 5 layers, is used as a template for further decoration of nanodiamonds (NDs). The hybrid materials were self-organized into 3D-laminated nanostructures, where spherical NDs with a diameter of 4–8 nm are homogeneously distributed on the surface of the FLG–GO complex (referred to as FLG–GO@NDs). It was found that GO plays a dual role, it (1) mediated exfoliation of expanded graphite in aqueous solution resulting in a FLG–GO colloid system, and (2) incorporated ND particles for the formation of composites. A high catalytic performance in the dehydrogenation of ethyl-benzene on FLG–GO@ND metal-free catalyst is achieved; 35.1% of ethylbenzene conversion and 98.6% styrene selectivity after a 50 h reaction test are observed which correspond to an activity of 4.9 $mmol_{ST}\ g_{catalyst}^{-1}\ h^{-1}$, which is 1.7 and 5 times higher than those of the unsupported NDs and traditional catalysts, respectively. The results demonstrate the potential of the FLG–GO@ND composite as a promising catalyst for steam-free industrial dehydrogenation applications.

1. Introduction

Graphene and few-layer graphene (FLG), containing different numbers of graphene layers up to thirty, have attracted tremendous scientific interest due to their exceptional physical and chemical properties which allow them to be applied in several potential applications.[1–3] These materials can be synthesized by several methods, such as micromechanical cleavage,[4] epitaxial growth on silicon carbide or metal surfaces,[5–7] exfoliation of oxidized graphite and/or graphene oxide (GO),[8–11] mechanical ablation,12 and unzipping of multiwalled carbon nanotubes.[13–16] Despite this large number of efforts, mass production of graphene and FLG with a low number of graphene layers by a versatile and low-cost method is still an active field of research, especially solution-phase methods where graphene or FLG is directly obtained from exfoliation of graphite precursors.[17,18] This method, however, still has some drawbacks: (1) the synthesis is mostly carried out in organic solvents (e.g., MNP, DMF) which need to be carefully recycled,[19,20] (2) the low exfoliation yield (1–3 wt.%) despite a very long sonication time (a few tens to hundred hours),[21,22] and (3) in the case of exfoliation of graphite in aqueous solution, the use of an amphiphilic surfactant may affect the quality and needs further steps of treatments.[23–25] In fact, direct exfoliation of hydrophobic graphite to graphene sheets in aqueous solution without dispersing agents has been considered to be extremely difficult or even unfeasible.[26] The ideas based on the use of GO as a dispersion agent for stabilization of carbon materials, such as CNTs and graphite, have been recently demonstrated in a few studies. For example, Kim and co-workers reported for the first time that GO, with its amphiphilic nature, can act as a surfactant to process insoluble materials of graphite in aqueous solution.[27,28] It has also been reported that GO can act as a surfactant to prevent the aggregation of CNTs during the process.[29] Gogotsi and co-workers have performed an extensive reduction of GO attached on the expanded graphite (EG) surface through microwave irradiation.[30] However, the use of GO as a physical agent for the synthesis of large scale single-to-few layer graphene, with a stable dispersion in a greener solvent, i.e. water, still remains a challenge to be tackled.

Synthetic NDs produced by detonation methods have an average size ranging from 4–10 nm, and their large surface-to-volume ratio endows them with higher surface reactivity than other forms of carbon. Together with a large surface area, NDs also have high entropy, high structural defects and low toxicity which make them a promising candidate for several applications in tribology, drug delivery, bio-imaging and tissue engineering just to cite a few of them.[31] Hybrid materials consisting of graphene and nanodiamonds (NDs) could potentially display not only the unique properties of NDs and those of graphene, but also additional novel properties due to the synergistic effects between them. Those materials are very interesting for future applications such as supercapacitors,[32] photocatalysts,[33,34] and

electrocatalysts.[35] Recently, NDs have been reported by Su and co-workers[36] to be efficient metal-free catalysts in the steam-free dehydrogenation of ethyl-benzene into styrene. The dehydrogenation mechanism can be described as follows: activation of the alkane fragment of the ethylbenzene by the ketone group to generate styrene along with the formation of a carbon hydroxyl group as an intermediate followed by the release of hydrogen and the consecutive generation of the former C=O group. However, the NDs are used in powder form which is not well dispersed and leads to a considerable decrease of the effective surface area for the catalytic process and also induce a significant pressure drop along the catalyst bed. Thus the idea is to take advantage of the flat surface of graphene-based materials to disperse the ND particles, which would increase the effective contact surface area and the number of active sites, leading to an enhancement of their catalytic properties. Wang et al.[37] have reported that NDs are steadily dispersed on the reduced graphene oxide surface which leads to a significant improvement of the specific capacitance of the composite owing to the high exposed surface area and short diffusion length of the NDs.

In this work, we have tried to address three main aspects including: (1) direct exfoliation of expanded graphite in aqueous solutions (with high yield and short sonication time) using GO as the surfactant; (2) the use of GO attached few-layer-graphene (FLG–GO) aqueous dispersion as a template for further self-organized decoration of homogeneous nanodiamonds (NDs), and (3) such ND-decorated GO–FLG composites (referred to as FLG–GO@NDs) will be used as metal-free catalysts in the steam-free dehydrogenation (DH) of ethylbenzene (EB) to styrene reaction which is one of the largest catalytic processes nowadays. Herein, GO acts as an adsorbent layer that concentrates ND nanoparticles on the surface of FLG–GO, meanwhile FLG plays the role of a reinforcement support for GO which is easily shrinkable during ND adsorption. The resulting 3D-sandwich structure of the FLG–GO@ND composite is tested as an advanced catalyst in the DH of EB to styrene reaction. The activities are compared with the ones obtained from traditional catalysts. According to the results the FLG–GO@ND composite displays predominant performances along with a high stability as a function of time on stream compared to the other catalysts. The present high-performance FLG–GO@ND composite with great advantages such as a simple and mass production method, and the absence of cytotoxicity could be foreseen as a potential metal-free catalyst in the steam free industrial synthesis of styrene.

2. Experimental

2.1. Exfoliation of expanded graphite in aqueous medium using graphene oxide as a surfactant

Graphene oxide was prepared by a modified Hummer's method from flake graphite as described in supporting information (SI). A FLG-GO complex was prepared by aqueous solution-processed exfoliation of expanded graphite in GO suspension under ultrasonic (see SI). Briefly, GO suspension with a concentration of 1 mg/mL was obtained by dispersing GO powders in distilled water with the aid of ultrasonic bath for 30 min. Then the different weight ratios of EG/GO, i.e. 1, 3, 5, were subjected to sonication with a tip sonicator of 30 W for different time ranging from 1 to 5 h. Subsequently, the as-prepared suspension was left to stand for 2 days to settling down unstable graphite aggregates. The supernatant was next extracted by pipette, and then centrifuged at 3000 rpm for 30 min to get the stable FLG-GO suspension which will be further processed.

2.2. Self-organized decoration of nanodiamonds on the FLG-GO sheets

The commercial NDs with diameter in the range of 5-10 nm in a powder form were supplied by the Hightech Co (Finland) and were used without any further purification. For preparation of a FLG-GO@NDs composite, typically 200 mg pristine NDs were dispersed in 300 mL deionized (DI) water and sonicated in a sonic bath for 30 min. It was then well-mixed with a 286 mL as-synthesized FLG-GO complex suspension (0.35 mg/mL) by droplet under stirring condition. ND particles were steadily adsorbed in a homogeneous manner on the surface of FLG-GO and the resulted composite settled down after few minutes. The mixture was then filtered and dried at 100 **°C** in the oven for 6 hours to get a constant weight of the FLG-GO@NDs composite.

3. Results and discussion

The FLG was synthesized by mild sonication at 40 °C of aqueous mixtures containing EG and GO with different weight ratios, i.e. 1:1, 3:1 and 5:1 (ESI, SI†). The sonication was

done for different durations and the products of these treatments were collected for subsequent analysis. Fig. 52A shows the digital photo of the EG–GO mixtures after 5 h of sonication, it highlights the extremely high dispersion of the resultant materials when GO was added to the EG suspension: indeed no precipitation was observed after several weeks of standing. On the other hand, the FLG formed from the EG suspension in water, without adding GO, and after the same sonication treatment, steadily precipitates after a few tens of minutes due to its hydrophobic nature and strong attraction forces. Similar results have also been observed by Hu et al.30 during the sonication process with an EG–GO mixture with a high GO concentration. The high stability of the obtained FLG could be explained by a number of physical methods that clearly demonstrated the production of single-to-few-layer graphene as shown in the schematic exfoliation process (schematic 1, ESI†).

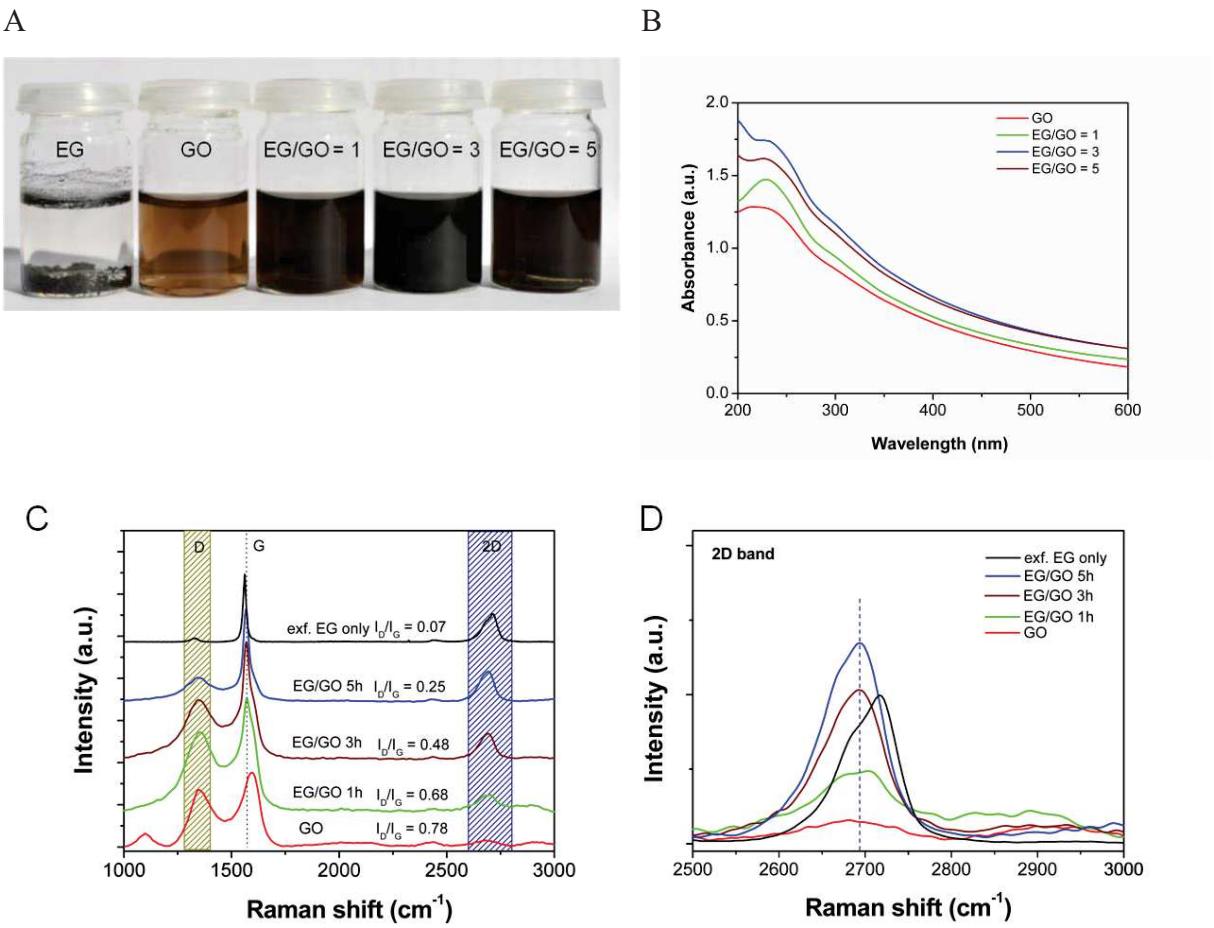

Figure 52. (A) A digital photo of the different EG/GO mixtures in aqueous medium after sonication for 3h. (B) UV-vis spectra of the different EG/GO mixtures which show the degree of the EG exfoliation, (C and D) Raman spectra recorded on different samples according to sonication time and the enlargement of the 2D peak.

The formation of a stable FLG–GO suspension as a function of EG/GO was monitored by UV-vis spectroscopy as depicted in Fig. 52B. The broad π–π* transition of the aromatic C=C peak of GO centered at 230 nm^{-1} is gradually red shifted several nm up to 238 nm when the EG/GO ratios increase from 0 to 5. The absorption intensity increases as well, and the highest intensity is observed with a mixture of EG/GO equal to 3; that shows the best dispersion degree of EG/GO and the stabilization of exfoliated FLG in the solution. When the EG/GO ratio is higher or lower than 3 (i.e., 5, 1), the absorption intensity tends to decrease, suggesting a lower concentration of chromophores in the suspension, so a lower stabilization of the FLG sheets. The degree of exfoliation as a function of sonication time was also investigated for the EG/GO ratio equal to 3 as shown in Fig. S1A (ESI).† The amount of FLG in the FLG–GO complex increased up to 0.35 mg mL−1 for 5 h sonication, and then exhibited a plateau trend for a longer sonication time (Fig. S1B†). The optical absorbance (A) divided by the length (l) as a function of the concentration of the aqueous suspension of FLG–GO shows a Lambert–Beer behavior, and a linear fit of the concentration values gives an average absorption coefficient at 660 nm of $\alpha = 2244\ L\ g^{-1}\ m^{-1}$ (Fig. S1C†), which is consistent with the value reported previously for exfoliation of graphene in NMP.[19]

The XRD patterns of the as-synthesized materials as a function of the EG–GO ratio are presented in Fig. S2.† The patterns showed that the 2θ peak of GO at 11° was gradually decreased when the EG/GO ratio increased, while two peaks corresponding to (002) and (004) reflections of graphite are increased consecutively. It means that the crystallinity of the FLG–GO complex increased as a function of EG/GO ratio, and when the EG/GO ratio reached 5, it would correspond to a large graphite-like structure in the products, which is consistent with the UV-vis measurements. The layer thickness and structural change of the FLG–GO film as a function of sonication time, compared to its precursor materials (exfoliated EG and GO), were efficiently monitored by Raman spectroscopy (Fig. 52C). While the Raman spectrum shows a typical D-band at 1345 cm^{-1} (sp3 defects) and a G-band at 1592 cm^{-1} (tangential vibration of sp2 carbon atoms) for GO, those peaks appeared at 1350 and 1580 cm^{-1} respectively for FLG. A comparison of the intensity ratio of D and G bands (ID/IG) as a function of sonication time for all samples was also performed. The ID/IG decreased from 0.78 for pure GO to 0.24 for the FLG–GO complex after 5 h sonication confirming the better graphitic behavior of the sample. In addition, the G-band of the FLG–GO complex was red shifted (8 cm^{-1}) and blue shifted (12 cm^{-1}) as compared to that of FLG and GO, respectively, which confirms a physical interaction of GO and the FLG sheets. The π-conjugated aromatic domains existing in the GO basal plane interact with the surface of FLG via π–π interactions.[28,30] Moreover, it is known that the 2D band corresponds to the specific number of stacked graphene films.[38] As compared to exfoliated EG, the 2D peak positions in FLG–GO shifted considerably to a lower wavenumber by 25 cm^{-1}, from 2718 to 2693 cm^{-1}, and the intensities of symmetric peaks are higher than with FLG after 3 h sonication, suggesting a

successful exfoliation to less than 5 layers FLG in the FLG–GO complex.[18,39] All of the above results have shown that GO sheets significantly promote the effective exfoliation of EG in aqueous solution after a relatively short time of sonication. The excellent water solubility of GO made the FLG–GO complex to have a micelle system-like behavior.

Representative TEM micrographs of the as-synthesized FLG decorated with GO sheets are presented in Fig. 53. They confirm the high degree of exfoliation of the process as almost FLG containing less than five graphene layers is observed among the sample (Fig. 53A). High-resolution TEM micrographs also evidence the non-covalent stacking between the FLG and GO as presented in Fig. 53B and C, where a perfect graphitized structure of the FLG is visible underneath the disordered structure of the GO.

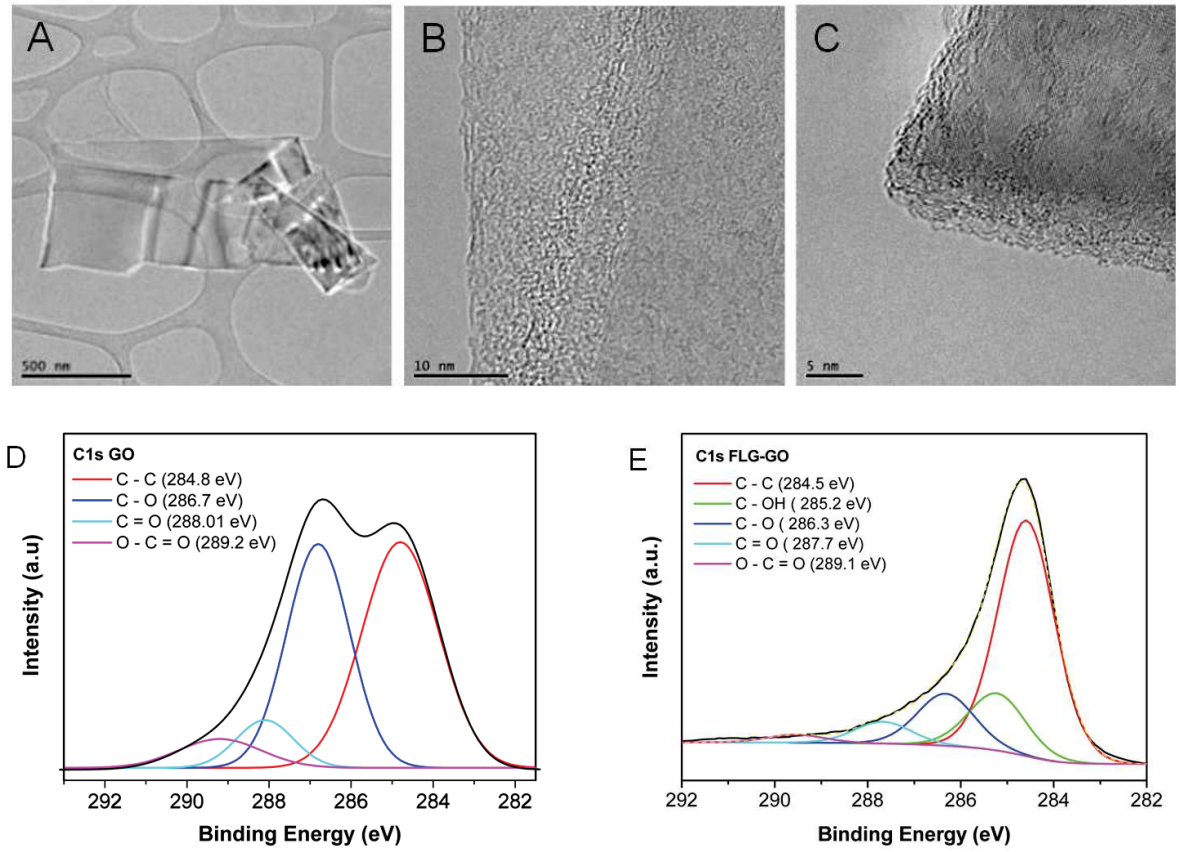

Figure 53. (A-C) Representative TEM micrographs of the GO mediated exfoliated EG with different magnifications. (D and E) C1s XPS spectra of the GO and FLG-GO showing a strong reduction of the oxygen functional groups and increase of the carbon species after mixing.

The nature and concentration of the oxygen species present on the different samples were also analyzed by XPS and the results are presented in Fig. 53D and E. The C1s XPS spectrum of GO, with an oxygen content of ~ 32.6 at.%, is presented in Fig. 53D and can be deconvoluted into four peaks corresponding to carbon atoms in different functional groups:

the C–C in aromatic rings, the oxygenated C in C–O, C[double bond, length as m-dash]O, and O–C=O. However, the high percentage of oxygen in GO was steadily decreased in the FLG–GO complex (Fig. 53E), with an oxygen content of ~ 8.3 at.%. In addition, the ratio of C/O obtained from the C1s and O1s peaks increased from 2 (for GO) to 10 (for FLG–GO), respectively. Such a result could be attributed to the intimate mixing between the GO and the exfoliated FLG with low oxygen content. It is expected that during the sonication process, a part of the oxygen content could also be removed from the GO surface due to the energy input.

The yield of the exfoliation process as a function of the sonication duration is presented in Figure 53. The FLG exfoliation yield was calculated based on the weight of initial and final materials and defined by Eq. 4:

$$exf\,(\%) = \frac{ini(EG+GO) - (unexfEG + setl.exfMLG@GO)}{ini(EG+GO)} 100\% \qquad (4)$$

where ini(EG + GO) is the initial mass sum of EG and GO before sonication, unexfEG is the un-exfoliated EG decanting after 2 days standing, and setl.exfMLG@GO is the GO adsorbed on multi-layer-graphene that settled down after centrifugation at 3000 rpm. The exfoliation of EG that was calculated according to eqn (4) increases from 2.2, 5.3, 8.8, 12.3 to 16.8 wt% relative to the initial raw materials (EG added GO) for the sonication time ranging from 1, 2, 3, 4 to 5 hours, respectively. The exfoliation yield was also measured by UV-vis on the different concentrations of FLG–GO suspensions (Fig. 54B). The red line is a linear fit in which the yield is relative to initial EG (if assumed that no GO was decanted during the synthesis process), while the blue line is the yield relative to the total EG–GO mass. The exfoliation yield increases with sonication time, and reaches the value of up to ~ 25 wt% relative to the initial EG after 5h sonication. The GO mass percentage in the FLG–GO mixture can be estimated to be 25 wt % after 5 h sonication. These data are consistent with TGA measurement as shown in Fig. S3,† in which the curve corresponding to the GO has the onset temperature of 130 and 450 °C, which can be related to the decomposition of different oxygen containing groups, while the onset temperatures of the GO–FLG complex are increased and was found to be 360 and 560 °C. The amount of GO in the GO–FLG complex is estimated to be about 24% by mass. According to the results one can state that the GO mediated EG exfoliation process is among the best method to obtain thin FLG with high yield and under mild treatment conditions.

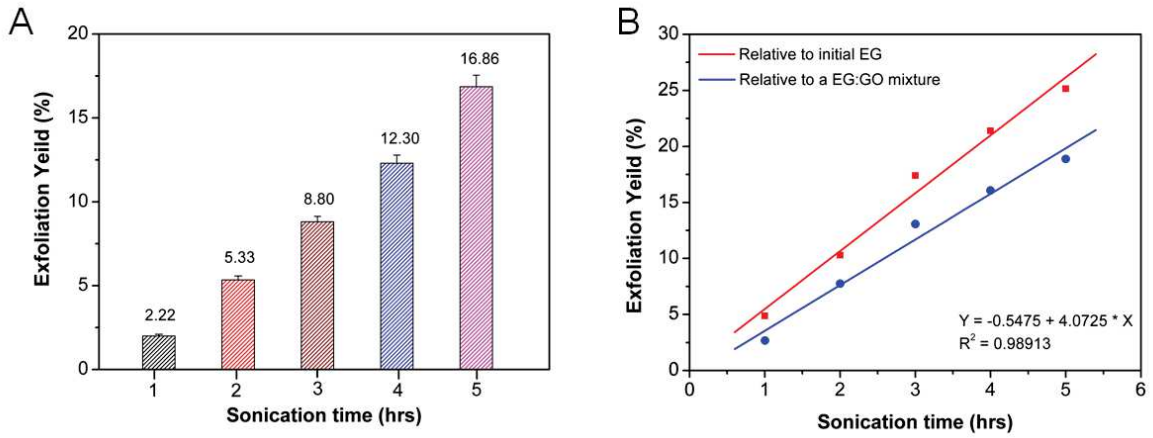

Figure 54. Exfoliation yield of EG by calculated with the Eq.4 (A), data calculated from the maximum concentration relative to starting materials and fit linear (B).

From the reported results, we have shown that a thin FLG–GO complex was successfully prepared in aqueous suspension medium by the solution-phase method. The as-synthesized FLG–GO mixture is used as a template for further self-organized decoration of FLG–GO with homogeneous nanodiamonds (NDs), for application as a metal-free catalyst in the steam-free dehydrogenation (DH) of ethyl benzene (EB) to styrene reaction.

Fig. 55A shows a digital photo of the aqueous dispersion of pristine NDs after 15 min tip sonication (Fig. 55A, left), and a colloidal suspension of the FLG–GO (3–1) complex (Fig. 55A, middle). When the ND dispersion (2 parts) is dropped into the FLG–GO suspension (1 part) under stirring conditions, ND particles are steadily adsorbed onto the surface of the FLG–GO complex, which results in the precipitation of the FLG–GO@ND (1:2) product in water (Fig. 55A, right). The complete adsorption of the NDs was evidenced by the colour change from pale-yellow to colourless of the medium upon precipitation. Herein, the aqueous dispersion of NDs has a positive charge with a zeta potential of +16 mV, whereas the FLG–GO suspension is negatively charged (−46 mV); thus, the interaction between them can be considered as electrostatic attractions (a zeta potential of the re-dispersed FLG–GO@ND suspension shows a value of −28 mV (Fig. S4A†)). Other possible interactions between FLG–GO and NDs may be hydrogen-bonding attractions because of the presence of oxygen-containing groups including hydroxyl, carboxylic, lactones, ketones and ethers[31,40] on the surface of NDs which can strongly interact with the GO surface.

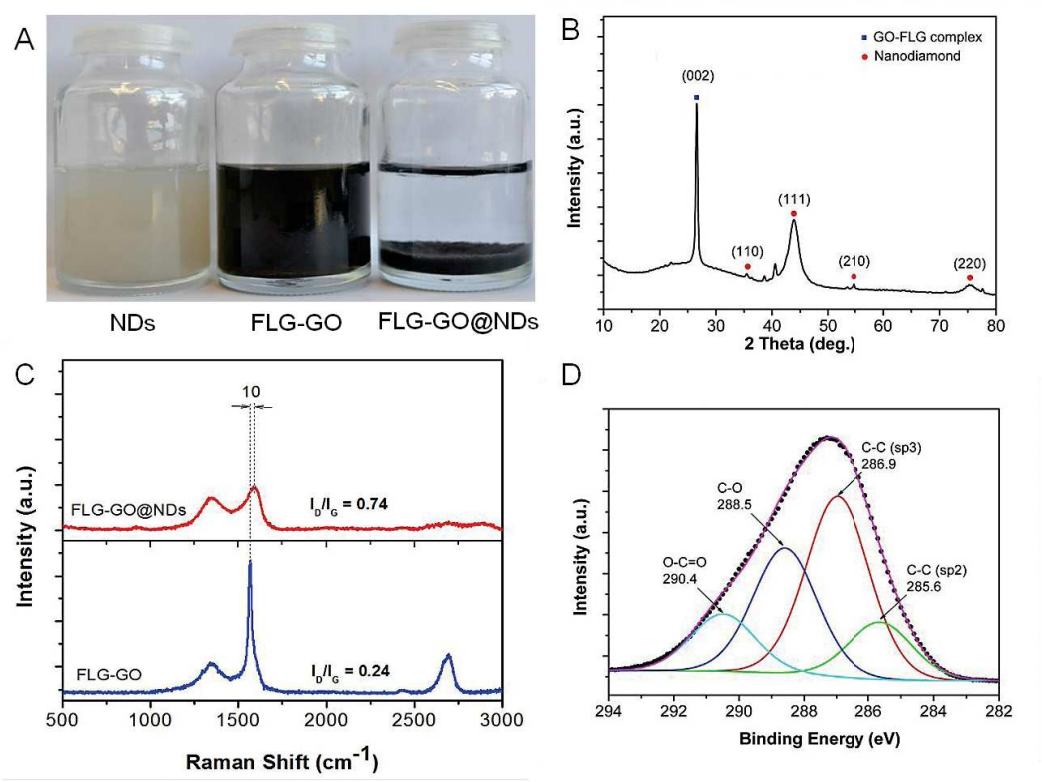

Figure 55. (A) A digital photo of aqueous dispersion of pristine NDs (left), FLG-GO complex suspension (middle) and ND-absorbed FLG-GO (right). (B) XRD spectra, (C) Raman spectrum and (D) C1s XPS spectrum of FLG-GO@NDs composite.

It should be noted that NDs are not adsorbed onto the surface of FLG under similar conditions (Fig. S5B†). The microstructure of the FLG–GO@ND composite was investigated by SEM (Fig. S5†), which shows that the FLG–GO powder consists of thin FLG platelets covered by a slightly wrinkled GO layer. The FLG–GO@NDs showed 3D laminated structures where the GO sheets were homogeneously decorated with ND particles. The XRD pattern of FLG–GO@NDs is shown in Fig. 55B, while the strong diffraction peak at 2θ = 26.5° is attributed to the (002) reflection from the graphite, the other peaks correspond to the self-organized adsorption of NDs onto the surface of the FLG–GO support. Raman spectroscopy at λexc = 532 nm was employed to investigate a change in the graphitic structure after adsorption of NDs, as shown in Fig. 55C. The Raman spectrum of FLG–GO@NDs shows an increased intensity and a broadening of sp3 defects (D-band) as compared to the FLG–GO complex since it overlapped with a peak of NDs itself ~1324 cm^{-1}). The tangential vibration of sp^2 carbon atoms in the hexagonal plane (G-band) is significantly decreased, and the ID/IG ratio increases more than 3 times from 0.24 to 0.74. It reflects that NDs cover the surface of FLG–GO and that the vibration of the graphitic domains is considerably attenuated. In addition, the G-band shifted by about 10 cm^{-1} to a higher wavenumber, which may be attributed to the functional groups on the surface of NDs such as the O–H bending and C=O stretching.31 The composition of the FLG–GO@ND

composite was analyzed by XPS and the results are presented in Fig. 55D. The C1s XPS spectrum clearly indicates four different major components (C sp^2, C sp^3, C–O and O=C–O), in which the non-oxygenated sp2 carbon of graphene is significantly decreased when compared to the FLG–GO complex, whereas the sp^3 allotrope of carbon at 286.9 eV becomes a prominent peak. This peak corresponds to the ND incorporation.

The dispersion of the NDs on the surface of the FLG–GO has been characterized by TEM microscopy (Fig. 56). It is clearly seen that the FLG–GO sheets are homogeneously decorated by spherical ND particles. Herein, the GO acts as an adsorption layer for randomly distributed NDs on the surface of the FLG–GO complex, while FLG plays the role of an inactive support to strengthen the FLG–GO complex, i.e. to hinder the GO layer shrinkage during ND adsorption. The high anchorage strength of the NDs on the GO surface could be attributed to the presence of OH groups on the ND surface. Wang et al.[37] have reported that those OH groups also actively participate in the reduction process of the GO after further heating treatments.

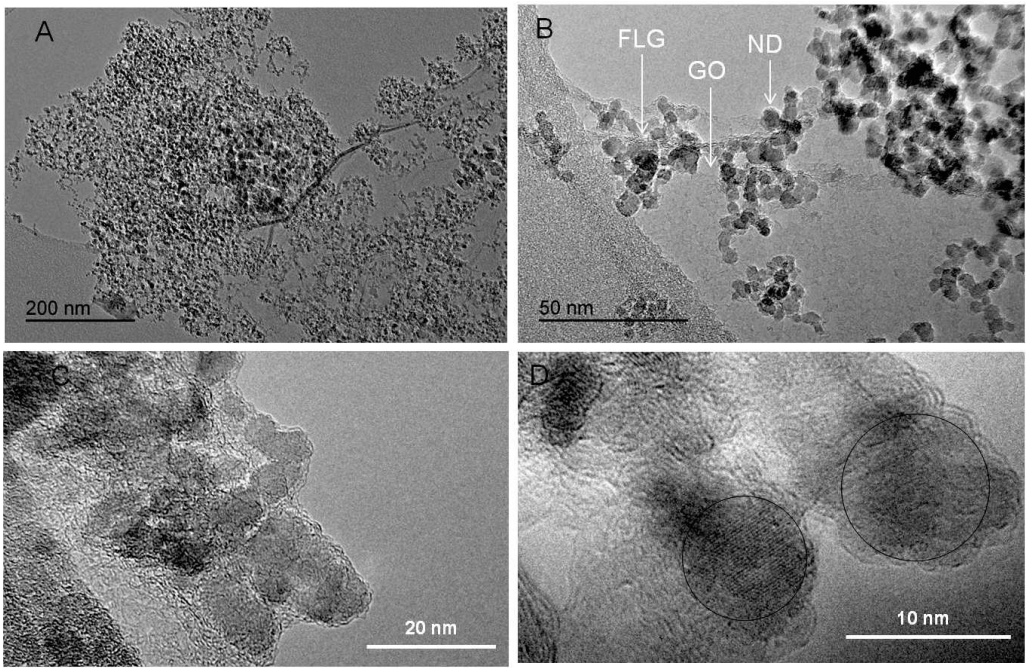

Figure 56. Representative TEM micrographs of FLG-GO@NDs composite with different magnifications. (A) General view showing the homogeneous dispersion of the NDs on the composite surface. (B) Medium view evidencing the high affinity of the NDs to adsorb on the GO surface. (C-D) High-resolution views showing the microstructure of the NDs and a detail view of the ND's top surface

From higher magnification TEM images, it can be seen that the ND nano-crystallites with an average diameter ranging from 4 to 8 nm are isolated over FLG–GO sheets. A

distribution of ND particle sizes has been measured using the Image-Pro Plus program on TEM images and presented in Fig. S6.† This is an important factor for a significant improvement of catalyst performances of the FLG–GO@NDs which will be considered in the following.

In order to evaluate the catalytic performance of the FLG–GO supported ND catalyst in the dehydrogenation of ethyl-benzene, 300 mg of the composite material were placed at the centre of a quartz reactor. The reaction was carried out at 550 °C under atmospheric pressure conditions similar to those reported by Su et al.[36] The reaction rate was expressed as the amount of styrene produced per gram of catalyst per hour. The catalyst selectivity to styrene has also been investigated. Fig. 57A shows a comparison of the styrene formation rate (ST. rate) and styrene selectivity (ST. Sel.) on the FLG–GO@ND composite-based catalyst versus those obtained on unsupported NDs and commercial iron-based catalysts (denoted as K–Fe). It was observed that the K–Fe catalyst exhibits extremely high DH activity at the beginning of the test (4.6 $mmol_{ST}\ g_{catalyst}^{-1}\ h^{-1}$) followed by a sharp deactivation to be next stabilized after 8 h of reaction at around 1 $mmol_{ST}\ g_{catalyst}^{-1}\ h^{-1}$. The low DH activity obtained on the iron-based catalyst could be attributed to the rapid saturation of the active sites by the carbonaceous residue under steam-free reaction conditions. On the other hand, both the unsupported NDs and FLG–GO@ND composite-based catalysts display a significant improvement of the DH activity, compared to the K–Fe catalyst, with a gradual decrease from 5.8 to 2.2 $mmol_{ST}\ g_{catalyst}^{-1}\ h^{-1}$ and 9.2 to 3.2 $mmol_{ST}\ g_{catalyst}^{-1}\ h^{-1}$, respectively, after the same duration of test, i.e. 50 h of time on stream. However, in contrast to the commercial catalyst, ND-based catalysts display a slow deactivation after the first deactivation slope. Such observation indicates that site blockage as a function of time on stream still occurs unlikely to the industrial catalyst where a balance of site blockage by the deposited carbonaceous residue was reached after a few hours of reaction. The significant improvement of the DH activity per unit weight of the NDs obtained on the supported FLG–GO catalyst could be attributed to the higher dispersion of the NDs on the GO surface, as evidenced by SEM and TEM analyses presented above. The dehydrogenation rate as a function of time on stream observed on both catalysts, NDs and FLG–GO@NDs, is similar which indicates that the nature of the active site is unchanged and the DH activity improvement is mostly due to the higher active sites on the FLG–GO@NDs consecutive to the dispersion of the NDs on the FLG–GO surface. This provides a higher specific surface area and density of active sites to perform the dehydrogenation reaction. The BET value increased from 283 $m^2\ g^{-1}$ for pristine NDs to 304 $m^2\ g^{-1}$ for FLG–GO@NDs along with a significant rise in mesoporous contribution (Fig. S7†). In the FLG–GO@ND catalyst the FLG with higher mechanical strength plays a role of an inactive support to prevent the clumping of the catalyst. To confirm our discussion on the role of FLG in the composite, a GO@ND (without FLG) sample was tested under the same reaction conditions (Fig. S8†). The GO@ND catalyst exhibits an intermediate DH activity compared to the ND and FLG–GO@ND catalysts. The low DH activity on the GO@ND

catalyst might be linked to the fact that GO clumped during adsorption of NDs, without FLG underneath, which will be limited to the density of active sites and thus, leading to the lower DH performance.

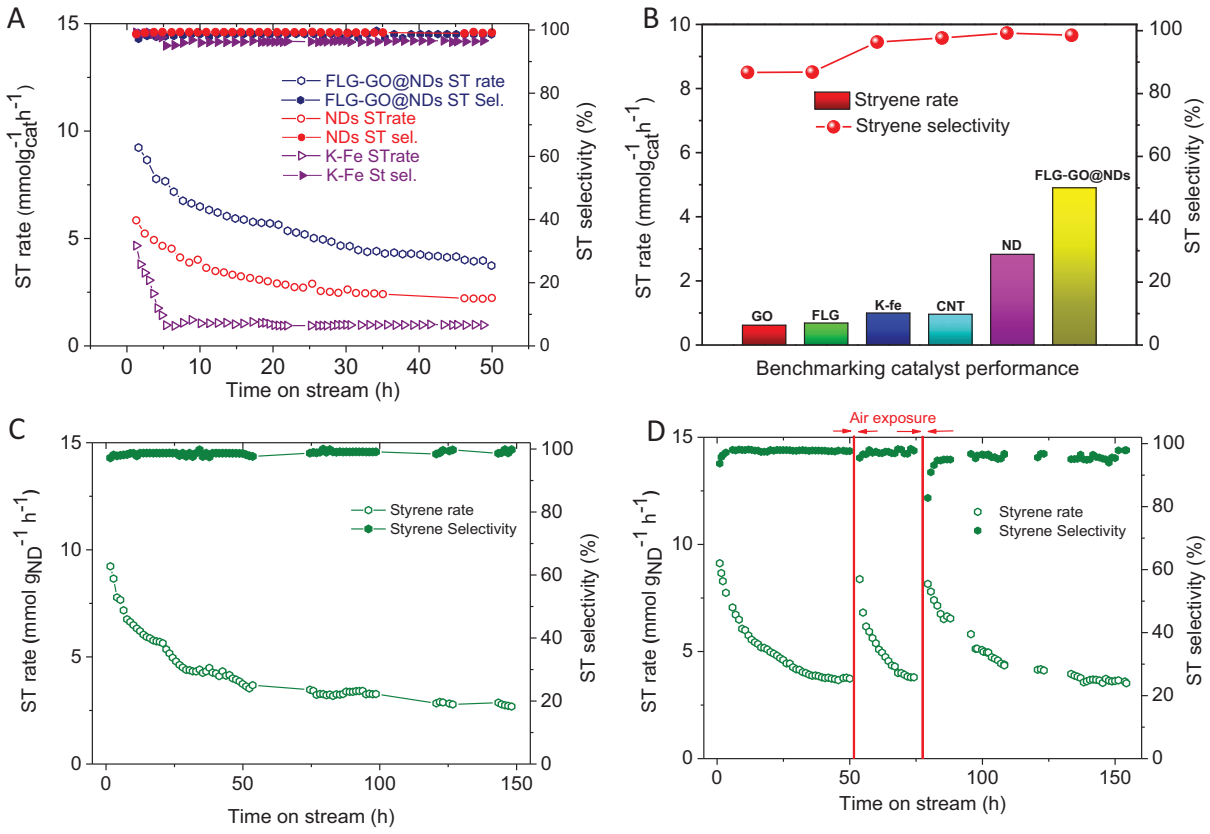

Figure 57. (A) DH activity of FLG-GO@NDs in comparison with commercial, unsupported NDs catalysts, (B) Benchmarking of different carbon-based nanomaterials in the DH process, (C) Long-term DH test at 550 °C of the FLG-GO@NDs catalyst, and (D) Regeneration test during cyclic air-exposure showing a high DH activity recovery of the GO-FLG@NDs-based composite catalyst.

The steady-state DH activity of the FLG–GO@ND catalyst was compared also with those obtained on different carbon-based and K–Fe catalysts (Fig. 57B). The results evidence the high DH activity of the FLG–GO@ND catalyst compared to the other carbon-based nanomaterial catalysts such as stacked GO, thick FLG, and CNTs. The high DH activity observed on the ND-based catalyst could be attributed to the high effective surface area of the catalyst and also to the high stability of the oxygenated functional groups on the ND surface compared to that exists on the other carbon-based materials.

The stability of the FLG–GO@ND catalyst as a function of time on stream is also evaluated by performing a long-term test up to 150 h (Fig. 57C). The DH activity was

stabilized at around 2.8 $mmol_{ST}\ g_{catalyst}^{-1}\ h^{-1}$, after 150 h of test, while the selectivity towards styrene remains unchanged for the whole test. Such results indicate that the deactivation was mostly linked with the loss of active sites and not to a modification of the active site nature.The DH activity can be recovered by submitting the spent catalyst to the regeneration process in air at 400 °C for 2 h (Fig. 57D). It is also worth noting that successive regenerations contribute also to a better stability of the catalyst as a function of time on stream, as evidenced in Fig. 57D. Similar behavior has been also reported by Su and co-workers[36] in a previous report.

In order to understand the cause of the deactivation and the regeneration mechanism, the XPS analysis was performed on the catalyst at different stages, i.e. fresh, spent and regenerated catalyst, and the results are shown in Fig. S9.† As can be seen from the XPS data, the carbon-to-oxygen ratio on the catalyst steadily increases from 13.8 for the fresh catalyst to 18.6 for the one after reaction. Such results indicate that carbonaceous species were deposited onto the catalyst surface during the course of the reaction which slowly covers the surface of the active sites leading to catalyst deactivation. It is also worth noting that during the reaction part of the oxygen species presents on the catalyst surface, especially the quinoic group which is expected to be the active site, could be also removed. The C/O ratio steadily decreases from 18.6 to 7.7 after the regeneration process indicating that part of the carbonaceous residues has been removed, leading to a higher active site exposure. The change in the oxygen-containing functional groups, such as C–O and O–C=O, is well matched with the DH activity behaviour observed on the catalyst performances. According to the results, the decrease of the oxygenated functional groups, especially the carboxylate group, is well fitted with the decrease of the DH activity of the catalyst. The C=O groups slightly decrease from 11 to 8 at.% which corresponds to the decrease of the DH activity from 9.2 $mmol_{ST}\ g_{catalyst}^{-1}\ h^{-1}$ to 3.9 $mmol_{ST}\ g_{catalyst}^{-1}\ h^{-1}$. After regeneration, the C=O functional groups steadily increase from 8 to about 57 at.% while the DH activity is fully restored (Fig. 6D). Our results are consistent with those previously reported by Su and co-workers in which the reduced DH activity agrees well with the consumption of the C=O content.[36] The physical properties of the spent catalysts have been evaluated by XPS and temperature-programmed oxidation (TPO) techniques. The XPS results of the oxygen-based species recorded for the different samples, as-received FLG–GO@NDs, pre-treated at 550 °C under He and the post-reaction FLG–GO@ND composite are summarized in Fig. S10.† It shows that the O–H bond of the FLG–GO@NDs remained unchanged, for the sample before and after the reaction, at about 7.9 at.%, which indicates that hydrogenation of the catalyst, during the course of the reaction, was unlikely to occur. In

addition, the TPO mass spectrum of the post-reaction composite displayed no peaks corresponding to H_2O during the combustion, which suggested that hydrogen generated from the reaction was directly released out from the catalyst.

4. Conclusion

We have demonstrated in this report an easy and scalable method to produce a "sandwich structure" between GO and FLG, where GO plays the role of a dispersant allowing the exfoliation of expanded graphite into a thin FLG structure and prevents the re-stacking of the FLG. The GO layer also provides anchorage sites for adsorbing ND particles through a charge compensation leading to the high dispersion of this layer on the hybrid support surface. The NDs–GO–FLG composite was further used as a metal-free catalyst in the steam-free dehydrogenation of ethyl-benzene to styrene. The hybrid composite exhibits a high and relatively stable DH performance compared to the other carbon-based and doped iron industrial catalysts. The DH activity per weight unit of NDs was about two times higher than the one obtained on the unsupported, which is due to the high dispersion of the NDs on the GO–FLG surface. The NDs–GO–FLG also exhibits a relatively high DH stability as a function of time on stream, up to 150 h. The deactivated catalyst can be efficiently regenerated by air calcination at 400 °C which allows the recovery of the C=O functional groups and the removal of the carbonaceous residues deposited during the course of the reaction. The results obtained in the present work can be further extended to other liquid-phase catalytic applications where a highly reactive surface of the GO is required for adsorption of metal nanoparticles.

Acknowledgements

T. T.Tung and T. P. Lai would like to thank the European Union for the grant through the Freecats project. The SEM and TEM analysis were performed at the facilities of the IPCMS (UMR 7504 CNRS-University of Strasbourg) and T. Romero (ICPEES) is gratefully acknowledged for performing SEM analysis; P. Bernhardt (ICPEES) is gratefully acknowledged for performing XPS analysis.

References

(1) K. S. Novoselov, A. K. Geim, S. V. Morozov, D. Jiang, M. I. Katsnelson, I. V. Grigorieva, S.V. Dubonos and A. A. Firsov, Two-dimensional gas of massless Dirac fermions in graphene, Nature, **2005**, 438, 197–200.

(2) A. K. Geim and K. S. Novoselov, The rise of graphene, Nat. Mater., 2007, 6, 183–191.

(3) F. Schedin, A. K. Geim, S. V. Morozov, E. W. Hill, P. Blake, M. I. Katsnelson and K. S. Novoselov, Detection of individual gas molecules adsorbed on graphene, Nat. Mater., **2007**, 6, 652–655.

(4) K. S. Novoselov, A. K. Geim, S. V. Morozov, D. Jiang, Y. Zhang and S. V. Dubonos, et al., Electric field effect in atomically thin carbon films, Science, **2004**, 306, 666–669.

(5) C. Berger, Z. M. Song, X. B. Li, X. S. Wu, N. Brown and C. Naud, et al., Electronic confinement and coherence in patterned epitaxial graphene, Science, **2006**, 312, 1191–1198.

(6) B. Dlubak, M. Martin, C. Deranlot, B. Servet, S. Xavier and R. Mattana, Highly efficient spin transport in epitaxial graphene on SiC, Nat. Phys., **2012**, 8, 557–561.

(7) N. C. Bartelt and K. F. McCarty, Graphene growth on metal surfaces, MRS Bull., **2012**, 37), 1158–1165.

(8) S. Park and R. S. Ruoff, Chemical methods for the production of graphenes, Nat. Nanotechnol., **2009**, l4, 217–224.

(9) W. Gao, L. B. Alemary, L. Gi and P. M. Ajayan, New insights into the structure and reduction of graphite oxide, Nat. Chem., **2009**, 1, 403–408.

(10) S. Stankovich, D. A. Dikin, R. D. Piner, K. A. Kohlhaas, A. Kleinhammes and Y. Jia, Synthesis of graphene-based nanosheets via chemical reduction of exfoliated graphite oxide, Carbon, **2007**, 45, 1558–1565.

(11) J. T. Robinson, F. K. Perkins, E. S. Snow, Z. Wei and P. E. Sheehan, Reduced graphene oxide molecular sensors, Nano Lett., 2008, 8, 3137–3140.

(12) I. Janowska, F. Vigneron, D. Bégin, O. Ersen, P. Bernhardt and T. Romero, et al., Mechanical thinning to make few-layer graphene from pencil lead, Carbon, **2012**, 50, 3106–3110.

(13) D. M. Kosynkin, A. L. Higginbotham, A. Sinitskii, J. R. Lomeda, A. Dimiev and B. K. Price, et al., Longitudinal unzipping of carbon nanotubes to form graphene nanoribbons, Nature, **2009**, 458, 872–876.

(14) L. Jiao, L. Zhang, X. Wang, G. Diankov and H. Dai, Narrow graphene nanoribbons from carbon nanotubes, Nature, **2009**, 458, 877–880.

(15) L. Jiao, X. Wang, G. Diankov, H. Wang and H. Dai, Facile synthesis of high-quality graphene nanoribbons, Nat. Nanotechnol., **2010**, 5, 321–325.

(16) I. Janowska, O. Ersen, T. Jacob, Ph. Vénnégues and D. Bégin, et al., Catalytic unzipping of carbon nanotubes to few-layer grapheme sheets under microwaves irradiation, Appl. Catal. A: Gen, **2009**, 371, 22–30.

(17) L. Jaber-Ansari and M. C. Hersam, Solution-processed graphene materials and composites, MRS Bull., **2012**, 37, 1167–1175.

(18) C. Shih, A. Vijayaraghavan, R. Krishnan, R. Sharma, J. H. Han and M. H. Ham, Bi- and trilayer graphene solutions, Nat. Nanotechnol., **2011**, 6, 439–445.

(19) Y. Hernandes, V. Nicolosi, M. Lotya, F. M. Blighe and Z. Sun, et al., High-yield production of graphene by liquid-phase exfoliation of graphite, Nat. Nanotechnol., **2008**, 3, 563–568.

(20) J. N. Coleman, Liquid exfoliation of defect-free graphene, Acc. Chem. Res., **2013**, 46, 14.
(21) A. O'Neill, U. Khan, P. N. Nirmalraj, J. Boland and J. N. Coleman, Graphene dispersion and exfoliation in low boiling point solvents, J. Phys. Chem. C, **2011**, 115, 5422–5428.
(22) U. Khan, A. O'Neill, M. Lotya, S. De and J. N. Coleman, High-concentration solvent exfoliation of graphene, Small, **2010**, 6(7), 864–871.
(23) M. Lotya, P. J. King, U. Khan, S. De and J. N. Coleman, High-concentration, surfactant-stabilized graphene dispersions, ACS Nano, **2010**, 4, 3155–3162.
(24) M. Lotya, Y. Hernandez, P. J. King, R. J. Smith, V. Nicolosi and L. S. Karlsson, et al., Liquid phase production of graphene by exfoliation of graphite in surfactant/water solution, J. Am. Chem. Soc., **2009**, 131, 3611–3620.
(25) A. A. Green and M. C. Hersam, Solution phase production of graphene with controlled thickness via density differentiation, Nano Lett., **2009**, 9, 4031–4036.
(26) D. Li, M. B. Muller, S. Gilje, R. B. Kaner and G. Wallace, Processable aqueous dispersions of graphene nanosheets, Nat. Nanotechnol., **2008**, 3, 101–103.
(27) J. Kim, L. J. Cote, F. Kim, W. Yuan, K. R. Shull and J. Huang, Graphene oxide sheets at interfaces, J. Am. Chem. Soc., **2010**, 132, 8180–8186.
(28) L. J. Cote, J. Kim, V. C. Tung, J. Luo, F. Kim and J. Huang, Graphene oxide as surfactant sheets, Pure Appl. Chem., **2011**, 83(1), 95–110.
(29) S. H. Lee, D. H. Lee, W. J. Lee and S. O. Kim, Tailored assembly of carbon nanotubes and Graphene, Adv. Funct. Mater., **2012**, 21, 1338–1354 .
(30) H. Hu, Z. Zhao, Q. Zhou, Y. Gogotsi and J. Qiu, The role of microwave absorption on the formation of graphene oxide, Carbon, **2012**, 50, 3267–3273.
(31) V. N. Mochalin, O. Shenderova, D. Ho and Y. Gogotsi, The properties and applications of nanodiamonds, Nat. Nanotechnol., **2012**, 7, 11–23.
(32) Y. Sun, Q. Wu, Y. Xu, H. Bai, C. Li and G. Shi, Highly conductive and flexible mesoporous graphitic films prepared by graphitizing the composites of graphene oxide and nanodiamond, J. Mater. Chem., **2011**, 21, 7154–7160.
(33) D. M. Jang, J. Myung, H. S. Im, Y. S. Seo, Y. J. Cho, C. W. Lee, J. Park, A. Y. Jee and M. Lee, Nanodiamonds as photocatalysts for reduction of water and graphene oxide, Chem. Commun., **2012**, 48, 696–698.
(34) D. M. Jang, H. S. Im, J. Myung, Y. S. Seo, Y. J. Cho, H. S. Kim, S. H. Back, J. H. Park, E. H. Cha and M. Lee, Hydrogen and carbon monoxide generation from laser-induced graphitized nanodiamonds in water, Phys. Chem. Chem. Phys., **2013**, 15, 7155–7160.
(35) J. Zang, Y. Wang, L. Bian, J. Zhang, F. Meng, Y. Zhao, R. Lu, X. Qu and S. Ren, Graphene growth on nanodiamonds as a support for a Pt electrocatalyst in methanol electro-oxidation, Carbon, **2012**, 50, 3032–3038.
(36) J. Zhang, D. S. Su, R. Blume, R. Schlögl, R. Wang, X. Yang and A. Gajović, Surface chemistry and catalytic reactivity of a nanodiamond in the steam-free dehydrogenation of ethylbenzene, Angew. Chem., Int. Ed., **2010**, 49, 8640–8644.
(37) Q. Wang, N. Plylahan, M. V. Shelke, R. R. Devarapalli and M. Li, et al., Nanodiamond particles/reduced graphene oxide composites as efficient supercapacitor electrodes, Carbon, **2014**, 68, 175–184.
(38) A. C. Ferrari and D. M. Basko, Raman spectroscopy as a versatile tool for studying the properties of graphene, Nat. Nanotechnol., **2013**, 8, 235–243.
(39) A. C. Ferrari, J. C. Meyer, V. Scardaci, C. Casiraghi, M. Lazzeri, F. Mauri, S. Piscanec, D. Jiang, K. S. Novoselov, S. Roth and A. K. Geim, Raman spectrum of graphene and graphene layers, Phys. Rev. Lett., **2006**, 97, 187401.

(40) Y. Liu, Z. Gu, J. L. Margrave and V. N. Khabashesku, Functionalization of nanoscale diamond powder: fluoro-, alkyl-, amino-, and amino acid-nanodiamond derivatives, Chem. Mater., **2004**, 16, 3924–3930.

Supporting Information

1. Synthesis of graphene oxide (GO) and GO-mediated exfoliation of expanded graphite (EG) in water

Graphene oxide (GO) powder was prepared from graphite flakes using modified Hummers method.[1,2] Briefly, 5 g of graphite (Sigma-Aldrich, cat # 332461, ~ 150 μm) and 3.75 g of $NaNO_3$ were placed in a flask. Then, 375 mL of H_2SO_4 (95%) was added drop-wise while the system was kept under stirring in an ice-water bath, and 25 g of $KMnO_4$ were slowly added during 1 h. Stirring was continued for 2 h in the ice-water bath. The ice bath was then removed and the mixture was stirred at room temperature until it became pasty brownish and then 250 mL deionized (DI) water was slowly added to the system. The reaction temperature was rapidly increased to 98°C, and the color changed to brown after 2 h. Finally, 15 mL of 30 wt% aqueous solution of H_2O_2 was added to complete the oxidation process. The ions of oxidant and other inorganic impurities were removed by repeating cycles of centrifugation, followed by the removal of the supernatant liquid, and the solid was redispersed using 3 wt % HCl aqueous solution. After filtration, the solid was dispersed again in water using ultrasonication for 2 h and centrifuged at 6000 rpm for 30 min to remove the multilayered- carbon species.

For the synthesis of GO-FLG complex, GO suspension with a concentration of 1 mg/mL was obtained by dispersing GO powders in distilled water with the aid of ultrasonic bath for 30 min. Then the mixture of EG/GO with different weight ratios, i.e. 1:1, 3:1 and 5:1 were subjected to sonication. The typically procedure is the following: 600 mg of expanded graphite (EG) dispersed in 280 mL DI water was placed in a 500 mL capped-round bottom flask and pre-sonicated with a tip sonicator with a power of 28 W for 30 min to swelling the EG. It was then mixed with a 200 mL GO suspension (1mg/mL) and followed by sonication for various time, from 1 to 5 hours. The reaction temperature was kept at around 40-50 °C by adding water to the sonicator bath. After the sonicating step, the as-prepared suspension was left to stand 2 days for settling down unstable expanded graphite aggregates, and the supernatant was extracted by pipette, then further centrifuged at 3000 rpm for 30 min. The aqueous GO-stabilized FLG with a concentration of 0.35 mg/mL is turned out to be a stable suspension for few days without any observable aggregation. It was then used for characterization and further application.

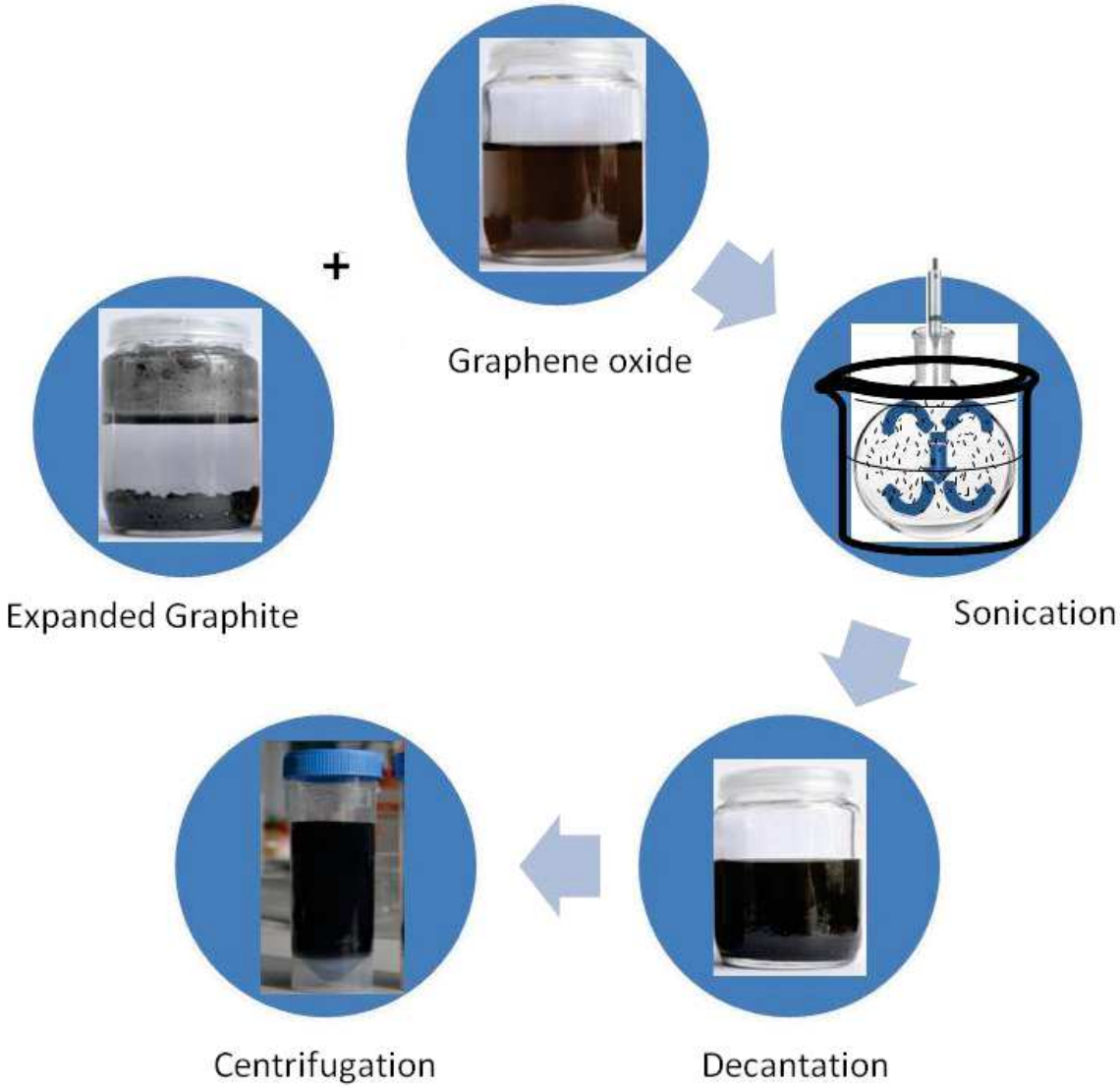

Schematic1. Solution-processed few-layer graphene/graphene oxide by exfoliating expanded graphite in the presence of GO suspension under sonication.

2. Self-organized decoration of nanodiamonds on the surface of GO-FLG

The commercial nanodiamonds (NDs) with diameter in the range of 4-10 nm in a powder form were supplied by the Hightech Co (Finland) and were used without any further purification. For the preparation of a GO-FLG@NDs composite, typically 200 mg pristine NDs was dispersed in 200 mL DI water and sonicated with a tip sonicator for 15 min. It was then well-mixed with a 286 mL of the as-synthesized GO-FLG complex suspension (0.35 mg/mL) by droplet under stirring condition. Nanodiamond particles were steadily absorbed homogeneously on the surface of FLG-GO sheets and the formed composite was settled down after few minutes. The mixture was then filtered and dried in the oven at 110 °C for 6 hours to get the constant weight of FLG-GO@NDs composite.

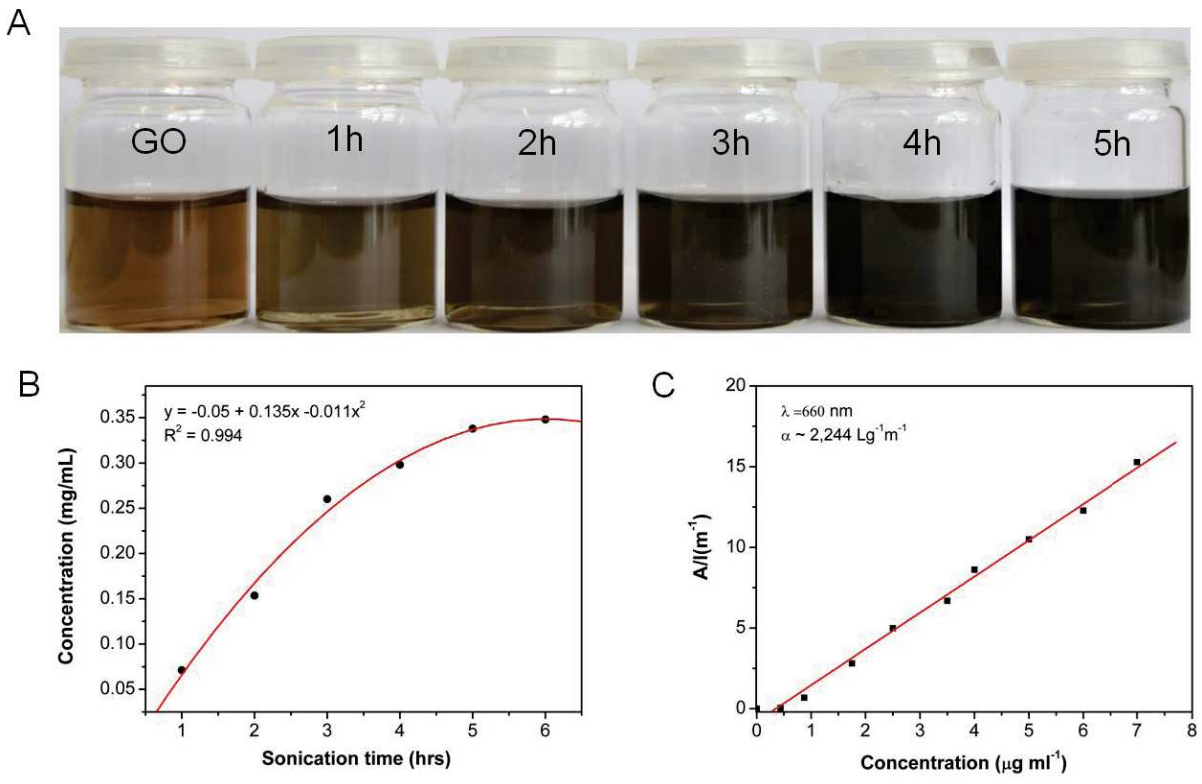

Figure S1. A digital photo of diluted FLG-GO complex suspension as a function of sonication time (A), their concentration (B), the curve obtained from the absorbance value as a function of concentration. The linear fit (C) confirms the Lambert-Beer behavior with an average absorption of α =2,244 $Lg^{-1}m^{-1}$ by recording the diluted 50 times of maximum concentration at optical absorbance of 660 nm.

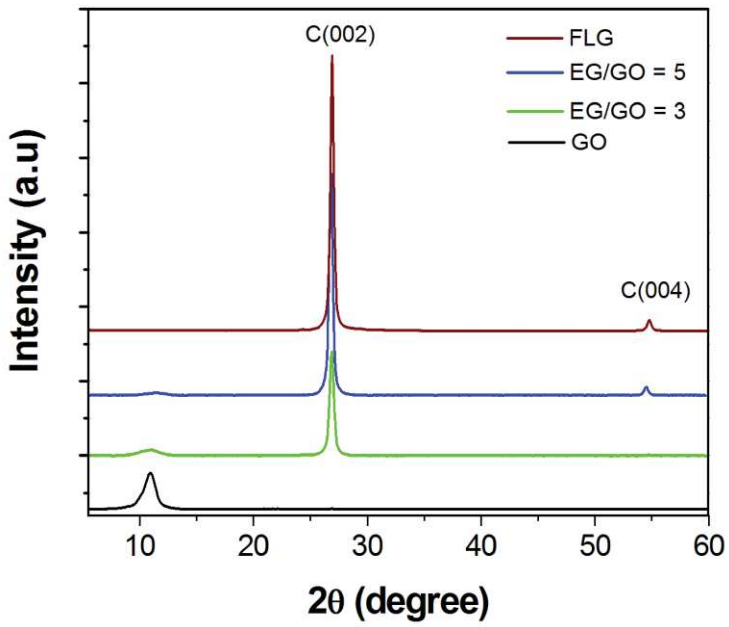

Figure S2. The XRD patterns of different EG/GO mixtures with different EG/GO weight ratio as compared to GO and FLG.

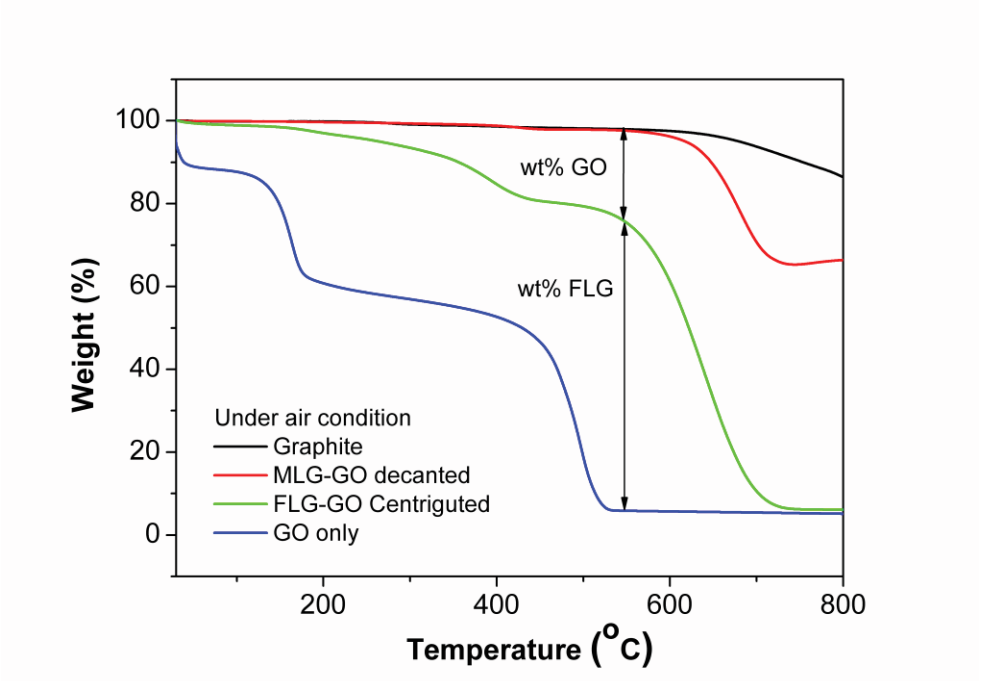

Figure S3. TGA curves of FLG-GO complex (green), as compared to GO (blue), sediment GO-multilayer graphene (red) and expanded graphite (black).

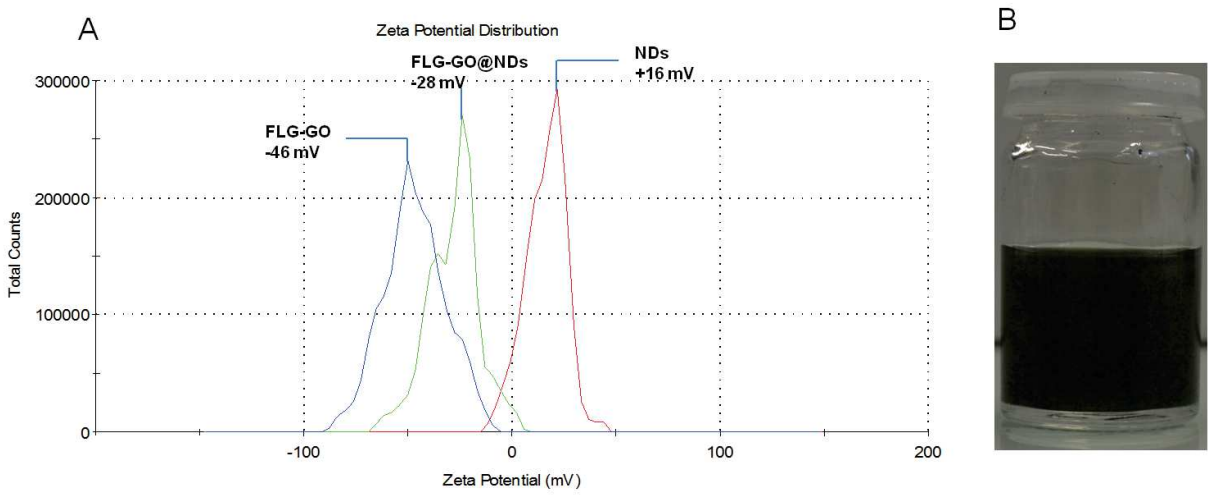

Figure S4. (A) Zeta potential distribution confirms the electrostatic interaction between FLG-GO and NDs, (B) a digital photo showing no NDs are adsorbed on the FLG surface.

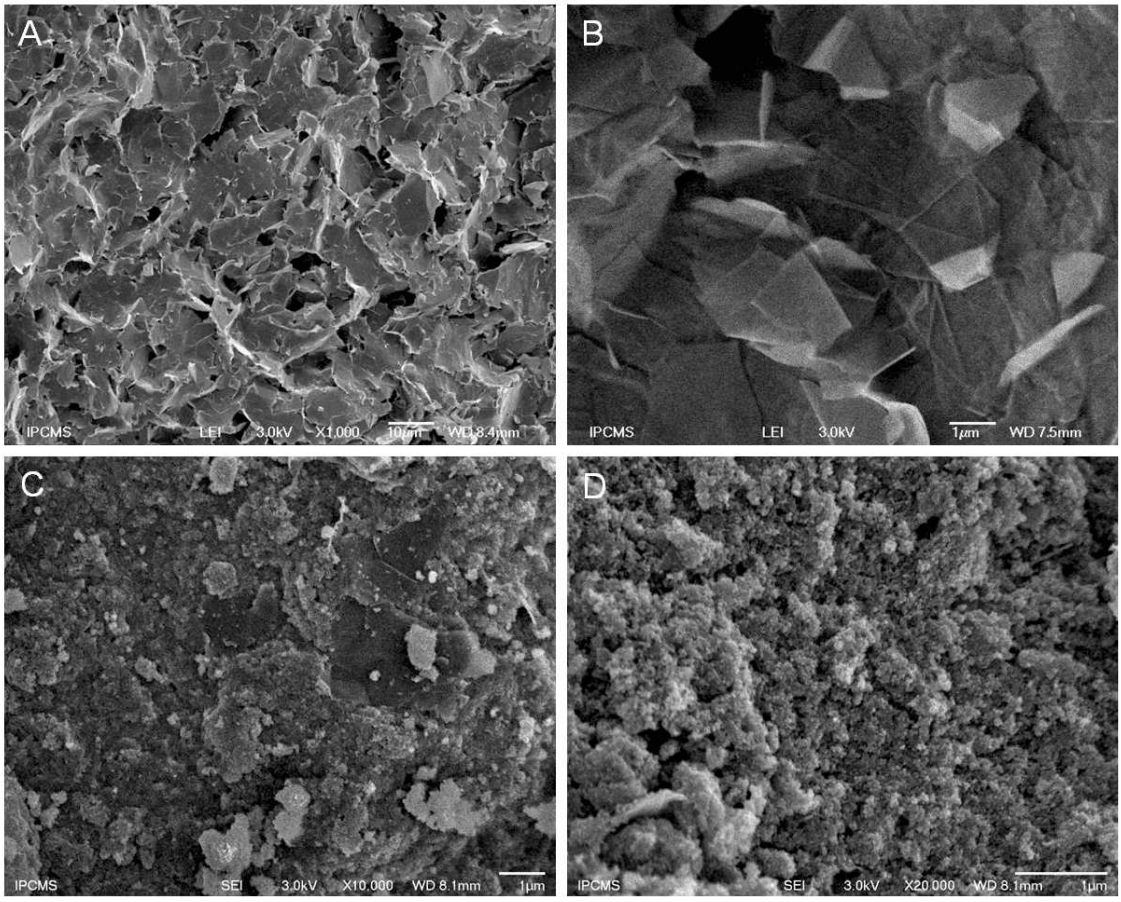

Figure S5. SEM images of FLG-GO complex powders (A, B), nanodiamond particles adsorbed on the surface of FLG-GO (C, D).

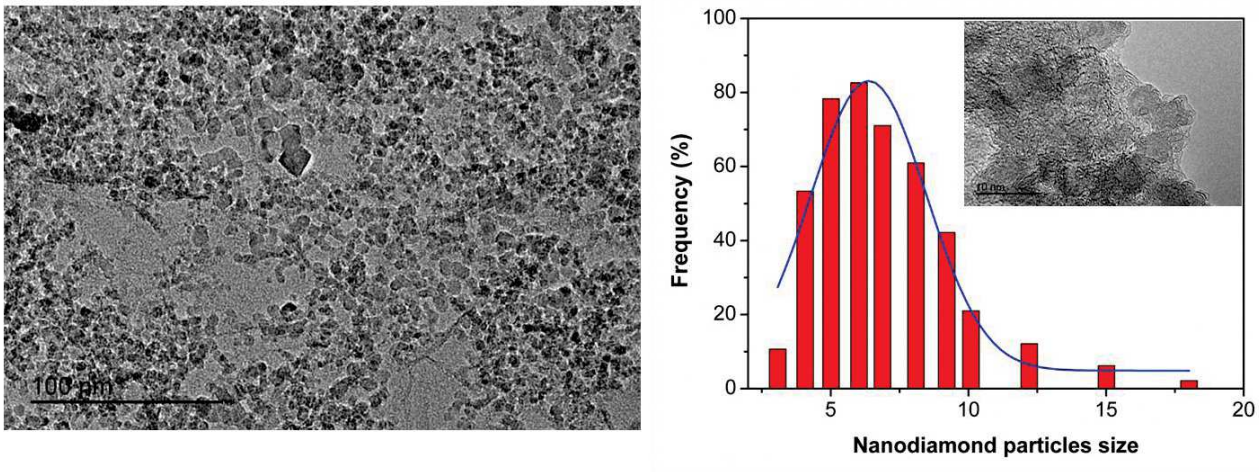

Figure S6. Representative TEM micrograph of the ND/GO/FLG and frequency distribution of ND particles size on the surface of FLG-GO complex using *Image-Pro plus* software measured from TEM images.

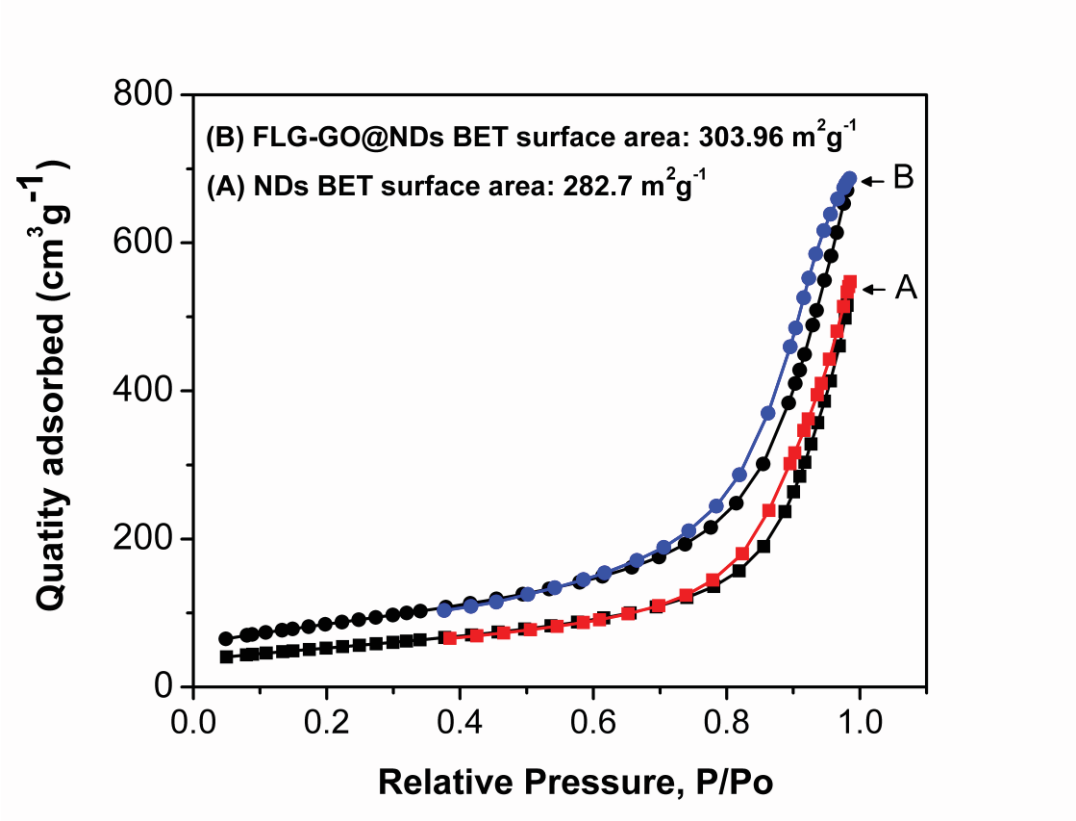

Figure S7. Nitrogen absorption-desorption isotherms of pristine NDs (A) and GO-FLG@NDs composite (B).

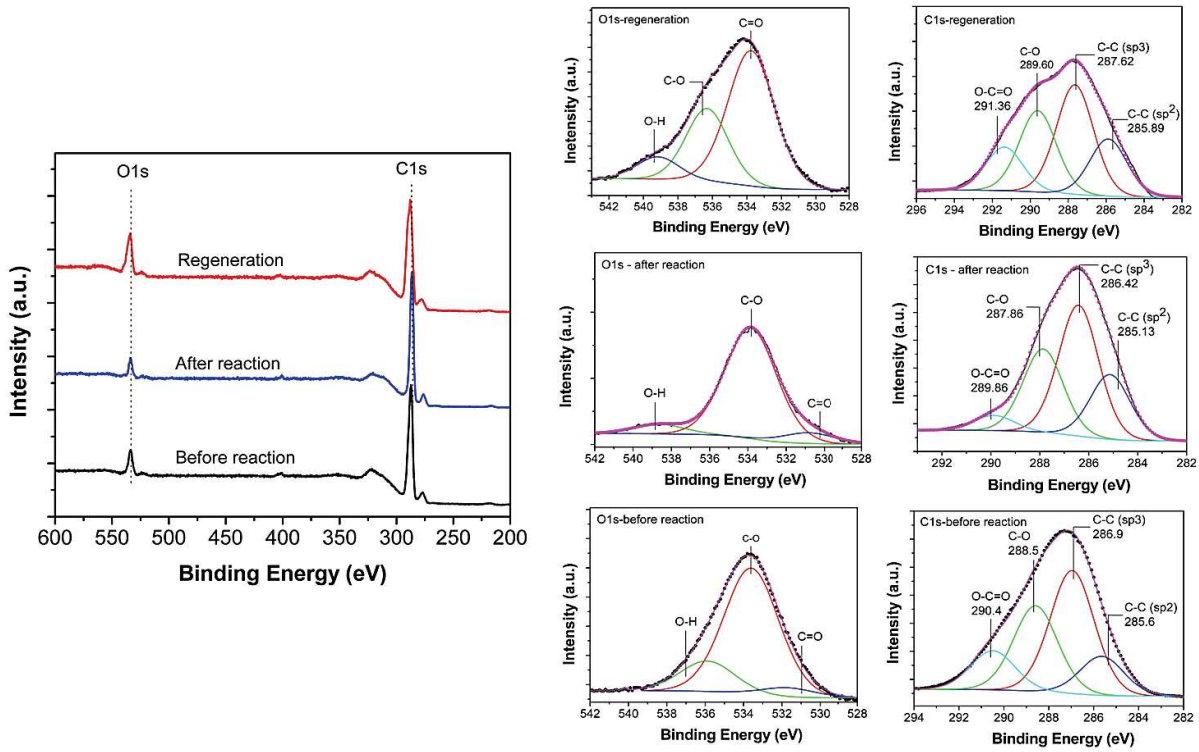

Figure S8. XPS measurements showing the structural changes between carbon and oxygen species during the dehydrogenation test.

Reference

(1) Hummers, W. S.; Offeman, R. E. Preparation of graphitic oxide. *J Am Chem Soc* **1958**, 80, 1339.
(2) Liang, Y.; Wu, D.; Feng, X.; Mullen, K. Dispersion of graphene sheets in organic solvent supported by ionic interactions. Adv Mater **2009**, 21, 1679-83.

CHAPTER 4

3D nanoscopic carbon architecture as a metal-free catalyst for styrene production

Nanodiamonds decorated graphene-carbon nanofibers 3D architecture as a metal-Free catalyst for styrene production

Housseinou Baa,c†*, Lai Truong-Phuoca†, Yuefeng Liua, Cuong Duong-Vieta, Jean-Mario Nhuta, Lam Nguyen-Dinhb, Pascal Grangerc, Ovidiu Ersend, Cuong Pham-Huua*

[a]*Institut de Chimie et Procédés pour l'Energie, l'Environnement et la Santé (ICPEES), ECPM, UMR 7515 du CNRS-Université de Strasbourg, 25 rue Becquerel, 67087 Strasbourg Cedex 02, France. E-mail: cuong.pham-huu@unistra.fr*

[b] *The University of Da-Nang, University of Science and Technology, 54 Nguyen Luong Bang, Da-Nang, Viet-Nam*

[c]*Unité de Catalyse et Chimie du Solide (UCCS), UMR 8181 CNRS-Université de Lille-, 59655 - Villeneuve d'Ascq Cedex France.*

Article Submitted in Carbon

Graphical abstract

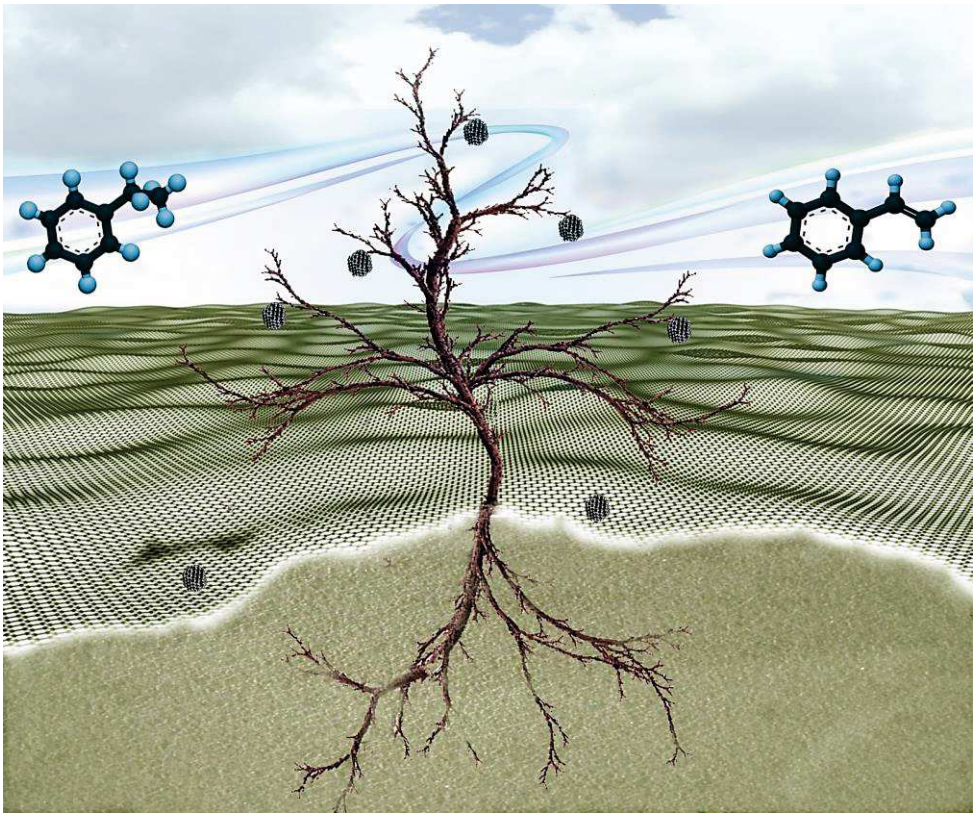

Abstract

Hierarchical structure consisting with the decoration of few-layer graphene surface with a dense network of carbon nanofibers was synthesized by Chemical Vapor Deposition. The hierarchical composite was further used as host matrix for the dispersion of nanodiamonds to generate a metal-free catalyst for the direct dehydrogenation process of ethylbenzene. The as-synthetized 3D metal-free composite (ND/FLG-CNF) exhibits a very high activity and stability for the steam-free direct dehydrogenation of ethylbenzene into styrene. The outstanding catalytic performance and the superior stability of the hybrid ND/FLG-CNF composite compared to the other carbon-based and promoted iron industrial catalysts, render it among the most promising metal-free catalyst for industrial direct dehydrogenation process.

1. Introduction

Styrene also known as phenylethylene, vinylbenzene, styrol, or cinnamene, C_6H_5–CH=CH_2 (ST) is one of the most important unsaturated aromatic monomers in modern petrochemical industry. The synthesis of styrene by direct gas-phase dehydrogenation (DH) of ethylbenzene (EB) is among the most developed industrial processes nowadays.[1] The world production of styrene monomer is significantly increased since the last decades to reach about 26 Mt per annum in 2012 and continue to face a high growing rate in the future.[2] The most employed industrial catalyst for such reaction is the iron-based catalyst, accounting for almost 95 wt. % of iron oxide, promoted with different elements such as alumina and potassium.[3,4] However, during the course of the reaction a large amount of coke, generated through the polymerization of the formed product, was deposited on the catalyst surface leading to the progressive plugging of the active site which significantly decreases the DH activity with time on stream.[5] In order to avoid such deactivation a large amount of steam was co-feeded in the reactor, H_2O:EB ratio of ca. 10:1, in order to produce oxygen through catalytic water splitting to burn-out the carbonaceous residue formed during the process. The steam production is a cost incentive process and thus, the development of new alternative catalysts with better coke resistance is of interest. In addition, the wastewater generated from the process calls for extensive recycling which also contributes to the overall increase of the process cost. Schlögl and co-workers[6] have reported the development of a metal-free based on nanodiamonds (ND) for the steam-free DH of ethylbenzene into styrene. According to the results the NDs-based catalyst exhibits DH activity about three times higher than the one obtained with the bulk iron-based industrial catalyst along with a high selectivity towards styrene formation. It is expected that carbonaceous residue, issued from the polymerization process, is under balance on the carbon-based catalyst which prevent excessive deactivation with time on stream. However, the ND is used in a powder form which leads to a significant pressure drop along the catalyst bed according to reports in the literature .[7] The ND-based catalyst also shows a high tendency to form agglomerates which significantly reduce the effective surface area of the catalyst for the subsequence catalytic process. It is well known in the heterogeneous catalysis field that the performance of solid catalysts is not only dependent in their chemical composition but also in the morphological properties where accessibility and diffusion phenomena are key issues.[8,9] In the present article, the idea is to improve the dispersion of the NDs particles, which would increase the effective contact surface area and the number of active sites per catalyst weight, leading to an enhancement of their catalytic properties. More recently hybrid materials consisting of ND particles uniformly dispersed onto a 2D graphene oxide and or few-layer-graphene (FLG) lead to a significant improvement of the DH activity, respectively 1.7 and 3.4 times higher than the un-supported nanodiamond.[10,11]

Recently, it has been reported that by computational studies that 3D hybrid materials consisted of graphene sheets decorated with a super-structure of carbon nanotubes (CNTs) or nanofibers (CNFs) present a highly open structure with high effective surface area and accessibility for numerous field of applications.[12] The theoretical prediction was rapidly followed by experimental works to prepare such hybrid materials for application in the field of electronics, energy storage, polymer reinforcement, and catalyst as well.[13,14,15,16] The CNTs and CNFs present on the graphene surface are acting as spacers to prevent the re-stacking of the graphene sheets from each other.

The aim of the present work is to report the synthesis of a three-dimensional (3D) hierarchical composite consisted of a few-layer graphene (FLG) decorated with a densely packed layer of carbon nanofibers (CNFs) exhibiting a high and fully accessible surface area. The CNFs layer also prevents the re-stacking of the FLG through van der Walls forces as usually reported in the literature which provide a high accessibility for the reactant to the active sites.[17,18] Those hybrid materials will be further employed as support for the nanodiamonds (NDs) which provide anchorage sites for dispersing the NDs leading to a high active sites exposure per catalyst weight. The as-synthesized 3D carbon composite materials were further used as metal-free catalyst in the steam-free selective dehydrogenation of ethylbenzene (EB) into styrene. The DH activity of the as-synthesized catalyst will be bench-marked with those of bulk NDs and iron-based industrial catalysts under the same reaction conditions. The stability of the catalyst as a function of time on stream was also evaluated by performing a long-term test along with regeneration cycling. The catalyst, after each step, will be thoroughly characterized in order to get more insight about the active site nature and the dehydrogenation performance.

2. Experimental

2.1 Few-layer graphene synthesis and characterization

The few-layer graphene (FLG) was synthesized by a mechanical ablation method using pencil lead as a starting raw material.[19] The TEM analysis indicates that the material synthesized by this method is consisted of FLG sheets with a dimension of about few μm^2 and are consisted with FLG contain between two up to thirty graphene sheets (Figure S1). The TEM analysis also evidences the high graphitization degree of the as-synthesized FLG while the XPS analysis indicates relatively low oxygen content in the sample.

2.2 Synthesis of FLG supported Ni nanoparticles

The nickel nanoparticles were deposited onto the FLG surface via hydrothermal synthesis. Briefly, 200 mg of FLG was dispersed in 200 mL of ethanol by tip sonicating for 15 min. Subsequently, a solution of 18 mg of nickel acetylacetonate ($Ni(Acac)_2$) dissolved in an ethanol solution was slowly added into the FLG suspension under vigorous stirring. The mixture was placed into an autoclave for hydrothermal treatment at 150 °C for 24 h. After cooling to room temperature, the product was filtered and washed several times with ethanol, and oven-dried at 100 °C for overnight. Finally, it was then calcinated at 400 °C for 3h resulted to the formation of Ni-2%/FLG which will be used as the growth catalyst of the CNFs.

2.3 Synthesis of a 3D CNF/FLG composite

The CNF/FLG composite was synthesized by a chemical vapor deposition (CVD) method using a mixture of C_2H_6 and H_2 and the Ni/FLG as growth catalyst [20]. The Ni/FLG catalyst was placed inside a tubular quartz reactor and flushed with argon (100 mL/min) for 30 minutes at room temperature, and then, the argon flow was replaced by a H_2 flow (200 mL/min) and the reactor temperature was increased from room temperature to 400 °C (heating rate of 10°C/min) and maintained for 2 h to allow the reduction of the nickel oxide into its corresponding metal. After the reduction step the H_2 flow was further replaced by a mixture of C_2H_6/H_2 (50/50 v/v %), while the reactor temperature was increased from 400 to 800 °C (heating rate of 10°C/min) and kept at this temperature for additionally 2 h. Upon completion of the CVD growth, the reactor was cooled down under the reactant mixture to 400 °C and then, C_2H_6 and H_2 gas feeds were stopped, and the furnace was cooled to the room temperature under argon gas flow.

The as-synthesized CNT-FLG composite was further purified of the nickel growth catalyst by an acid treatment using HNO_3 (35 vol. %) at 80°C. The as-treated composite was further washed several times with deionized water until neutral pH.

2.4 Deposition of nanodiamonds onto a CNF-FLG composite

The nanodiamonds (NDs) were purchased from the Carbodeon Ltd Oy (Finland) and were used without any further treatment. TEM analysis indicates that the NDs have a regular size and were closely aggregated from each other according to the TEM analysis (Figure

S2.A). High resolution TEM analysis indicates that the NDs diameter is centered at around 6 nm (Figure S2.B).The NDs also possesses a relatively high specific surface area, i.e. 280 m^2/g, which is in good agreement with its nanoscopic dimension.

The NDs were deposited onto the CNF-FLG surface via a wet impregnation method. A suspension of NDs with a concentration of 1 mg/mL was obtained by dispersing NDs in ethanol with the aid of sonication for 30 min at room-temperature. The resulted NDs-decorated CNF-FLG composite was first oven-dried at 110°C for overnight and then heat treated under helium at 550 °C for 2 h in order to desorb moisture. After cooling down, the final products were washed and dried to obtain the purified composite which will be tested in the DH process.

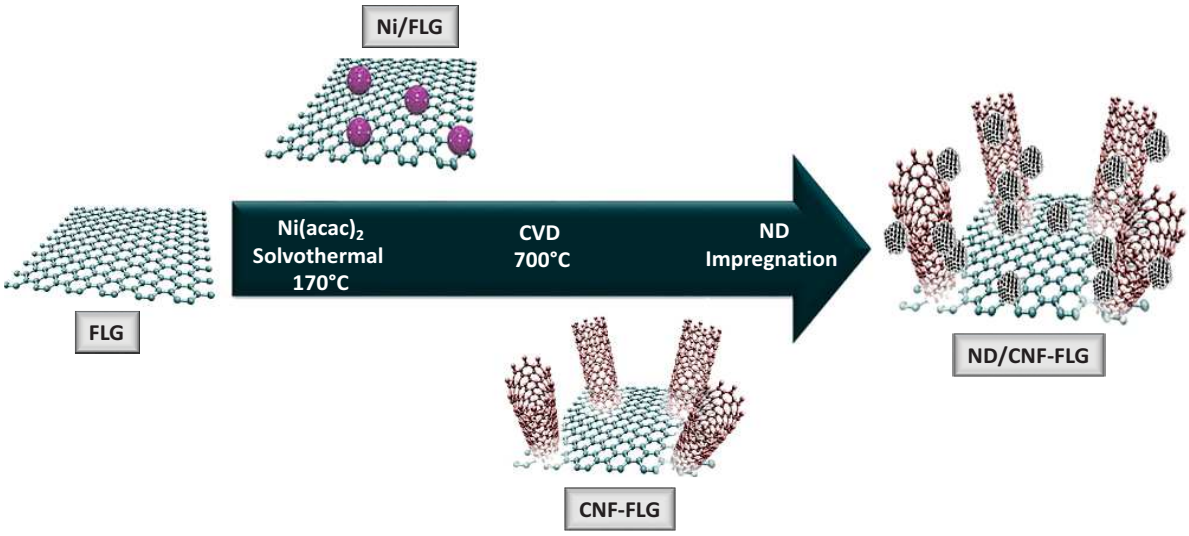

Figure 58. Schematic representation of the synthesis process of the hierarchical ND/FLG-CNF composite.

3. Results and discussion

3.1 FLG supported Ni nanoparticles characteristics

The representative SEM micrographs of the Ni/FLG catalyst after the hydrothermal treatment are presented in Figure S1 in the SI. The SEM analysis indicates that the nickel particles were relatively homogeneous in size, 65 ± 10 nm, and are evenly decorated the FLG surface and edges. The relatively high dispersion of the nickel nanoparticles is attributed to the presence of structural defects on the basal planes and on the edge of the FLG surface which playing the role of anchorage sites for the metal. Similar results have already been

reported elsewhere with platinum supported on FLG.[21] Yuge et al. and Sanz-Navarro et al. have reported that edge sites decorated with carboxyl groups and defects are preferential sites for trapping and stabilizing metallic nanoparticles.[22,23]

3.2 CNF/FLG composite characteristics

The SEM micrographs of the CNF/FLG composite synthesized at 800 °C with different magnification are presented in Figure 59A and B. According to the SEM analysis the FLG surface was completely covered with a dense and homogeneous layer of CNFs (Figure 59A). The magnified SEM micrograph (Figure 59B) indicates that the formed CNFs were relatively homogeneous in diameter centered at around 80 ± 10 nm. Such observation is in good agreement with the size of the growth catalyst as it is a general consensus that the size of the final CNFs is close to the size of the metal growth catalyst.[24] The high covering of the FLG surface by a layer of CNFs was attributed to a multiple growth of CNFs from a single catalytic center, i.e. octopus-like growth mechanism.[25] The relatively homogeneous diameter of the CNFs could also be attributed to the high metal-support interaction between the FLG surface and the nickel nanoparticles which prevent excessive metal sintering during the heating process. Such high interaction has also been reported on the Pt nanoparticles dispersed onto the FLG surface which display an extremely high sintering resistance upon thermal treatment.[21] The introduction of the CNFs onto the FLG surface also leads to a significant increase of the final composite specific surface area compared to the pristine FLG, 162 m^2/g instead of 30 m^2/g. Such a specific surface area increase can be directly attributed to the nanoscopic dimension of the CNFs[25] and also to the role played by the CNFs for preventing the FLG re-stacking upon drying through van der Waals forces.[18] Indeed, the FLGs have a high tendency to re-stack upon drying due to the van der Waals forces attraction which significantly lowers the specific surface area of the final material. The presence of a layer of CNFs on both surface of the FLG will thus acting as a nanospacer to prevent the excessive re-stacking process allowing the maintain of the high and accessible surface area of the final composite and to maintain it pseudo-3D shape for subsequence catalytic use. The increase of the specific surface area also goes along with a significant change of the porosity as depicted in Figure 1.

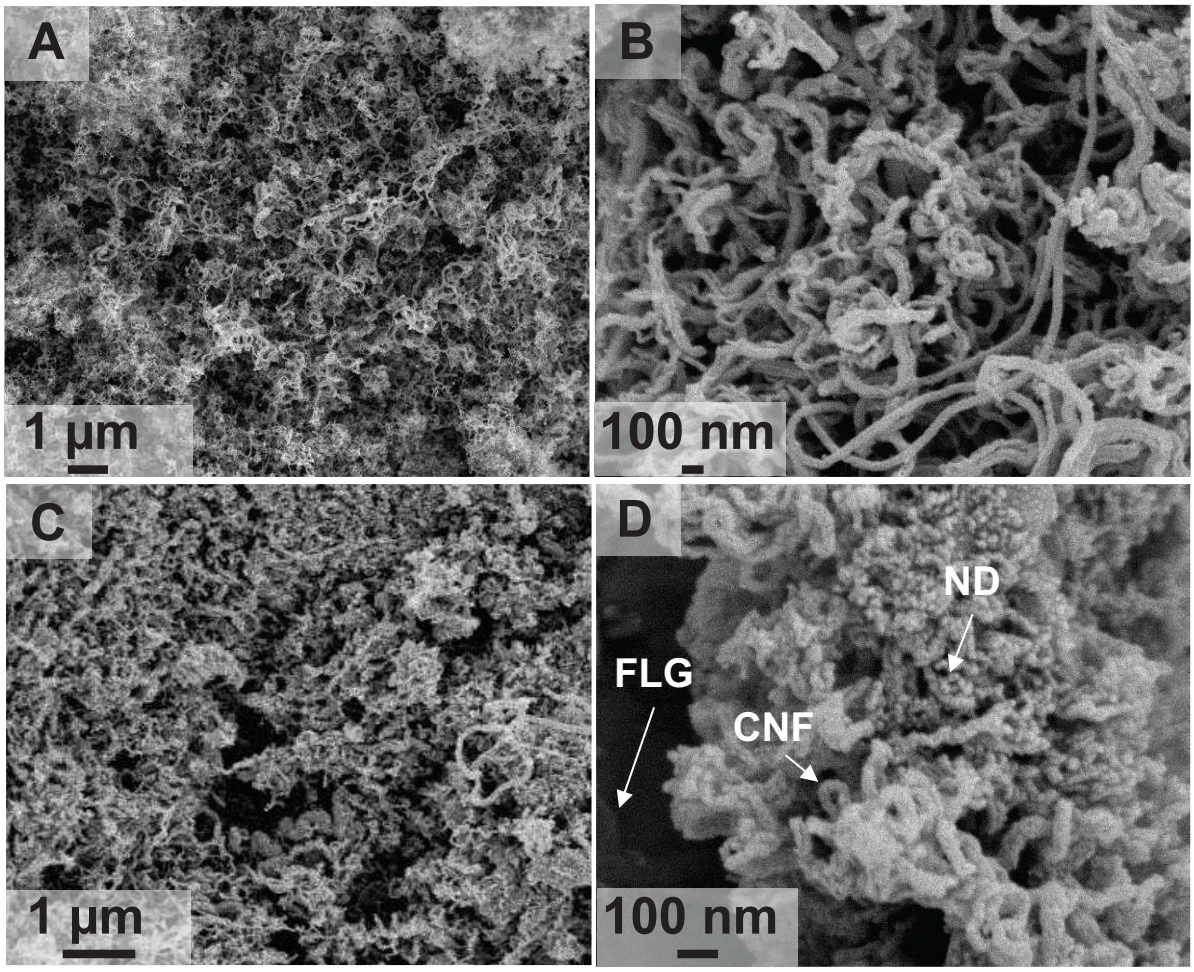

Figure 59. (A, B) SEM micrographs of the densely packed layer of carbon nanofibers decorated the FLG surface synthesized in the presence of a C_2H_6/H_2 mixture at 800 °C. **(C, D)** SEM micrographs of the ND/CNF-FLG catalyst in powders form showing the well distribution of the NDs on the CNF outer surface.

3.3 ND/FLG-CNFs composite

The microstructure of the ND/FLG-CNF composite is investigated by SEM and the representative micrographs are presented in Figure 59C and D. The SEM micrographs allow one to get insight about the localization of the different components inside the composite structure. According to the SEM results the NDs were evenly decorated the surface of the CNFs and NDs agglomerates are no longer observed which indicates the high efficiency of the CNFs structure for dispersing and anchoring ND nanoparticles. The high dispersion of the NDs particles on the CNFs surface was attributed to the high reactivity of the graphite prismatic planes which play a role of anchorage sites.[26]

The microstructure of the CNFs-FLG and ND/CNF-FLG composites was also investigated by TEM and the results are presented in Figure 60. The TEM analysis evidences the high and homogeneous coverage of the FLG surface by a dense layer of CNFs transforming in such a way a 2D structure into a pseudo-3D structure with higher effective surface (Fig. 3A). High magnification TEM micrograph (Fig. 60B) confirms the homogeneous diameter of the as-synthesized CNFs while high-resolution TEM (Inset of Fig. 60B) shows the fish-bone structure of the CNFs which had already been reported by several groups in the field [27,28]. The TEM analysis again confirms the well dispersion of the ND nanoparticles on the surface of the CNF-FLG composite (Fig. 60C). High magnification TEM micrograph (Fig. 3D) evidences the higher decoration of the CNFs by NDs which is due to the high reactivity of the fishbone structure compared to the basal planes of the FLG. High-resolution TEM analysis (Inset of Fig. 60D) evidences the well dispersion of the NDs as single-nanoparticle or small clusters instead of large aggregates in the pristine ND. However, some NDs were also observed on the FLG surface which could be attributed to some anchorage on defect sites present on the FLG basal plane. The microstructure and porosity of the ND/CNF-FLG composite will be further investigated with a TEM tomography mode [29] in order to get more insight about the porous network connectivity and its influence on the catalytic performance.

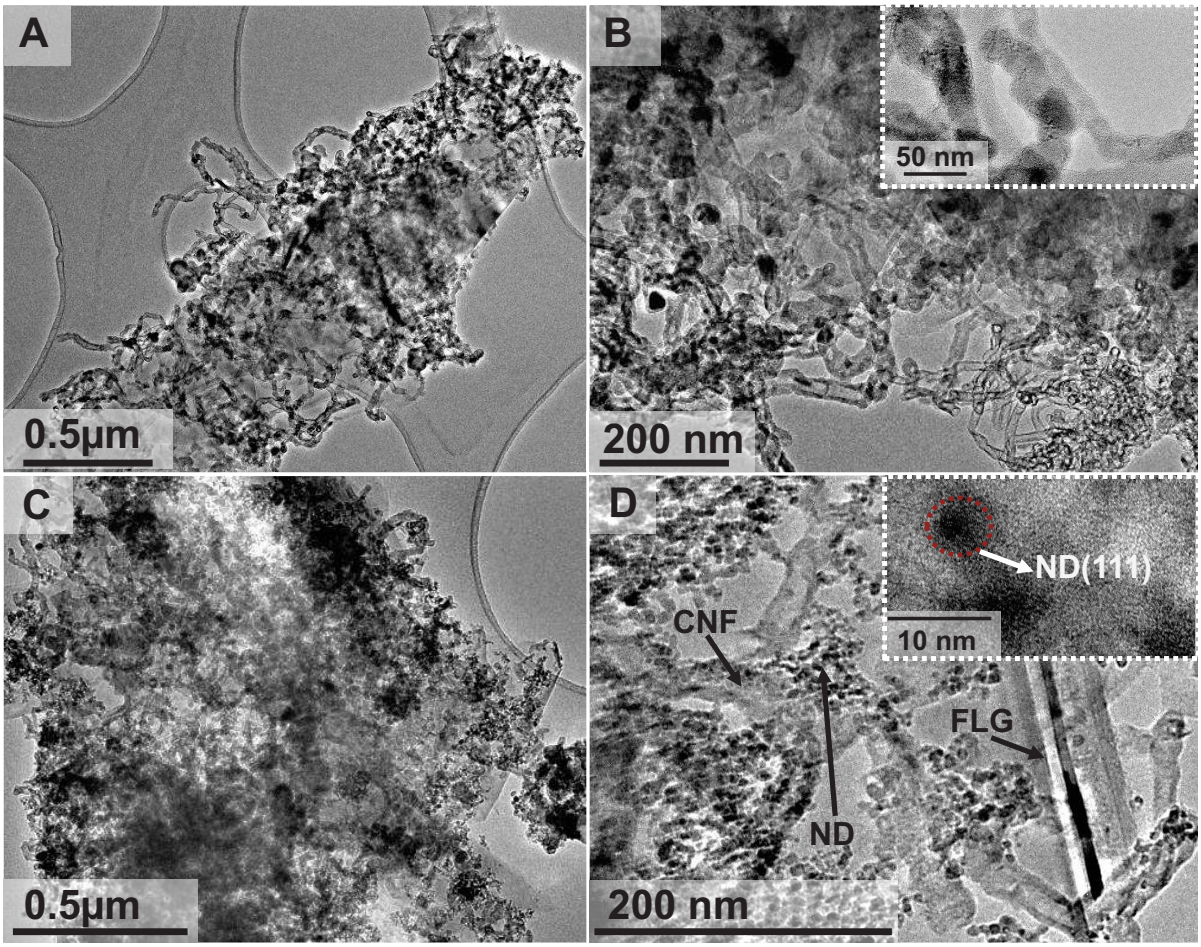

Figure 60. (**A, B**) Representative TEM micrographs showing the microstructure of the CNFs/FLG and the fishbone structure of the CNF (inset of Fig. 4B). (**C, D**) TEM micrographs of the ND/CNF-FLG composite where NDs cluster (few ten of nm) can be clearly observed on the surface of the CNFs and FLG.

The Raman spectrum shows a typical D-band at 1350 cm^{-1} (sp^3 defects) and G-band at 1578 cm^{-1} (tangential vibration of sp^2 carbon atoms)[30,31] for Ni/FLG, those peaks are appeared at 1343 and 1572 cm^{-1} for CNF-FLG and also ND/ CNF-FLG samples (Figure 61A). In order to get more insight about the change which occurs after CNFs growth and after ND deposition a comparison of the intensity ratio of D and G band (I_D/I_G) for all samples was also performed. The I_D/I_G is increased from 0.16 for Ni/FLG to 0.73 for CNFs-FLG composite which indicates that there are more defects and disorder in the carbon-carbon composite compared to the pristine FLG. In addition, the 2D-band, second-order vibration caused by the scattering of phonons at the zone boundary[30] of the CNFs-FLG composite was depressed and blue-shifted (20 cm^{-1}) as compared to that of the N/FLG, while an additional band of (D + G) appears. This could be due to the presence of the fishbone structure of CNFs together with cracks and defects of those hybrid materials. An addition of 16wt % ND particles again induces a decrease of the defects vibration band leading to a decrease of the I_D/I_G ratio from

0.73 to 0.25 along with a broadening of sp^3 defects (D band) since it covered a peak of NDs (~1325 cm^{-1})[31] was observed.

The surface composition of the Ni/FLG, CNFs-FLG and ND/CNFs-FLG composites was analyzed by XPS and the results are presented in Figure 61B. The C1s XPS spectrum clearly indicates four different major components, among which the non-oxygenated ring sp^2 carbon and oxygen-containing functional groups,[32] in the Ni/FLG and CNFs-FLG. After deposition of ND these peaks are noteworthy decreased intensity and an additional sp^3 allotrope of carbon appears centered at 285 eV can be found for the ND/ CNF-FLG composite.

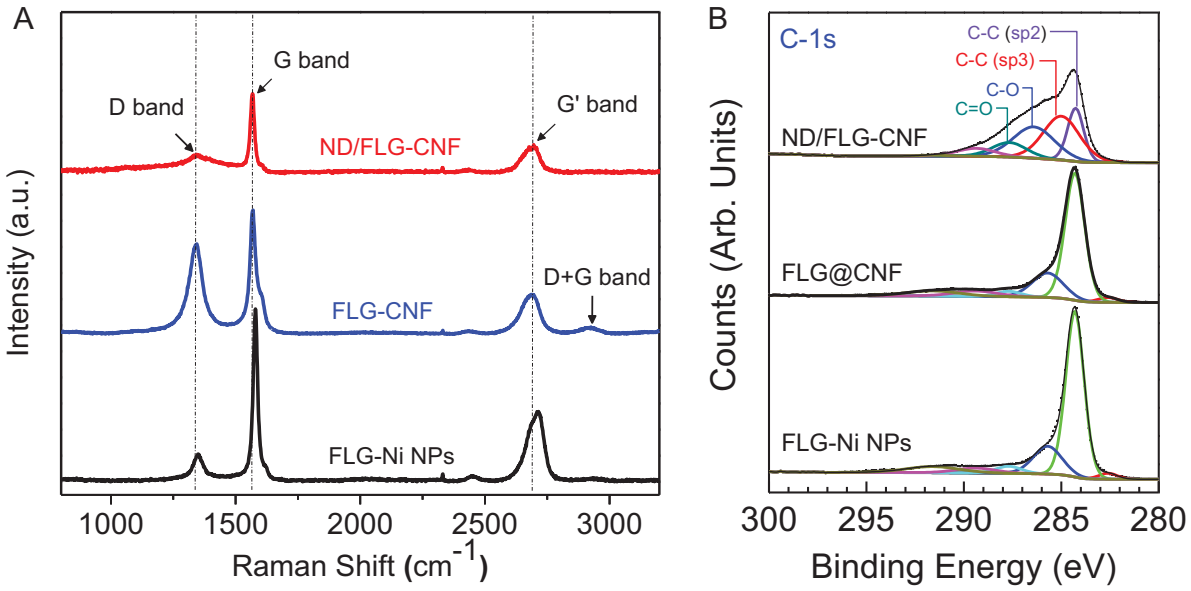

Figure 61. (A) Comparison of Raman spectra recorded on the different materials: Ni/FLG, CNFs-FLG and ND/CNFs-FLG. **(B)** The corresponding XPS spectra associate to the same materials in (**A**).

The specific surface area of the different samples measured by the BET method is presented in Table 5. Among the samples the FLG displays the lowest specific surface area, i.e. 30 m^2/g, which could be attributed to the high tendency of FLG to re-stack upon drying. The ND shows the highest specific surface area, 283 m^2/g, which was attributed to the nanoscopic size of the material with a high density of defects despite the presence of aggregates. The introduction of the CNFs onto the FLG surface significantly increases the overall surface area of the composite from 30 to 163 m^2/g. Such result could be attributed to the high intrinsic surface area of the CNFs thanks to the nanoscopic size and exclusive exposure of prismatic planes.[33] The ND/FLG-CNF composite displays a slightly higher surface area of 209 m^2/g compared to the FLG-CNF sample which could be attributed to the

high intrinsic specific surface area of the NDs and also to a better dispersion of the NDs onto the hierarchical composite. It is worthy to note that the ND/CNF-FLG composite displays a surface area significantly higher than the ND/FLG composite, 132 m^2/g, for the same ND loading. Such results could be attributed to the higher dispersion of the ND nanoparticles on the CNFs super-structure with higher reactivity than the FLG surface.

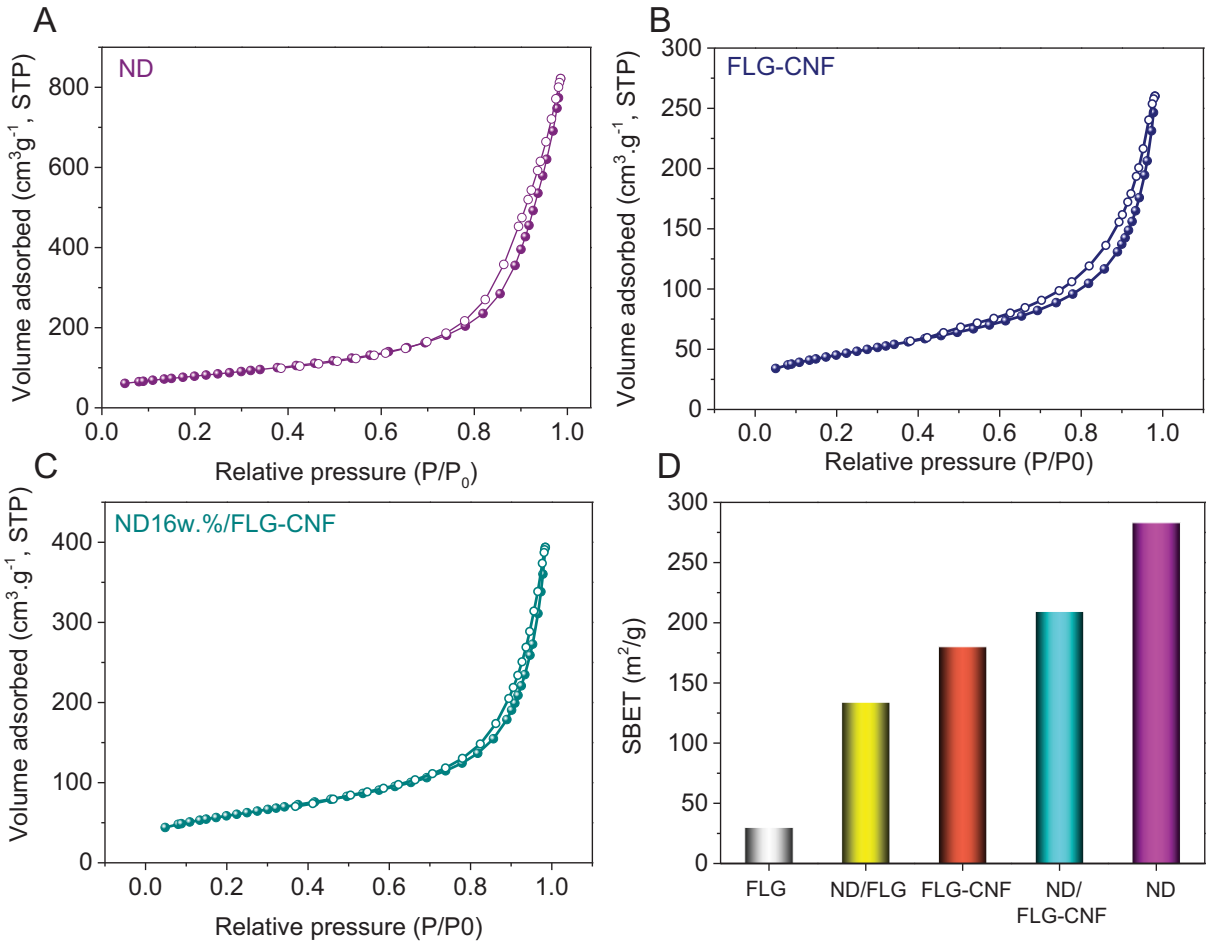

Figure 62. (A-C) N_2 isotherms and pore size distribution of the ND, CNF-FLG and ND/CNF-FLG materials. (B) Specific surface area of the different materials.

Samples	S_{BET} (m^2/g)	V_{total}	D_{BJH}
ND_{Pure}	283	1.27	15.8
FLG	30	0.13	18.5
CNF-FLG	162	0.48	10.4
ND-16 wt %/FLG	134	0.54	14.5
ND-16wt%/ CNF-FLG	209	0.6	11.7

Table 5. Physical characteristics of the different carbon-based composites determined from the BET method.

3.4 Dehydrogenation of ethylbenzene into styrene

The dehydrogenation (DH) activity, expressed in terms of $mmol_{ST}/g_{ND}/h$, and the styrene selectivity obtained on the bulk NDs and the ND-16/CNF-FLG catalysts are presented in Figure 63. For comparison the DH performance obtained on an industrial catalyst consisted of doped bulk iron oxide is also reported in the same figure. According to the results the bulk NDs shows a relatively higher DH activity compared to the industrial iron-based catalyst. The styrene selectivity is also extremely high, i.e. 99 %, on the NDs catalyst compared to that obtained on the industrial catalyst, 96 %. The DH performance of the carbon-based catalyst was further improved by supporting the NDs on the CNF-FLG composite as shown in Figure 63A along with a high selectivity towards the styrene formation. The improvement of the DH performance observed on the supported ND catalyst was attributed to the better dispersion of the NDs particles on the CNFs surface which provide a higher density of active sites for performing the DH reaction. The higher DH activity could also be attributed to the high effective surface of the composite which provide better accessibility of the reactant to the active site. The DH activity on the ND/CNF-FLG is high at the beginning of the reaction followed by a deactivation before reaching a steady-state after 30 h on stream. Such DH activity change could be explained as follow: at the beginning of the reaction a large amount of ST was formed on the catalyst surface which part of it undergo polymerized to form carbonaceous residue which partially block the access of the active site. As the reaction proceeds the number of unblocked active sites becomes lower and thus, the concentration of the ST molecules on the catalyst surface. At such stage of reaction, the DH performance reaches an equilibrium state between the ST formation and desorption rate and thus, the polymerization reaction is expected to be no longer operated leading to a steady-state level.

The DH performance of the different carbon-based catalysts is presented in Fig. 63B and compared with that of the iron-based catalyst. According to the results one can stated that the DH activity obtained on the ND/CNF-FLG is the most highest compared to the other catalysts. Such high DH performance could be attributed to the pseudo-3D structure of the catalyst with higher accessibility and also to the high dispersion of the ND nanoparticles on the CNF surface providing higher active sites density for the reaction.

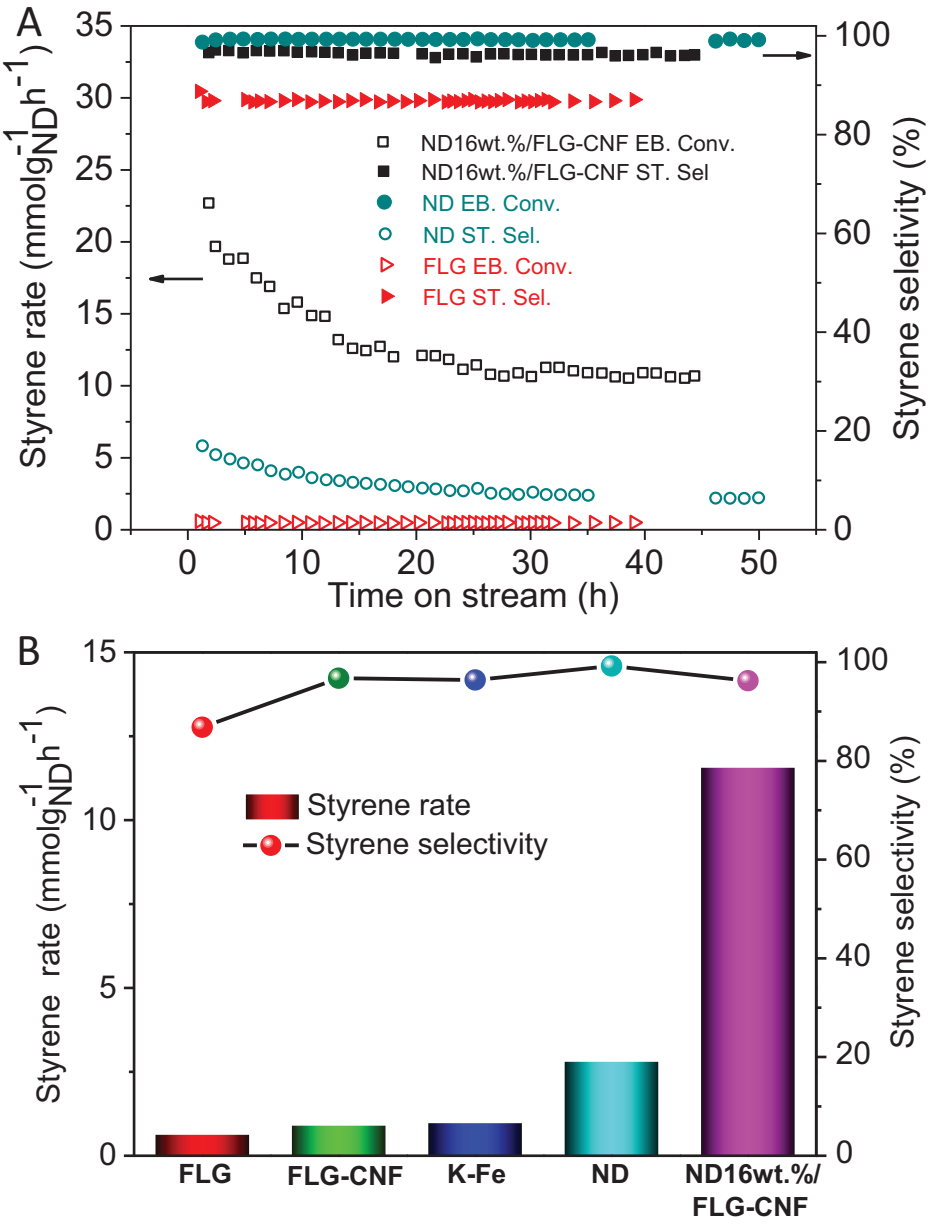

Figure 63. (A) Ethylbenzene (EB) dehydrogenation activity on of the NDs 16wt.%/CNF@FLG and Fe-K/Al_2O_3 industrial catalyst. **(B)** Benchmarking of various catalyst carbon based catalyst and the industrial promoted catalyst under steady-state (Reaction conditions: 300 mg, 550 °C, 2.8 % EB in helium, 30 mL·min^{-1}).

The DH activity of the ND/CNF-FLG catalyst was also evaluated as a function of the reaction temperature, from 550 to 600°C, in order to get more insight about the DH performance and the stability of the catalyst under the reaction conditions close to those used in the industrial process with the bulk iron oxide promoted with potassium (Figure 64). Such a high reaction temperature operating in the industrial process could be motivated by two facts: chemical transformation of the metastable iron-potassium active phase and to produce oxygen from catalytic water splitting for the gasification of the deposited carbon on the catalyst surface [34]. For comparison the DH performance of the ND/FLG is also reported in the same figure. According to the results the DH of both catalysts significantly increases as increasing the reaction temperature. However, the ND/CNF-FLG catalyst exhibits a high DH activity along with a minimum lost in terms of the styrene selectivity compared to the other catalysts. The DH activity of the ND/CNF-FLG catalyst also remains very stable as a function of the test duration regardless the reaction temperature (Fig. 64A) which is not the case for the ND/FLG catalyst where deactivation occurs at different reaction temperature (Fig. 64B). This stability could be attributed to the high effective surface area of the ND/CNF-FLG catalyst allowing a better accessibility of reagents and rapid escaping of the intermediate products which significantly lower the carbonaceous residue deposition on the catalytic sites.

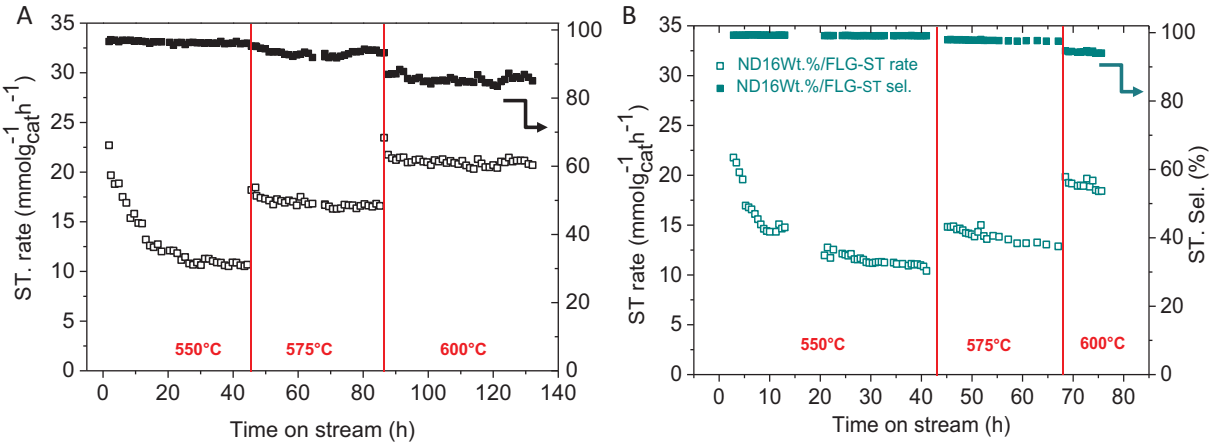

Figure 64. Influence of the reaction temperature on the DH performance of the (A) ND/CNF-FLG and (B) ND/FLG catalysts. Reaction conditions: catalyst weight = 300 mg, T = 550, 575, 600 °C, 2.8 % EB in helium, total flow rate = 30 mL·min^{-1}.

The DH performance as a function of the ethylbenzene concentration was also evaluated on the ND/FLG-CNF catalyst. Increasing the EB concentration in the flow rate leads to a significant increase of the DH activity which could be attributed to the higher adsorption of the EB on the available catalytic sites on the catalyst surface (Figure 65). In that case one should expected that the EB and ND interaction is higher than the ST and ND interaction and thus, as soon as the ST is formed on the ND surface the ST molecule is

steadily replaced by a new EB ones with higher interaction. Such reaction scheme is favored by increasing the reactant concentration in the processing feed. The increase of the EB adsorption on the catalyst surface also reduce the re-adsorption of the intermediate products and thus, significantly improve the selectivity of the styrene which going up from 85 % to 94%. The high desorption rate of the intermediate product, i.e. styrene, also explain the high stability of the catalyst as a function of time on stream by lowering the polymerization rate of this intermediate product which leads to the formation of carbonaceous residue.[35]

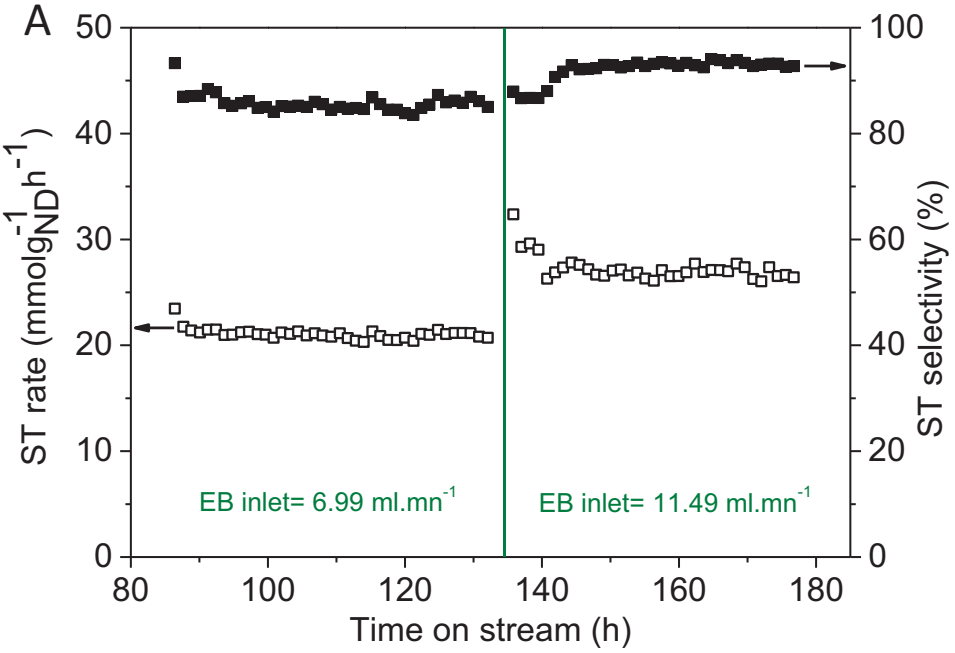

Figure 65. Influence of the ethylbenzene concentration on the DH performance of the ND/CNF-FLG catalyst. Reaction conditions: catalyst weight = 300 mg, 600 °C, EB concentration = 6.99 and 11.49 ml.min^{-1} EB in helium, total flow rate = 30 mL·min^{-1}.

4. Conclusion

In summary, a hierarchical composite with high effective surface area consisted with FLG decorated on both side with a super-structure of CNFs is prepared by a simple CVD process. Such composite displays a high anchorage surface thanks to the reactivity of the fishbone structure of the CNFs for evenly disperse nanodiamonds (ND/CNF-FLG) which significantly increase the active sites density per unit weight of catalyst. The hybrid metal-free composite exhibits a high and stable DH performance of ethylbenzene compared to the other carbon-based and promoted iron industrial catalysts. The stability of the ND/CNF-FLG

composite in the steam-free DH of ethylbenzene to styrene is clearly improved as compared with that ND/FLG catalyst, indicating it promising potential as metal-free catalyst in several catalytic processes. The DH activity per unit weight of the active phase on the ND/CNF-FLG catalyst was about four times higher than the one obtained on the unsupported ones. The improved DH performance, activity, selectivity and stability, is attributed to the 3D structure of the composite which provide high accessibility of the active site to the reactant and also to the easy escaping of the intermediate products reducing the formation of carbonaceous by-products. The DH performance on the ND/CNF-FLG catalyst can be significantly improved by increasing both the reaction temperature and the ethylbenzene concentration. It is expected that this family of metal-free composites will find use in several other catalytic processes where the combination of a high effective surface area and stable active phase are of great interest. The high effective surface area and the mechanical stability of the CNF-FLG support could also represent a net advantage for this system to be used as catalyst support in liquid-phase process where diffusion problem is generally encountered.

Acknowledgements

The present project is part of the FREECATS project financed by the European Union within the 7FP research program through a contract number NMP3-SL-2012-280658 would like to acknowledge the EU for financial support during they stay at the ICPEES. The authors would like to acknowledge T. Romero (ICPEES) for performing SEM analysis. The TEM experiments were carried out at the facilities of the IPCMS (UMR 7504 of the CNRS).

References

(1) Muhler, M.; Schütze, J.; Wesemann, M.; Rayment, T.; Dent, A.; Schlögl, R.; Ertl, G. The Nature of the Iron Oxide-Based Catalyst for Dehydrogenation of Ethylbenzene to Styrene: I. Solid-State Chemistry and Bulk Characterization. *J. Catal.* **1990**, *126*, 339–360.

(2) Liao, S.-J.; Chen, T.; Miao, C.-X.; Yang, W.-M.; Xie, Z.-K.; Chen, Q.-L. Effect of TiO2 on the Structure and Catalytic Behavior of Iron–potassium Oxide Catalyst for Dehydrogenation of Ethylbenzene to Styrene. *Catal. Commun.* **2008**, *9*, 1817–1821.

(3) Addiego, W. P.; Liu, W.; Boger, T. Iron Oxide-Based Honeycomb Catalysts for the Dehydrogenation of Ethylbenzene to Styrene. *Catal. Today* **2001**, *69*, 25–31.

(4) Abdalla, B. K.; Elnashaie, S. S. E. H.; Alkhowaiter, S.; Elshishini, S. S. Intrinsic Kinetics and Industrial Reactors Modelling for the Dehydrogenation of Ethylbenzene to Styrene on Promoted Iron Oxide Catalysts. *Appl. Catal. Gen.* **1994**, *113*, 89–102.

(5) Atanda, L. A.; Balasamy, R. J.; Khurshid, A.; Al-Ali, A. A. S.; Sagata, K.; Asamoto, M.; Yahiro, H.; Nomura, K.; Sano, T.; Takehira, K.; *et al.* Ethylbenzene Dehydrogenation over Mg3Fe0.5−xCoxAl0.5 Catalysts Derived from Hydrotalcites: Comparison with Mg3Fe0.5−yNiyAl0.5 Catalysts. *Appl. Catal. Gen.* **2011**, *396*, 107–115.

(6) Zhang, J.; Su, D. S.; Blume, R.; Schlögl, R.; Wang, R.; Yang, X.; Gajović, A. Surface Chemistry and Catalytic Reactivity of a Nanodiamond in the Steam-Free Dehydrogenation of Ethylbenzene. *Angew. Chem. Int. Ed.* **2010**, *49*, 8640–8644.

(7) Liu, Y.; Nguyen, L. D.; Truong-Huu, T.; Liu, Y.; Romero, T.; Janowska, I.; Begin, D.; Pham-Huu, C. Macroscopic Shaping of Carbon Nanotubes with High Specific Surface Area and Full Accessibility. *Mater. Lett.* **2012**, *79*, 128–131.

(8) De Cremer, G.; Bartholomeeusen, E.; Pescarmona, P. P.; Lin, K.; De Vos, D. E.; Hofkens, J.; Roeffaers, M. B. J.; Sels, B. F. The Influence of Diffusion Phenomena on Catalysis: A Study at the Single Particle Level Using Fluorescence Microscopy. *Catal. Today* **2010**, *157*, 236–242.

(9) Devred, F.; Dulgheru, P.; Kruse, N. 7.02 - Elementary Steps in Heterogeneous Catalysis. In *Comprehensive Inorganic Chemistry II (Second Edition)*; Poeppelmeier, J. R., Ed.; Elsevier: Amsterdam, 2013; pp. 7–38.

(10) Thanh, T. T.; Ba, H.; Truong-Phuoc, L.; Nhut, J.-M.; Ersen, O.; Begin, D.; Janowska, I.; Nguyen, D. L.; Granger, P.; Pham-Huu, C. A Few-Layer Graphene–graphene Oxide Composite Containing Nanodiamonds as Metal-Free Catalysts. *J. Mater. Chem. A* **2014**, *2*, 11349–11357.

(11) Ba, H.; Podila, S.; Liu, Y.; Mu, X.; Nhut, J.-M.; Papaefthimiou, V.; Zafeiratos, S.; Granger, P.; Pham-Huu, C. Nanodiamond Decorated Few-Layer Graphene Composite as an Efficient Metal-Free Dehydrogenation Catalyst for Styrene Production. *Catal. Today*.

(12) Omidvar, A.; Anafcheh, M.; Hadipour, N. L. Computational Studies on Carbon Nanotube–graphene Nanoribbon Hybrids by Density Functional Theory Calculations. *Sci. Iran.* **2013**, *20*, 1014–1017.

(13) Nguyen, D. D.; Tai, N.-H.; Chen, S.-Y.; Chueh, Y.-L. Controlled Growth of Carbon Nanotube–graphene Hybrid Materials for Flexible and Transparent Conductors and Electron Field Emitters. *Nanoscale* **2012**, *4*, 632–638.

(14) Chen, S.; Bao, P.; Wang, G. Synthesis of Fe2O3–CNT–graphene Hybrid Materials with an Open Three-Dimensional Nanostructure for High Capacity Lithium Storage. *Nano Energy* **2013**, *2*, 425–434.
(15) Patole, A. S.; Patole, S. P.; Jung, S.-Y.; Yoo, J.-B.; An, J.-H.; Kim, T.-H. Self Assembled Graphene/carbon Nanotube/polystyrene Hybrid Nanocomposite by in Situ Microemulsion Polymerization. *Eur. Polym. J.* **2012**, *48*, 252–259.
(16) Du, H.-Y.; Wang, C.-H.; Hsu, H.-C.; Chang, S.-T.; Huang, H.-C.; Chen, L.-C.; Chen, K.-H. Graphene nanosheet–CNT Hybrid Nanostructure Electrode for a Proton Exchange Membrane Fuel Cell. *Int. J. Hydrog. Energy* **2012**, *37*, 18989–18995.
(17) Yankowitz, M.; Wang, J. I.-J.; Birdwell, A. G.; Chen, Y.-A.; Watanabe, K.; Taniguchi, T.; Jacquod, P.; San-Jose, P.; Jarillo-Herrero, P.; LeRoy, B. J. Electric Field Control of Soliton Motion and Stacking in Trilayer Graphene. *Nat. Mater.* **2014**, *13*, 786–789.
(18) Lui, C. H.; Li, Z.; Chen, Z.; Klimov, P. V.; Brus, L. E.; Heinz, T. F. Imaging Stacking Order in Few-Layer Graphene. *Nano Lett.* **2011**, *11*, 164–169.
(19) Janowska, I.; Vigneron, F.; Bégin, D.; Ersen, O.; Bernhardt, P.; Romero, T.; Ledoux, M. J.; Pham-Huu, C. Mechanical Thinning to Make Few-Layer Graphene from Pencil Lead. *Carbon* **2012**, *50*, 3106–3110.
(20) Pham-Huu, C.; Keller, N.; Roddatis, V. V.; Mestl, G.; Schlögl, R.; Ledoux, M. J. Large Scale Synthesis of Carbon Nanofibers by Catalytic Decomposition of Ethane on Nickel Nanoclusters Decorating Carbon Nanotubes. *Phys. Chem. Chem. Phys.* **2002**, *4*, 514–521.
(21) Moldovan, M. S.; Bulou, H.; Dappe, Y. J.; Janowska, I.; Bégin, D.; Pham-Huu, C.; Ersen, O. On the Evolution of Pt Nanoparticles on Few-Layer Graphene Supports in the High-Temperature Range. *J. Phys. Chem. C* **2012**, *116*, 9274–9282.
(22) Yuge, R.; Zhang, M.; Tomonari, M.; Yoshitake, T.; Iijima, S.; Yudasaka, M. Site Identification of Carboxyl Groups on Graphene Edges with Pt Derivatives. *ACS Nano* **2008**, *2*, 1865–1870.
(23) Sanz-Navarro, C. F.; Åstrand, P.-O.; Chen, D.; Rønning, M.; van Duin, A. C. T.; Jacob, T.; Goddard, W. A. Molecular Dynamics Simulations of the Interactions between Platinum Clusters and Carbon Platelets. *J. Phys. Chem. A* **2008**, *112*, 1392–1402.
(24) Rainer, D. R.; Goodman, D. W. Metal Clusters on Ultrathin Oxide Films: Model Catalysts for Surface Science Studies. *J. Mol. Catal. Chem.* **1998**, *131*, 259–283.
(25) Louis, B.; Vieira, R.; Carvalho, A.; Amadou, J.; Ledoux, M. J.; Pham-Huu, C. Carbon Nanofibers Grown over Graphite Supported Ni Catalyst: Relationship between Octopus-like Growth Mechanism and Macro-Shaping. *Top. Catal.* **2007**, *45*, 75–80.
(26) Ledoux, M.-J.; Pham-Huu, C. Carbon Nanostructures with Macroscopic Shaping for Catalytic Applications. *Catal. Today* **2005**, *102–103*, 2–14.
(27) Ledoux, M. J.; Vieira, R.; Pham-Huu, C.; Keller, N. New Catalytic Phenomena on Nanostructured (fibers and Tubes) Catalysts. *J. Catal.* **2003**, *216*, 333–342.
(28) Jong, K. P. de; Geus, J. W. Carbon Nanofibers: Catalytic Synthesis and Applications. *Catal. Rev. - Sci. Eng.* **2001**, *42*, 481–510.
(29) Ersen, O.; Hirlimann, C.; Drillon, M.; Werckmann, J.; Tihay, F.; Pham-Huu, C.; Crucifix, C.; Schultz, P. 3D-TEM Characterization of Nanometric Objects. *Solid State Sci.* **2007**, *9*, 1088–1098.
(30) Kuzmany, H. Chapter 6 - Phonon Structures and Raman Effect of Carbon Nanotubes and Graphene. In *Carbon Nanotubes and Graphene (Second Edition)*; Iijima, K. T., Ed.; Elsevier: Oxford, 2014; pp. 99–149.
(31) Elomaa, O.; Singh, V. K.; Iyer, A.; Hakala, T. J.; Koskinen, J. Graphene Oxide in Water Lubrication on Diamond-like Carbon vs. Stainless Steel High-Load Contacts. *Diam. Relat. Mater.* **2015**, *52*, 43–48.

(32) Zhou, J.-H.; Sui, Z.-J.; Zhu, J.; Li, P.; Chen, D.; Dai, Y.-C.; Yuan, W.-K. Characterization of Surface Oxygen Complexes on Carbon Nanofibers by TPD, XPS and FT-IR. *Carbon* **2007**, *45*, 785–796.
(33) Vieira, R.; Pham-Huu, C.; Keller, N.; Ledoux, M. J. New Carbon Nanofiber/graphite Felt Composite for Use as a Catalyst Support for Hydrazine Catalytic Decomposition. *Chem. Commun.* **2002**, 954–955.
(34) Schlögl, R. Heterogeneous Catalysis. *Angew. Chem. Int. Ed.* **2015**, *54*, 3465–3520.
(35) Emig, G.; Hofmann, H. Action of Zirconium Phosphate as a Catalyst for the Oxydehydrogenation of Ethylbenzene to Styrene. *J. Catal.* **1983**, *84*, 15–26.

Supporting Information

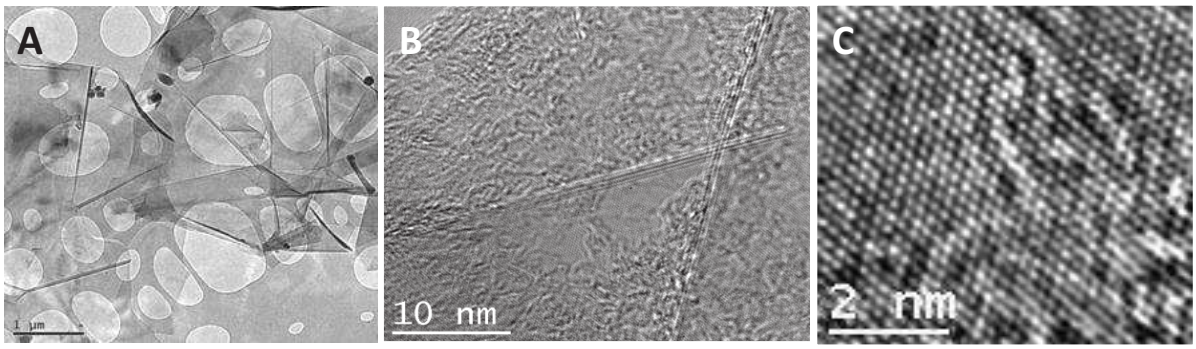

Figure S1. TEM micrographs with different magnifications of the FLG synthesized by a mechanical ablation method.

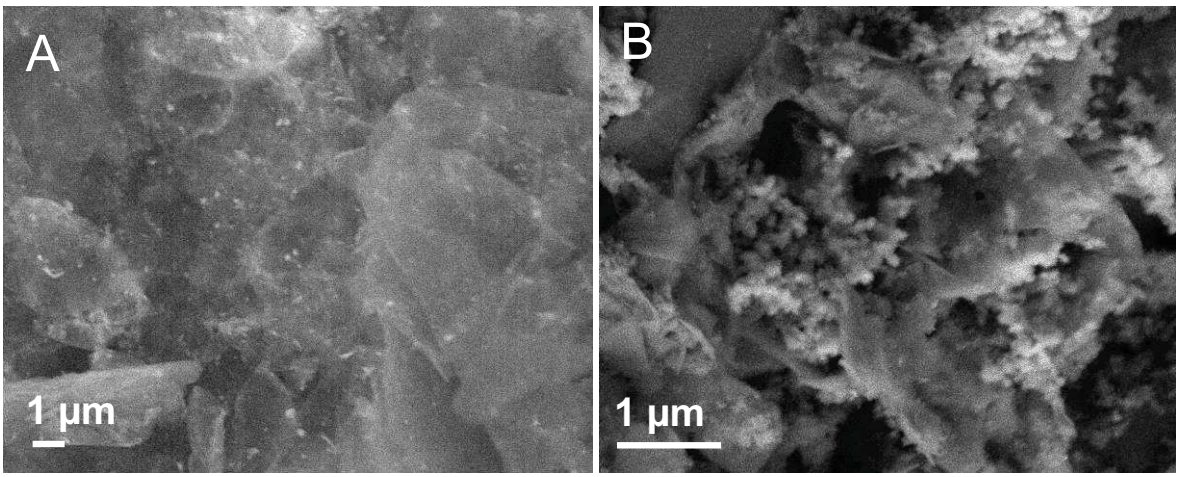

Figure S2. SEM micrograph of Ni NPs (white dots) are decorated homogeneity on the surface of FLG.

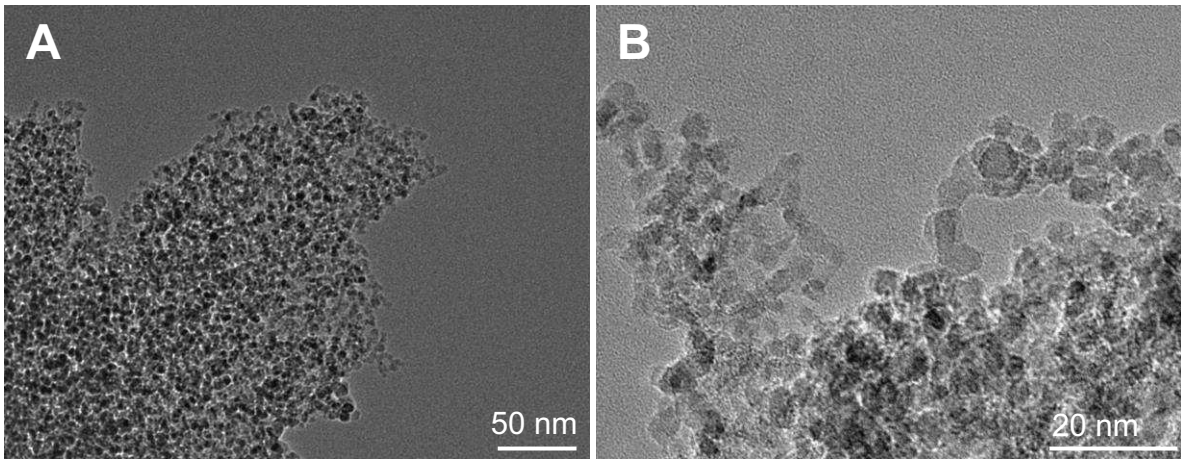

Figure S3. TEM micrographs of the as received NDs. (**A**) Low magnification TEM micrograph showing an agglomerate of NDs. (**B**) High resolution TEM micrograph of the NDs particles.

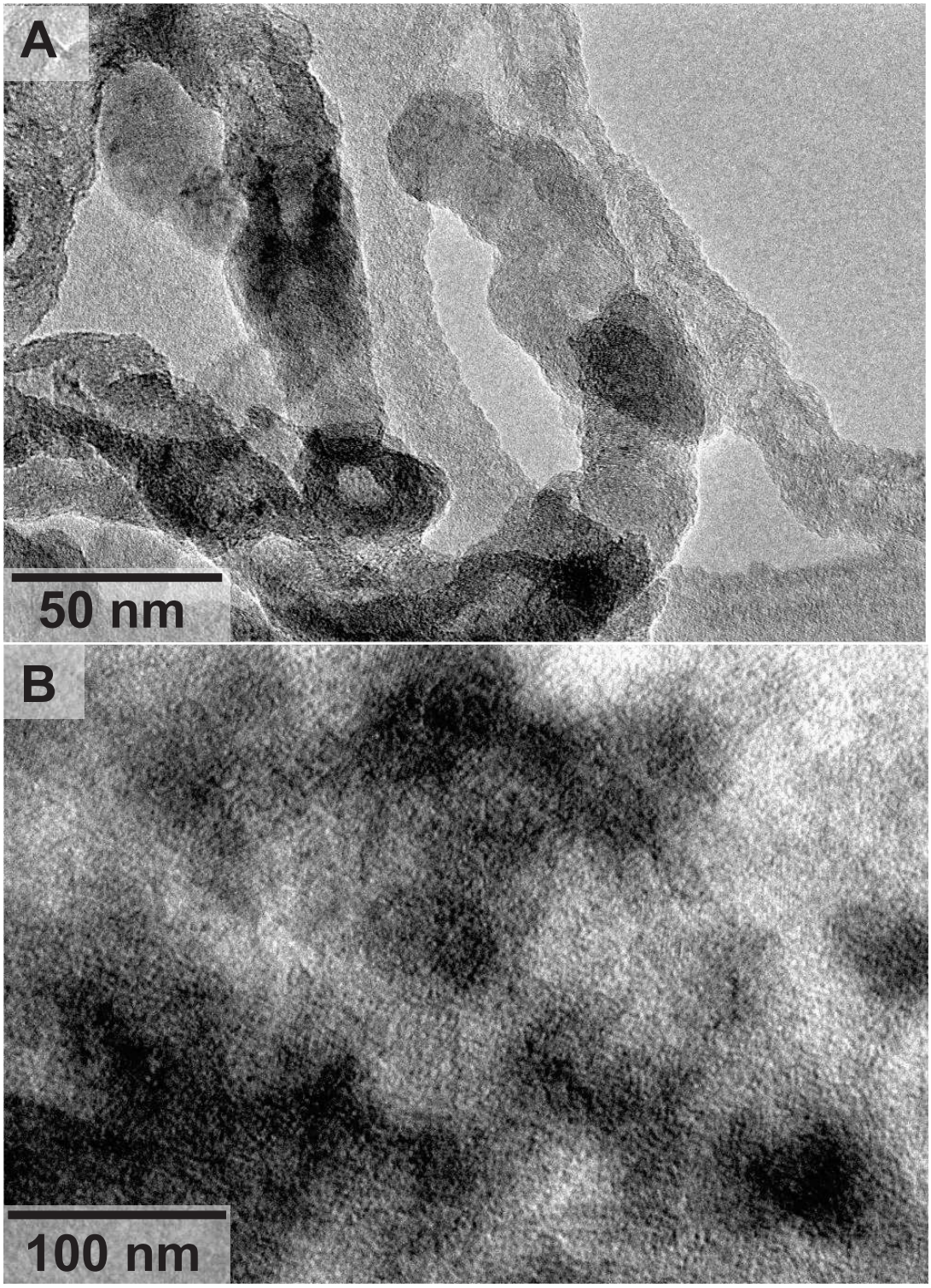

Figure S4. High resolution TEM picture (A) Carbon nanofibers evidencing the carbone prismatic planes and (B) aged nanodiamond particles.

CHAPTER 5

Carbon-based-materials supported on 3D host structure as a metal-free for catalyst for styrene production

Nanodiamonds/β-SiC Composite as an Efficient Metal-Free Catalyst for the Steam-Free Dehydrogenation of Ethylbenzene to Styrene

Housseinou Ba,[a,b] Yuefeng Liu,[a,*] Xiaoke Mu,[a] Won-Hui Doh,[a] Jean-Mario Nhut,[a] Pascal Granger,[b] Cuong Pham-Huu [a,*]

[a] *Institut de Chimie et Procédés pour l'Energie, l'Environnement et la Santé (ICPEES), UMR 7515 CNRS- Université de Strasbourg (UdS), 25, rue Becquerel, 67087 Strasbourg Cedex 08, France*

[b] *Unité de Catalyse et Chimie du Solide (UCCS), UMR 8181 CNRS-Université de Lille, 59655 - Villeneuve d'Ascq Cedex France*

Article published in Applied Catalysis DOI: 10.1016/j.apcata.2015.04.022

Graphical abstract

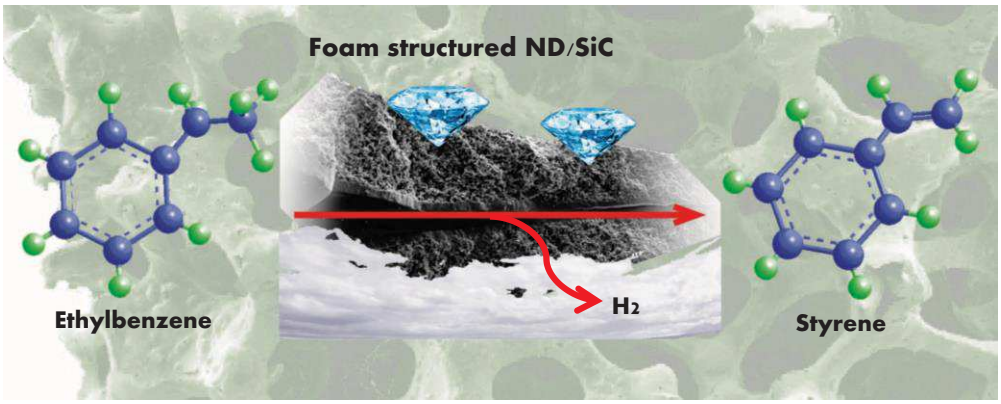

Abstract

Nanodiamonds (NDs), a typical sp^3-like carbon, have the average size less than 10 nm with a large surface-to-volume ratio, which contribute to a high surface activity than other types of carbon. However, the powder form of the material renders difficult its use in large-scale applications, especially in the field of heterogeneous catalysis where high pressure drop across the catalytic bed and difficulty of handling powder are the main drawbacks. In this work, a new hybrid structure consisting of nanodiamond decorated porous β-SiC foam matrix has been investigated as a metal-free catalyst in the steam-free dehydrogenation of ethylbenzene into styrene. The hybrid foam catalyst displays an excellent catalytic specific rate and stability in the direct catalytic dehydrogenation of ethylbenzene (EB) to styrene. The dehydrogenation activity (12.87 $mmol_{ST}g_{ND}^{-1}h^{-1}$, moles styrene products per gram of nanodiamonds per hour) is about 10 times higher with respect to the commercial K-Fe-based catalyst and 3.8 times higher than that of powder-form NDs without losing styrene selectivity (S_{ST} = 98%), and thus, demonstrates the high catalytic efficiency of this metal-free catalyst for the studied reaction. This study shows a new development towards the practical use of such structured composite catalyst in the field of catalysis where high performance and stable catalyst is still under scrutiny.

Keywords:

Foam-structured materials, Pressure drop, Nanodiamonds, Silicon Carbide, Metal-free catalyst, Elthybenzene dehydrogenation

1. Introduction

Styrene monomer is a basic raw material for the production of polymeric materials such as polystyrene, acrylonitrile-butadiene-styrene (ABS) resins and a variety of miscellaneous polymers. Catalytic dehydrogenation of ethylbenzene (EB) to styrene (ST), which accounts for 90 % styrene production, is one of the most important reaction processes up to date in the chemistry industry.[1,2] The most used catalysts in commercialized process of EB dehydrogenation is K-Fe-based catalyst with high iron loading.[3-5] However, the carbonaceous species deposit on the active sites of the K-Fe catalysts during the course of the reaction induces drastic deactivation of the catalysts in a direct steam-free EB dehydrogenation process.[6] Thus, a high amount of steam is added to the reactant mixture in order to prevent coke formation through the combustion process with carbon. Steam also help in the maintaining of the reaction temperature within the catalyst bed due to the endothermic character of the reaction. In such process a large energy input has been used to produce steam which significantly increases the carbon footprint of the process along with the extra cost linked with the post-reaction treatment of the wastewater. It is therefore of interest to develop new materials with higher resistance towards carbon fouling and high catalytic activity as well for operating in a steam-free reaction medium. The catalyst should also be relatively cheap to compete with the iron-based catalyst used nowadays. Recent reports have suggested that nanodiamond (ND), which is synthesized by a high temperature and pressure detonation method,[7,8] is a promising steam-free dehydrogenation catalyst, which could replace the traditional supported metal oxide catalysts.[6,9] Typical ND possesses the particles size around 4 - 10 nm, showing polyhedral structure with almost 20% of the total atom number (NDs particles size less 5 nm for example) are exposed on the surface.[10] Thanks to the large number of surface defects and the large surface-to-volume ratio, the ND presents a very high active surface comparing with that of other nanocarbon materials.[6] Unfortunately, the powder form of ND renders it difficult to be used in a fixed-bed reactor, due to the high pressure drop across the catalyst bed, and also for safety of handling. Thus, it is necessary to support the ND on a macroscopic support to generate macroscopic shape catalyst with easy handling and provide low pressure drop for catalytic applications.

The macroscopic shape of the support could also favor the escaping of the intermediate products and thus, contribute to the maintaining of the overall activity of the catalyst by lowering secondary reactions leading to coke formation. The silicon carbide (SiC) displaying most of the physical properties required for being used as a catalyst support, such as macropores with medium specific surface area, high mechanical strength and thermal conductivity, high oxidative resistance, and chemical inertness,[11-13] has been reported as an efficient support for various catalytic reactions during the last deacdes.[14-25] The foam-structured β-SiC with opened-structure, high mechanical stability and good intrinsic thermal

conductivity[26-28] could be expected as ideal support for nanodiamonds typical in the dehydrogenation process. Solid foam has long been studied by the group of Schouten[29-31] in several gas-liquid reactions and showed enhanced catalytic performance thanks to the peculiar physical properties of the foam. Indeed, foam displays a relatively high radial mixing degree due to the presence of struts along the foam matrix which favor the rapid homogeneization of the reactant flow. In such endothermic reaction the high thermal conductivity of the support could also be beneficial for maintaining a homogeneous temperature within the catalyst bed. Recently, Liu et al. developed a two-step method to support NDs onto the carbon nanotubes (CNTs) network decorated a SiC macroscopic host structure.[23] The SiC macroscopic host structure which was synthesized by a slurry coating method of such SiC displays a relatively low specific surface area and thus, cannot be directly used as a macroscopic support for NDs dispersion and thus, CNTs with high effective surface area is necessary to disperse the NDs on the composite. In our previously work,[32] hybrid materials with NDs uniformly dispersed on the graphene oxide/few layer graphene (FLG-GO) are prepared for use as metal-free catalyst in the steam-free dehydrogenation of EB to styrene. In this system the GO plays a role of support to incorporate ND particles through static attractive forces. However, the simple, low cost one-step synthesis of a macroscopic NDs/support composite has not been reported yet. Herein, we demonstrate a facile one-step synthesis method to support the nanosized ND on macroscopic β-SiC foam (ND/β-SiC foam) and its subsequent use as structured catalyst in the steam-free direct dehydrogenation of ethylbenzene to styrene. It is expected that the combination of the high voidage and good mixing foam and the nanoscopic dimension of NDs, with a high intrinsic surface area, in a single structured catalyst will lead to a high performance catalytic system with easy handling and processing. In addition, both nanodiamonds and SiC can be prepared in a large scale which could significantly reduce the time to market of the process. The catalytic activity is compared with that obtained on unsupported powder ND and alumina containing iron catalyst promoted with potassium (90 wt % of iron). The stability of the catalyst is also studied with a long-term catalytic evaluation.

2. Experimental Section

2.1 Metal-free catalysts preparation

Silicon carbide (β-SiC) with different shapes was synthesized via gas-solid reaction between the SiO vapor and dispersed solid carbon.[15,33] Typically, the foam structure β-SiC was synthesized by using polyruethane foam (PU foam) as template, in which all the

geometry of the foam could be finely tuned by modifying the characteristics of the PU foam template. The PU foam was infiltrated with a mixture of phenolic resin containing micrometric Si and carbon black at room temperature. After drying, the obtained solid containing the resin, Si and carbon black was heated up in flowing argon from room temperature to the carburization temperature of 1350ºC. During the heating from room-temperature to 700°C the resin underwent carbonization leaving behind a solid carbon skeleton containing oxygenated groups. At the carburization temperature, the oxygen issued from the resin reacted with Si to generate SiO vapor which further reacted with the carbon structure to form the SiC. The synthesis method allowed the complete conservation of the foam structure when passing from PU to carbon and finally SiC. The obtained SiC material was further calcinated in air at 800ºC for 2 h in order to burn off the residual un-reacted carbon material.

The commercial NDs in a powder form with diameter in the range of 4 - 8 nm were supplied by the Hightech Co (Finland) and were used without any further treatment. The suspension of NDs in ethanol was prepared by using sonication process at room-temperature for 2 h. The formed dispersed NDs was deposited on the porous SiC surface through pore volume impregnation process, and then oven dried at 80ºC for 12 h until the complete evaporation of solvent leading to the formation of the ND/SiC composite. The as-synthesized catalyst was further annealed in argon flow at 550°C for 2 h before it evaluation in the direct steam-free dehydrogenation process. The amount of the deposited NDs can be adjusted by performing additional impregnation step followed by a thermal treatment.

2.2 Characterization techniques

Pressure drop was measured on sample bed with various gas velocity in the 0 - 5 m/s range with differential pressure sensor (Keller Druckmesstechnik PD-41 (0 - 200 mbar)). Gas velocity is measured with anemometer Testo 435-1 equipped with a hot wire probe (0 - 20 m/s).

Thermal gravimetry analysis (TGA) was performed on a Setaram apparatus with an air flow rate of 25 $mL \cdot min^{-1}$ and a heating rate of 10 $^{o}C \cdot min^{-1}$ from room temperature to 1000ºC.

The specific surface area of the different samples was measured by the BET method using N_2 as adsorbent at liquid nitrogen temperature (TriStar sorptometer). Before measurement, the samples were outgassed at 250 ºC overnight in order to desorb moisture and impurities on their surface.

The XPS measurements of the support were performed on a MULTILAB 2000 (THERMO VG) spectrometer equipped with Al Kα anode (hν = 1486.6 eV) with 10 min of acquisition. Peak deconvolution has been made with “Avantage” program from

Thermoelectron Company. The C1s peak at 284.6 eV was used to correct charging effects. Shirley backgrounds were substracted from the raw data to obtain the areas of the C1s peak.

The gross morphology of the materials were observed by scanning electron microscopy (SEM) on a JEOL F-6700 FEG with a lattice resolution 1 nm, at accelerating voltage 10 kV. The sample was covered by a thin layer of gold in order to decrease the problem of charge during the analysis.

Transmission electron microscopy (TEM) observations were conducted on a JEOL 2100F microscope working at 200 kV accelerated voltage with a point-to-point resolution of 0.17 nm. The sample was sonicated in an ethanol solution and a drop was deposited onto a copper grid covered with a holey carbon membrane for observation.

Temperature programmed oxidation was determined in a Micromeritics ASAP-2100 setup equipped with a multi-channel mass spectrometer. The typical sample with 5 mg was loaded in the reactor and then flushed with 1% O_2/He mixture (25 ml/min) at room temperature (RT) for 30 min. The temperature was raised from RT to 900 ^oC at a heating rate of 10^oC/min. The evolved species were monitored with m/e intensities for 2(H_2), 18 (H_2O), 28 (CO) and 44 (CO_2), respectively.

2.3 Catalytic activity measurements

The steam-free ethylbenzene dehydrogenation reaction was carried out in a fixed-bed continuous flow reactor under atmospheric pressure. The catalyst (300 mg) is loaded onto a quartz fritted disk located inside a tubular quartz reactor (id: 8 x 800 mm). Helium gas was fed into the reactor at a flow rate of 30 mL·min^{-1} through a mass flow controller (BROOKS MFC) and passed through a glass evaporator filled with liquid EB maintained at 40 ^oC (EB partial pressure of 2922 Pa) using an automatic thermal regulated bath.

The reaction system was heated to 550^oC and kept for 2h under the He. The reactant flow (2.8 vol. % EB diluted in helium, total flow rate of 30 mL·min^{-1}) was then fed to the reactor. The reactant and the products (styrene (ST), benzene (BZ) and toluene (TOL) exit from the reactor was analyzed on-line with a PERICHROM (PR 2100) gas chromatography equipped with a flame ionization detector (FID) and CP WAX S2CB column which was previously calibrated. In order to avoid any possible condensation of the reactant or the products all the tube lines were wrapped with a heating wire maintaining at 110°C.

The ethylbenzene conversion (X_{EB}) and styrene selectivity (S_{ST}) were evaluated using equations: (1) and (2):

$$X_{EB} = \frac{F_0 C_{EB,inlet} - F C_{EB,outlet}}{F_0 C_{EB,inlet}} \times 100\% \quad (1)$$

$$S_{ST} = \frac{C_{ST,outlet}}{C_{ST,outlet} + C_{TOL,outlet} + C_{BZ,outlet}} \times 100\% \quad (2)$$

where F and F_0 are the flow rates of the outlet and inlet, respectively, and C_{EB}, C_{ST}, C_{TOL} and C_{BZ} represent the concentration of ethylbenzene, styrene, toluene and benzene. The specific styrene yield is expressed as amount of styrene produced per gram of active compounds per hours ($mmol_{ST}g_{AC}^{-1}h^{-1}$). The carbon balances amounted to ≥ 96 % in all investigations. The results are obtained after more than 20 h on stream with stable catalytic performance under testing conditions.

3. Results and discussion

The β-SiC foam was synthesized by a gas-solid reaction from a solid mixture of silicon, carbon black and solid resin at temperature ca. 1300ºC under argon flow.[15,34] Low magnification SEM micrograph (Figure 66a) shows the high porosity of the SiC foam. SEM micrograph also evidences the highly porous structure of the SiC foam with a bimodal pore size distribution, i.e. meso- and macropores (Figure 66b and Table 6).

Typical SEM and TEM micrographs of commercial NDs are present in Figure S1. SEM micrograph (Figure S1a) evidences the presence of NDs aggregates with an average size of around 200 nm. The ND particles with size of 4-8 nm can be collected with the assistance of sonication treatment in ethanol medium as shown in the TEM images (Figure S1b). Figures 66c, 66d and S2 show the SEM images of ND anchored on the different porous macroscopic SiC materials (foam, grains and powder). The NDs loading was set at 13 wt %. The low magnification SEM image (Figures 66c) indicates that NDs are homogeneously coated on the surface of the porous β-SiC foam. The same ND dispersion can be also found when the NDs were loaded on the SiC grains (Figure S2a and b) and powder (Figure S2c and d). The high-magnification SEM image (Figure 66d) reveals that NDs particles are uniformly dispersed on the surface of the porous layer of SiC. TEM images of ND/SiC foam presented in Figure 66e-f also clearly show that NDs are well anchored on the SiC surface, which is in good agreement with the SEM results. It is worthy to note that the used SiC contains a thin layer of SiO_2 on the surface which could play a role of washcoat layer for the anchorage and dispersion of NDs particles. The advantage of such washcoat layer for anchoring metal nanoparticles has already been reported in our previous publications.[15,35] In Figure 66g, the typical 4 - 8 nm NDs particles on the SiC surface are detected by high-resolution TEM. The

HRTEM images show the (111) orientation of commercial diamond with an interplanar spacing of about 0.206 nm.[36, 37] It is worth noting that nanodiamond particles are typical polyhedral-shape with sp^3 carbon as core and graphitic carbon (sp^2 carbon) or amorphous carbon that is consisted of dangling bonds terminated by functional groups as shell.[10,38] These sp^2-hybridized or amorphous carbon on the surface of NDs could also be act as the active site for the dehydrogenation reaction.[38]

The specific surface area and pore size distribution of the ND/SiC composites are analyzed by the nitrogen sorption measurements and the results are displayed in Table 6 and Figure 67. Indeed, the industry K-Fe catalyst displays the specific surface area of 4 m^2 g^{-1} by the measurement of N_2 adsorption and desorption technique. The SiC foam (SiC(F)) has a medium specific surface area of 28 m^2 g^{-1}, and is mainly consists of meso- and macroporous network (pore size of 10 - 100 nm) which significantly contribute to reduce the diffusion problem through the catalyst matrix. The deposition of NDs particles onto the SiC foam support leads to an increase of both the final specific surface area (S_{BET}) and total pore volume (V_{total}) of the composite compared to the pristine SiC foam (Table 6). The S_{BET} of 13 wt % ND/SiC(F) and 33 wt % ND/SiC(F) composites are 73 and 159 m^2/g respectively while the initial surface area of the SiC foam is about 28 m^2/g. The corresponding V_{total} also significantly increase to 0.26 and 0.33 cm^3/g, respectively. During the deposition process part of the NDs can be localized within the meso- and macropores of the SiC support. Such pores filling will contribute to the creation of a new porous network with a final pore size smaller than the ones of the pristine support. It is thus expected that at high ND loading part of the porosity of the SiC support will be completely filled by the ND and thus, the available active sites will be reduced accordingly leading to a catalyst with lower DH activity. However, as the NDs mass loading increases to 44 wt %, the S_{BET} decreases to 152 m^2/g and the V_{total} value changes from 0.33 to 0.64 cm^3/g. These results could be explained by the fact that at high NDs loading the pore volume of the SiC was completely filled by the NDs and forms the new porosity network (the V_{total} of pure NDs up to 1.27 cm^3/g) which would leads less accessible for the reactant. At high NDs loading one should also expect that the dispersion is decreased and NDs aggregates are formed, as Figure S3 presents SEM images of the 33 wt % ND/SiC(F) and 44 wt % ND/SiC(F).

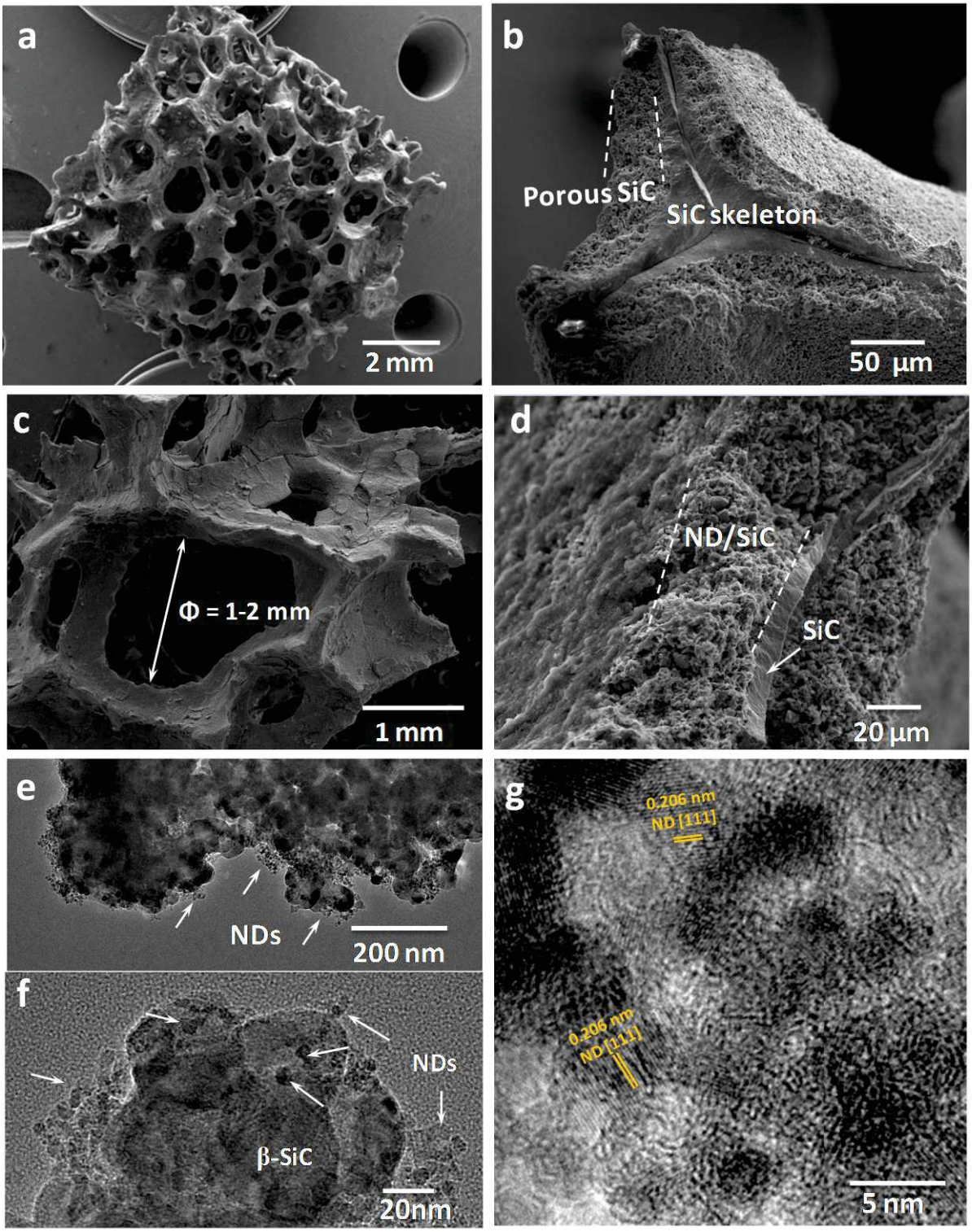

Figure 66. (a) Digital photo of SiC foam with the diameter of 8 mm used as a macroscopic host matrix for the NDs. (b) Typical SEM image of β-SiC foam which shows the SiC skeleton with a layer of porous SiC. SEM micrographs (c, d) and TEM images (e, f) of macroscopic ND/SiC foam. (g) HRTEM image of nanodiamonds on the surface of SiC. The 13 wt % mass loading of ND was introduced on the SiC foam surface.

The specific surface area and pore size distribution of the ND/SiC composites are analyzed by the nitrogen sorption measurements and the results are displayed in Table 6 and Figure 67. Indeed, the industry K-Fe catalyst displays the specific surface area of 4 m^2 g^{-1} by the measurement of N_2 adsorption and desorption technique. The SiC foam (SiC(F)) has a medium specific surface area of 28 m^2 g^{-1}, and is mainly consists of meso- and macroporous network (pore size of 10 - 100 nm) which significantly contribute to reduce the diffusion problem through the catalyst matrix. The deposition of NDs particles onto the SiC foam support leads to an increase of both the final specific surface area (S_{BET}) and total pore volume (V_{total}) of the composite compared to the pristine SiC foam (Table 6). The S_{BET} of 13 wt % ND/SiC(F) and 33 wt % ND/SiC(F) composites are 73 and 159 m^2/g respectively while the initial surface area of the SiC foam is about 28 m^2/g. The corresponding V_{total} also significantly increase to 0.26 and 0.33 cm^3/g, respectively. During the deposition process part of the NDs can be localized within the meso- and macropores of the SiC support. Such pores filling will contribute to the creation of a new porous network with a final pore size smaller than the ones of the pristine support. It is thus expected that at high ND loading part of the porosity of the SiC support will be completely filled by the ND and thus, the available active sites will be reduced accordingly leading to a catalyst with lower DH activity. However, as the NDs mass loading increases to 44 wt %, the S_{BET} decreases to 152 m^2/g and the V_{total} value changes from 0.33 to 0.64 cm^3/g. These results could be explained by the fact that at high NDs loading the pore volume of the SiC was completely filled by the NDs and forms the new porosity network (the V_{total} of pure NDs up to 1.27 cm^3/g) which would leads less accessible for the reactant. At high NDs loading one should also expect that the dispersion is decreased and NDs aggregates are formed, as Figure S3 presents SEM images of the 33 wt % ND/SiC(F) and 44 wt % ND/SiC(F).

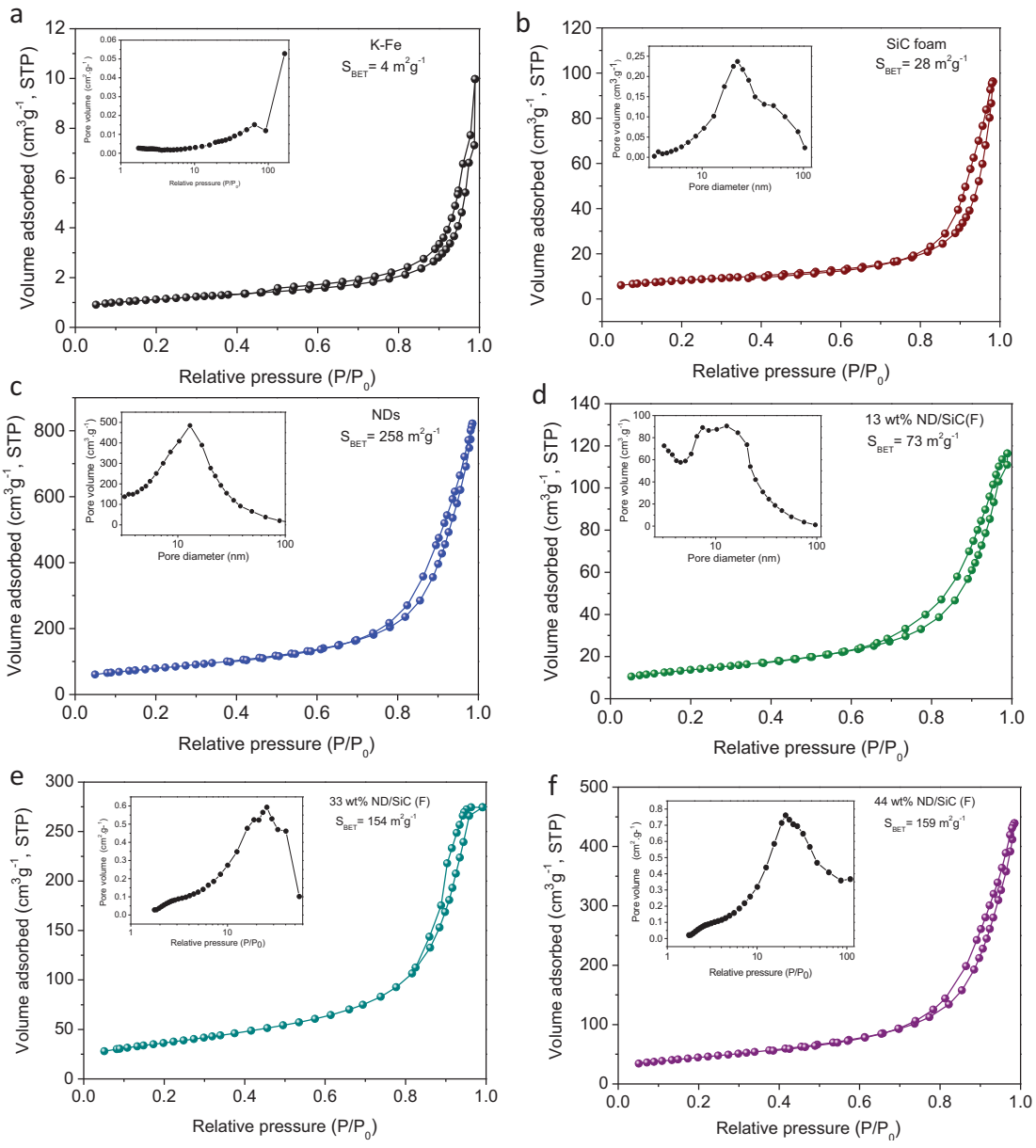

Figure 67. N_2 adsorption-desorption isotherms for the SiC foam, commercial ND, K-Fe and different NDs loaded on the SiC foam catalysts. The inset in each figure is the corresponding pore size distribution.

Table 6. Physical characteristics of NDs, SiC and NDs anchored on the SiC foam catalysts.

Samples	NDs loading[a]	S_{BET} (m^2/g)	V_{total} (cm^3/g)	D_{BJH} (nm)	C (at. %)	O (at. %)	O/C	Si/C
NDs	-	258	1.27	16	92.8	7.2	0.08	-
β-SiC(F)	-	28	0.15	20	33.6	25.3	0.75	1.22
13 wt % ND/SiC(F)	13	73	0.26	14	81.4	13.0	0.16	0.07
33 wt % ND/SiC(F)	33	159	0.33	15	86.1	11.6	0.14	0.03
44 wt % ND/SiC(F)	44	152	0.64	15	86.9	11.4	0.13	0.02

[a] The NDs weight loading was measured by thermogravimetry analysis.

X-ray photoelectron spectroscopy (XPS) is used to characterize the surface chemical composition of different NDs supported on SiC foam. The atomic ratio of carbon, oxygen and silicon obtained by XPS are summarized in Table 6, and related XPS spectra are presented in Figure 68. The spectra for the ND/SiC(F) samples with different loading showed O_{1s}, C_{1s} and Si_{1s} peaks at 530 eV, 286 eV and 101 eV, respectively.[32,34,39] The surface oxygen content ranges from 11.4 at % to 13.0 at % as a function of the NDs loading. The pure SiC has 36 at. % surface oxygen due to the presentation of a amorphous phase thin layer of the SiO_2 and SiO_xC_y compounds mixture.[15,26] However, this oxygenated functional groups present on the SiC surface is relatively marginal as blank test carried out on the SiC support only showed a relatively low DH performance (see the catalytic results). The oxygenated functional groups present on the SiC surface is mostly involved as anchorage sites for improving the dispersion of the deposited ND. It is also expected that the strong anchorage of the NDs particles on the SiO_2 layer of SiC could prevent ND particles movement and as a consequence, significantly lower the sintering process. Similar results have already been reported elsewhere.[15, 26] The Si peak becomes much smaller as the NDs loading increases which could be attributed to an extensive coverage of the SiC surface by the NDs. The Si/C ratio significantly decreases as a function of the NDs loading, i.e. from 1.22 for pure SiC to 0.02 for the 44 wt % ND on SiC (Figure 68) which could be attributed to the higher coverage or plugging of the SiC surface by NDs particles.

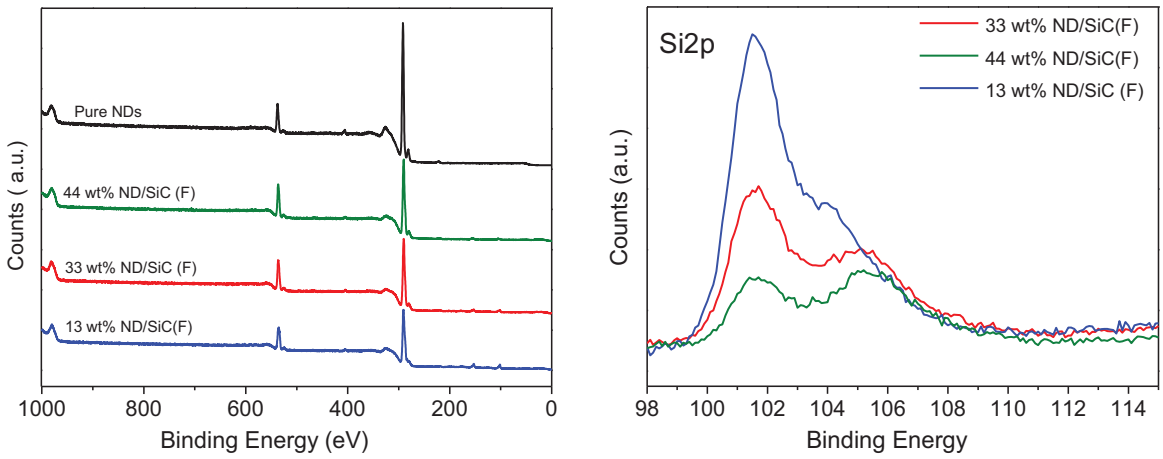

Figure 68. Survey scan (a) and Si2p(b) XPS spectra of SiC foam supported NDs catalysts with different NDs loading.

In order to quantify the pressure-drop across the different composites measurements ($\Delta P/L$) are carried out and the results are presented in Figure 69**.** The experimental pressure drop (ΔP) across various shapes of β-SiC supported ND catalysts per unit length as a function of the linear gas velocity (u_g) is displayed, which is the typical model of pressure drop measurement reported elsewhere in the literatures.[40-42] According to the results we can clearly observe that, when the gas shuttles crossing the powder-like SiC or grains SiC supported ND, a large pressure drop was observed, especially at higher gas velocity. On the other hand, the SiC foam composite displays an extremely low pressure drop for the whole range of linear gas velocity. At high gas velocity, i.e. 3 m/s, pressure drop is only 0.067 $*10^5$ Pa/m of ND/SiC foam, whereas for the ND supported on SiC grains a pressure drop higher than 6.8 $*10^5$ Pa/m was observed. Moreover, the pressure drop of powder-like SiC supported ND materials is even higher than 12 $*10^5$ Pa/m at the gas velocity of 1.8 m/s. Such result again confirms the advantage of using SiC foam structure for fixed-bed reaction. As catalyst supports for packed bed reactors, foam-structured supports with lower pressure drop, high effective surface area and high mixing degree area of great interest for industrial applications.[26,41,43,44] The pressure drop results clearly indicate that the direct use of NDs (∅ ranged between 4 to 8 nm) or the powder-like carriers supported catalysts (powder, grains, etc) in a fixed-bed reactor configuration is problematic due to the high pressure drop across the catalyst bed even at low gaseous space velocity.

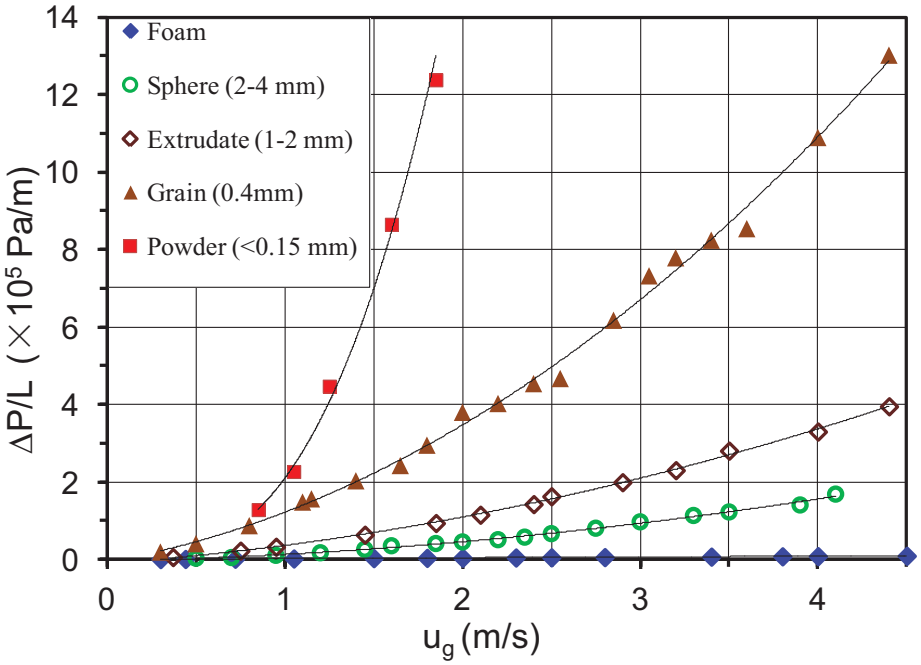

Figure 68. Pressure drop measurements on the various states of ND on silicon carbide materials. The 13 wt % mass loading of ND was introduced on the various shapes SiC surface.

The steam-free, direct dehydrogenation of ethylbenzene reaction is performed on the NDs decorated porous SiC foam catalyst (with NDs loading of 13 wt %, 33 wt% and 44 wt%, respectively) as well as commercial nanodiamond under atmosphere pressure at 550 ^{o}C at a gaseous space velocity of 30 ml/min. The dehydrogenation activity (styrene rate, styrene products per gram of nanodiamonds per hour) is expressed in terms of $mmol_{ST}\ g_{ND}^{-1}\ h^{-1}$ recorded on SiC-based catalysts with different NDs loadings, pristine NDs and SiC foam support, and the results are presented in Figure 69a and b. The DH activity gradually decreases as increasing the NDs loading on the SiC foam surface which is directly related to the lower dispersion of NDs onto the SiC surface at high loading (Figure 69a). The highest DH activity is obtained with the 13 wt% ND/SiC under the reaction conditions used. When NDs are dispersed on the surface of porous SiC foam, the ND/SiC foam composites present relative higher activity per weight of NDs compared to pure NDs catalyst, especially at NDs mass loading at 13 wt %, the styrene production yield shows about 3.8 times of that on pure NDs without losing the selectivity. Taken into account these results the optimization tests will be further carried out on the 13 wt% ND/SiC catalyst. On the SiC foam supported 13 wt% NDs catalyst, the styrene rate is significant improved on the basis of the effective weight of the NDs, i.e. 12.86 $mmol_{ST}g_{ND}^{-1}h^{-1}$, and the styrene selectivity is as high as pure NDs (98.3% of styrene selectivity; the other products are consisted of light hydrocarbons such as benzene and toluene.) It also can be found in Figure 69b that the SiC materials perform almost no catalytic activity under the tested reaction conditions and thus, confirming the chemical

inertness character of the support. The conversion of ethylbenzene over SiC only achieves 7% (styrene rate on per weight of SiC catalyst is 0.54 $mmol_{ST}\ g_{cat}^{-1}\ h^{-1}$) with styrene selectivity of 88%. In the mean time, the styrene rate obtained on the unsupported commercial ND is amounted to about 2.89 $mmol_{ST}\ g_{cat}^{-1}\ h^{-1}$ at the steady state after 50 h on stream, and styrene selectivity remains as high as 99%, displaying the similar results to those already reported in the literature.[6,45]

The steam-free DH tests are also carried out over the ND/SiC catalysts using the SiC in different shapes (powder (P), grains (G), foam (F)) and the results are presented in Figure 69c. The selectivity towards styrene is extremely high over all the tested catalysts. The NDs supported on SiC foam exhibits an extremely high stability as a function of time on stream compared to the other catalysts. The activity improvement of the ND/SiC foam could be attributed to the higher dispersion of ND on the SiC surface which provides a higher density of active sites for the reaction and also to the possible micro-turbulences generated through the contact between the reactant and the SiC foam structures.

The catalytic stability of the ND/SiC (13 wt %) catalyst is also evaluated during a long-term test (> 100 h) and the results are presented in Figure 69d. According to the experimental results a slow decline of the DH activity is observed on the ND/SiC catalyst at the first 40 h of test and then remains almost unchanged for the whole test. As pointed out in Figure 69d, the DH activity of the ND/SiC foam still remains at about 10.97 $mmol_{ST}\ g_{ND}^{-1}\ h^{-1}$ with the styrene selectivity of 98% after 100h of reaction which renders it a promising catalyst for further industrial development.

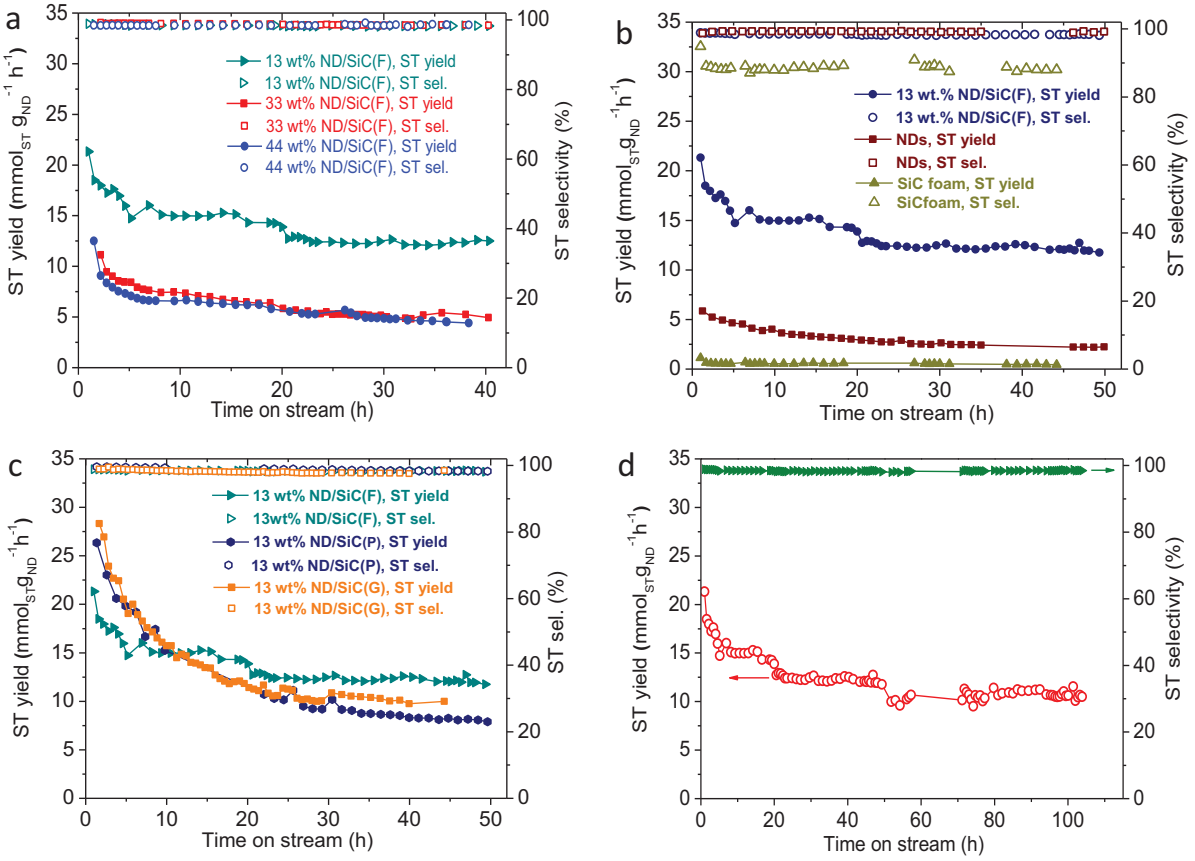

Figure 69. Catalytic performance of stream-free ethylbenzene dehydrogenation. (a, b) EB dehydrogenation over different NDs mass loading on SiC (foam), SiC foam supported and unsupported NDs catalysts. The ST yield of pristine SiC foam is expressed as styrene rate per weight of the SiC per hour ($mmol_{ST}$ g_{cat}^{-1} h^{-1}) (c) EB dehydrogenation catalytic activity on different shaped SiC supported NDs catalysts. (d) Long-term test at 550°C over 13 wt% ND/SiC(F) catalyst. Reaction conditions: 300 mg, 550°C, 2.8 % EB in helium, 30 mL·min^{-1}.

The high resistance towards deactivation of the ND/SiC(F) could be attributed to the open porosity of the support and a connected pores which significantly reduce the residence time of the products on or next to the active site and as a consequence, the amount of carbonaceous deposit. It is worthy to note here that the pressure drop is not inference severely under the laboratory-scale conditions but especially under the industrial conditions when hundreds kilograms of catalysts are loaded. The medium thermal conductivity of the SiC could also help to maintaining the catalyst bed temperature unchanged for this endothermic reaction. The temperature decrease could be partly responsible for intermediate products condensation or polymerization leading to the catalyst surface fouling as well.

Figure 70 summarized the ethylbenzene DH catalytic performance on the steady-state on pure NDs and different ND loaded on the SiC foam, as well as the other carbon-based catalysts, ND supported on commercial SiO_2 carrier and industrial K-Fe/Al_2O_3 (with 90 wt %

of iron loading) catalysts. For comparison the DH activity of the ND loaded on few-layer-graphene (16 wt% ND/FLG) is also reported in the same figure.[46] The industrial K-Fe/Al_2O_3 catalyst exhibits a high DH activity at the beginning of the test followed by a rapid deactivation before reaching a steady-state at around 1.0 $mmol_{ST}\ g_{cat}^{-1}\ h^{-1}$. Such deactivation phenomenon can be attributed to the active site plugging by carbonaceous residu during the course of the reaction in the absence of steam in the processing feed. The unsupported NDs present the best DH activity (2.89 $mmol_{ST}\ g_{cat}^{-1}\ h^{-1}$) compared to the other carbon-based catalysts and to the industrial K-Fe catalyst, which show similar catalytic behavior as reported in ref.[6] The bench-marking tests carried out on the different ND-based catalysts have shown that the 13wt% ND/SiC catalyst displays a highest DH activity compared to the others. The insulator carrier such as porous SiO_2 is also applied for supporting NDs and the DH results obtained are further compared with those of the different ND-based catalysts. It can be found in Figure 70 that the NDs dispersed on the supports result in the higher DH activity comparing with the one on the pristine ND, either thermally supports, i.e. FLG and SiC, or insulator supports, i.e. SiO_2. Such results could be attributed to the medium loading and also to the high dispersion of the ND on the catalyst which provides higher reactive sites for the reaction. For the catalysts with higher ND loading the ND nanoparticles are less dispersed and thus, lead to a lower DH activity. Work is ongoing to optimize the dispersion step, i.e. solvent nature or deposition process, in order to improve the styrene production per weight of loaded catalyst. The ND/FLG (16 wt% of ND) catalyst showed a slightly similar dehydrogenation performance compared to that of ND/SiC (with 13 wt% of ND loading) under the same reaction conditions. In the mean time, the ND/SiO_2 catalyst shows a much lower DH activity compared to the ND/SiC catalysts. According to the results one can stated that when the NDs are dispersed on thermally conductive supports, either on FLG or SiC, the dehydrogenation performance is higher compared to those supported on insulator supports. Such result could be attributed to the better homogenization of the temperature within the catalyst bed which is not the case for the insulator catalysts where temperature drops, due to the endothermic character of the reaction and the absence of steam in the feed as a time carrier, could lower the DH activity. However, for the industrial application the macroscopic SiC would be more benefit compared to the ND/FLG as it allows the reduction of pressure drop across the catalyst bed and also for the cost of production of the support.

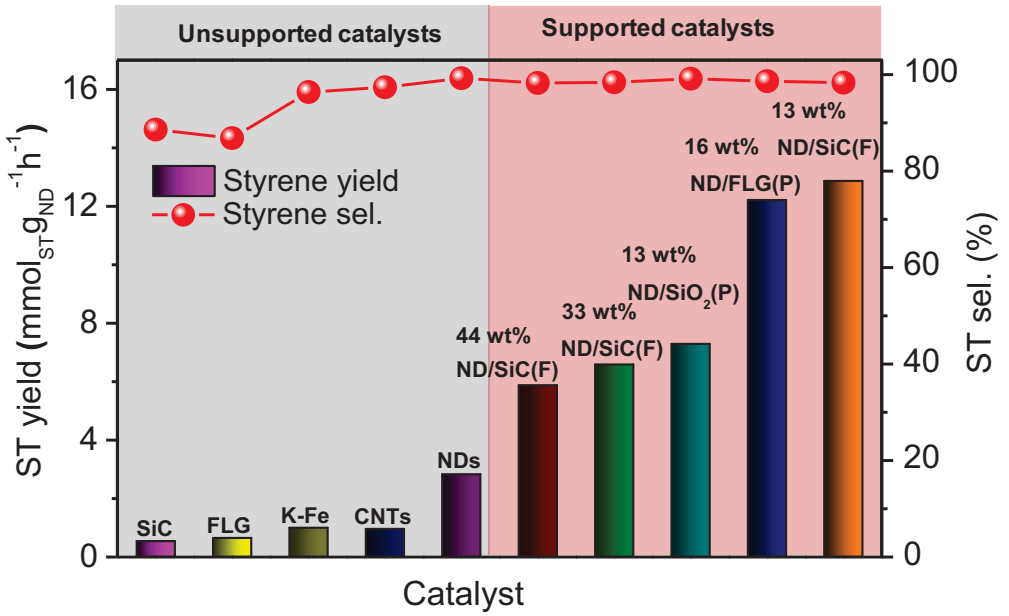

Figure 70. Styrene specific rate of carbon-based catalysts and commercial K-Fe catalyst under steady state. The ST yield of ND-free catalysts is expressed as styrene formation rate per weight of catalysts per hour ($mmol_{ST}$ g_{cat}^{-1} h^{-1}). Reaction conditions: 550°C, 2.8 % EB in helium, 30 $mL \cdot min^{-1}$, atmospheric pressure.

The summarized dehydrogenation performance obtained on the different ND and industrial K-Fe catalysts are shown in Table 7. The catalytic activity is defined as the amount of styrene produced per hour per weight of the active phase or per amount of specific surface area. It can be found that the dispersed ND (ND/SiC) catalyst displays higher activity value per the amount of NDs than that of prisitne ND and industrial K-Fe catalysts, which are also illustrated in the Figures 69 and 70. Since different catalysts present different active site density, the relative areal activity should also taken into account for the future development of the active catalysts. The dispersed ND catalyst (13 wt% ND/SiC(F)) presents a relative areal activity as high as 0.0087 $mmol_{ST}m^{-2}h^{-1}$ at reaction temperature of 550°C, which displays the best DH value among the ND-based, but lower areal activity than the industrial K-Fe catalysts. It is worth to note that the specific surface area of K-Fe catalyst is very low, i.e. 4 m^2/g, compared to that of the ND-based catalysts and thus, leads to a high DH rate per surface unit. However, for the industrial application the specific rate per weight of the catalyst is the most critical factor.

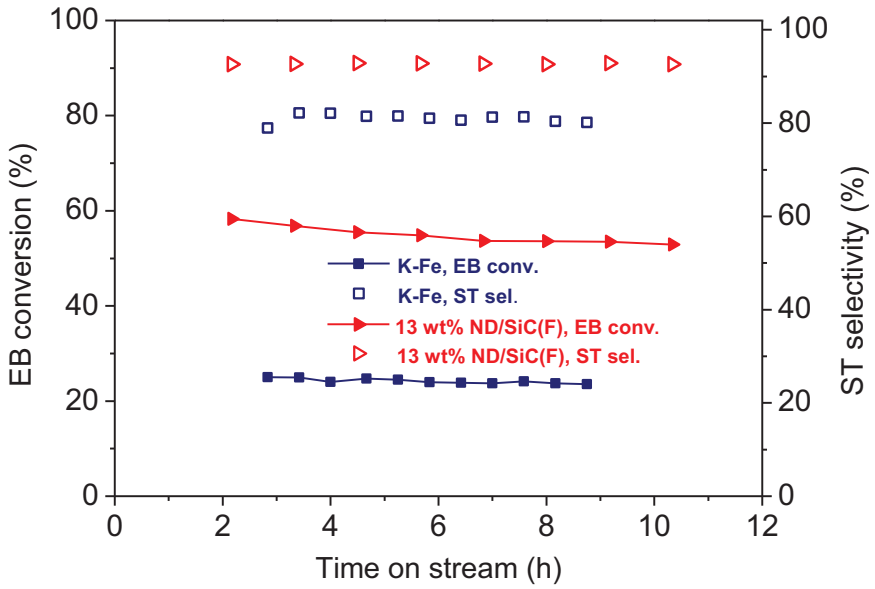

Figure 71. Comparison of EB conversion and ST selectivity over 13 wt% ND/SiC(F) and K-Fe catalysts at reaction temperature of 600 ºC. Reaction conditions: 2.8 % EB in helium, 30 $mL \cdot min^{-1}$, 300 mg of catalyst, atmospheric pressure.

The EB dehydrogenation performance of the 13 wt% ND/SiC(F) catalyst is also performed at reaction temperature of 600 ºC, and compared with the one obtained over the K-Fe catalyst (Figure 71 and Table 7). According to the results, the 13 wt% ND/SiC(F) catalyst displays a EB conversion of 54.7% with a relatively high styrene selectivity of 92.6% (Figure 71). On the other hand, at the same reaction conditions, the K-Fe-based catalyst only shows a EB conversion of 24.3% and styrene selectivity of only 81.6%. As shown in Table 7, the styrene formation rate of the 13 wt% ND/SiC(F) catalyst is about 3.8 $mmol_{ST}g_{catalyst}^{-1}h^{-1}$, which is more than two times the activity of the K-Fe-based catalyst .

Table 7. Dehydrogenation activities of various carbon-based materials and industrial K-Fe_2O_3 catalyst.[a]

Catalyst	T/ °C	X(EB)/ %	S(ST)/ %	Y(ST)/ $mmol_{ST}g_{catalyst}^{-1}h^{-1}$	Y(ST)/ $mmol_{ST}g_{ND}^{-1}h^{-1}$	Y(ST)/ $mmol_{ST}m^{-2}h^{-1}$
β-SiC(F)	550	7.9	88.6	0.54	-	0.0058
CNTs	550	12.8	97.4	0.96	-	0.0015
FLG	550	9.8	86.8	0.65	-	0.0065
NDs	550	37.2	99.2	2.83	2.83	0.0033
K-Fe_2O_3	550	13.4	96.4	0.99	-	0.074
	600	22.7	81.0	1.41	-	0.105
13 wt % ND/SiC(F)	550	28.4	98.3	2.14	12.86	0.0087
	600	53.0	92.0	3.74	26.2	0.015
33 wt % ND/SiC(F)	550	31.1	98.4	2.35	6.58	0.0046
44 wt % ND/SiC(F)	550	29.0	98.3	2.19	5.87	0.0041

[a] Reaction conditions: 300 mg of catalyst, 2.8 % EB in helium, 30 $mL \cdot min^{-1}$, atmospheric pressure.

The temperature-programmed oxidation (TPO) combing with mass spectrometry is also performed on the ND/SiC (13 wt %) catalyst before and after EB dehydrogenation test (Figure 72a) to evidence the low carbonaceous deposit and to better explain the high stability of the catalyst for the long-term test. For comparison, the spent industrial K-Fe-based catalyst is also analyzed and the results are compared with that of the ND/SiC catalyst (Figure 72b). It can be found in the figures that the spent ND/SiC(F) catalyst showed similar combustion profile in the temperature range from 500 to 700°C, which can be issued from the oxidation of NDs. The low CO_2 intensity at temperature between 400 and 450°C is attributed to the organic compounds and low temperature coke deposition during the long-term DH reaction. On the contrary, the spent industrial K-Fe_2O_3 catalyst shows obviously a large amount of deposit coke as the intensity of the CO_2 peaks steadily increased, especially at temperature higher than 500°C which could be attributed to the irreversible or inert coke.[47] This could be the major reason for the low activity obtained from metal-based catalyst due to the coke

deposition which severely blocked most of the active surface under steam-free reaction conditions.

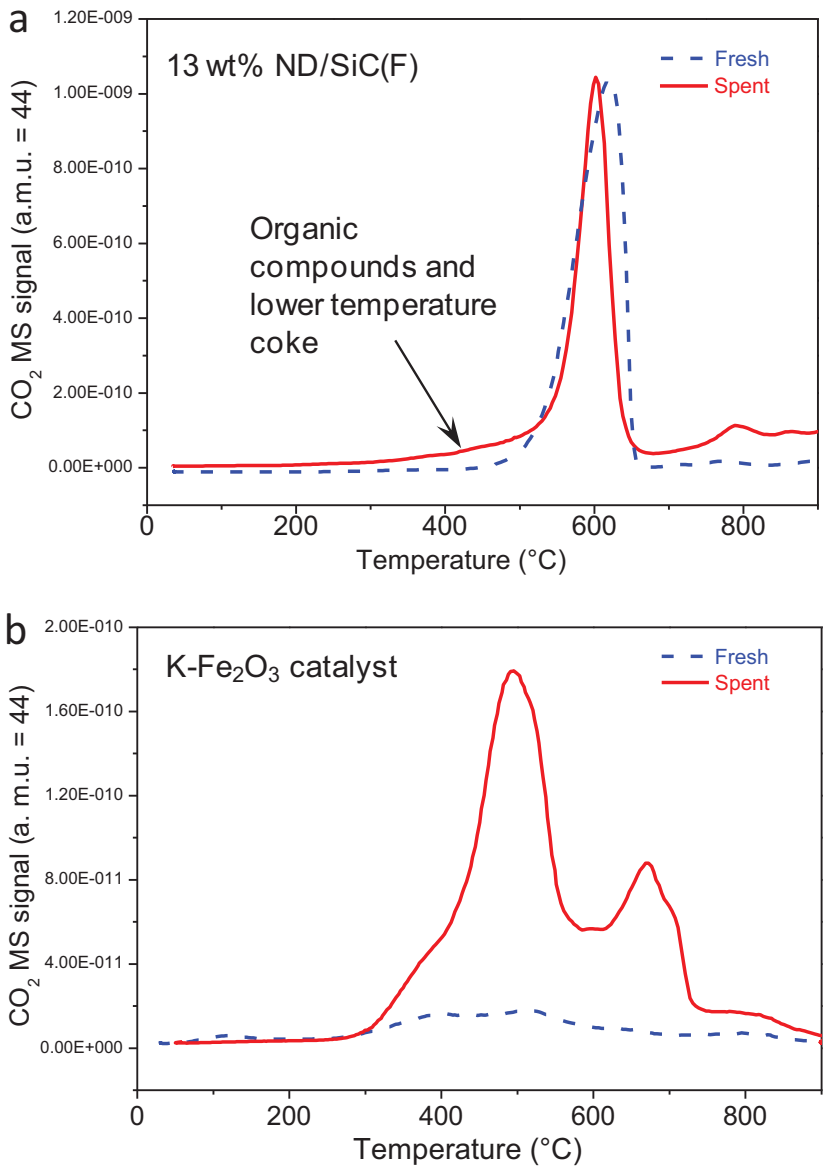

Figure 72. Temperature programmed oxidation tests on fresh and after DH reaction samples of the (a) 13 wt% ND/SiC(G) and (b) industrial K-Fe-based catalysts. The spent catalysts were tested under DH conditions of 550 ºC for more than 50 h on stream.

The ND/SiC catalyst is tested for the regeneration process by diluted oxygen at 450 ºC in order to understand the catalytic performance over this type of hybrid composite as a function of the regeneration cycles. Base on the TPO-MS results, it can be found that the organic compounds and low temperature carbonaceous deposits could be fully removed by

oxygen during the oxidative regeneration step. This coverage could be attributed to the sharp deactivation at the beginning of the test. As explanation in the previous research work by XPS, XRD, TPO-MS and TEM techniques on the fresh and spent ND/FLG catalysts,[46] the first period of deactivation could be attributed to the formation of low temperature coke on the surface of the active sites and some carbon allotropes rearrangement during the reaction. The equilibrium is achieved afterwards by reaction between the low temperature coke with H_2, generated from the dehydrogenation process, and then further sharp deactivation is unlikely to occur. Moreover, as one can observe such deactivation become less pronounced after repeated regeneration which probably modifies the surface structure of the catalyst leading to a more stable catalyst as a function of time on stream (Figure 73). Such deactivation period could be significantly shorter after some regeneration and will not represent a real problem for the process as almost no deactivation was observed afterward on the regenerated catalyst. As shown in Figure 73, similar DH activates are observed over the ND/SiC catalyst after three regeneration cycles lasting for a total of 300 hours. More interesting, the regenerated catalyst also displays high stability over more than 150 hours time on stream at the single regeneration run, which is also one of the prerequisite for developing the future direct dehydrogenation catalysts.

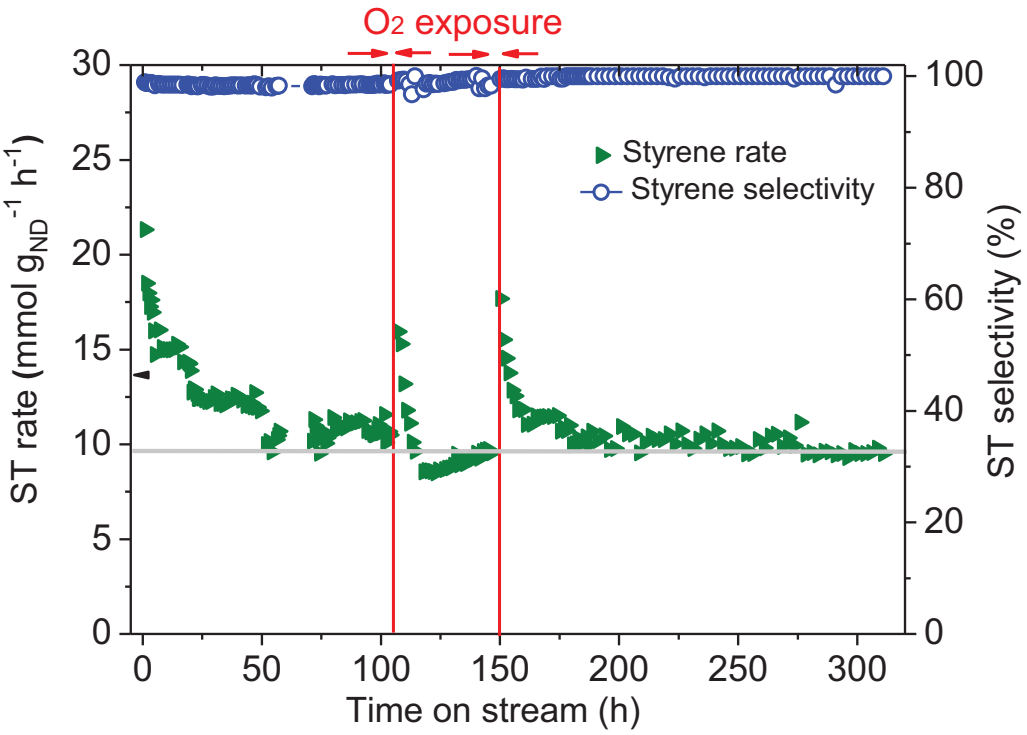

Figure 73. EB dehydrogenation catalytic performance of regenerate ND/SiC catalyst by diluted air flow. Reaction conditions: 13 wt% of NDs, 300 mg, 550 °C, 2.8 % EB in helium, 30 mL·min^{-1}, atmospheric pressure. Regenerated conditions: 450° C, 30 ml min^{-1} of diluted oxygen flow (20 vol. % O_2 in helium).

4. Conclusions

In conclusion, we successfully prepared the macroscopic ND/β-SiC porous hybrid composite via a facile one-step method. The NDs particles are uniformly dispersed on the surface of the porous SiC foam network displaying a high effective surface area for the steam-free dehydrogenation reaction along with a low pressure drop which is of extreme interest when operated in large scale industrial fixed-bed reactor. The ND/SiC foam displays a styrene production rate of 12.86 $mmol_{ST}\ g_{ND}^{-1}\ h^{-1}$ along with a styrene selectivity of 98% at 550 ºC. Such performance leads to a styrene production rate of about more than 10 times higher than the commercial K-Fe-based catalyst and 3.8 times higher than pure ND powder. The ND/SiC catalyst also displays an extremely high stability as a function of time on stream, i.e. more than 100 hours, unlikely to the metal-based catalysts. Such high stability is attributed to the open porosity of the catalyst which efficiently prevents coke deposition during the course of the reaction. It is expected that such hybrid catalyst could also be used in other applications reaching far beyond the catalysis field, i.e. bacterial removal[48] or chemical sensor. Work is ongoing to evaluate such structured catalyst in a more drastic reaction conditions, i.e. high partial pressure of EB and high space velocity.

Acknowledgements

The present work is financially supported by a European project (FREECATS) under a contract number NMP3-SL-2012-280658. The SiC samples were supplied by SICAT Co. (www.sicatcatalyst.com) within the framework of the FREECATS project. The TEM is performed at the facilities of the IPCMS (UMR 7504 CNRS-University of Strasbourg). Dr. L.-D. Nguyen is gratefully acknowledged for helpful discussion in this work.

†Electronic Supplementary Information (ESI) available: Extra catalyst characterizations such as TEM, SEM, XPS, TG analysis (Figures S1-S4).

References

(1) F. Cavani, F. Trifiro, Appl Catal A-Gen. 133 (**1995**) 219-239.
(2) O. Shekhah, W. Ranke, R. Schlogl, J Catal. 225 (**2004**) 56-68.
(3) M. Muhler, R. Schlogl, A. Reller, G. Ertl, Catal Lett. 2 (**1989**) 201-210.
(4) M. Muhler, J. Schutze, M. Wesemann, T. Rayment, A. Dent, R. Schlogl, G. Ertl, J Catal. 126 (**199**0) 339-360.
(5) M. Muhler, R. Schlogl, G. Ertl, J Catal. 138 (**1992**) 413-444.
(6) J.A. Zhang, D.S. Su, R. Blume, R. Schlogl, R. Wang, X.G. Yang, A. Gajovic, Angew Chem Int Ed. 49 (2010) 8640-8644.
(7) A. Krueger, Adv Mater. 20 (**2008**) 2445-2449.
(8) V.N. Mochalin, O. Shenderova, D. Ho, Y. Gogotsi, Nat Nanotechnol. 7 (**2012**) 11-23.
(9) X. Liu, B. Frank, W. Zhang, T.P. Cotter, R. Schlogl, D.S. Su, Angew Chem Int Ed. 50 (**2011**) 3318-3322.
(10) S. Osswald, G. Yushin, V. Mochalin, S.O. Kucheyev, Y. Gogotsi, J Am Chem Soc. 128 (**2006**) 11635-11642.
(11) M.J. Ledoux, C. Pham-Huu, Cattech. 5 (**2001**) 226-246.
(12) A. Deneuve, I. Florea, O. Ersen, P. Nguyen, C. Pham, D. Begin, D. Edouard, M.J. Ledoux, C. Pham-Huu, Appl Catal A-Gen. 385 (**2010**) 52-61.
(13) R. Philippe, M. Lacroix, L. Dreibine, C. Pham-Huu, D. Edouard, S. Savin, F. Luck, D. Schweich, Catal Today. 147 (**2009**) S305-S312.
(14) L. Borchardt, C. Hoffmann, M. Oschatz, L. Mammitzsch, U. Petasch, M. Herrmann, S. Kaskel, Chem Soc Rev. 41 (**2012**) 5053-5067.
(15) Y. Liu, O. Ersen, C. Meny, F. Luck, C. Pham-Huu, ChemSusChem. 7 (**2014**) 1218-1239.
(16) X.Y. Li, X.L. Pan, L. Yu, P.J. Ren, X. Wu, L.T. Sun, F. Jiao, X.H. Bao, Nat Commun. 5 (**2014**) doi:10.1038/ncomms4688.
(17) Y.F. Liu, B. de Tymowski, F. Vigneron, I. Florea, O. Ersen, C. Meny, P. Nguyen, C. Pham, F. Luck, C. Pham-Huu, ACS Catalysis. 3 (**2013**) 393-404.
(18) X.G. Guo, G.Z. Fang, G. Li, H. Ma, H.J. Fan, L. Yu, C. Ma, X. Wu, D.H. Deng, M.M. Wei, D.L. Tan, R. Si, S. Zhang, J.Q. Li, L.T. Sun, Z.C. Tang, X.L. Pan, X.H. Bao, Science. 344 (**2014**) 616-619.
(19) H.M.T. Galvis, J.H. Bitter, C.B. Khare, M. Ruitenbeek, A.I. Dugulan, K.P. de Jong, Science. 335 (**2012**) 835-838.
(20) R. Dhiman, E. Johnson, E.M. Skou, P. Morgen, S.M. Andersen, J Mater Chem A. 1 (**2013**) 6030-6036.
(21) J.Y. Hao, Y.Y. Wang, X.L. Tong, G.Q. Jin, X.Y. Guo, Int J Hydrogen Energ. 37 (**2012**) 15038-15044.
(22) S. Hajiesmaili, S. Josset, D. Begin, C. Pham-Huu, N. Keller, V. Keller, Appl Catal A-Gen. 382 (**2010**) 122-130.
(23) H. Liu, J. Diao, Q. Wang, S. Gu, T. Chen, C. Miao, W. Yang, D. Su, Chem Comm. 50 (2014) 7810-7812.
(24) A.N. Kouame, R. Masson, D. Robert, N. Keller, V. Keller, Catal Today. 209 (**2013**) 13-20.
(25) Y. Liu, I. Florea, O. Ersen, C. Pham-Huu, C. Meny, Chem Comm. 51 (**2015**) 145-148.
(26) M. Lacroix, L. Dreibine, B. de Tymowski, F. Vigneron, D. Edouard, D. Bégin, P. Nguyen, C. Pham, S. Savin-Poncet, F. Luck, M.-J. Ledoux, C. Pham-Huu, Appl Catal A-Gen. 397 (**2011**) 62-72.

(27) K. Chizari, A. Deneuve, O. Ersen, I. Florea, Y. Liu, D. Edouard, I. Janowska, D. Begin, C. Pham-Huu, ChemSusChem. 5 (**2012**) 102-108.
(28) L. Truong-Phuoc, T.H. Tri, N.D. Lam, W. Baaziz, T. Romero, D. Edouard, D. Begin, I. Janowska, C. Pham-Huu, Appl Catal A-Gen. 469 (**2014**) 81-88.
(29) M.A. Leon, R. Tschentscher, T.A. Nijhuis, J. van der Schaaf, J.C. Schouten, Ind Eng Chem Res. 50 (**2011**) 3184-3193.
(30) M.A. Leon, T.A. Nijhuis, J. van der Schaaf, J.C. Schouten, Chem Eng Sci. 73 (**2012**) 412-420.
(31) R. Tschentscher, T.A. Nijhuis, J. van der Schaaf, J.C. Schouten, Ind Eng Chem Res. 51 (**2012**) 1620-1634.
(32) T. Tran Thanh, H. Ba, L. Truong-Phuoc, J.-M. Nhut, O. Ersen, D. Begin, I. Janowska, D.L. Nguyen, P. Granger, C. Pham-Huu, J Mater Chem A. 2 (**2014**) 11349-11357.
(33) M.J. Ledoux, S. Hantzer, C.P. Huu, J. Guille, M.-P. Desaneaux, J Catal. 114 (**1988**) 176-185.
(34) P. Nguyen, C. Pham, Appl Catal A-Gen. 391 (**2011**) 443-454.
(35) B. de Tymowski, Y.F. Liu, C. Meny, C. Lefevre, D. Begin, P. Nguyen, C. Pham, D. Edouard, F. Luck, P.H. Cuong, Appl Catal A-Gen. 419 (**2012**) 31-40.
(36) Y.V. Butenko, S. Krishnamurthy, A.K. Chakraborty, V.L. Klznetsov, V.R. Dhanak, M.R.C. Hunt, L. Siller, Phys Rev B. 71 (**2005**) 075420.
(37) O. Shenderova, A. Koscheev, N. Zaripov, I. Petrov, Y. Skryabin, P. Detkov, S. Turner, G. Van Tendeloo, J Phys Chem C. 115 (**2011**) 9827-9837.
(38) J. Zhang, D.S. Su, A.H. Zhang, D. Wang, R. Schlogl, C. Hebert, Angew Chem Int Ed. 46 (**2007**) 7319-7323.
(39) D.M. Jang, H.S. Im, S.H. Back, K. Park, Y.R. Lim, C.S. Jung, J. Park, M. Lee, Phys Chem Chem Phys. 16 (2014) 2411-2416.
(40) M. Lacroix, P. Nguyen, D. Schweich, C. Pham-Huu, S. Savin-Poncet, D. Edouard, Chem Eng Sci. 62 (**2007**) 3259-3267.
(41) J.T. Richardson, Y. Peng, D. Remue, Appl Catal A-Gen. 204 (**2000**) 19-32.
(42) D. Edouard, S. Ivanova, M. Lacroix, E. Vanhaecke, C. Pham, C. Pham-Huu, Catal Today. 141 (2009) 403-408.
(43) L. Giani, C. Cristiani, G. Groppi, E. Tronconi, Appl Catal B-Environ. 62 (**2006**) 121-131.
(44) V.V. Ordomsky, J.C. Schouten, J. van der Schaaf, T.A. Nijhuis, ChemCatChem. 4 (**2012**) 129-133.
(45) Z. Zhao, Y. Dai, J. Lin, G. Wang, Chem Mater. 26 (2014) 3151-3161.
(46) H. Ba, S. Podila, Y. Liu, X. Mu, J.-M. Nhut, V. Papaefthimiou, S. Zafeiratos, P. Granger, C. Pham-Huu, Catal Today (**2014**) doi:10.1016/j.cattod.2014.1010.1029.
(47) D. Ma, D.Z. Wang, L.L. Su, Y.Y. Shu, Y. Xu, X.H. Bao, J Catal. 208 (2002) 260-269.
(48) J. Wehling, R. Dringen, R.N. Zare, M. Maas, K. Rezwan, ACS Nano. 8 (**2014**) 6475-6483.

Supporting Information

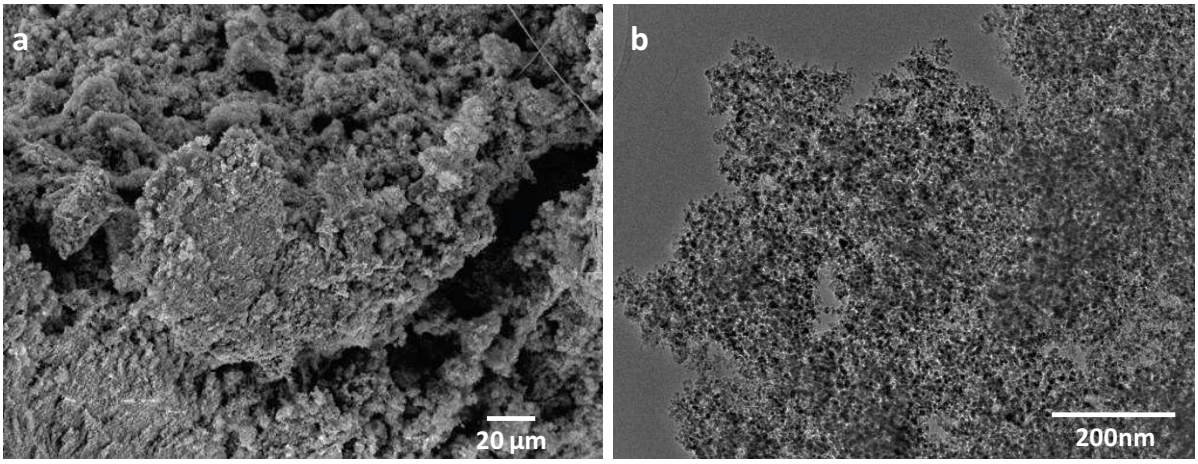

Figure S1. SEM and TEM micrographs of the pristine NDs powder.

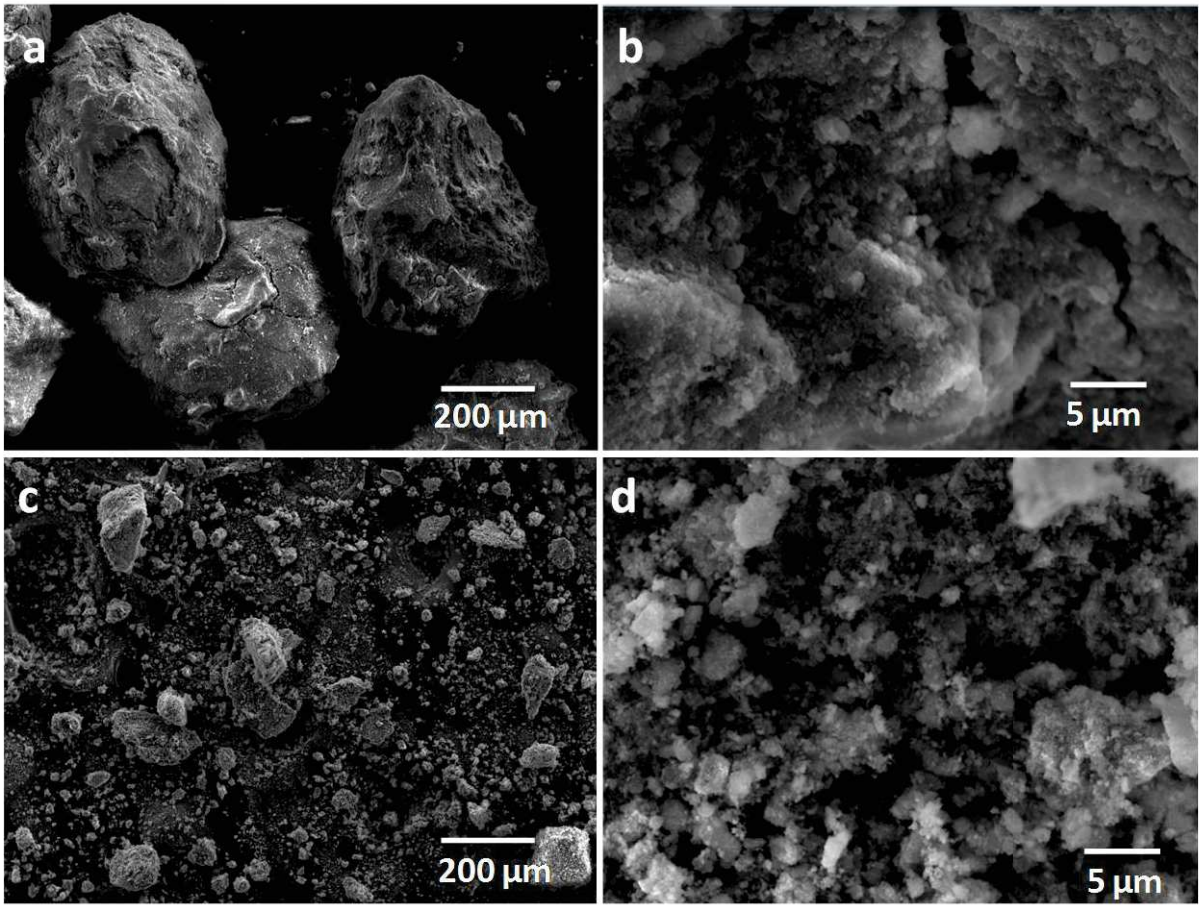

Figure S2. SEM images of NDs supported on the grain (a, c) and powder (c, d) SiC. NDs weight loading is 13 wt %.

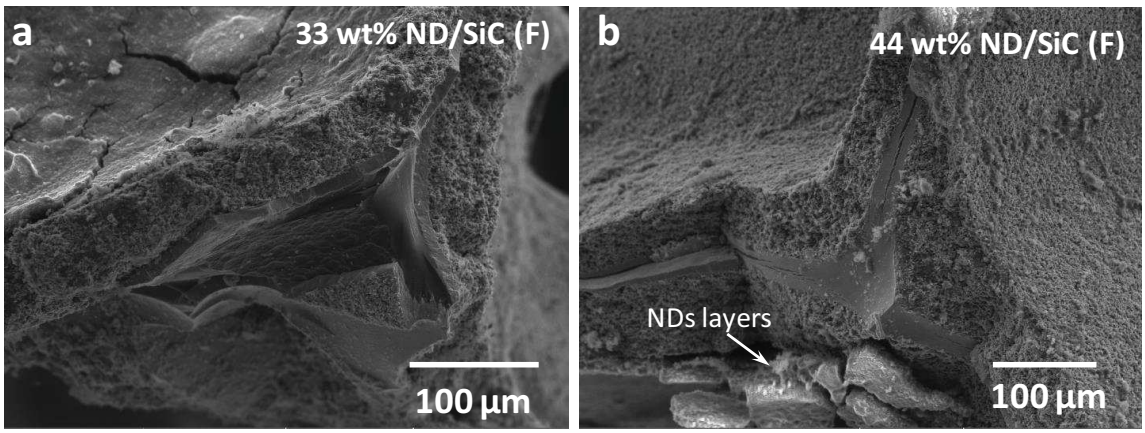

Figure S3. SEM images of ND/SiC foam catalysts with NDs loading of (a) 33 wt.% NDs and (b) 44 wt.%.

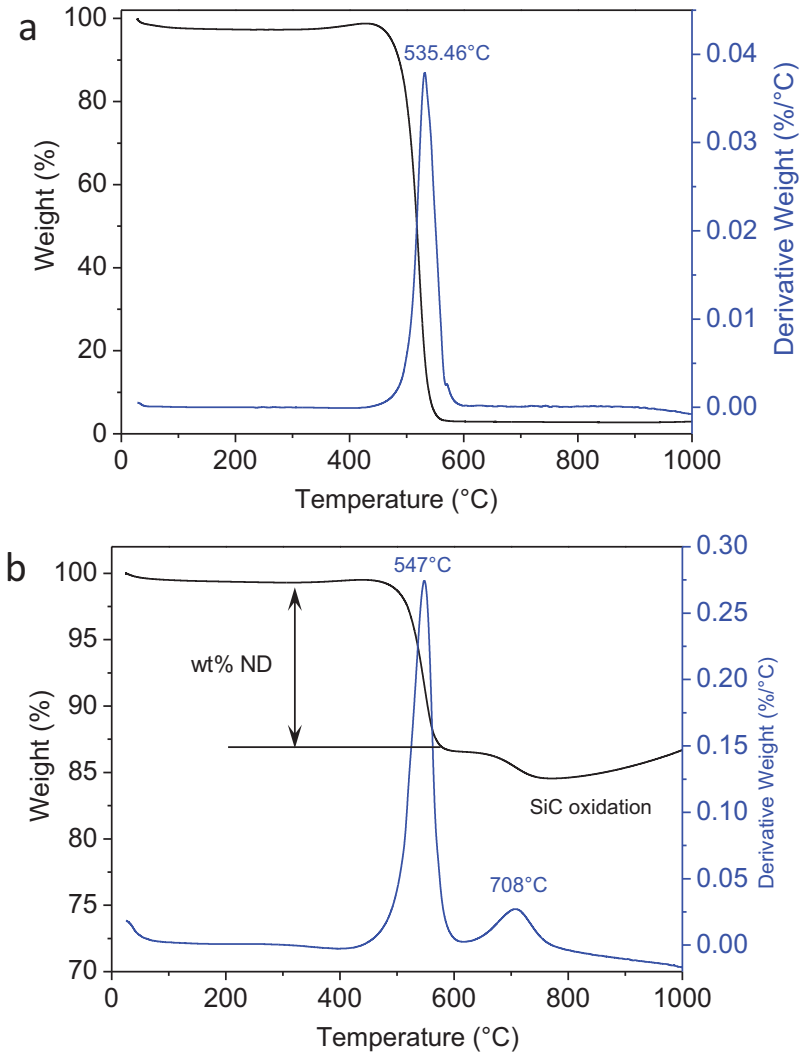

Figure S4. Thermogravimetric analysis (TGA) of the pristine ND and ND/SiC foam composite. The mass loading of ND is 13 wt % on the as-prepared catalyst.

Chapter 6

One-step synthesis of macroscopic carbon catalyst with high N-content active phase

Green chemical route to produce hierarchical carbon nanotubes coated with nitrogen-doped porous carbon as metal-free catalyst

Housseinou Ba,[1,2] Yuefeng Liu,[1], * Lai Truong-Phuoc,1 Jean-Mario Nhut,[1] Lam-Dinh Nguyen,[3] Ovidiu Ersen,[4] Pascal Granger,[2] Gulia Tuci[5], Giuliano Giambastiani[5], Cuong Pham-Huu[1],*

[1] *Institut de Chimie et Procédés pour l'Energie, l'Environnement et la Santé (ICPEES),UMR 7515 CNRS- University of Strasbourg (UdS), 25, rue Becquerel, 67087 Strasbourg Cedex 02, France.*

[2] *Unité de Catalyse et Chimie du Solide (UCCS), UMR 8181 CNRS-Université de Lille, 59655 - Villeneuve d'Ascq Cedex France*

[3] *The University of Da-Nang, University of Science and Technology, 54, Nguyen Luong Bang, Da-Nang, Viet nam*

[4] *Institut de Physique et Chimie des Mate´riaux de Strasbourg (IPCMS),UMR 7504, CNRS-University of Strasbourg (UdS), 23, rue du Loess,67034 Strasbourg Cedex 02, France*

Article submitted in Nature Communication

Graphical abstract

Abstract

Nitrogen-doped carbon materials have received an ever increasing scientific interest for applications as metal-free catalysts in several catalytic processes and also in the field of new energy conversion and storage. However, the conventional relative harsh synthetic conditions, low nitrogen doping together with handling and transport of these materials significantly hindered their wide applications. We report herein a facile, scalable route to synthesize macroscopic porous nitrogen-doped carbon foam composite with relatively high nitrogen doping, up to 19 wt %, from food processing raw materials, i.e. ammonium carbonate, D-glucose and citric acid. Another advantage of the synthesis is that the nitrogen species are mainly located on the surface of the composite which display high active sites for processing the reaction. The as-synthesized nitrogen-doped carbon composite was evaluated in two most demanded catalytic reactions namely the oxygen reduction reaction and the selective dehydrogenation of ethylbenzene into styrene. In the oxygen reduction reaction the nitrogen-doped carbon catalyst displays electrochemical activity close to the commercial 20 wt% Pt/C catalyst and moreover, superior long-term durability than 20wt% Pt/C catalyst. Furthermore, in the dehydrogenation reaction the nitrogen-doped carbon catalyst exhibits activity more than twice of that of the commercial Fe-K/Al_2O_3 catalyst.

Keywords:

Nitrogen-doped carbon, metal-free catalysts, macroscopic shaping, oxygen reduction reaction, dehydrogenation, Ethylbenzene.

1. Introduction

Heteroatom doped carbon materials with high specific surface area and controllable macroscopic shape have been extensively applied in various fields such as energy conversion and storage, catalysis and wastewater treatment.[1-4] Porous carbon materials doped with nitrogen element could be efficiently employed as metal-free catalyst in several catalytic processes in place of noble metal or transition metal-based catalysts.[5-9] The introduction of heteroatom, especially nitrogen, into carbon materials, is accomplished using either "in-situ" doping or "ex-situ" doping. The "in-situ" doping is carried out by direct introducing the doping precursor agent in the synthesis process of porous carbon materials.[10] The "ex-situ" doping is consisted by a post-treatment of the as-synthesized carbon materials with a nitrogen-containing precursor (nitrogen, amines, ammonia, etc.).[9,1,12] A numbers of harsh methods such as high temperature arc-discharge, pyrolysis, chemical vapor deposition (CVD), or solvothermal synthesis are used to transformed the nitrogen precursors mentioned above into N-doped carbon. The "in-situ" doping method requires the N-rich precursors such as, dicyandiamide,[13] melamine,[14,15] polypyrrole16 and poly (ionic liquids) (PILs),[17-19] etc. The "ex situ" doping allows one to selectively decorate the outer surface of the carbon-based materials with specific nitrogen species.[20] Recently, the poly (ionic liquids) has been reported as the efficient nitrogen source,[17-19] however, the process suffered from the multi-step synthesis of the PILs and the control of final composite shape. In general, the "ex-situ" doping, using organic precursors, suffers from the temperature sensitivity of the nitrogen decorated species which hinder the use of these composites in medium- and high-temperature processes and thus, in-situ doping remains the most preferred methods for the synthesis of nitrogen-doped carbon composites. It is worthy to note that the nitrogen distribution within the doped composites synthesized through traditional routes described above is localized randomly within the final carbon matrix[21] and thus, only a small part of the incorporated nitrogen is accessible for the subsequent applications. In addition, the nitrogen loading is hardly controlled by both in-situ and ex-situ doping due to the impossibility to predict the amount of nitrogen incorporated in the final composite. It is therefore of interest to find method for preparing carbon-based materials doped with nitrogen which displays high nitrogen concentration, exclusive localization, preferentially only on the topmost layer of the final composite, along with controlled macroscopic shaping for the numerous potential catalytic applications. The synthesis method should also employed cheap and non-toxic nitrogen precursor along with an easy scalability for mass production regarding the further industrial development.

Herein, we report the synthesis of a novel hybrid N-doped carbon (N@C/CNT) foam material with hierarchical structure through a simple, scalable and economic strategy. The method also use non-toxic and cheap raw materials which represent also a net advantage

compared to the traditional ones. The as-synthesized hierarchical N@C/CNT carbon foam displays several advantages such as: a open structure with low mass transfer limitation, a high thermal and electrical conductivity provide by the carbon nanotubes (CNTs) network and a high exposed active sites due to the thin layer of the coated nitrogen-doped porous carbon layer with high intrinsic surface area. The N@C/CNT foam materials are used as metal-free catalysts and show excellent catalytic performance for the oxygen reduction reaction (ORR) and steam-free selective dehydrogenation of the ethylbenzene into styrene. The catalytic performance of the N@C/CNT composites will be also compared with those of the state-of-the-art catalysts in these relevant reactions.

2. Results and discussion

The strategy used for the synthesis of the structured 3D foam N@C/CNT composite is illustrated in Figure 74a. The mechanical mixing powder mixture of ammonium carbonate ($(NH_4)_2CO_3$, citric acid, D-glucose and CNTs with appropriate concentrations was heated up at 130°C under air for 2h. During the low-temperature thermal transformation at 130°C the porous foam structure, containing nitrogen, carbon and oxygen species, was obtained consecutively to the reaction between ammonium and citric acid while the macropores were formed from the decomposition of the ammonium carbonate into NH_3, CO_2 and H_2O. The macroscopic shape of the foam was generated by a melting of the D-glucose in the mixture which also plays a role of carbon source for the N@C. The oven treated composite was further calcined in air at 450°C followed by an annealing step in helium at 900°C in order to complete the carbonization reaction and to generate the carbon structure containing nitrogen species with an open and connected porosity. The CNTs are used as structural template to precise control of the final macroscopic shape and mechanical strength of the composite after thermal treatment for subsequence applications. Indeed, in the lack of CNTs (Figure 74b,c and Figure S1), the composite is constituted by smooth carbon sheet structures with no mesopores and also neither the macroscopic shape nor the mechanical strength can be controlled. In the presence of CNTs as skeleton the N@C/CNT composite with different macroscopic shapes, i.e. disk, monolith, pellets, and size are synthesized (Fig. 74d). The SEM micrographs of the N@C/CNT composite is presented in Figure 1 e and f and evidence the complete coverage of the CNTs skeleton with a thin layer and homogeneous layer of N@C leading to the formation of structured foam composite with opened-structure constituting of both meso- and macroporous networks and high effective surface area (Figure 74b-f, S1, S2).

The meso-/macroporous network of the composite was generated consecutively to the formation of H_2O and CO_2 during the shaping and calcination processes (Figure S4). The

nitrogen concentration inside the composite can be tuned from 14 to 20 at% by changing the mass ratio between $(NH_4)_2CO_3$ and dextrose (Figure 75A, and Table S1). It is worthy to note that the raw materials are used in a solid state and thus, the concentration of them can be adjusted at will to allow one to produce N@C/CNT composites with a large range of physical properties, i.e. nitrogen concentration, porosity and specific surface area, depending to the downstream applications. The specific surface areas of the N@C/CNT composites are high (> 400 m^2/g) which render them suitable for being used in the field of heterogeneous catalysis. For example, in this method, the surface areas (S_{BET}) of N@C/CNT-15 and N@C/CNT-19 (containing respectively 15.3 and 19.4 at.% of nitrogen) are 418 and 461 m^2/g, respectively (Table S2) with an average pore sizes, derived from N2 isotherm using the BJH method, centered at 4.8 and 3.2 nm. As shown in Figure S2, the N@C/CNT-15 composite exhibit type IV isotherms with a hysteresis loop in the relative pressure (P/P0) range of 0.3-0.4, corresponding to the existence of mesoporous structure. From the pore size distribution, it can also be concluded that the total porosity increases as increasing the amount of $(NH_4)_2CO_3$ in the precursor mixture.

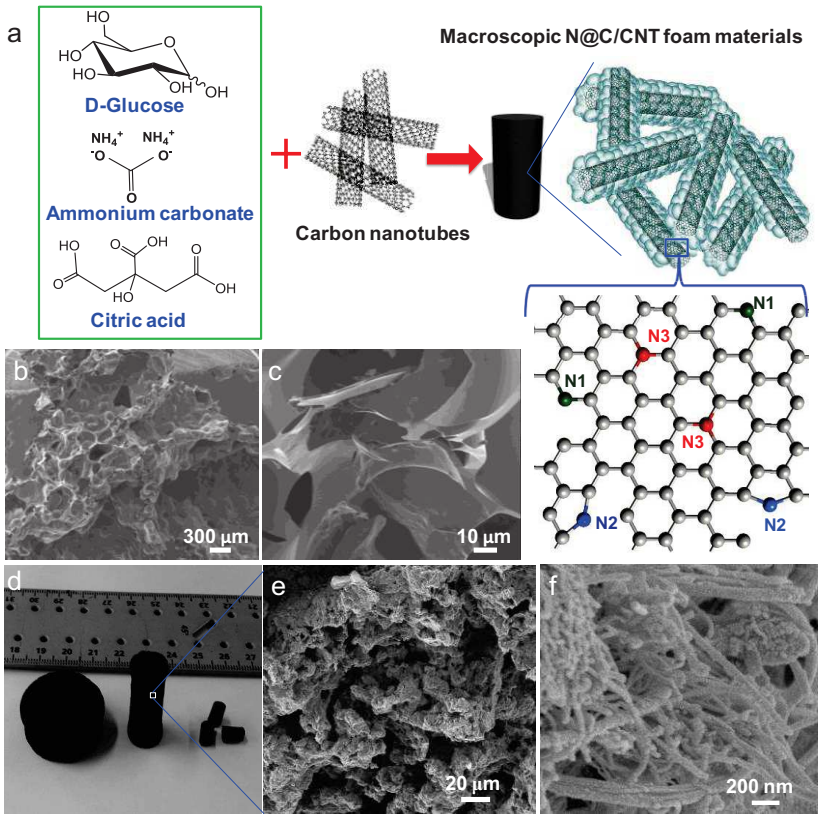

Figure 74. (a) Schematic illustration of the synthesis method of the N@C/CNT composite (N1: pyridinic-N; N2: pyrrolic-N, N3: quaternary-N). (b-c) SEM images of nitrogen-doped carbon composite without CNTs. (d) Digital photos of representative N@C/CNT composites with various shapes. (e, f) SEM micrographs of the N@C/CNT composite with an entangled network covering the CNT skeleton with interconnected and large pore size.

Fig. 75a clearly evidences the direct influence of the ammonium carbonate/dextrose weight ratio on the total nitrogen content in the final N@C/CNT composites. According to the results the optimal ratio is about 3 as with higher ratio the nitrogen content remains almost unchanged. The X-ray photoelectron spectroscopy (XPS) indicates that nitrogen atoms are structurally integrated into the N@C/CNT foam matrix. The survey XPS spectrum of the N@C/CNT composite (Figure 75b) shows three peaks, at 284.6, 400.0 and 531.8 eV, which can be attributed to C1s, N1s and O1s, respectively. The deconvolution of the C1s peak of N@C/CNT-15 reveals five peaks (Figure S3), which can be assigned, respectively, to the sp2 hybridized C=C bonds (C1) in graphitic structure, alternate defect carbon structures associated with C–N, C–O, C=O and -COO bonds overlapping (285.6 - 288.2 eV, C 2-4), and the shake-up π-π* transition of carbon (289.7 eV, C5).[22] The absence of C-N peak is observed in the CNTs and C/CNT-composite samples confirming that the nitrogen species only issued from ammonium carbonate. The decomposed N1s spectrum of N@C/CNT-15 composite (Figure 75c) shows different nitrogen species, named pyridinic (N1, 399.0 eV), pyrrolic (N2, 400.3 eV), quaternary (N3, 401.5 eV) and intercalated nitrogen (404.0 eV), with a respective concentration of 40.7, 30.3, 18.9, and 6.1 at %, respectively.[8,11,23] According to the XPS analysis the N@C/CNT-15 clearly possesses high pyridinic (40.7 at %) and high pyrrolic (30.3 at %) nitrogen contents compared to the nitrogen species distribution reported up to now on the CVD samples in the literature. The results evidence that the nitrogen species are strongly depending to the nature of the nitrogen precursor and also to the synthesis route.[4,17,18] Figure 2d compares the Raman spectra of CNT, C/CNT and N@C/CNT-15 materials. The D band around 1340 cm−1 is known to be resulted from the structural defects and partially disordered structures of the sp2 domains. The G peak around 1570 cm−1 is associated with the E2 g vibration mode of sp2 carbon domains correspond to the graphitization degree of the material.[24,25] The peak-fitted Raman spectra (Figure S4) show two sp3-type carbon around 1230 and 1450 cm-1. The ratios of the D band to G band integrated intensity (ID/IG) for the CNT, C/CNT and N@C/CNT-15 samples are 0.79, 0.91, and 0.87, respectively. The increase of the ID/IG ratios in the C/CNT and N@C/CNT samples with respect to the pristine CNT is consisting with the presence of a layer of carbon and nitrogen-doped carbon with higher defects covering the pristine CNT.

Energy-filtered TEM analysis (EFTEM) is employed to elucidate the distribution of nitrogen in N-doped carbon composite (N@C/CNT-15). Elemental mapping results (Figure 75e-f) show a homogeneous distribution of C and N atoms, which indicates the good dispersion of nitrogen on the surface of N-doped carbon materials. According to the TEM-EELS analysis the nitrogen atoms were exclusively localized within the layer of disordered carbon, with mesoporous network, in the composite according to the synthesis recipe (Figure 75h). The exclusive localization of the N-atoms on the topmost surface of the sample allows one to fully exploit the active sites associate with these nitrogen-doped carbon sites compared

to the samples synthesized by in-situ method where a large part of the nitrogen atoms were buried inside the tube wall[21] and thus, were not involved in the catalytic reaction. The corresponding high-resolution TEM images (Figure S5) confirm the facts observed from the SEM analysis and clearly show the presence of disordered nitrogen-carbon species around the graphite wall of the CNTs skeleton. According to the results the CNTs skeleton provides a high effective surface for dispersing the nitrogen-doped carbon phase generated from the decomposition of the dextrose, ammonium carbonate and citric acid mixture.

More evidence can be found in thermal gravimetric analysis of typical nitrogen-doped carbon composite (Figure S6). The weight loss area located below 100°C is ascribed to the adsorbed water in the material. The significant weight loss appearing at 598 °C is attributed to the oxidation of skeleton carbon nanotubes while a shoulder appearing at around 500°C could be attributed to the combustion of the N@C with lower graphitization degree (Figure S6a). In the TGA spectrum of the C/CNT composite (Figure S6b) similar weight loss at 481°C and 609°C, respectively, are observed which could be attributed to the oxidation of carbon species (with lower thermal resistance compared to the N@C) and CNTs.

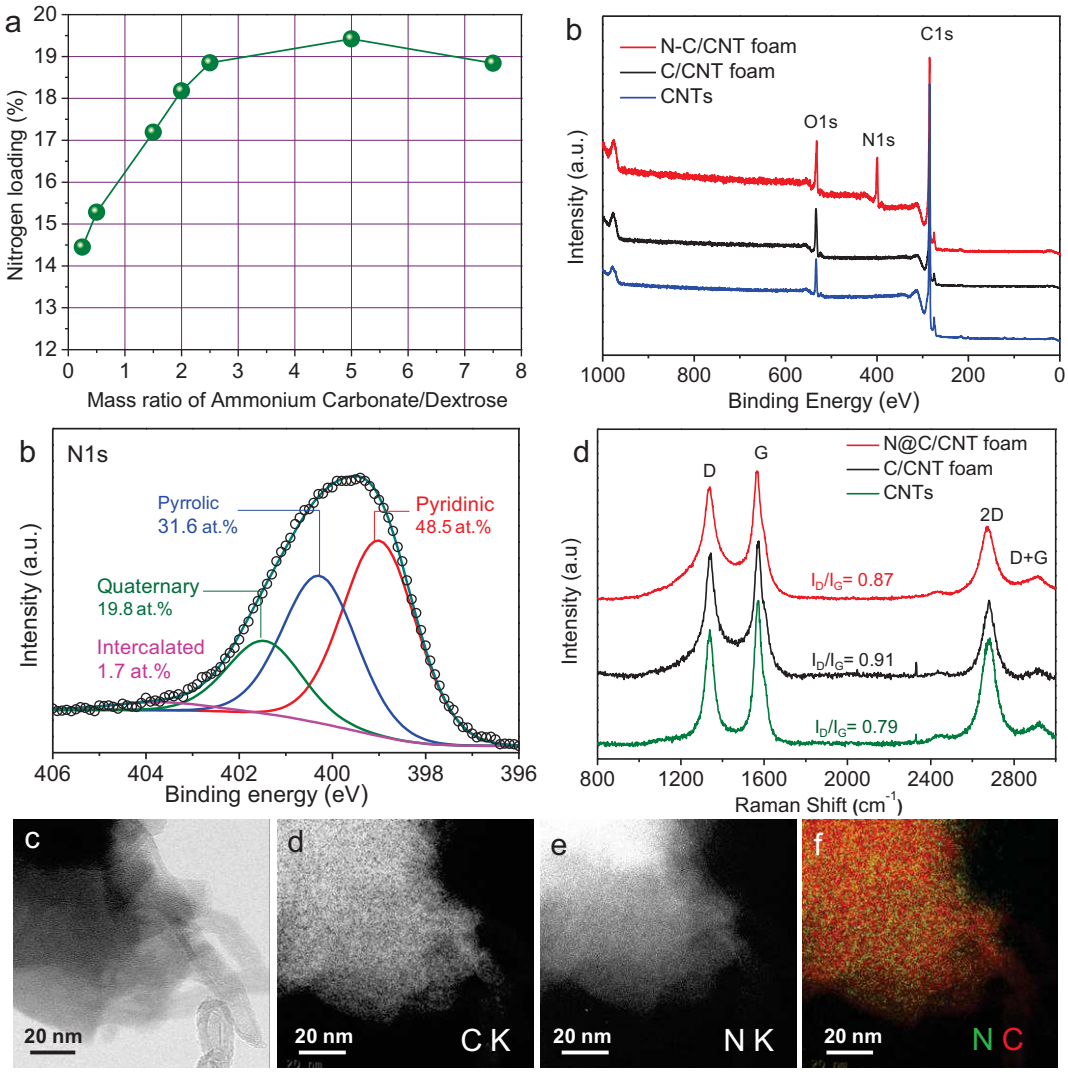

Figure 75. (a) Nitrogen concentration in various N@C/CNT composites with different mass ratio of ammonium carbonate and dextrose. (b) XPS survey spectra of C/CNT foam, N@C/CNT-15 foam and CNTs. (c) High-resolution N1s spectrum of the N@C/CNT-15 composite. (d) Raman spectra of the CNT, C/CNT and N@C/CNT samples. (e-f) TEM image and energy filtered TEM images of N@C/CNT-15 foam at the carbon and nitrogen K-edges, and the corresponding superposition of both carbon and nitrogen maps (carbon in red and nitrogen in green).

2.1. Oxygen reduction reaction (ORR)

Figure 76a presents the ORR performance of the glassy carbon electrode decorated with a thin film of CNTs, N@C/CNT-15(G) composite (after graphitization at 900°C in helium) and commercial 20 wt% Pt/C catalysts. The ORR curve of the CNTs catalyst (Figure 76a) shows a typical feature of a two-electron pathway with two onset potentials located at 0.75 V and 0.55 V (vs. RHE (reversible hydrogen electrode)), respectively. The presence of a N@C

layer on the CNTs surface significantly enhanced the ORR catalytic activity and reaction kinetics which become almost similar to that of the commercial Pt/C catalyst. The Koutecky-Levich (K-L) plots (Figure 76b) for the N-C/CNT-15(G) composite at different rotation rates exhibit a near four-electron process which are similar to those obtained on the Pt/C catalyst. To confirm the conclusion obtained from the K–L plots, we implemented rotating-ring-disk electrode (RRDE) measurements, by which the yield of H_2O_2 and the electron transfer number (n) could be accurately calculated from the disk and ring currents (Figures 76c and S7). The on-set and half-wave potentials, the intensity at 0.9V and the number of transferred electrons per O_2 molecule (n) measured for each catalyst are listed in Table S3. Taking the average of n calculated by the two methods above, the calculated n is equal to 2, 3.8 and 4 for the CNT, N@C/CNT-15(G) foam and Pt/C catalysts, respectively. The on-set and half-wave potentials of N-C/CNT-15(G) foam material are 1.05 V and 0.84 V, respectively, which are closed to those of commercial Pt/C catalyst displaying on-set and half-wave potentials at 1.08 V and 0.90 V, respectively (Table S3). To our knowledge, this ORR activity of N-C/CNT-15(G) foam ranked among the highest activities reported up to now for metal-free N-doped carbon materials with competitive synthesis and economic strategy.[10, 26-30]

The stability of the N@C/CNT-15(G) catalyst is also investigated under potential cycling between 0.2 V and 1.2 V at 100 mV·s-1 and 900 rpm in 0.1 M KOH at 25°C, which is also one of important concerns for the potential replaceable ORR noble metal catalyst. The ORR performance stability of the N@C/CNT-15(G) catalyst is evaluated for 1500 cycles and the results are presented in Figure 76d. It is observed that the polarization curve only slightly changed during the whole durability test which indicates the high resistance of the catalyst towards deactivation. The intensity recorded at 0.9V indicates that the N@C/CNT-15(G) catalyst retains 90% of the initial electrocatalytic performance after 1500 cycles while for the Pt/C only 70% of the initial performance is retained (Figure S8), suggesting higher catalytic durability of the N@C/CNT-15(G) composite.

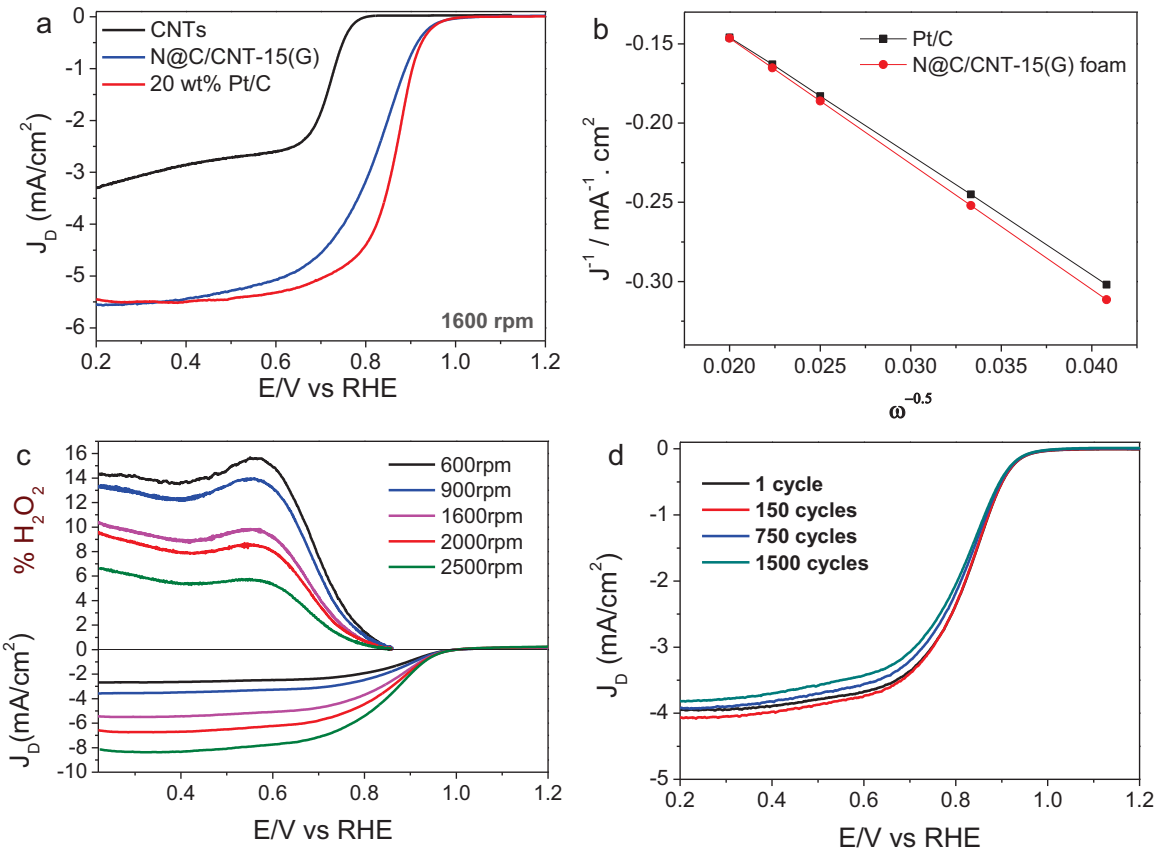

Figure 76. ORR electrocatalytic performance of the different catalysts. (a) RED polarization curves of CNTs, N@C/CNT-15(G) and the commercial Pt/C catalyst (20 wt% Pt, Sigma). (b) The Koutecky-Levich slope at 0.4eV showing the similar $4e^-$ transfer mechanism between the Pt/C and N@C/CNT catalysts. (c) Rotating-ring-disk electrode (RRDE) measurements at different rotation rate for electron transfer number determination. (d) Stability of the N@C/CNT-15(G) composite in the ORR cycling tests.

2.2. Steam-Free Dehydrogenation of Ethylbenzene into Styrene.

The dehydrogenation catalytic activity obtained on the N@C/CNT-15 and industrial K-promoted Fe_2O_3 (K-Fe) catalysts at 550 °C by using diluted EB as reactant is present in Figure 77a. The initial ethylbenzene (EB) conversion of 64% with a styrene selectivity of almost 100% is observed on N@C/CNT-15 catalyst followed by a slow deactivation up to 30 h on stream to reach a steady-state conversion at around 34% with selectivity to styrene (ST) of 98%. The specific reaction rate, expressed as the amount of styrene obtained per gram of catalyst per hour, calculated at the steady-state is 2.41 $mmolSTg_{Catal}^{-1}h^{-1}$. For comparison, the DH activity of N@C/CNT-15 catalyst is compared with that obtained on the industrial K-promoted Fe_2O_3 catalyst.[31] The industrial catalyst displays a relatively high DH activity at the beginning of reaction followed by a relative rapid deactivation after few hours on stream to

reach a steady-state at about 13% of EB conversion which corresponds to a specific reaction rate of about 0.99 mmolSTgCatal-1h-1. The styrene selectivity is also high on the commercial catalyst at almost 100%.

The selectivity of styrene, on both catalysts, remains unchanged during the whole test indicating that the deactivation observed was mostly linked with the active sites encapsulation but not to its chemical modification during the course of the reaction.[31,32] For comparison with the literature results on the metal-free and steam-free dehydrogenation process, the DH reaction was also carried out on the bulk nanodiamonds (NDs) which have been reported to be one of the most active metal-free catalysts for the steam-free dehydrogenation of EB.[31,33] The DH catalytic performance of the N@C/CNT-15 catalyst is also compared with those obtained on the other DH catalysts including the Fe-K and other carbon-based catalysts and the results are depicted in Figure 77b. The N@C/CNT-foam displays a highest styrene production rate along with a high selectivity comparing to the other carbon catalysts. As can be found in Table S2 and Figure 4b, the difference in activity could be attributed to the difference in specific surface area for the as-prepared CNTs, C/CNTs-foam and N@C/CNTs-foam. In that case, the activated carbon (AC) which is one of highest surface area among the carbonaceous materials (i.e. S_{BET} of 1511 m^2g^{-1}) was utilized for EB dehydrogenation reaction. However, the CA only presents a medium styrene yield of 1.64 $mmolSTg_{Catal}^{-1}h^{-1}$, which displays lower dehydrogenation activity than the N@C/CNT-15 catalysts. All the carbon-based metal-free catalysts display a high ST selectivity except the few-layer graphene.

XPS analysis (Figures S9 and S10) of the used N@C/CNT-15 sample indicates a slight decrease in the nitrogen concentration while the other species remain unchanged which confirm the high stability of the catalyst. The nitrogen decreases in the N@C/CNT-15 sample could be attributed to the carbon deposition during the prolonged reaction period which partly masked the nitrogen signal. The coke deposition is confirmed by temperature-programmed oxidation (TPO), which showed only low temperature combustion peak, which can be attributed to the low graphitized coke deposit (Figure 77c). On the contrary, the TPO analysis of the industrial K-Fe catalyst presents heavy coke formation after reaction (Figure 77d). This could be the major reason for the low activity obtained on the K-Fe catalyst due to the rapid blocking of the active surface. The spent N@C/CNT-15 catalyst can be fully generated by treating with diluted oxygen at 450^{o}C for 1h. As show in Figure S11 the DH performance of the N@C/CNT-15 foam catalyst is fully recovered (or even slightly enhanced) after two regenerations.

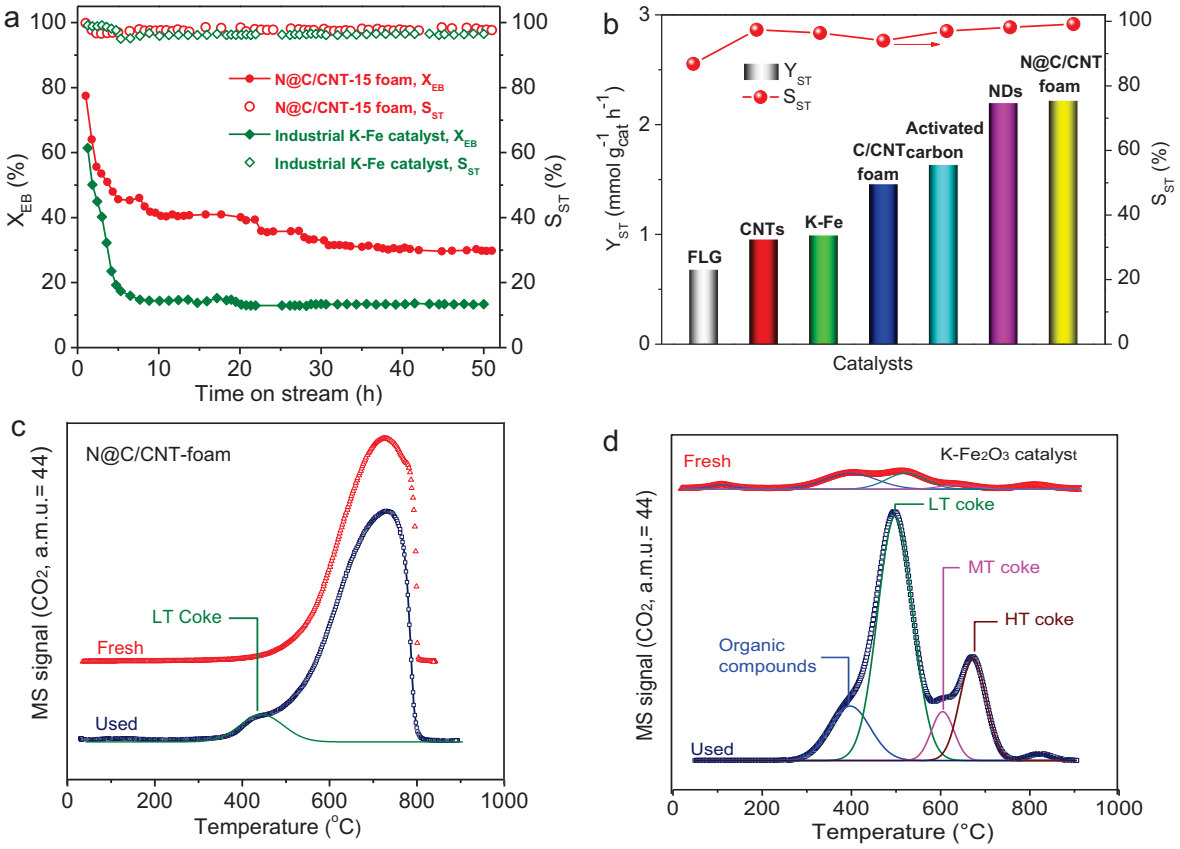

Figure 77. (a) Ethylbenzene (EB) dehydrogenation activity on N@C/CNT and industrial K-Fe catalysts. (b) Catalytic performance of various carbon-based catalysts and K-Fe2O3 catalyst under steady state. Reaction conditions: 300 mg, 550°C, 2.8 % EB in helium, 30 mL·min-1. X = conversion, S = selectivity, Y = yield. (c, d) CO2 formation during the temperature programmed oxidation tests on fresh and after DH reaction on the N@C/CNT-15 and (d) K-Fe_2O_3 catalysts. LT = low temperature, MT = medium temperature, HT = high temperature.

3. Conclusions

In conclusion, the N@C/CNT composite with controlled macroscopic shape was synthesized by a simple and low cost method using non-toxic food stuffs carbon and nitrogen precursors. The method also allows one to prepare porous carbon materials possessing high nitrogen loading which is not easy by traditional methods. The metal-free N@C/CNT composite exhibits a high efficiency in the ORR which is close to that of commercial Pt/C catalyst along with a superior long-term durability. In addition, such metal-free N@C/CNT catalyst also showed excellent activity in the steam-free dehydrogenation of ethylbenzene compared to that of the industrial K-Fe based catalyst. The same synthesis method could be

extended in the development of novel heteroatom-doped carbon material which could find use in the fields of catalysis, wastewater treatment and sustainable energy conversion and storage.

Acknowledgment

The present work is financially supported by a PF7 European project (FREECATS) under a contract number NMP-SL-2012-280658. The TEM and some part of SEM analysis were performed at the facilities of the IPCMS (UMR 7504 CNRS-University of Strasbourg) and T. Romero (ICPEES) is gratefully acknowledged for performing the SEM analysis. P. Bernhardt (ICPEES) is also gratefully acknowledged for the XPS analysis.

References

(1) Su, D. S.; Perathoner, S.; Centi, G., Nanocarbons for the Development of Advanced Catalysts. Chemical Reviews **2013**, 113, 5782-5816.

(2) Paraknowitsch, J. P.; Thomas, A., Doping carbons beyond nitrogen: an overview of advanced heteroatom doped carbons with boron, sulphur and phosphorus for energy applications. Energ Environ Sci **2013**, 6, 2839-2855.

(3) Gao, Y. J.; Hu, G.; Zhong, J.; Shi, Z. J.; Zhu, Y. S.; Su, D. S.; Wang, J. G.; Bao, X. H.; Ma, D., Nitrogen-Doped sp2-Hybridized Carbon as a Superior Catalyst for Selective Oxidation. Angew Chem Int Edit **2013**, 52, 2109-2113.

(4) Gong, K. P.; Du, F.; Xia, Z. H.; Durstock, M.; Dai, L. M., Nitrogen-Doped Carbon Nanotube Arrays with High Electrocatalytic Activity for Oxygen Reduction. Science **2009**, 323, 760-764.

(5) Qu, L. T.; Liu, Y.; Baek, J. B.; Dai, L. M., Nitrogen-Doped Graphene as Efficient Metal-Free Electrocatalyst for Oxygen Reduction in Fuel Cells. Acs Nano **2010**, 4, 1321-1326.

(6) Yang, W.; Fellinger, T. P.; Antonietti, M., Efficient Metal-Free Oxygen Reduction in Alkaline Medium on High-Surface-Area Mesoporous Nitrogen-Doped Carbons Made from Ionic Liquids and Nucleobases. J Am Chem Soc **2011**, 133, 206-209.

(7) Fellinger, T. P.; Hasche, F.; Strasser, P.; Antonietti, M., Mesoporous Nitrogen-Doped Carbon for the Electrocatalytic Synthesis of Hydrogen Peroxide. J Am Chem Soc **2012**, 134, 4072-4075.

(8) Chizari, K.; Deneuve, A.; Ersen, O.; Florea, I.; Liu, Y.; Edouard, D.; Janowska, I.; Begin, D.; Pham-Huu, C., Nitrogen-Doped Carbon Nanotubes as a Highly Active Metal-Free Catalyst for Selective Oxidation. Chemsuschem **2012**, 5, 102-108.

(9) Li, X. Y.; Pan, X. L.; Yu, L.; Ren, P. J.; Wu, X.; Sun, L. T.; Jiao, F.; Bao, X. H., Silicon carbide-derived carbon nanocomposite as a substitute for mercury in the catalytic hydrochlorination of acetylene. Nat Commun **2014**, 5.

(10) Zhang, P.; Sun, F.; Xiang, Z. H.; Shen, Z. G.; Yun, J.; Cao, D. P., ZIF-derived in situ nitrogen-doped porous carbons as efficient metal-free electrocatalysts for oxygen reduction reaction. Energ Environ Sci **2014**, 7, 442-450.

(11) Kundu, S.; Nagaiah, T. C.; Xia, W.; Wang, Y. M.; Van Dommele, S.; Bitter, J. H.; Santa, M.; Grundmeier, G.; Bron, M.; Schuhmann, W.; Muhler, M., Electrocatalytic Activity and Stability of Nitrogen-Containing Carbon Nanotubes in the Oxygen Reduction Reaction. J Phys Chem C **2009**, 113, 14302-14310.

(12) Lin, Y. M.; Su, D. S., Fabrication of Nitrogen-Modified Annealed Nanodiamond with Improved Catalytic Activity. Acs Nano **2014**, 8, 7823-7833.

(13) Li, X. H.; Antonietti, M., Polycondensation of Boron- and Nitrogen-Codoped Holey Graphene Monoliths from Molecules: Carbocatalysts for Selective Oxidation. Angew Chem Int Edit **2013**, 52, 4572-4576.

(14) Liang, J.; Du, X.; Gibson, C.; Du, X. W.; Qiao, S. Z., N-Doped Graphene Natively Grown on Hierarchical Ordered Porous Carbon for Enhanced Oxygen Reduction. Adv Mater **2013**, 25, 6226-6231.

(15) Li, H. B.; Kang, W. J.; Wang, L.; Yue, Q. L.; Xu, S. L.; Wang, H. S.; Liu, J. F., Synthesis of three-dimensional flowerlike nitrogen-doped carbons by a copyrolysis route and the effect of nitrogen species on the electrocatalytic activity in oxygen reduction reaction. Carbon **2013**, 54, 249-257.

(16) Wang, H. G.; Wu, Z.; Meng, F. L.; Ma, D. L.; Huang, X. L.; Wang, L. M.; Zhang, X. B., Nitrogen-Doped Porous Carbon Nanosheets as Low-Cost, High-Performance Anode Material for Sodium-Ion Batteries. Chemsuschem **2013**, 6, 56-60.
(17) Zhang, P. F.; Yuan, J. Y.; Fellinger, T. P.; Antonietti, M.; Li, H. R.; Wang, Y., Improving Hydrothermal Carbonization by Using Poly(ionic liquid)s. Angew Chem Int Edit **2013**, 52, 6028-6032.
(18) Zhang, S.; Miran, M. S.; Ikoma, A.; Dokko, K.; Watanabe, M., Protic Ionic Liquids and Salts as Versatile Carbon Precursors. J Am Chem Soc **2014**, 136, 1690-1693.
(19) Fellinger, T. P.; Thomas, A.; Yuan, J. Y.; Antonietti, M., 25th Anniversary Article: "Cooking Carbon with Salt": Carbon Materials and Carbonaceous Frameworks from Ionic Liquids and Poly(ionic liquid)s. Adv Mater **2013**, 25, 5838-5854.
(20) Tuci, G.; Zafferoni, C.; Rossin, A.; Milella, A.; Luconi, L.; Innocenti, M.; Phuoc, L. T.; Cuong, D. V.; Cuong, P. H.; Giambastian, G., Chemically Functionalized Carbon Nanotubes with Pyridine Groups as Easily Tunable N-Decorated Nanomaterials for the Oxygen Reduction Reaction in Alkaline Medium. Chem Mater **2014**, 26, 3460-3470.
(21) Florea, I.; Ersen, O.; Arenal, R.; Ihiawakrim, D.; Messaoudi, C.; Chizari, K.; Janowska, I.; Pham-Huu, C., 3D Analysis of the Morphology and Spatial Distribution of Nitrogen in Nitrogen-Doped Carbon Nanotubes by Energy-Filtered Transmission Electron Microscopy Tomography. J Am Chem Soc **2012**, 134, 9672-9680.
(22) Liu, S.; Tian, J. Q.; Wang, L.; Zhang, Y. W.; Qin, X. Y.; Luo, Y. L.; Asiri, A. M.; Al-Youbi, A. O.; Sun, X. P., Hydrothermal Treatment of Grass: A Low-Cost, Green Route to Nitrogen-Doped, Carbon-Rich, Photoluminescent Polymer Nanodots as an Effective Fluorescent Sensing Platform for Label-Free Detection of Cu(II) Ions. Adv Mater **2012**, 24, 2037-2041.
(23) Zhao, Y.; Nakamura, R.; Kamiya, K.; Nakanishi, S.; Hashimoto, K., Nitrogen-doped carbon nanomaterials as non-metal electrocatalysts for water oxidation. Nat Commun **2013**, 4.
(24. Sheng, Z. H.; Shao, L.; Chen, J. J.; Bao, W. J.; Wang, F. B.; Xia, X. H., Catalyst-Free Synthesis of Nitrogen-Doped Graphene via Thermal Annealing Graphite Oxide with Melamine and Its Excellent Electrocatalysis. Acs Nano **2011**, 5, 4350-4358.
(25) Chizari, K.; Vena, A.; Laurentius, L.; Sundararaj, U., The effect of temperature on the morphology and chemical surface properties of nitrogen-doped carbon nanotubes. Carbon **2014**, 68, 369-379.
(26) Sa, Y. J.; Park, C.; Jeong, H. Y.; Park, S. H.; Lee, Z.; Kim, K. T.; Park, G. G.; Joo, S. H., Carbon Nanotubes/Heteroatom-Doped Carbon Core-Sheath Nanostructures as Highly Active, Metal-Free Oxygen Reduction Electrocatalysts for Alkaline Fuel Cells. Angew Chem Int Edit **2014**, 53, 4102-4106.
(27) Wen, Z. H.; Ci, S. Q.; Hou, Y.; Chen, J. H., Facile One-Pot, One-Step Synthesis of a Carbon Nanoarchitecture for an Advanced Multifunctonal Electrocatalyst. Angew Chem Int Edit **2014**, 53, 6496-6500.
(28) He, W. H.; Jiang, C. H.; Wang, J. B.; Lu, L. H., High-Rate Oxygen Electroreduction over Graphitic-N Species Exposed on 3D Hierarchically Porous Nitrogen-Doped Carbons. Angew Chem Int Edit **2014**, 53, 9503-9507.
(29) Panomsuwan, G.; Chiba, S.; Kaneko, Y.; Saito, N.; Ishizaki, T., In situ solution plasma synthesis of nitrogen-doped carbon nanoparticles as metal-free electrocatalysts for the oxygen reduction reaction. Journal of Materials Chemistry A **2014**, 2, 18677-18686.
(30) Liang, H.-W.; Wu, Z.-Y.; Chen, L.-F.; Li, C.; Yu, S.-H., Bacterial cellulose derived nitrogen-doped carbon nanofiber aerogel: An efficient metal-free oxygen reduction electrocatalyst for zinc-air battery. Nano Energy **2015**, 11, 366-376.

(31) Zhang, J.; Su, D. S.; Blume, R.; Schlogl, R.; Wang, R.; Yang, X.; Gajovic, A., Surface chemistry and catalytic reactivity of a nanodiamond in the steam-free dehydrogenation of ethylbenzene. Angew Chem Int Ed **2010**, 49, 8640-4.
(32) Balasamy, R. J.; Khurshid, A.; Al-Ali, A. A. S.; Atanda, L. A.; Sagata, K.; Asamoto, M.; Yahiro, H.; Nomura, K.; Sano, T.; Takehira, K.; Al-Khattaf, S. S., Ethylbenzene dehydrogenation over binary FeOx-MeOy/Mg(Al)O catalysts derived from hydrotalcites. Appl Catal a-Gen **2010**, 390, 225-234.
(33) Ba, H.; Podila, S.; Liu, Y.; Mu, X.; Nhut, J.-M.; Papaefthimiou, V.; Zafeiratos, S.; Granger, P.; Pham-Huu, C., Nanodiamond decorated few-layer graphene composite as an efficient metal-free dehydrogenation catalyst for styrene production. Catal Today **2015**, doi:10.1016/j.cattod.2014.10.029.
(34) Louis, B.; Gulino, G.; Vieira, R.; Amadou, J.; Dintzer, T.; Galvagno, S.; Centi, G.; Ledoux, M. J.; Pham-Huu, C., High yield synthesis of multi-walled carbon nanotubes by catalytic decomposition of ethane over iron supported on alumina catalyst. Catal Today **2005**, 102, 23-28.
(35) Gulino, G.; Vieira, R.; Amadou, J.; Nguyen, P.; Ledoux, M. J.; Galvagno, S.; Centi, G.; Pham-Huu, C., C2H6 as an active carbon source for a large scale synthesis of carbon nanotubes by chemical vapour deposition. Appl Catal a-Gen **2005**, 279, 89-97.

Supporting information

Synthesis of nitrogen-doped carbon foam composite

In the synthesis procedure 2 g of dextrose was mixed with 3 g of citric acid by mechanical crushing at room temperature. Then, a known amount of ammonium carbonate (i.e. 1g) was added via a mechanical mixing to obtain a homogeneous solid mixture. The ammonium carbonate is used as nitrogen source and pores forming agent during the thermal treatment. In this synthesis the toxic nitrogen source precursors usually employed in the traditional process is replaced by a non-toxic and cheap one, i.e. ammonium carbonate which is well-known as a leavening agent. In order to control the shape and mechanical strength of the final nitrogen-doped carbon composite, carbon nanotubes (CNT) was used as a solid skeleton. Carbon nanotubes were synthesized by a chemical vapour deposition (CVD) process using a Fe/γ-Al2O3 as growth catalyst and a mixture of C2H6 and H2 as carbon source.34, 35 The product was submitted to a basic and acid treatment at 110 °C in order to remove as much as possible the residual growth catalyst before further processing. The CNTs were mechanically mixed with the ammonium carbonate, dextrose and citric acid mixture followed by thermal treatments to produce the nitrogen-doped carbon nanotubes foam composite with high nitrogen loading. The mixture was reacted in an oven at 130 °C for 5 h to obtain the shaped carbon nanotubes foam precursor. The shaped carbon foam precursor was further treated by heating up to 450 °C (2 oC/min) under air flow for 3 h followed an annealing step in helium at 900 oC (5 oC/min) for 2 h for improve the graphitization degree for ORR test. The annealed composite was marked as N@C/CNT-X(G), where X denoted the total nitrogen content in composite, G means graphitization treatment at 900 oC under helium flow.

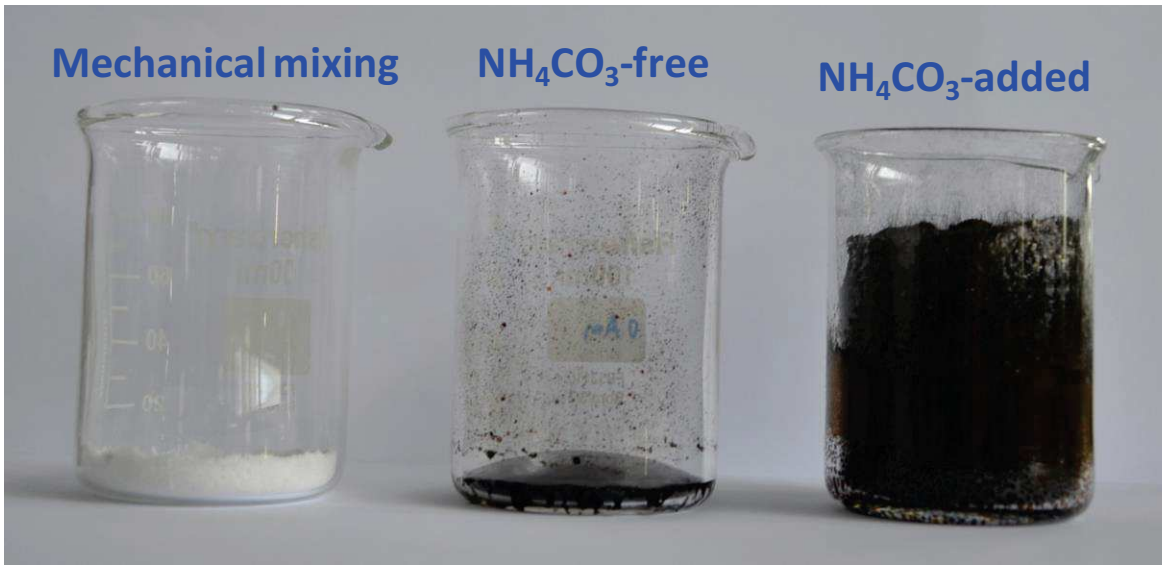

Figure S1. Optical photos show the sample self-macronized when $(NH_4)_2CO_3$ presented.

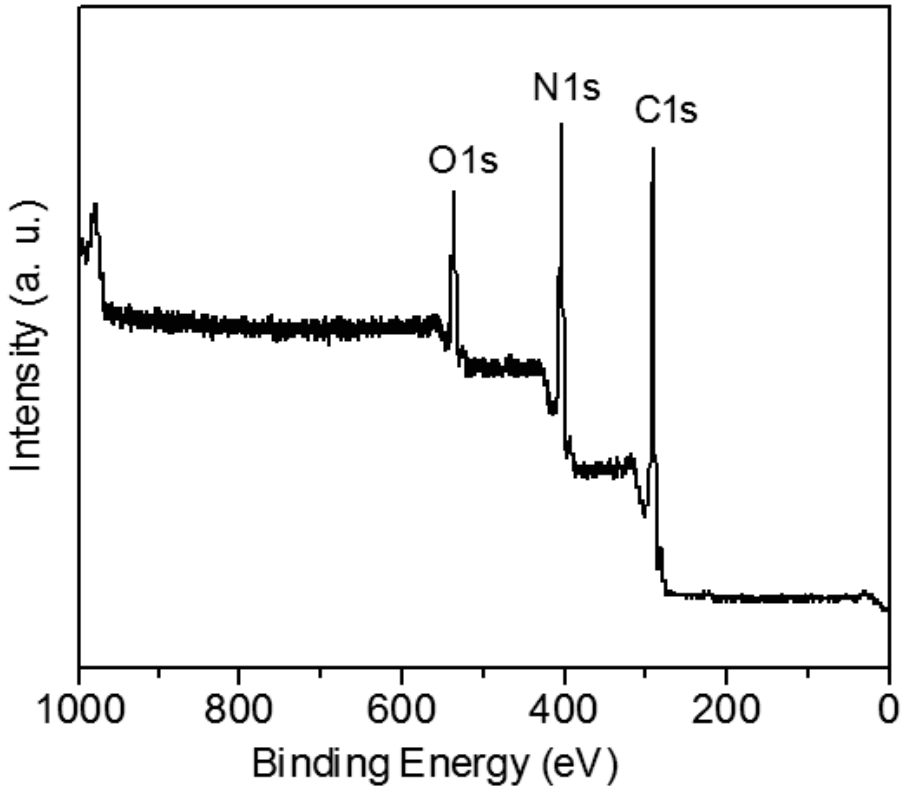

Figure S2. Survey scan XPS spectra of porous nitrogen-doped carbon materials.

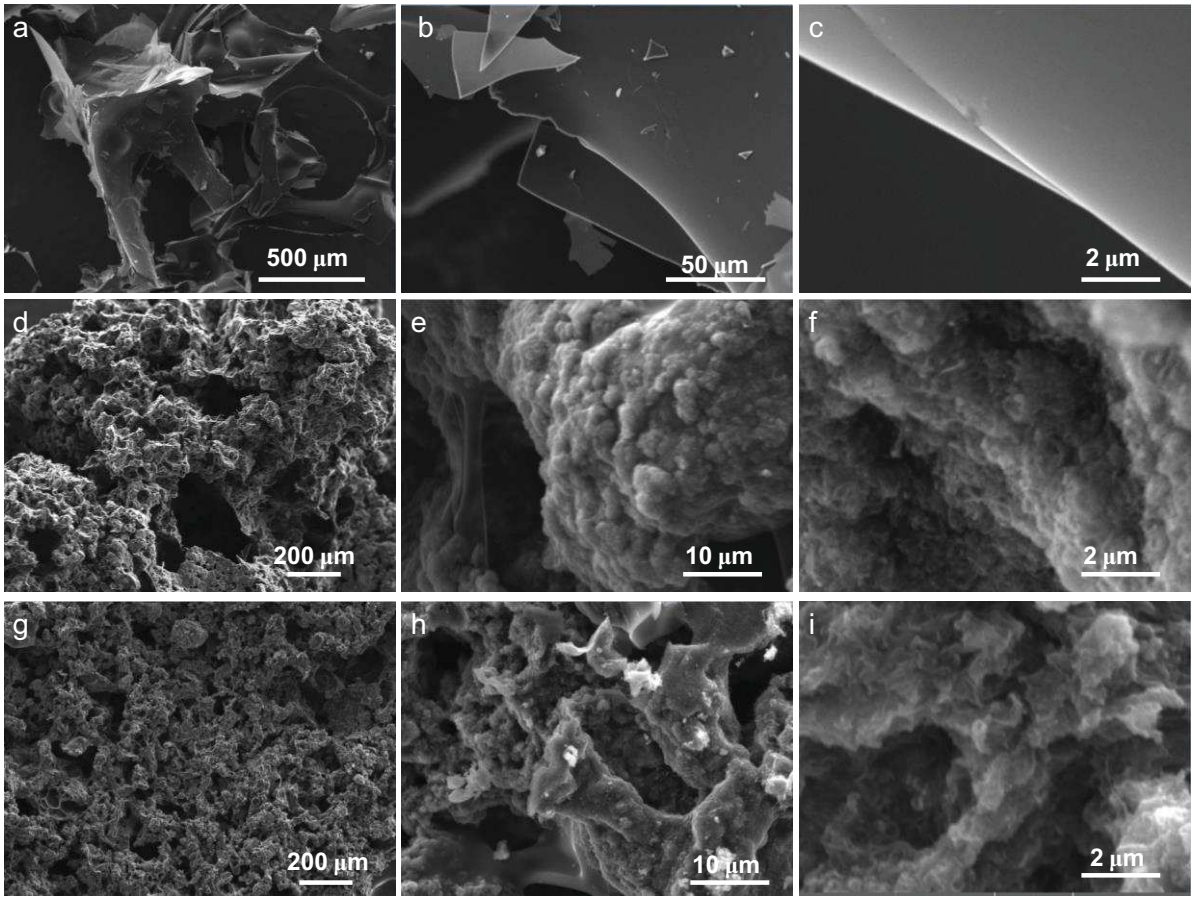

Figure S1. SEM images of nitrogen-doped carbon materials synthesized with different CNTs amounts. (a-c) CNTs-free, CNTs/dextrose mass ratio of (d-f) 0.25 and (g-i) 0.5, respectively.

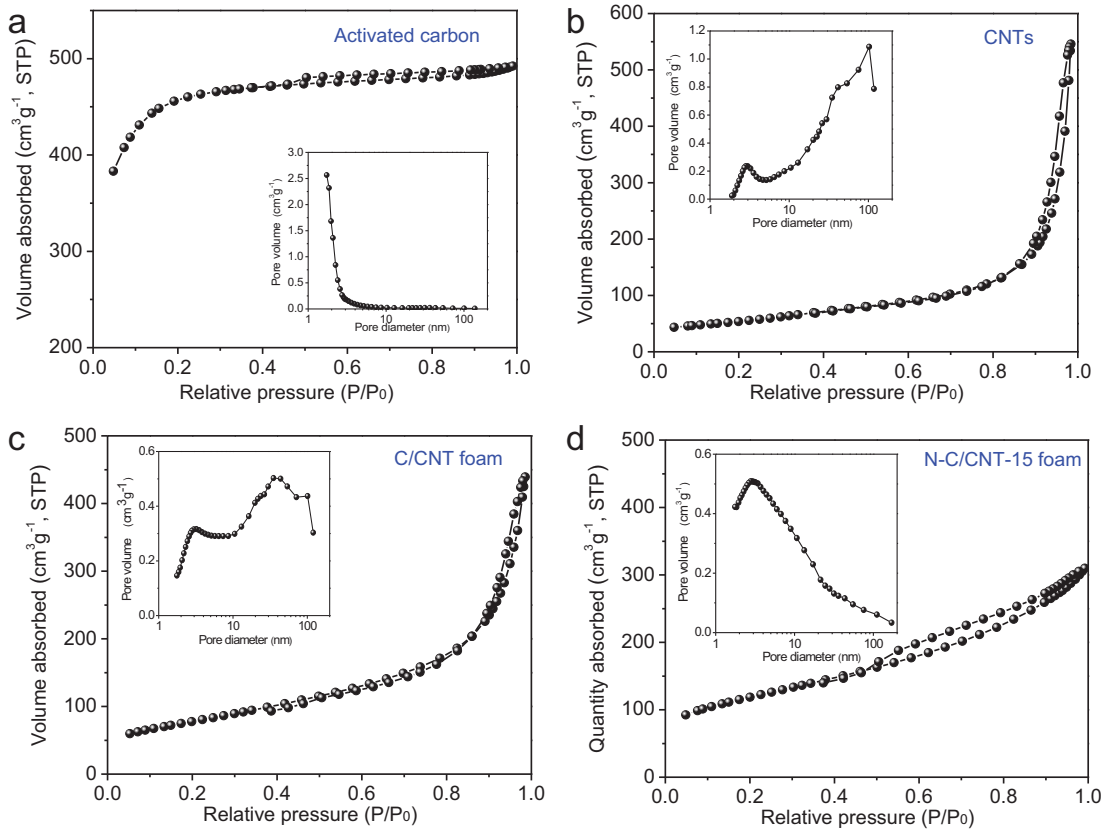

Figure S2. N_2 adsorption-desorption isotherms and corresponding pore size distribution (inset) of various carbon materials.(a) activated carbon, (b) pristine carbon nanotubes, (c) C/CNT foam and (d) N-C/CNT-15 foam (the composite with nitrogen concentration of around 15.28 at.%).

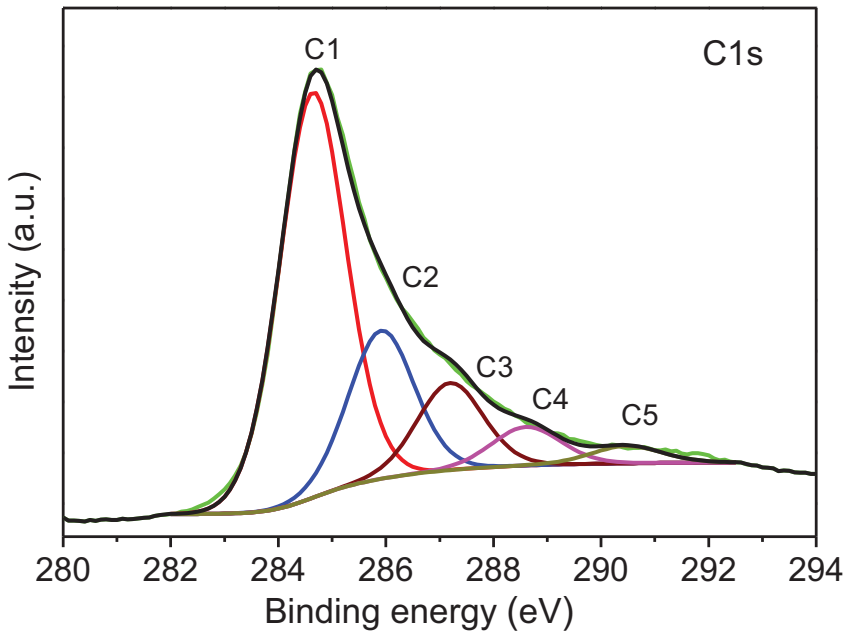

Figure S3. C1s high-resolution XPS spectra of N-C/CNT-15 foam composite.

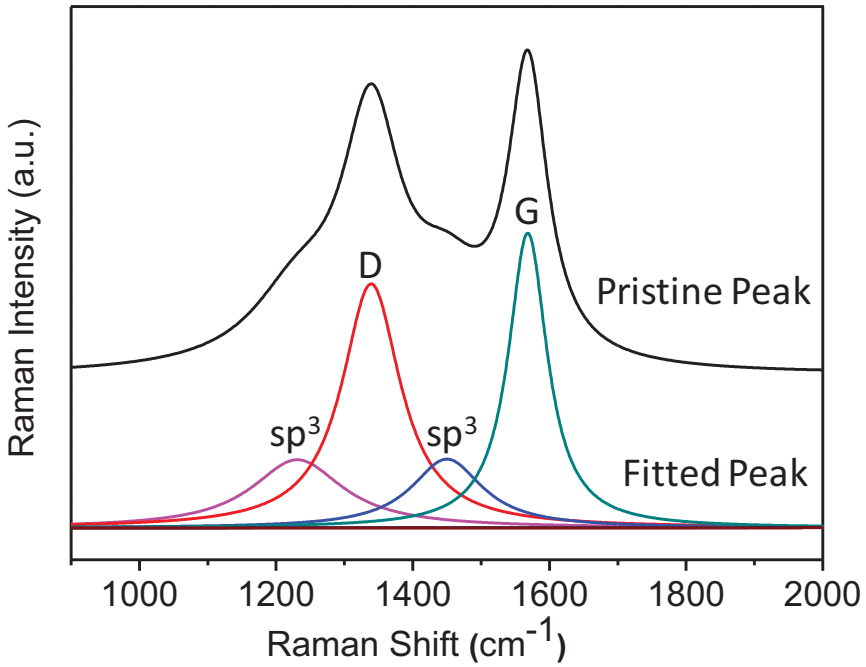

Figure S4. Peak-fitted and assigned Raman spectrum of C-N/CNT-15 foam composite.

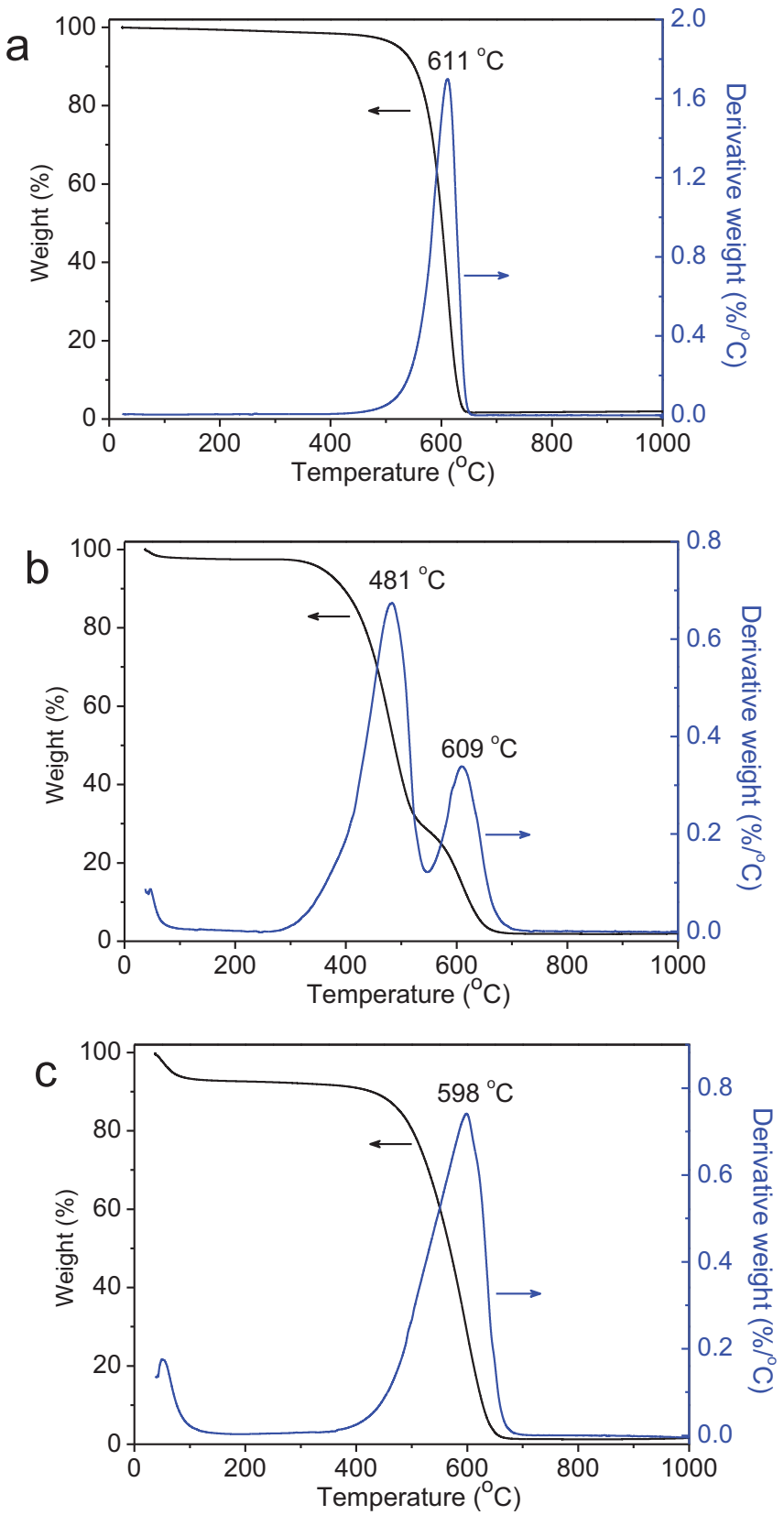

Figure S5. Thermal gravimetric analysis curve of (a) carbon nanotubes, (b) C/CNT foam and (c) N-C/CNT-15 foam composites.

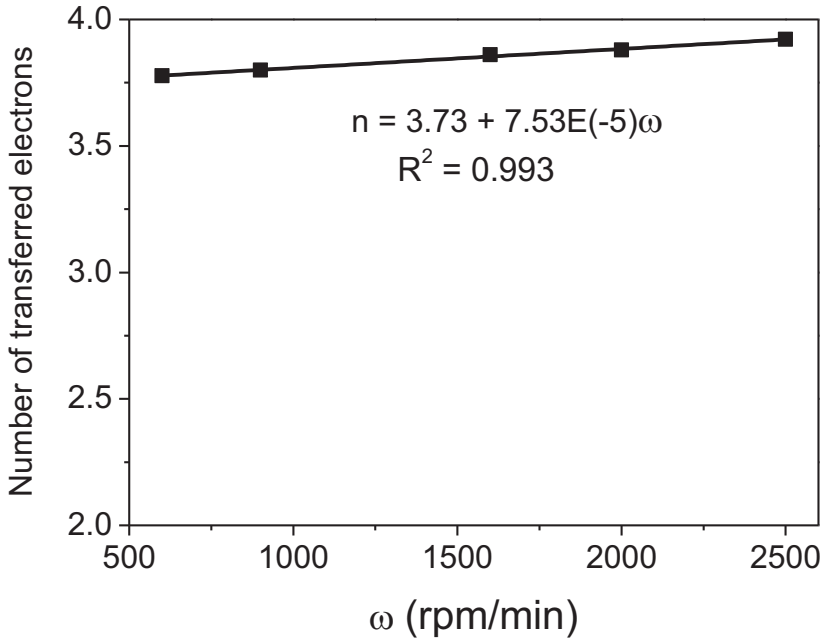

Figure S6. The Koutecky-Levich (K-L) slope at 0.4eV showing the similar 4e$^-$ transfer mechanism between the Pt/C and N@C/CNT catalysts.

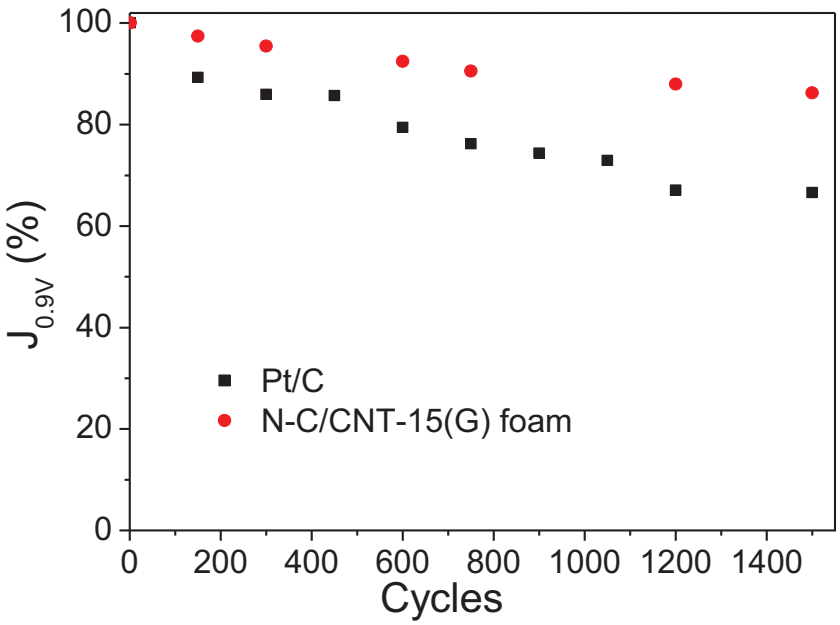

Figure S7. Stability of the Pt/C and N-C/CNT-15(G) foam catalysts for the ORR

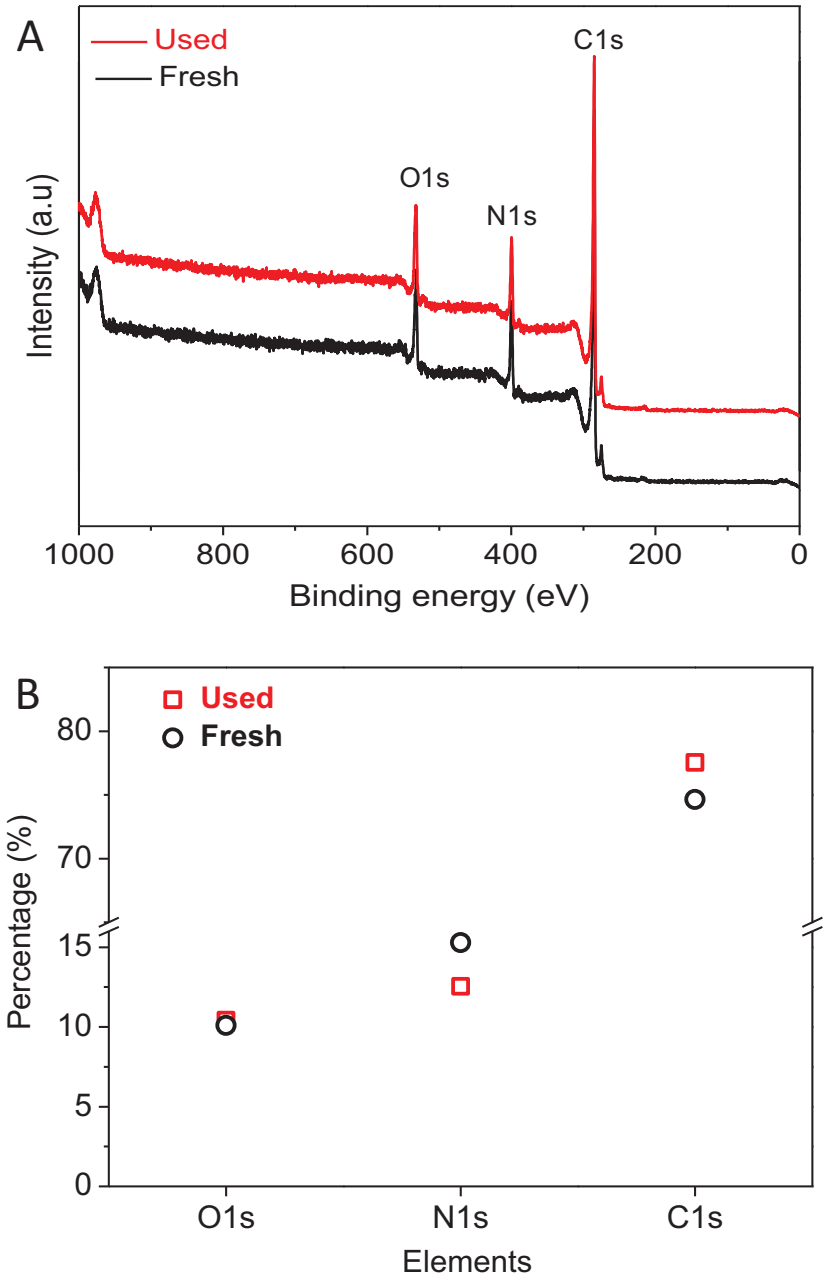

Figure S8. (A) XPS survey spectra and (B) evolution of various elements present on the surface of nitrogen-rich CNT-foam (N-C/CNT-15 foam) before and after EB dehydrogenation reaction.

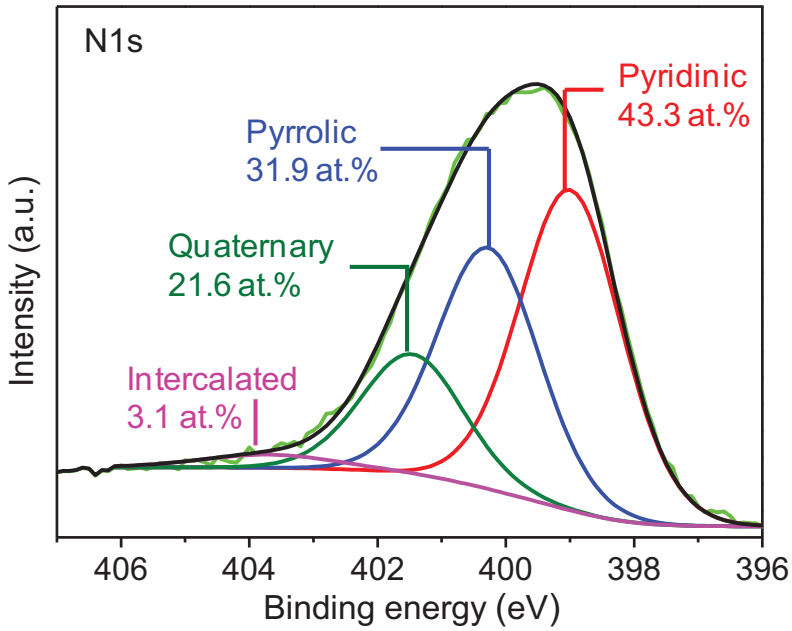

Figure S9. N1s high-resolution XPS spectra and N species concentration of N-C/CNT-15 foam after EB dehydrogenation reaction.

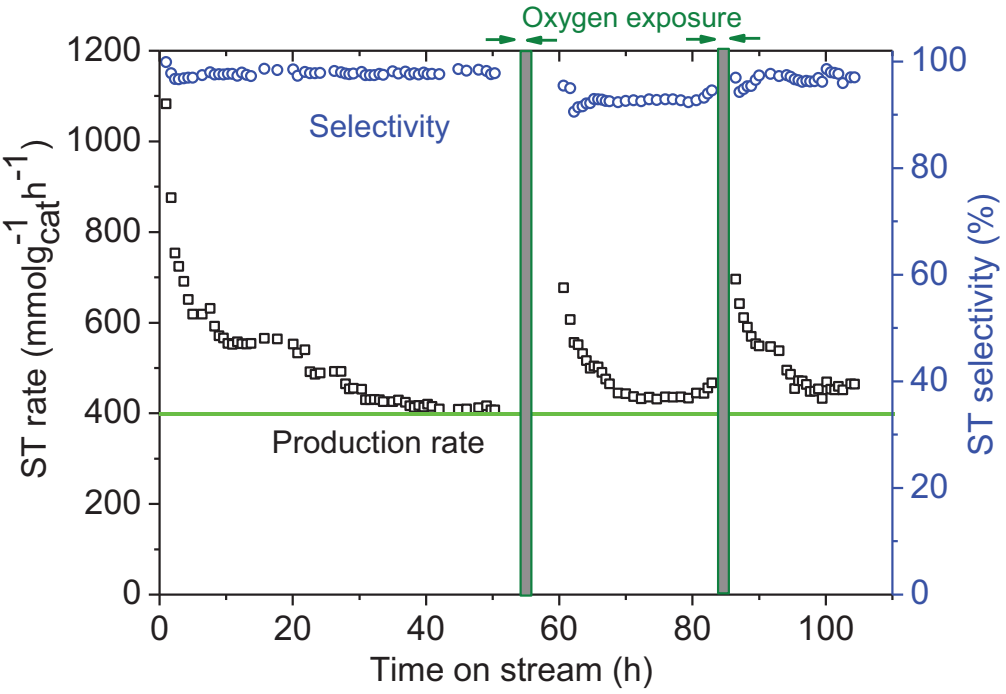

Figure S10. Results of cycling dehydrogenation reaction followed oxygen exposure on N-C/CNT-15 foam composite. Reaction conditions: 300 mg, 550 °C, 2.8 % EB in helium, 30 mL·min^{-1}. Oxygen exposure conditions: 450 °C, O_2/He 20 v/v%, 30 mL·min^{-1}, 2 h.

Table S1. Elemental composition of prepared N-C/CNT-foam composite

Sample	Mass ratio of ammonium carbonate and dextrose	C (at. %)	O (at. %)	N (at. %)	N/C ratio
CNTs	-	90.68	9.32	-	
C/CNT foam	-	83.02	16.98	-	
N-C/CNT-14 foam	0.25	76.84	8.71	14.45	0.19
N-C/CNT-15 foam	0.5	74.63	10.09	15.28	0.20
N-C/CNT-17 foam	1.5	73.38	9.43	17.19	0.23
N-C/CNT-18 foam	2	68.05	13.77	18.18	0.27
N-C/CNT-19 foam	2.5	68.33	12.80	18.87	0.28
N-C/CNT-19.5 foam	5	72.43	8.07	19.50	0.26
N-C/CNT-18.5 foam	7.5	73.19	7.97	18.84	0.26

Table S2 BET surface area and pore volume of prepared carbon materials.

Sample	Surface area ($m^2 \cdot g^{-1}$)	Total pore volume ($cm^3 \cdot g^{-1}$)	BJH pore diameter (nm)
Activated carbon	1511	0.76	2.2
CNTs	189	0.85	17
C/CNT foam	279	0.68	9.4
N-C/CNT-15 foam	418	0.50	4.8
N-C/CNT-19.5 foam	461	0.16	3.2

Table S3. Electrocatalytic performance of N-C/CNT-15(G) foam and 20 wt% Pt/C

	E_{on} / mV	$E_{1/2}$ / mV	I at 0.9V ($mA.cm^{-2}$)	n / e
20 wt% Pt/C	1080 ± 10	902 ± 5	-2.35	4
N-C/CNT-15(G) foam	1050 ± 10	841 ± 5	-1.48	3.78 ÷ 3.92

A Highly N-Doped Carbon Phase "Dressing" of Macroscopic Supports for Catalytic Applications

Housseinou Ba,[a,c,§] Yuefeng Liu,[a,§] Lai Truong-Phuoc,[a] Cuong Duong-Viet,[a] Xiaoke Mu,[a] Won Hui Doh,[a] Tung Tran-Thanh,[a] Walid Baaziz,[a] Lam Nguyen-Dinh,[b] Jean-Mario Nhut,[a] Izabela Janowska,[a] Dominique Begin,[a] Spiridon Zafeiratos,[a] Pascal Granger,[c] Giulia Tuci,[d] Giuliano Giambastiani,[d,f,*] Florian Banhart,[e] Marc J. Ledoux[a] and Cuong Pham-Huu[a]

[a].*Institut de Chimie et Procédés pour l'Energie, l'Environnement et la Santé (ICPEES), ECPM, UMR 7515 CNRS-Université de Strasbourg, 25, rue Becquerel, 67087 Strasbourg Cedex 02, France. E.mail: cuong.pham-huu@unistra.fr*

[b].*The University of Da-Nang, University of Science and Technology, 54 Nguyen Luong Bang, Da-Nang, Viet-Nam.*

[c].*Unité de Catalyse et Chimie du Solide (UCCS), UMR 8181 du CNRS-Université de Lille-1, Bâtiment C3, Université Lille-1, 59655 Villeneuve d'Ascq Cedex, France.*

[d].*Institute of Chemistry of OrganoMetallic Compounds, ICCOM-CNR and Consorzio INSTM, Via Madonna del Piano, 10 – 50019, Sesto F.no, Florence, Italy. E-mail: giuliano.giambastiani@iccom.cnr.it*

[e].*Institut de Physique et Chimie des Matériaux de Strasbourg (IPCMS), UMR 7504 CNRS-University of Strasbourg, 23, rue du Loess, 67034 Strasbourg Cedex 02, France.*

[f].*Kazan Federal University, 420008 Kazan, Russian Federation.*

Article published in Chemical Communications: 10.1039/C5CC05259A

Graphical and textual abstract

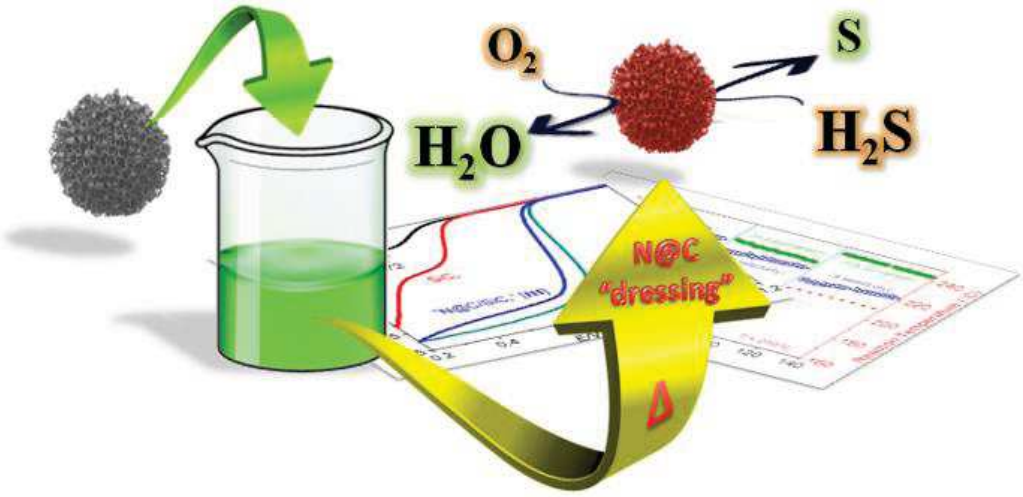

Various macroscopic and porous host scaffolds are easily "dressed" with highly N-doped carbon-based coatings.The as prepared composites act as effective metal-free catalysts in industrial key-processes.

Abstract

A challenging matter of modern and sustainable catalysis is to re-think key-processes at the heart of renewable energy and environmental technology in light of metal-free catalytic architectures designed and fabricated from cheap and easily accessible building blocks. An innovative synthetic protocol based on cheap foodstuff components, allows for the effective “dressing” of an assorted range of macroscopic scaffolds with a coating of a highly N-doped, mesoporous carbon phase. The as-obtained composites can be exploited as metal-free catalysts in industrial key-processes, offering high (and to some extent better) catalytic performance and long-term stability compared with those of the classical metal-based systems of the state-of-the-art. The versatility of the described technology allows for an easy scaffold selection (in the form of powder, grains, beads, extrudates or foams) depending on its ultimate downstream application (gas or liquid-phase catalytic reactors). The remarkable achievements in the electrochemical oxygen reduction reaction (ORR) as well as in the partial H2S oxidation from refinery tail gas are promising, and they set the way to the exploitation of the outlined catalyst technology to other industrial contexts.

1. Introduction

One main challenge of modern and sustainable catalysis is to re-think fundamental metal-based catalytic processes while eliminating critical raw components like expensive noble metals. The exploitation of tailored metal-free catalytic architectures designed and fabricated from cheap and easily accessible building blocks may represent a valuable and green alternative. Nitrogen-doped 1D and 2D carbon nanomaterials (N-CNMs), have emerged in the last decade as effective metal-free systems, capable of promoting a high number of catalytic processes.[1-8] Since the pioneering work by Gong et al.,[1] independent studies have demonstrated how the inclusion of nitrogen(s) in the honeycomb carbon structure breaks the electroneutrality of the Csp^2 network[9,10] and generates charged active sites.[11] Their presence plays a pivotal role on the ultimate material catalytic activity, sometimes offering performance comparable or even better than that observed with classical metal-based systems. Among the synthetic approaches known for the production of N-CNMs systems, Chemical Vapour Deposition (CVD) still remains the most popular and widely used technique. At odds with its feasibility, CVD suffers from a number of serious drawbacks: (i) the use of nitrogen precursors with relatively high toxicity [i.e. pyridine,[12,13] acetonitrile,14 ammonia[15,16]]; (ii) tricky reaction environments based on hydrocarbons and/or hydrogen atmosphere (which typically necessitate of specific safety operative precautions); (iii) high operation temperatures. In addition, significant loss of the N- and C-containing gaseous reagents throughout the synthesis (including their partial thermal decomposition into waste and toxic by-products), denotes a rather low atom efficiency of the CVD technique. All together, these aspects make CVD unattractive, because of its heavy environmental impact and unsustainable production costs.

In recent years, the joint efforts of chemists, physicists and engineers have paved the way to the development of a number of innovative synthetic tools for the efficient and controlled carbon nanomaterials N-decoration/doping.[11,17,18] Despite of the potential interest for N-doped CNMs as metal-free, single-phase catalysts in a series of industrially relevant processes, none of the emerging synthetic technologies has really fulfilled the requirements for their sustainable and environmentally friendly large-scale production. In addition, the difficult handling, caused by the prevalent powdery texture of the CNMs, has dramatically limited their extensive exploitation as catalysts in both gas- and liquid phase processes.

This contribution describes a straightforward and environmentally benign methodology for the preparation of highly N-doped CNMs starting from non-toxic, raw and abundant organic building blocks. A shape-adaptable, highly N-doped mesoporous carbon phase is properly grown as a truly metal-free “catalytic clothing” at the surface of macroscopically shaped supports. Various matrices based on silicon carbide (β-SiC)[19,20] in the form of powder

(< 40 μm), grains (150 - 400 μm), extrudates (1 x 2 mm) and foams (from mm to cm) or α-Al_2O_3 beads (mm), are selected as catalyst scaffolds (Fig. S2†).

Ammonium carbonate [$(NH_4)_2CO_3$], citric acid ($C_6H_8O_7$) and D-glucose are the non-toxic foodstuff constituents of a homogeneous aqueous pre-catalytic phase to be used as an impregnating solution where the catalysts scaffolds are soaked.[21,22] Successive thermal treatments of the impregnated β-SiC (or α-Al_2O_3) supports generate highly N-doped, carbonaceous surface coatings featured by Specific Surface Areas (SSA) and basicity higher than those of the pristine host matrices (vide infra).

A first thermal treatment at 130 °C in air (drying) produces a thin pre-catalytic coating of the host scaffolds essentially made of D-glucose and basic ammonium citrate (Figs. 1 and S1†). The soaking/drying treatment can be repeated for a number of times at will, thus increasing the thickness of the pre-catalytic deposit. The coating C/N ratio can also be tuned by adopting various compositions of the impregnating phase [i.e. solutions at various D-glucose/$(NH_4)_2CO_3$/citric acid molar ratios] during the successive soaking/drying cycles (Table S1†, entries 1 vs. 4 and 2 vs. 5).

Two final treatments, at 450 °C under air and at 900 °C under inert atmosphere (annealing), "dress" the support with a N-doped mesoporous carbon phase (N@C) (Figs. 78, S2†).[22]

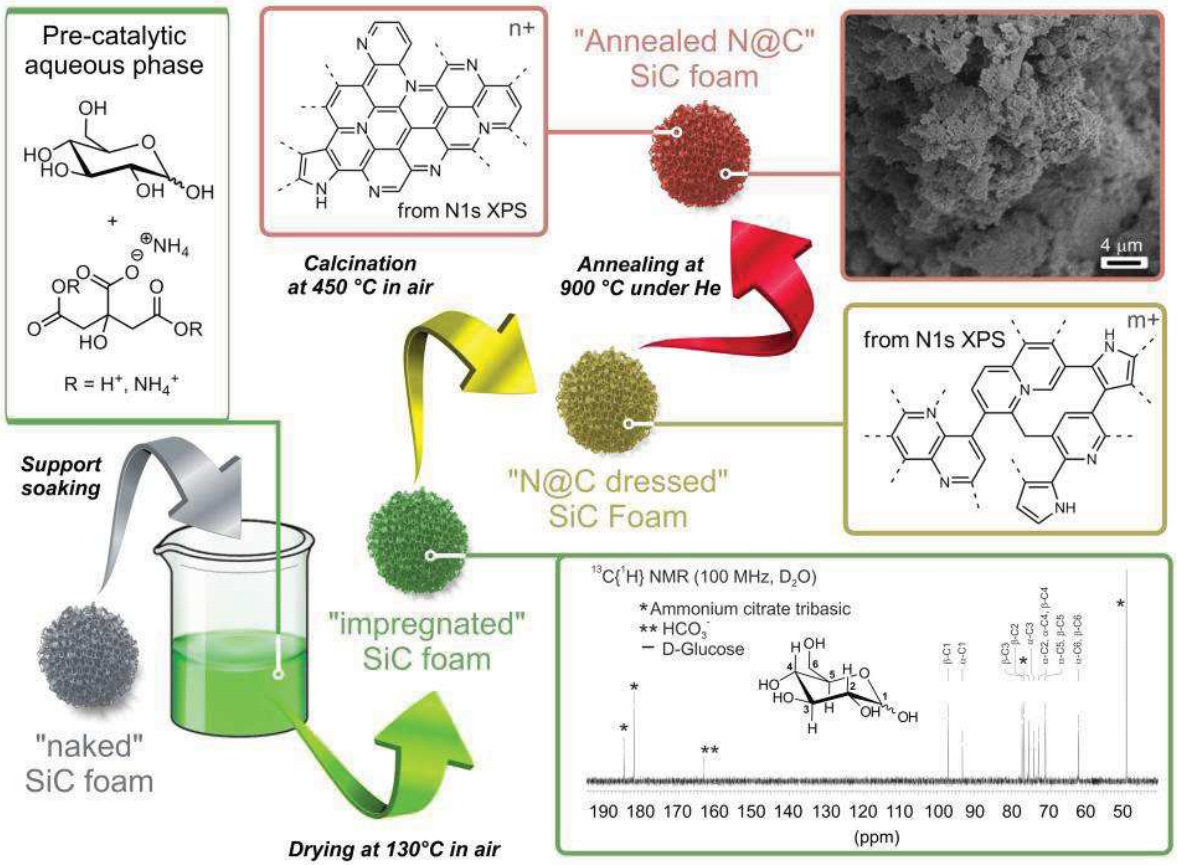

Fig. 78 Synthesis of a highly N-doped carbon-based coating (N@C) on a model macroscopically shaped host matrix (SiC foam). Arrows refer to the four sequential synthetic steps; from the material soaking and drying up to its calcination at 450 °C in air followed by annealing at 900 °C under inert atmosphere. The N@C surface coating composition is determined by either $^{13}C\{1H\}$ NMR spectroscopy (for the water-soluble pre-catalytic phase at the surface of the impregnated composite) and N1s XPS analysis for the samples treated at 450 and 900 °C, respectively (see also Fig. 2). NMR spectrum refers to a model pre-catalytic phase prepared dissolving 2g of D-Glucose, 3g of citric acid and 2.3g of $(NH_4)_2CO_3$ in 500 mL of ultrapure Milli-Q water and repeating the soaking/drying phase twice. SEM image refers to the typical porous texture of the N@C phase after material annealing.

Thermal treatments induce polymerization/condensation processes that enhance the N@C phase adhesion to the host scaffold; at the same time, they improve its ultimate electrical and thermal conductivity.

D-Glucose represents the main source of carbon in the process, while the basic ammonium citrate (in the forms of tri-, di- or mono-basic, depending on the ammonium carbonate/citric acid molar ratio used) plays the double role of N-reservoir and pore forming agent ("leavening" agent; Fig. S3†) throughout the two last thermal phases.

The as-prepared composites are conventionally designated as follows: AN@C/(supp)xy, where the superscript "A" denotes "annealed samples" (900°C under inert atmosphere), "N@C/(supp)" stands for a composite made of a catalyst support (supp = β-SiC or α-Al_2O_3)

coated with the N@C active-phase, the "X" subscript illustrates the pristine support texture (P = powder; G = grains; E = extrudates; F = foams) and the "Y" superscript displays the number of performed impregnation/drying cycles.

2. Results and discussion

The N@C composites show higher SSA values compared to the respective pristine supports (Fig. S4†, and Table S1†). For the model AN@C/$(SiC)_E^2$ composite [**V**] (Table S1†, entry 5), the SSA increases up to five times above its original value (Fig. S4†, SSA (SiC_E): 29 m^2/g vs. SSA [AN@C/$(SiC)_E^2$]: 144 m^2/g).[22] A higher basicity of the N@C composites, compared to the bare catalyst supports, has also been measured. The pH value of an aqueous dispersion of [**III**] (Table S1†, entry 3) grows to 9.6 from pH 6.6 of the bare SiC_P support (Fig. S5†).23

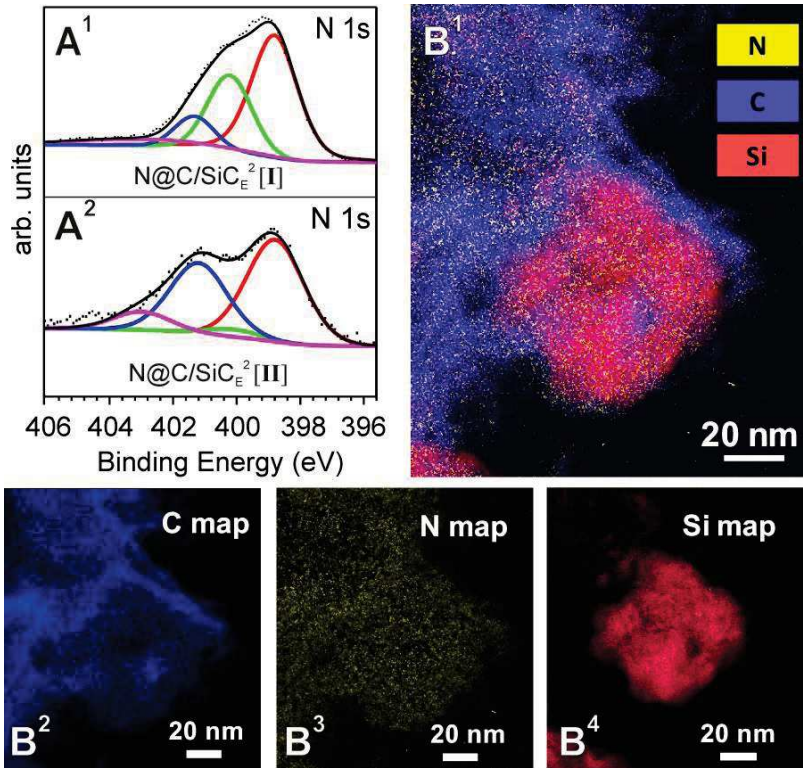

Fig. 79 (A) High-resolution N 1s XPS spectra of two samples prepared from extrudate SiC supports (Table S1†, entries 1-2). SiC_E undergoes two impregnation/drying cycles before being heated at 450 °C in air for 2h (A1) and annealed at 900 °C under He atmosphere for 1h (A2). (B) STEM-EELS analysis of the annealed sample [**III**] (Table S1†, entry 3). Colours labelling in the elemental map B1 are: yellow for Nitrogen, red for Silicon and blue for Carbon. Separate element maps are shown in Fig. B2 (carbon), B3 (nitrogen) and B4 (silicon).

Such a distinctive feature, not observed in traditionally prepared (CVD) N-doped CNMs, is ascribed to an exceptionally high density of surface-exposed basic N-sites. N 1s XPS analysis provides details on the nature of the N-species available at the N@C phase and how they change throughout the successive thermal treatments. As Fig. 79 [A1 vs. A2] shows, the model composites [**I**] and [**II**] (Table S1†) present three and two main components, respectively, along with a common minor shoulder at higher binding energies (403,1 eV ascribed to N-oxidized species). Curve fitting for sample [**I**] is consistent with the presence of pyridinic (398.8 eV – red line; 55 %), pyrrolic (400.2 eV – green curve; 29 %) and quaternary (401.3 eV; 11 %) nitrogens, respectively [Fig. 79, A1]. Thermal annealing translates into an N@C phase made of N-pyridinic (398.8 eV; 43 %) and quaternary N-groups (401.3 eV; 37 %) almost exclusively (Fig. 79, A2 Table S1†, entries 1 vs. 2 and 4 vs. 5). Thermo gravimetric (TGA, Fig. S6†) and elemental analyses (Table S1†) are then used to determine the N wt. % at the N@C phase for each sample[24] (Table S1†). Measurements have unveiled remarkably high N-contents (normalized to the N@C mass deposit on the catalyst support): 32 wt. % (Table S1†, entry 1) for samples treated in air at 450°C and 23 wt. % for annealed composites (Table S1†, entry 3). Electron energy-loss spectroscopy (EELS) in High-Resolution STEM (STEM-EELS) analysis conducted on the model composite [**III**] (Table S1†, entry 3) confirms the high N-concentration at the material topmost surface [Figs. 79, B1-B4 and S7†, S8†][22].

3. Conclusions

In summary, the proposed methodology offers a really sustainable and valuable approach to the generation of highly adaptable N-doped, carbon porous active phases (N@C) capable of “dressing” different macroscopic host scaffolds. Depending on the downstream catalytic application of the final composites (gas-phase or liquid-phase reactors), the porous N@C carbon phases are grown in the form of tight coatings on different supports: powders, grains, beads, extrudates and foams. At odds with the classical CVD technique, C and N sources for this methodology are cheap solid feedstock, neither toxic nor dangerous or explosive. Most importantly, their conversion into highly N-doped porous carbon phases meets the requirements of atom efficiency, negligible environmental impact and low production.

Acknowledgments

This work was financially supported by the Freecats FP7 European project (contract n° NMP3-SL-2012-280658). The authors would like to thank Sicat Co. (www.sicatcatalyst.com) for supplying the SiC supports within the framework of the above mentioned project.

References

(1) K. Gong, F. Du, Z. Xia, M. Durstock, L. Dai, Science, **2009**, 323, 760.
(2) Y. Li, W. Zhou, H. Wang, L. Xie, Y. Liang, F. Wei, J.-C. Idrobo, S. J. Pennycook, H. Dai, Nat. Nanotechnol., **2012**, 7, 394.
(3) R. Liu, D. Wu, X. Feng, K. Müllen, Angew. Chem. Int. Ed., 2010, 49, 2565.
(4) K. Chizari, A. Deneuve, O. Ersen, I. Florea, Y. Liu, D. Edouard, I. Janowska, D. Begin, C. Pham-Huu, ChemSusChem, **2012**, 5, 102.
(5) D. S. Su, S. Perathoner, G. Centi, Chem. Rev., **2013**, 113, 5782.
(6) F. Bonaccorso, L. Colombo, G. Yu, M. Stoller, V. Tozzini, A. C. Ferrari, R. S. Ruoff, V. Pellegrini, Science, **2015**, 347, 1246501.
(7) S. Yang, X. Feng, X. Wang, K. Müllen, Angew. Chem. Int. Ed., 2011, 50, 5339.
(8) X. Li, X. Pan, L. Yu, P. Ren, X. Wu, L. Sun, F. Jiao, X. Bao, Nat. Commun., **2014**, 5, ncomms4688-1.
(9) C. Zhou, J. Kong, E. Yenilmez, H. Dai, Science, **2000**, 290, 1552.
(10) X. Wang, X. Li, L. Zhang, Y. Yoon, P. K. Weber, H. Wang, J. Guo, H. Dai, Science, **2009**, 324, 768.
(11) G. Tuci, C. Zafferoni, A. Rossin, A. Milella, L. Luconi, M. Innocenti, L. Truong Phuoc, C. Duong-Viet, C. Pham-Huu, G. Giambastiani, Chem. Mater., **2014**, 26, 3460.
(12) C. Shan, W. Zhao, X. L. Lu, D. J. O'Brien, Y. Li, Z. Cao, A. L. Elias, R. Cruz-Silva, M. Terrones, B. Wei, J. Suhr, Nano. Lett., **2013**, 13, 5514.
(13) Y. Xue, B. Wu, L. Jiang, Y. Guo, L. Huang, J. Chen, J. Tan, D. Geng, B. Luo, W. Hu, G. Yu, Y. Liu, J. Am. Chem. Soc., **2012**, 134, 11060.
(14) Y. Xia, G. S. Walker, D. M. Grant, R. Mokaya, J. Am. Chem. Soc., **2009**, 131, 16493.
(15) T. Susi, A. Kaskela, Z. Zhu, P. Ayala, R. Arenal, Y. Tian, P. Laiho, J. Mali, A. G. Nasibulin, H. Jiang, G. Lanzani, O. Stephan, K. Laasonen, T. Pichler, A. Loiseau, E. I. Kauppinen, Chem. Mater., **2011**, 23, 2201
(16) L. Qu, Y. Liu, J.-B. Baek, L. Dai, ACS Nano, 2010, 4, 1321.
(17) W. He, C. Jiang, J. Wang, L. Lu, Angew. Chem. Int. Ed., **2014**, 53, 9503.
(18) Y. Meng, X. Zou, X. Huang, A. Goswami, Z. Liu, T. Asefa, Adv. Mater., **2014**, 26, 6510.
(19) Y. Liu, O. Ersen, C. Meny, F. Luck, C. Pham-Huu, ChemSusChem, **2014**, 7, 1218.
(20) P. Nguyen, C. Pham, Appl. Catal. A-Gen., **2011**, 391, 443.
(21) C. Pham-Huu, G. Giambastiani, Y. Liu, H. Ba, L. Nguyen-Dinh, J.-M. Nhut, Eur. Pat. Appl. No. EP 15-152038 (**2015**).
(22) Details available on the ESI material.
(23) R. Arrigo, M. Hävecker, S. Wrabetz, R. Blume, M. Lerch, J. McGregor, E. P. J. Parrott, J. A. Zeitler, L. F. Gladden, A. Knop-Gericke, R. Schlögl, D. S. Su, J. Am. Chem. Soc., **2010**, 132, 9616.
(24) N-content as calculated from the XPS analysis is invariably underestimated as a consequence of unpredictable contributions from Si and C arising from the SiC scaffold background

Supporting information

Methods

General procedure for the synthesis of highly N-doped mesoporous carbon-based coating (N@C) on macroscopically shaped supports.

In a typical procedure, 2 g of D-Glucose and 3 g of citric acid were added to 500 mL of ultrapure Milli-Q water at room temperature. A proper amount of ammonium carbonate (i.e. 0.75, 1.5 or 2.3 g) was then added in a single portion to the solution at r.t. and an instantaneous effervescence due to CO_2 evolution was observed. The obtained clear solution was exploited as an aqueous pre-catalytic phase for the soaking/impregnation of a series of suitable supports (2 g): SiC extrudates (29 $m^2 \cdot g^{-1}$; SICAT) and powder (25 $m^2 \cdot g^{-1}$; SICAT), SiC foams (30 $m^2 \cdot g^{-1}$; SICAT) and α-Al_2O_3 beads (6 $m^2 \cdot g^{-1}$; Sasol). The wet solids were slowly heated (10 °C min^{-1}) in air from room temperature to 130 °C and kept at this temperature for 1 h. The as obtained dry solids were further impregnated with the same three component solution for several times at will, until the desired loading is achieved. The solids underwent a thermal treatment in air at 450 °C (2 °C·min^{-1}) for 2 h during which the macroscopic host support was coated with a highly N-doped mesoporous carbon phase. The as-prepared solids can be further heated in He atmosphere at 900 °C (10 °C·min^{-1}) for 2 h in order to increase the graphitization/conjugation degree of the final materials.

Table S1. Physico-chemical characterization of N@C phases of various SiC/Al_2O_3-based composites.[a]

Entry	Sample[b] [Cat. label]	1st impregn. cycle	2st impregn. cycle	Thermal treatment/ atmosphere	N@C wt % loading from TGA	N wt % from EA[c]	N wt % at the N@C phase[d]	SSA (m^2/g)	Nitrogen species (%)[e]			
		$(NH_4)_2CO_3$ (g)	$(NH_4)_2CO_3$ (g)						Pyridinic	Pyrrolic	Graphitic	Oxidized
1	$N@C/(SiC)_E^2$ [**I**]	2.3	0.75	450 °C/Air	10.3	3.34	32.4	108	55.2	28.8	11.2	4.8
2	$^{A}N@C/(SiC)_E^2$ [**II**]	2.3	0.75	900 °C/He	10.4	2.12	20.4	109	43.2	7.5	37.2	12.1
3	$^{A}N@C/(SiC)_P^2$ [**III**]	2.3	0.75	900 °C/He	15.2	3.55	23.4	110	44.6	17.4	32.4	5.6
4	$N@C/(SiC)_E^2$ [**IV**]	2.3	1.5	450 °C/Air	17.1	5.11	29.9	138	45.9	27.6	19.6	6.9
5	$^{A}N@C/(SiC)_E^2$ [**V**]	2.3	1.5	900 °C/He	10.4	1.61	15.5	144	38.9	10.5	37.9	12.7
6	$^{A}N@C/(\alpha Al_2O_3)_B^2$ [**VI**]	2.3	0.75	900 °C/He	13.0	1.47	12.9	91	40.6	11.2	35.6	12.6

[a] All SiC/α-Al_2O_3-composites are prepared by repeating the soaking/impregnation step of the pristine SiC support twice and using impregnating solutions prepared dissolving 2g of D-Glucose, 3g of citric acid and $(NH_4)_2CO_3$ (from 0.75 to 2.3 g) in 500 mL of ultrapure Milli-Q water. [b] Composites are designated as follows: $^{A}N@C/SiC_x^y$ where superscript "A" denotes "annealead samples" (treatment at 900 °C under inert atmosphere), "N@C/SiC" or "$N@C/\alpha$-Al_2O_3" stand for the SiC/α-Al_2O_3 material coated with the (N@C) active-phase, "X" subscript illustrates the pristine support form (P = powder; E = extrudates; B = beads) while "Y" superscript displays the number of impregnation cycles. [c] Elemental analysis: average values calculated over three independent runs per sample. [d] N wt.% normalized to the N@C content (active phase) calculated by TGA analysis. [e] Estimated from fitting of the N 1s XPS profile.

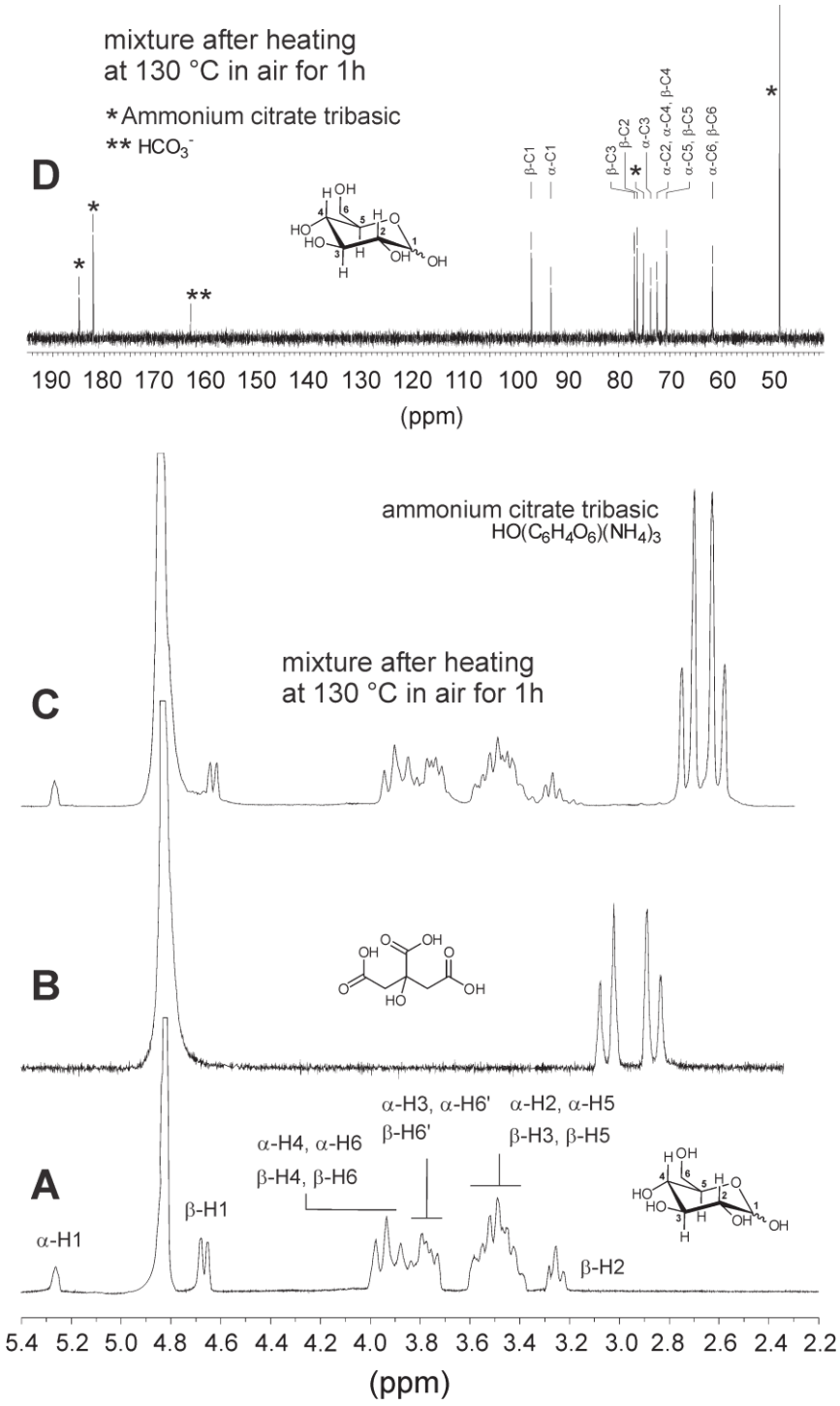

Fig. S1. ^{1}H and $^{13}C\{^{1}H\}$ NMR spectra (D_2O, 298 K) of the three component mixture after heating at 130 °C for 1h (C, D) and ^{1}H NMR spectra (D_2O, 298 K) of the two separate components, D-Glucose (A) and citric acid (B). From a close inspection of the NMR spectra, the first thermal treatment at 130 °C of the three-component aqueous solution results into a homogeneous solid mixture of *α,β*-D-glucopyranose and ammonium citrate tribasic. Traces of either CO_3^{2-} or HCO_3^{-} are observed after this phase (D).

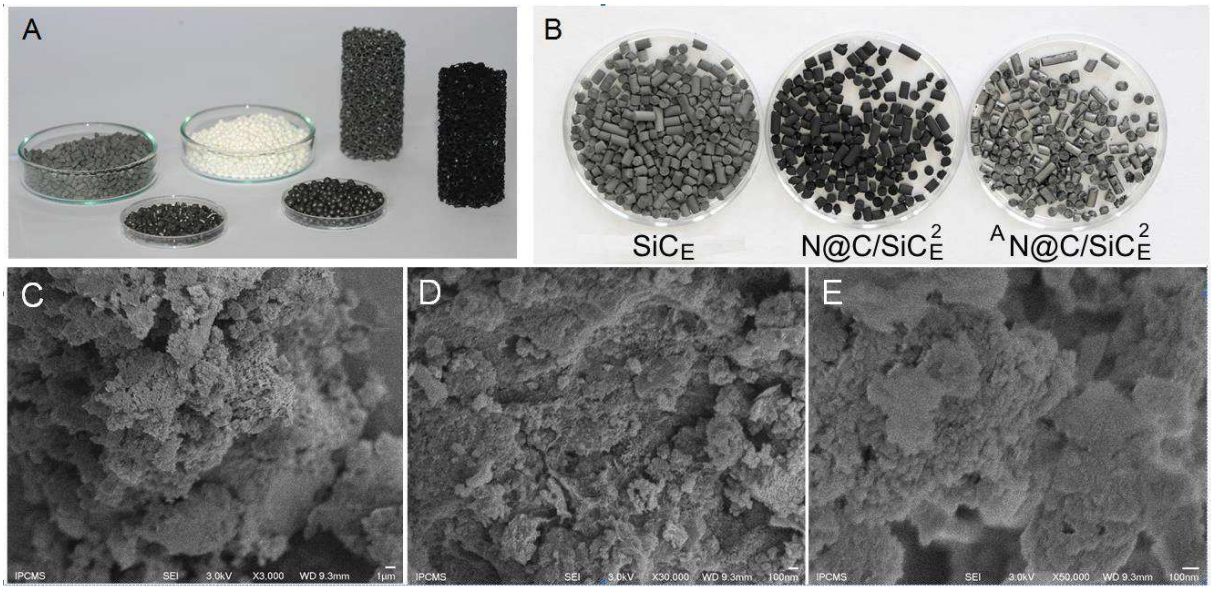

Fig. S2. Digital photos of pristine SiC supports with different macroscopic shapes (A) and SiC extrudate (SiC_E) samples (B) after N@C-coating and thermal treatment at 450 °C in air ($N@C/SiC_E^2$) (Table S1†, entry 1) and annealing at 900 °C under He atmosphere ($^AN@C/SiC_E^2$). Typical SEM images illustrating the N@C porous texture of the $^AN@C/SiC_E^2$ sample (Table S1†, entry 2) at different magnifications.

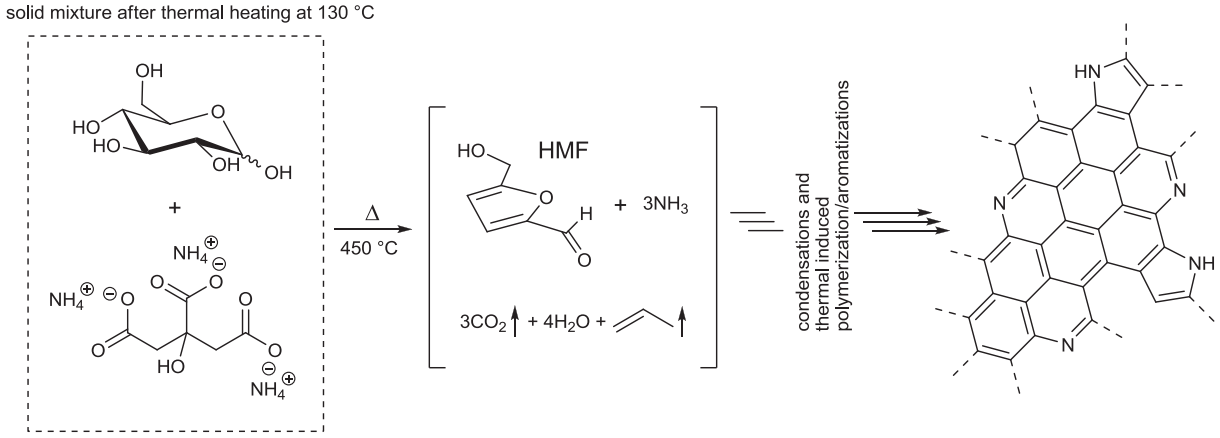

Fig. S3. Proposed mechanism for the thermal transformation of *α,β*-D-glucopyranose and ammonium citrate tribasic (pre-catalyst phase) into a N-rich, heteroaromatic, graphene-like network (N@C - catalytically active phase). The thermal treatment at 450 °C is supposed to start the progressive dehydration of the sugar into the 5-hydroxymethyl-furfural (5-HMF). Under these conditions, ammonium citrate tribasic, is expected to act as both a N-reservoir for the generation of N-containing heterocycles and a pore-forming agent (due to its complete decomposition into volatiles like NH_3, CO_2, H_2O and propene) thus contributing to the ultimate material mesoporosity.

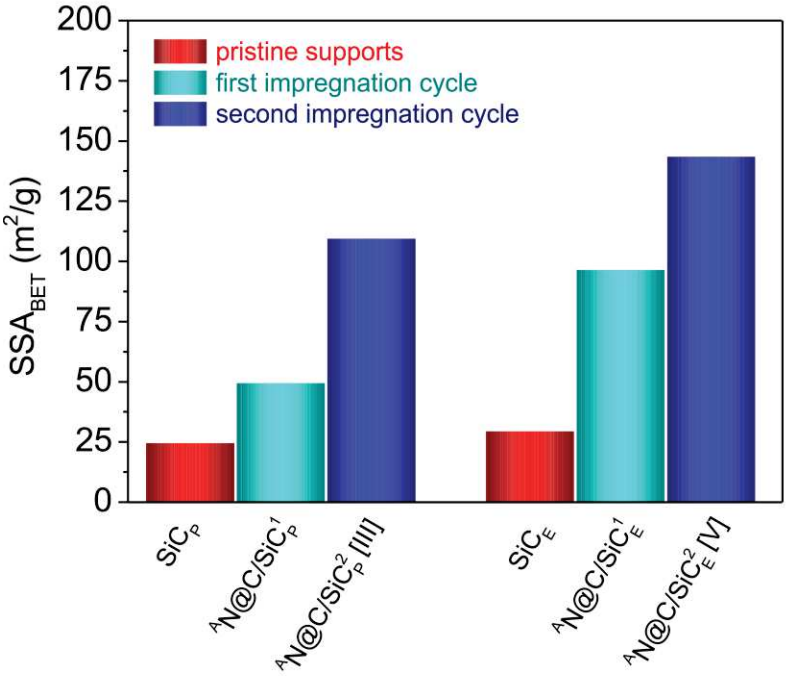

Fig. S4. BET Specific Surface Area of annealed composites after one or two impregnation cycles of differently shaped SiC matrices. For samples [**III**] and [**V**], refer to Table S1†.

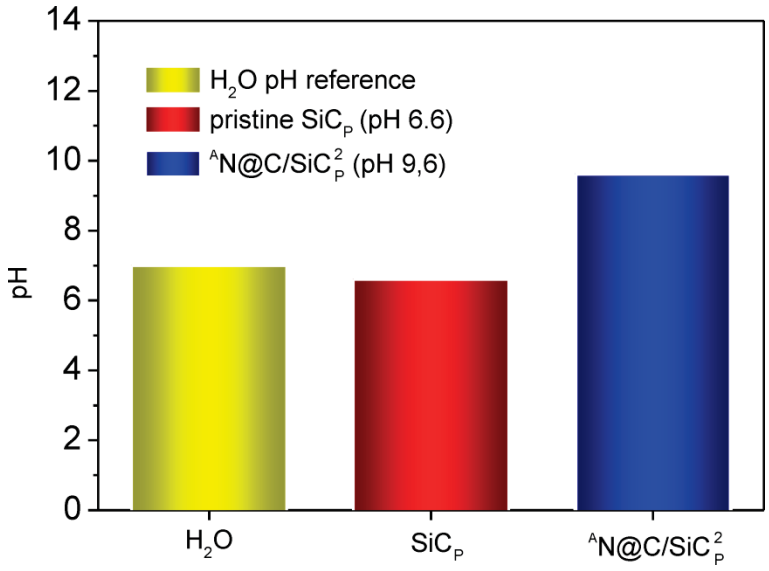

Fig. S5. Acid-basic properties of an aqueous dispersion of [**III**] (Table S1†, entry 3) at comparison with its pristine counterpart (bare SiC$_P$)

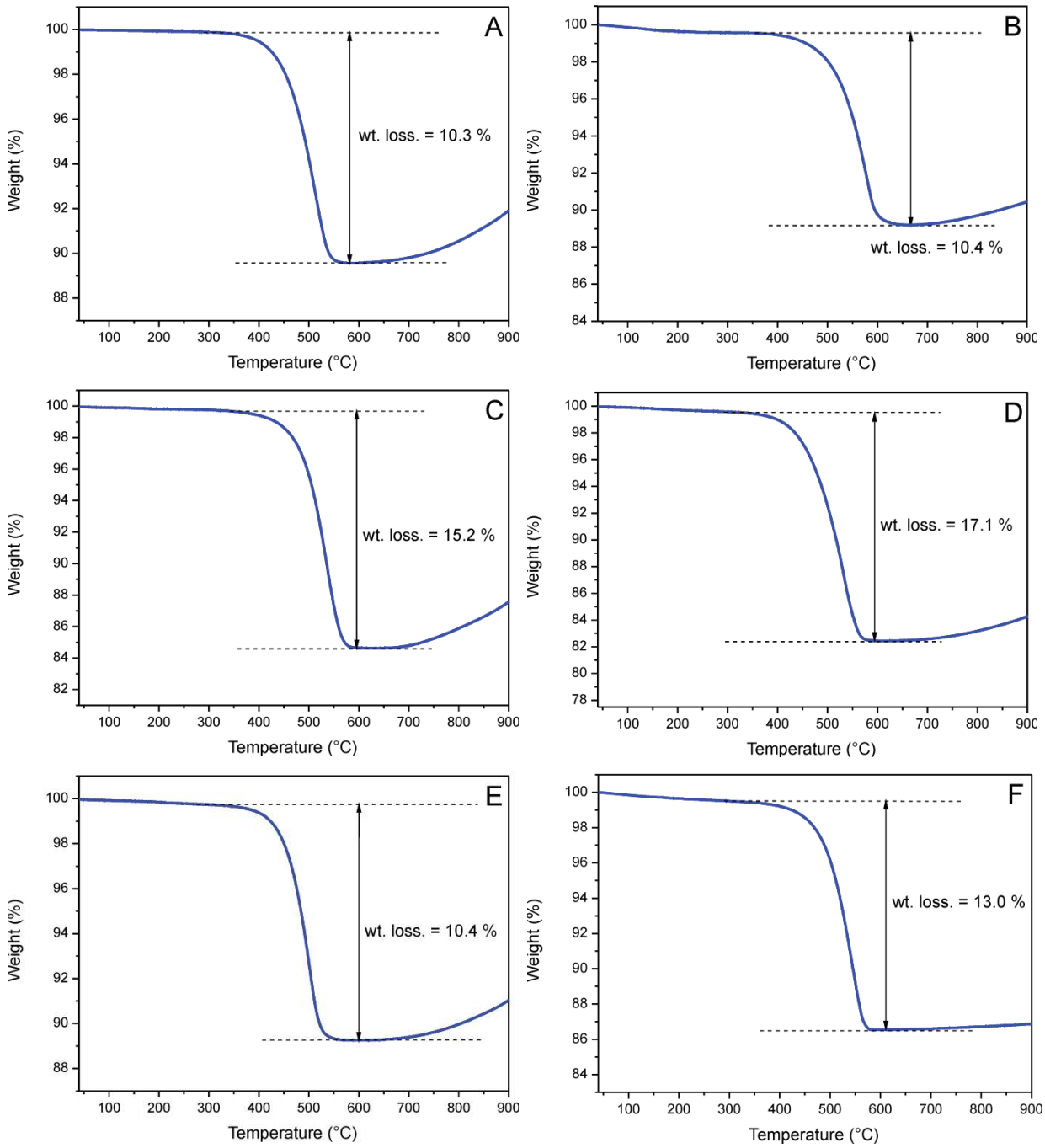

Fig. S6. TGA profiles of N@C/SiC composites (40-900 °C, 5°C/min, air 100 mL/min). All samples are dried at 40°C at 0.05 torr, overnight before each measurement. Weight losses refer to the complete burning of the N@C deposit at the SiC matrices: **A**) N@C/SiC_E^2 [**I**], see Table 1, entry 1. B) ^{A}N@C/SiC_E^2 [**II**], see Table 1, entry 2. C) ^{A}N@C/SiC_P^2 [**III**], see Table S1†, entry 3. D) N@C/SiC_E^2 [**IV**], see Table S1†, entry 4. E) ^{A}N@C/SiC_E^2 [**V**], see Table S1†, entry 5. F) ^{A}N@C/α-$Al_2O_{3B}^2$ [**VI**], see Table S1†, entry 6.

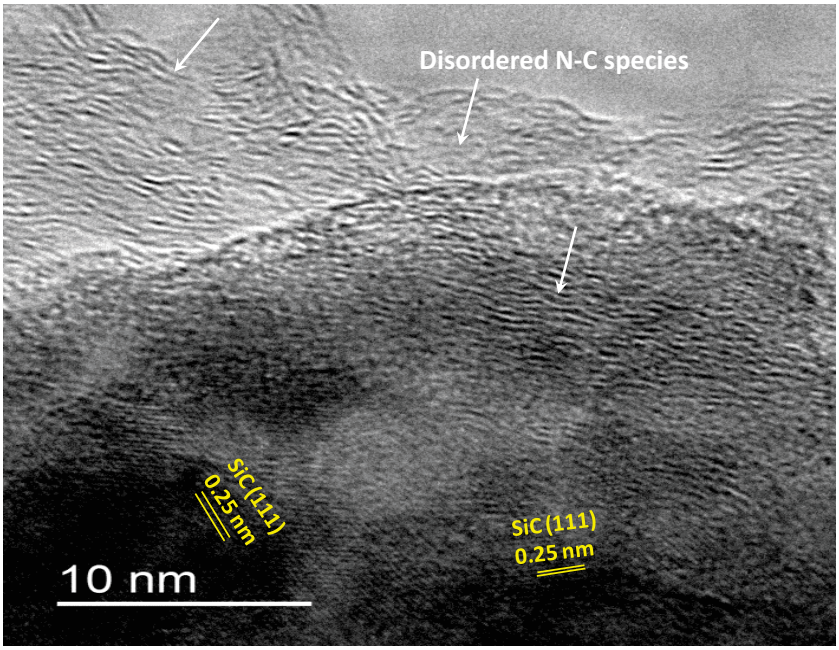

Fig. S7. HR-TEM high-resolution image of the ^{A}N@C/SiC$_p$^{2} [**III**] sample (Table S1†, entry 3) showing the N@C coating phase in the form of disordered and crumpled N-doped carbons at the SiC support.

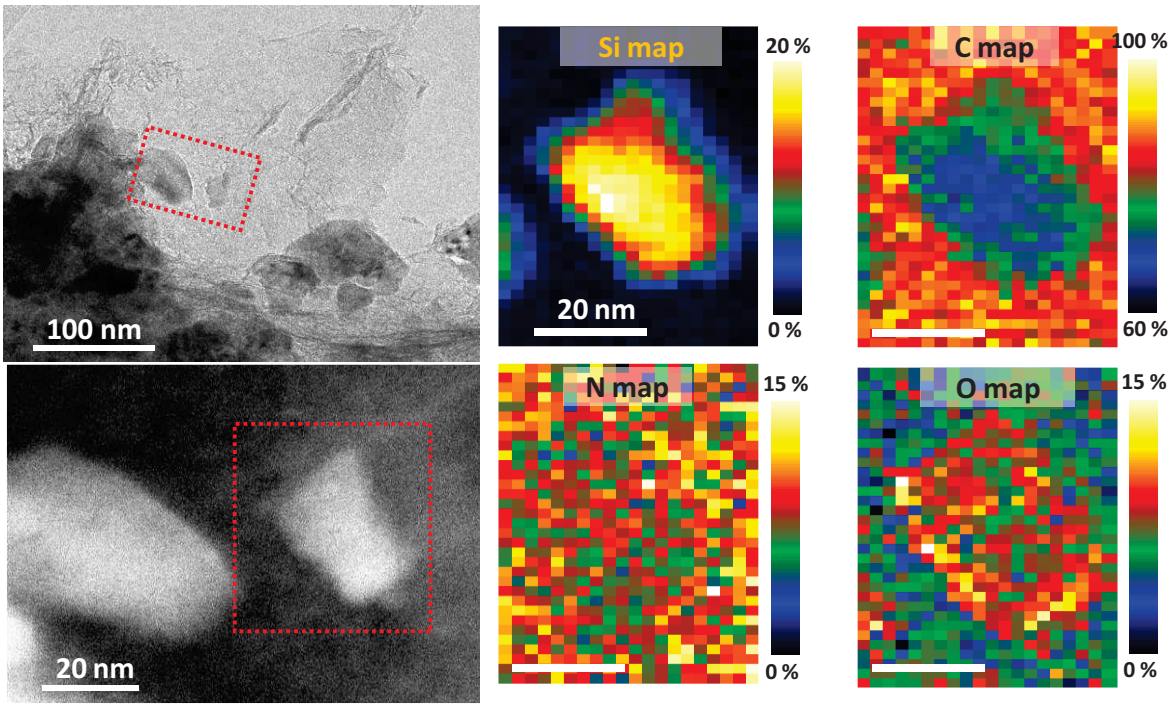

Fig. S8. Morphology of ^{A}N@C/SiC$_p$^{2} [**III**] sample (Table S1†, entry 3). An overview bright field TEM image (Top left). A high-angle annular-dark-field image (STEM-HAADF) which was taken from the area marked by the red dashed-line box in the top left image (Bottom left). Elemental maps of Silicon, Carbon, Nitrogen and Oxygen, respectively taken from the area highlighted by the red dashed-line box in the bottom-left image (Four color images on the right side). The colors correspond to the relative atomic composition ratio indicated by the adjacent vertical color bars.

References

(1) J. Chlistunoff, *J. Phys. Chem.,* 2011, **C115**, 6496.
(2) R.-J. van Putten, J. C. van der Waal, E. de Jong, C. B. Rasrendra, H. J. Heeres, J. G. de Vries, *Chem. Rev.*, 2013, **113**, 1499.
(3) F. W. Lichtenthaler, A. Brust, E. Cuny, *Green Chem.* 2001, **3**, 201.
(4) F. W. Lichtenthaler, *Accounts Chem. Res.*, 2002, **35**, 728.

Nitrogen-enriched carbon nanospheres decorated silicon carbide as a superior metal-free catalyst for styrene production

Housseinou Ba[a,c], Yuefeng Liu[a], Cuong Duong-viet[a], Lai Truong-Phuoc[a], Jean-Mario Nhut[a], Jingjie Luo , Pascal Granger[c], Cuong Pham-Huu[a*]

a Institut de Chimie et Procédés pour l'Energie, l'Environnement et la Santé (ICPEES), ECPM, UMR 7515 CNRS-Université de Strasbourg, 25, rue Becquerel, 67087 Strasbourg Cedex 02, France.

b The University of Da-Nang, University of Science and Technology, 54 Nguyen Luong Bang, Da-Nang, Viet-Nam.

c Unité de Catalyse et Chimie du Solide (UCCS), UMR 8181 du CNRS-Université de Lille-1, Bâtiment C3, Université Lille-1, 59655 Villeneuve d'Ascq Cedex, France.

d Institute of Chemistry of OrganoMetallic Compounds, ICCOM-CNR and Consorzio INSTM, Via Madonna del Piano, 10 – 50019, Sesto F.no, Florence, Italy.

e Institut de Physique et Chimie des Matériaux de Strasbourg (IPCMS), UMR 7504 CNRS-University of Strasbourg, 23, rue du Loess, 67034 Strasbourg Cedex 02, France.

* *Corresponding author: cuong.pham-huu@unistra.fr (C. Pham-Huu)*

Article submitted in ACS Catalysis

Abstract

Nitrogen-doped carbon-based 1D and 2D nanomaterials have received a great deal in the last few years particularly in the light of their application as metal-free systems capable to promote efficiently several catalytic transformations,[1,2,3] including many of those at the heart of renewable energy technology.[4,5] At odds with their remarkable catalytic performance a metal-free catalysts, the severe synthetic conditions required for their production, a relatively low N-content effectively available as active phase as well as all limitations dealing with both the material process ability and handling, have largely restricted their widespread application. Herein, we describe an original and straightforward approach to the synthesis of unique macroscopic and highly porous nitrogen-doped carbon-based foams featured by a high nitrogen content, up to 10 wt %, starting from easily accessible and food processing raw materials, i.e. ammonium carbonate, dextrose and citric acid. The reported procedure allows for a full exploitation of the nitrogen species at the material surface, where the catalytic process is expected to takes place. The as-synthesized nitrogen-doped carbon foams have been successfully scrutinized as metal-free catalysts in the industrially relevant dehydrogenation of ethylbenzene to styrene processes, and the catalyst admit a higher performance compared to the promoted iron-oxide based systems of the state-of-the-art.

1. Introduction

Styrene is one of the most important unsaturated aromatic monomers in modern petrochemical industry. Styrene is the raw material involving in the production of various polymeric materials, the most important being polystyrene, synthetic rubbers, plastics, acrylonitrile–butadiene–styrene (ABS) and styrene-acrylonitrile (SAN) resins, latex (SBL). The world production of styrene monomer is significantly increased since the last decade to reach about 26 Mt per annum in 2012 and continue to face a high growing rate in the future (Fig. 1).[6] Styrene is mostly produced by the gas-phase dehydrogenation (DH) of ethylbenzene. The most employed catalyst for such reaction is the low surface area bulky-like iron-based catalyst, accounting for almost 95 wt. %, promoted with different elements such as alumina and potassium.[7] The catalyst is cheap and highly selective for the styrene production. However, during the course of the reaction, generally carried out at a relatively high reaction temperature, i.e. 550 to 650°C, a large amount of coke was deposited on the iron-based catalyst surface which significantly decreases the DH activity. In order to avoid such deactivation a large amount of steam was co-feeded in the reactor in order to prevent coke formation. The steam production is a cost incentive process and thus, the development of new alternative catalysts with better coke resistance is of interest. Indeed, the high amount of steam leads to a huge energy consumption of the process which can be estimated to be 1.5×10^9 cal/ ton of styrene[8] and also to a large amount of wastewater containing trace amount of hydrocarbons which needs to be recycled downstream. The use of steam causes also other serious limitations, namely, (i) consumption of ethylbenzene and of styrene by steam-reforming, (ii) chemical reaction of steam with K_2CO_3 forming free KOH leading to the gradual loss of the promoter and finally, to the irreversible catalyst deactivation. Schlögl and co-workers[9] have recently reported the development of a metal-free based on nanodiamonds (ND) for the steam-free DH of ethylbenzene into styrene. The NDs-based catalyst exhibits DH activity about three times higher than the one obtained with the iron-based industrial catalyst along with a high selectivity towards styrene formation. However, the ND is used in a powder form which leads to a significant pressure drop along the catalyst bed. The ND also shows a high tendency to form agglomerates which significantly reduce the effective surface area of the catalyst. It is well known in the heterogeneous catalysis field that the performance of solid catalysts is not only dependant in their composition but also in the morphological properties where accessibility and diffusion phenomena are key issues.[10] The idea is to improve the dispersion of the NDs particles, which would increase the effective contact surface area and the number of active sites per catalyst weight, leading to an enhancement of their catalytic properties. More recently hybrid materials consisting of ND particles uniformly dispersed onto a 2D graphene oxide and or few-layer-graphene (FLG) lead to a significant

improvement of the DH activity, respectively 1.7 and 3.4 times higher than the un-supported nanodiamond.[11]

Carbon nanomaterials, including carbon nanotubes and graphene, doped with nitrogen atoms have been widely investigated in the last decade as an efficient metal-free catalyst in several highly demanding catalytic processes, e.g. the electrochemical oxygen reduction reaction (ORR),[12,13] the selective oxidation of impurities for gas cleaning[3] and alkane dehydrogenations.[14] It has been demonstrated that the incorporation of nitrogen(s) in the carbon matrix network give rises to an electronic modification of the adjacent carbons atoms leading to an unexpected adsorption properties and as a consequence, improved catalytic performance and stability. N-doping can also increase the catalytic sites through inducing strain and defect site.[15]

Here we report on the new synthesis method for preparing high dispersed nanodiamonds within a nitrogen-doped mesoporous carbon (NMC) composites based on the use of non-toxic raw foodstuffs materials such as ammonium carbonate (leavening agent), dextrose and citric acid. In such synthesis process, nanodiamond (ND) particles with diameter ranged between 5-10 nm will be used as nucleation centers of the NMC (Figure 1, route a). The NMC phase localized around the NDs will play a role of spacer to prevent excessive ND agglomeration during the subsequence thermal treatment steps leading to a high efficient metal-free catalyst for the DH process. The process was carried out in a solution and thus, the final macroscopic shape of the catalyst can be controlled in an easy way on any kind of macroscopic supports (**Figure 80, route b**). The macroscopic supports can be chosen at will, i.e. grains, pellets, ring, beads or foam, as a function of the downstream applications. Silicon carbide foam will be used as support in the present study, and the as-synthesized 3D composite (ND-NMC/SiC) will be evaluated in the selective steam-free dehydrogenation of ethylbenzene into styrene .[7,16]

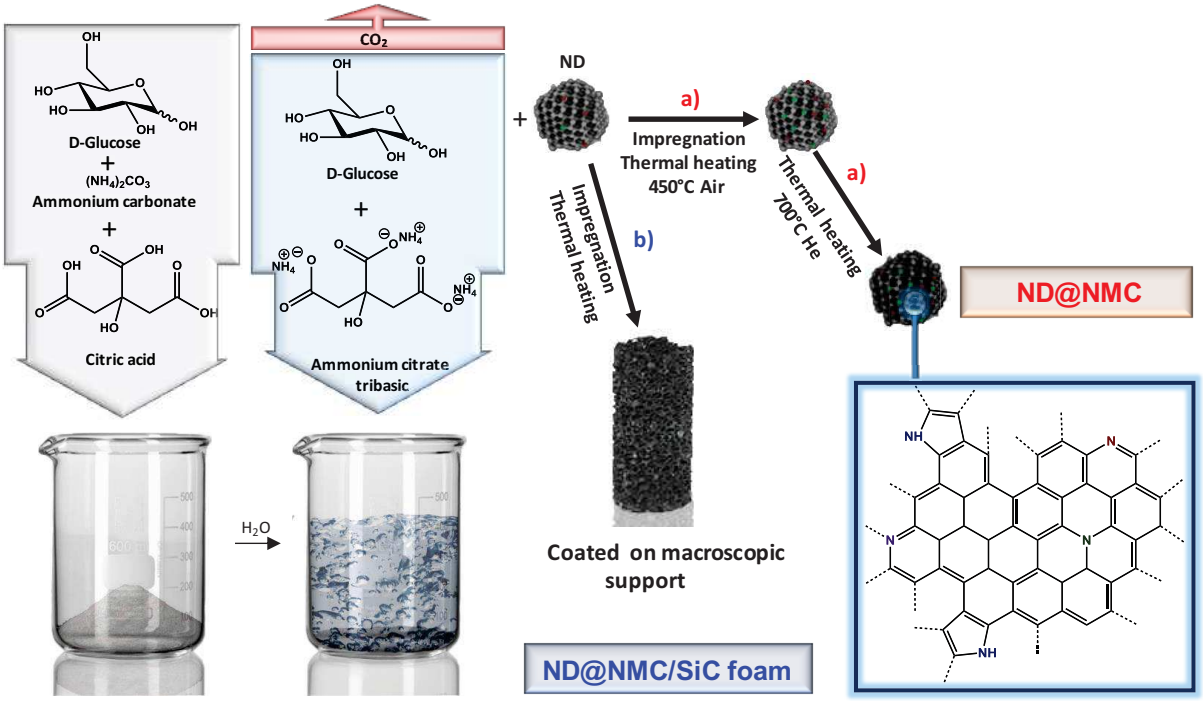

Figure 80. Schematic illustration of the synthesis process of the nitrogen-doped mesoporous carbon coated nanodiamonds (ND@NMC) hybrid composite (route a) and macroscopic shaping on a foam-structured carrier (ND@NMC/SiC foam, route b).

2. Experimental

2.1 Catalyst preparation

The nanodiamonds (ND) were purchased from the Carbodeon Ltd Oy (Finland) and were used without any further treatment. TEM analyses indicate that the ND has a regular size and were closely aggregated from each other according to the TEM analysis (Figure S1). High resolution TEM analysis indicates that the ND diameter is centered at around 6 nm (Figure S1 B- D). The ND-700 and ND-900 samples were produced by commercial ND at 700 and 900 °C for 2 h in helium atmosphere, respectively.

The fabrication of ND@NMC or macroscopic ND@NMC/SiC samples were illustrated in Figure 1. In a typical procedure, as can be seen route (a) in Figure 1, 2 g of D-Glucose and 3 g of citric acid were added in 10 mL of ultrapure Milli-Q water at room temperature. A proper amount of ammonium carbonate (i.e. 3 g) was then added in a single portion to the solution at r.t. and an instantaneous effervescence due to CO_2 evolution was observed. And then 2 g of ND particles were added by the assisted of sonication process at room temperature for 20 min. The obtained mixture was directly moved into an oven for the thermal treatment

at 130°C for 5 h. The solids underwent a thermal treatment in air at 450°C (2°C min^{-1}) for 2 h during, and then the as-prepared solids can be further heated in helium atmosphere at 700 or 900°C (10°C min^{-1}) for 2 h in order to increase the graphitization/conjugation degree of the final materials. The final samples were marked as ND@NMC-700 and ND@NMC-900. The ND-free sample was prepared following by the same process, and noted as NMC-700.

To fabricate the macroscopic ND@NMC/SiC sample (route b in Figure 1), the as-prepared solution was used to impregnate the supports, i.e. SiC foam (30 m^2 g^{-1}; SICAT) before thermal treatment at 130°C. The wet solids were slowly dried in air at room temperature. The dry solids were further impregnated with the same solution. The wet solids were slowly heated (10°C min^{-1}) in air from room temperature to 130°C kept at this temperature for 5 h. The as obtained dry solids were further impregnated with the same three component solution for several times at will, until the desired loading is achieved. The solids were then submitted to two thermal treatments, in air at 450°C (heating rate of 2°C min^{-1} from room temperature to 450°C) for 2h in order to convert the precursors into nitrogen-doped mesoporous carbon decorating the macroscopic host structures and in helium at 700°C to graphitize the surface. The final materials were noted as ND@NMC/SiC.

3. Results and discussion

3.1Morphology analyses of typical nitrogen-enriched carbon nanospheres

The SEM micrographs of the ND-NMC-700 composite with different magnification are summarized in Figure 81. According to the SEM image it can be seen that the ND particles are well dispersed inside the nitrogen mesoporous carbone layers which acting as anchorage site, thus promoting physical properties of the final composite.

The representative TEM micrographs of the two samples are presented in Figure 2 with different magnifications. The NMC-ND sample is consisting with regular spheres with a fuzzy structure with an average size of around 100 nm (Figure 81D-F). High resolution analysis indicates that the sphere is constituted by a disordered carbon structure with NDs dispersed inside (Figure 81G-H). According to the results one should expected that during the thermal treatment process the NDs nanoparticles are acting as nucleation centers for the subsequence growth of nitrogen-doped carbon phase while the regular size is controlled by the number of nucleation within the sample precursor. High resolution TEM micrograph of the sample indicates that the ND nanoparticles were relatively well dispersed in the NMC network. Such high dispersion could be attributed to the presence of the NMC phase playing a role of spacer to prevent excessive ND motion during the thermal treatment process.

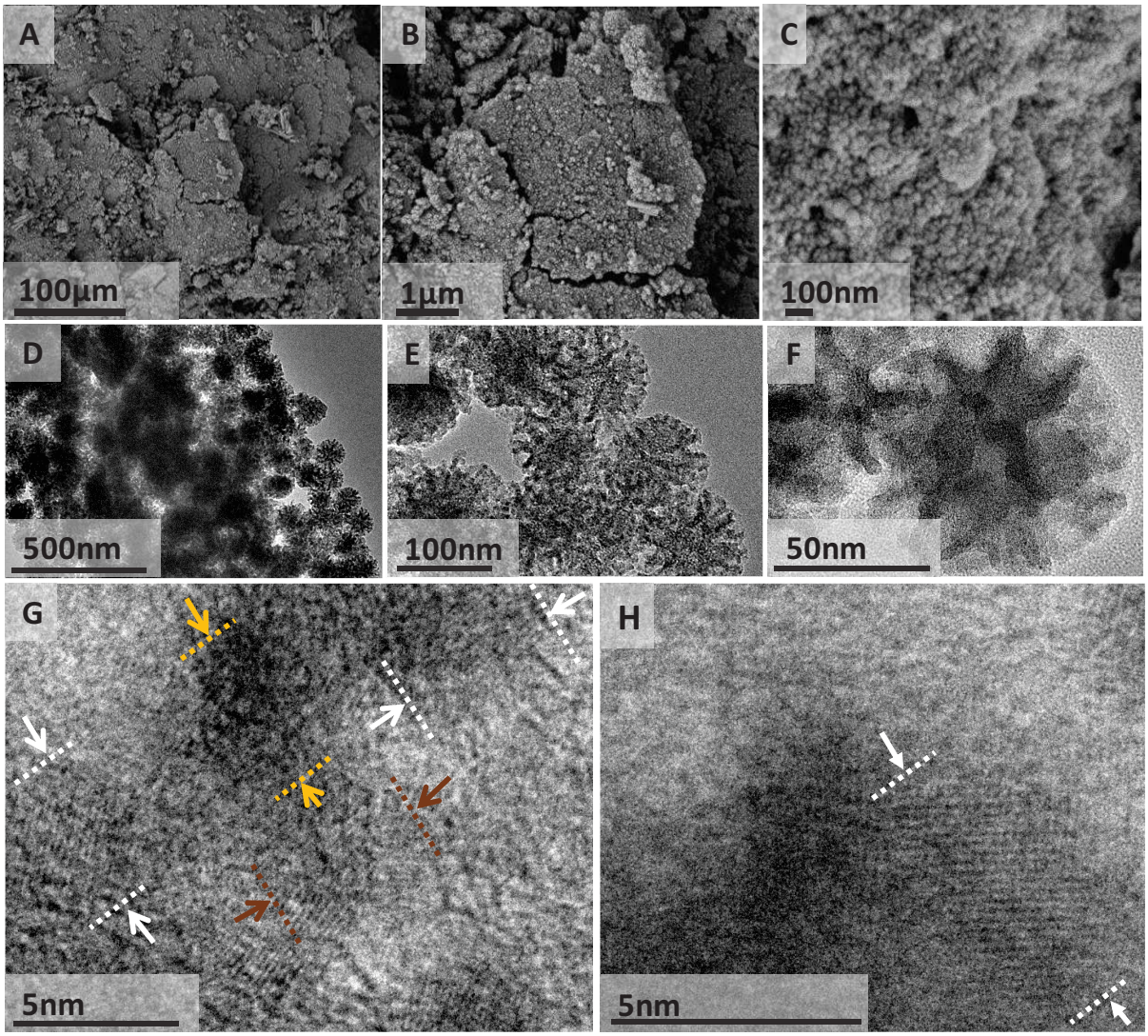

Figure 81. SEM micrographs (A-C) and TEM images with different magnification (D-H) of ND@NMC sample. (D-F) TEM micrographs with different magnifications of the powdery ND-NMC sphere after carbonization step at 700°C under argon. (G, H) High resolution TEM micrographs with different magnifications of the ND@NMC/SiC catalyst after a carbonization step at 700°C under argon showing the diamond particles (under arrows) well anchored on the nitrogen mesoporous carbon.

Figure 82 A shows the X-ray pattern of the pristine nanodiamond and as-prepared ND@NMC composite. The broad peaks of pure nanodiamond are located at 2 θ = 43.8° in curve (a), corresponding to (111) diffraction planes of the nanodiamond, which demonstrated that the nanodiamond crystal was cubic. It can be seen that the broader peak ranged between 2 θ = 18° to 27° corresponds to impurities generated during the diamond detonation decrease as function of thermal treatment.

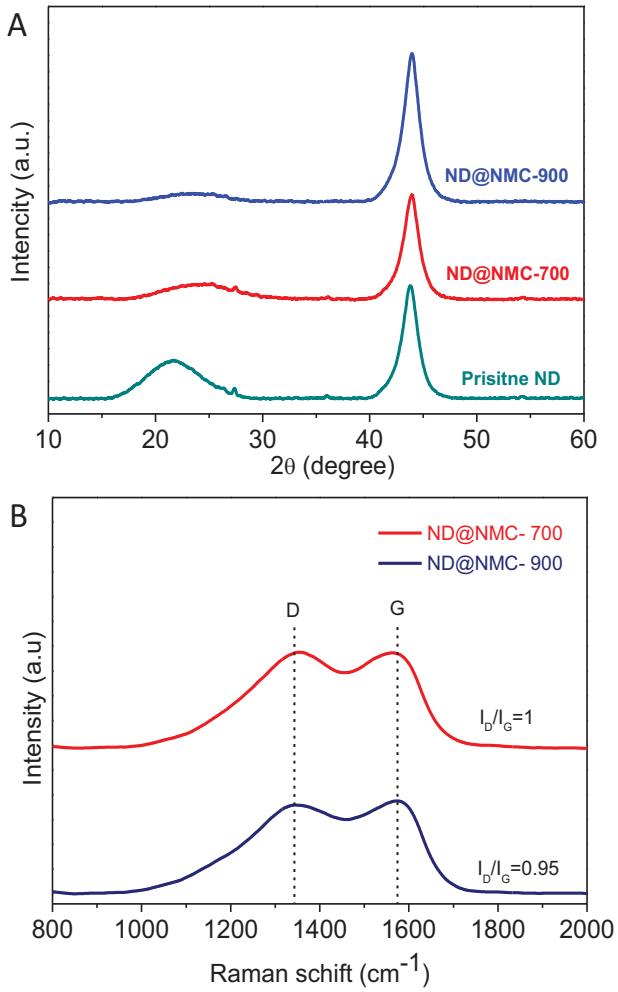

Figure 82. (A) XRD patterns of pristine nanodiamond and the synthesised nitrogen mesoporous (ND@NMC) carbon annealed at 700 and 900°C. (B) The corresponding Raman spectra of the ND@NMC-700 and ND@NMC-900.

The Raman spectra of ND@NMC treated with different thermal tempetature under helium atmosphere are presented in Figure 82B. It can be found thtt the D band (1350 cm^{-1}) is caused by disorder carbon typically characteristic to the sp^3 atoms and G band (1570 cm^{-1}) represents sp^2 bonded carbon. The intensity ratio (I_D/I_G) comparison between the two composites revealed that the one annealed at 700 °C admit more structural defect due to the fact of the higher graphitization temperature (900 °C) of the NMC-ND leading to decrease the density of the structural defect.

3.3 Physicochemical analyses of ND and ND@NMC composites

The specific surface of the different samples measured by the BET method is presented in Figure 83. According to the results specific surface area of the SiC after impregnation with NMC (NMD/SiC) and ND (ND/SiC) steadily increases from 28 m^2/g to 57 and 73 m^2/g, respectively. Such specific surface area increases is attributed to the high intrinsic surface area of the NMC and ND phases. Similar specific surface area increases is again observed for the ND-NMC and ND@NMC/SiC samples, i.e. 320 and 104 m^2/g, respectively. The specific surface area of the different samples is mostly consists of meso- and macropores which are of high interest for catalytic processes as micropores will induce problem of diffusion which in turn, could modify the overall selectivity of the process.

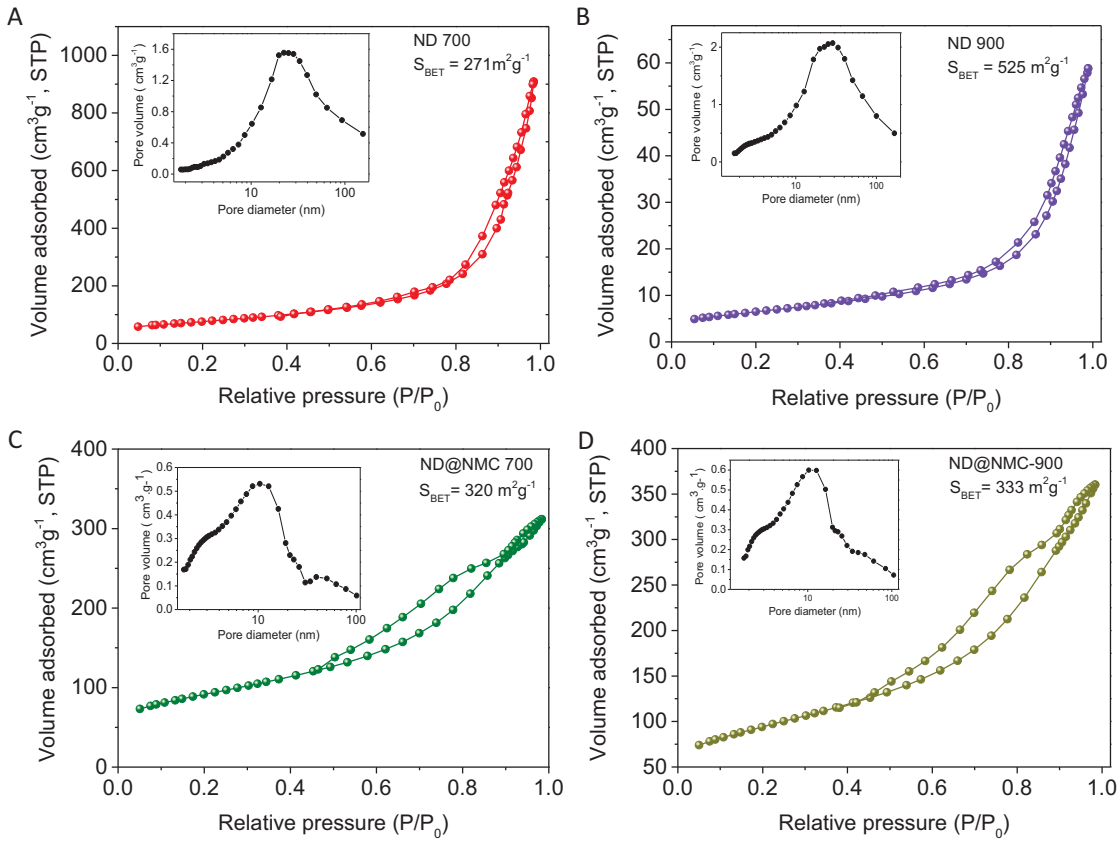

Figure 83. N_2 adsorption-desorption isotherms and pore size distribution (inset) of the ND-700, ND-900, ND@NMC-700 and ND@NMC-900.

The surface composition of the NMC-ND and ND-NC/SiC composites was analyzed by XPS and the results are presented in Figure 84. The N1s XPS spectrum clearly indicates the presence of four different nitrogen species major components (Figure 84B). Such result is in good agreement with those reported on the nitrogen-doped carbon composites in the

literature. The nitrogen doping, regardless the nature of the sample, is essentially consisted with pyridinic (399 eV) and pyrrolic (401 eV) nitrogen species according to the XPS analysis (Fig. 80B and S1). The total nitrogen doping are relatively high which is level-off at around 8 at.%. Zhao et al. [17] investigated a micro/mesoporous nitrogen-doped carbons with extremely high nitrogen content, up to 25 wt. %, by carbonizing of the PILs in nitrogen atmosphere. However, the process suffers from the multi-step synthesis of the PILs and low resistance to the heat treatment. Such high nitrogen doping compared to that usually reported in the literature[4] could be attributed to the method developed in the present study to prepare the doped composite according to our previous investigation.[18] In addition, the nitrogen-doped carbon phase is exclusively present on the topmost surface of the macroscopic support which provides a high accessibility of the active site towards the reactant.

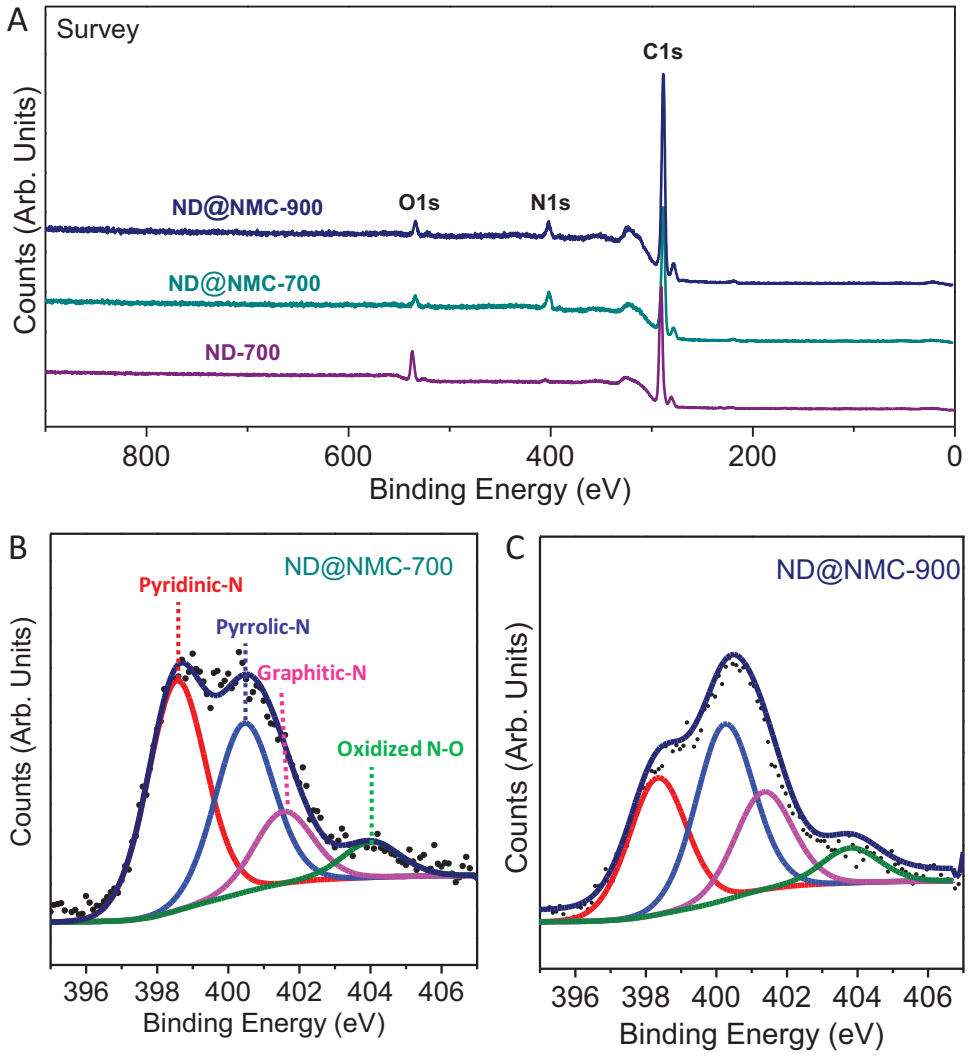

Figure 84. XPS spectra of ND@NMC-700 and ND@NMC-900 samples: (A) General spectra (NDs with thermal treatment at 700 °C was also displayed for comparison), (B, C) high resolution N1s spectra.

3.4 Catalytic performance on ND and ND@NMC composites

The ND-NMC/SiC was evaluated as a metal-free catalyst in the steam-free direct dehydrogenation of ethylbenzene (EB) into styrene in a fixed-bed configuration.[9] The effluent was analyzed by online gas chromatography (GC).[9] At 550°C, catalytic dehydrogenation rate was high at the beginning of the test and slowly decreased to reach a steady-state at about $mmol_{STG_{ND}}^{-1}h^{-1}$ (Figure 85A) after 30 h increased with increasing the reaction temperature to reach 26.5 $mmol_{STG_{ND}}^{-1}h^{-1}$ 600°C (Figure 87B). The catalyst exhibits an extremely high stability as no deactivation was observed for the whole test, after the first deactivated slope, under different reaction conditions. The selectivity towards styrene was almost 100% for the whole test at 550°C which indicates that secondary reactions are unlikely to occur, probably due to the two-dimensional structure of the active phase which favors the rapid desorption of intermediate product before further re-adsorption and cracking. A slight styrene selectivity decreases was observed at higher reaction temperature, i.e. 600°C, where a small amount of toluene and benzene (< 2%) was observed among the reaction products (Fig. 90A). Such selectivity decrease could be attributed to the high production rate of styrene per catalyst unit leading to some side adsorption process. The blank test carried out on the SiC pellets shows a relatively low DH activity (Fig. 85B) and confirms the high DH activity of the SiC supported nitrogen-doped porous carbon.

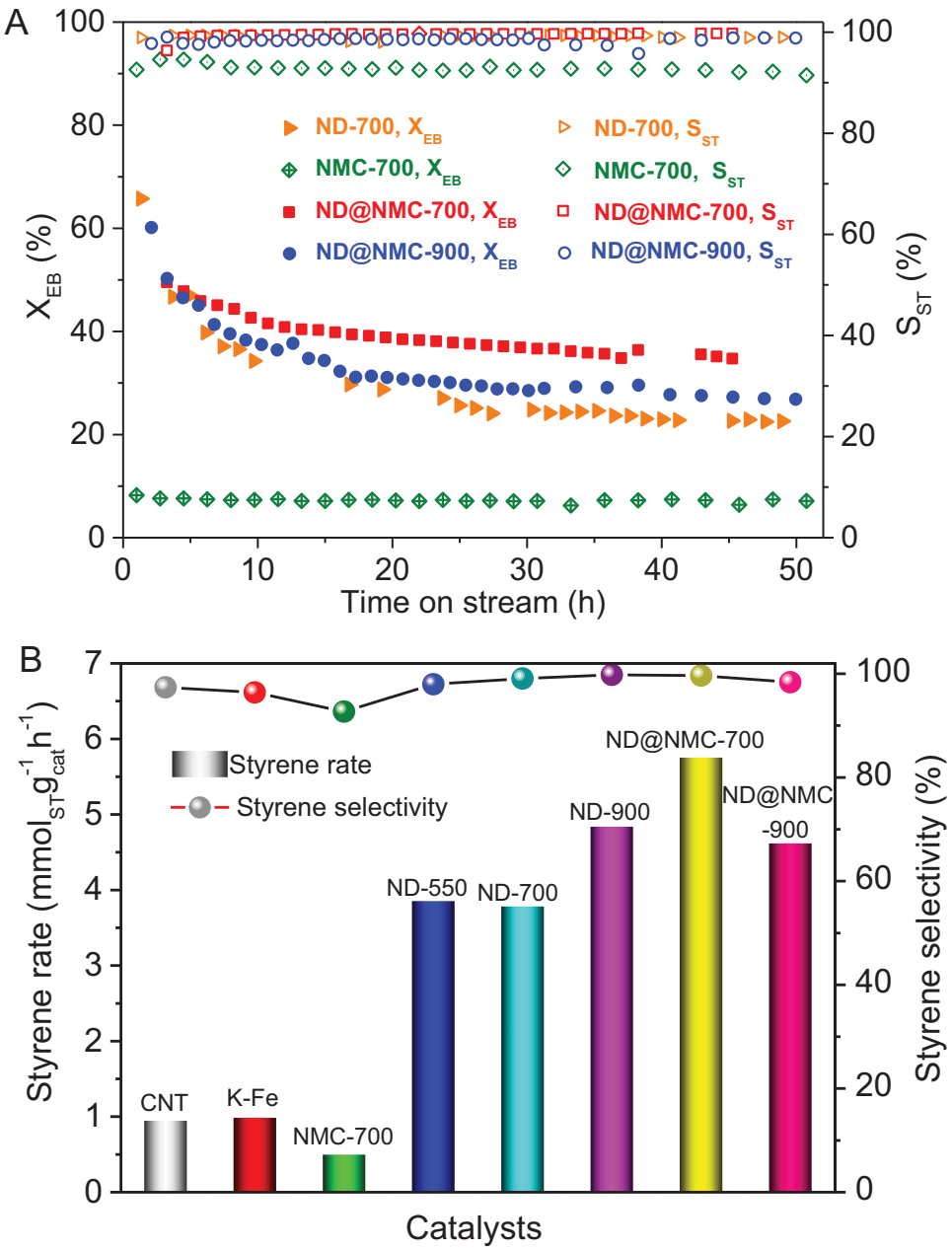

Figure 85. (A) Ethylbenzene conversion and styrene selectivity on metal-free ND@NMC and pristine ND with different thermal treatment under argon. (B) Steady state catalytic activity of various samples in the direct dehydrogenation of ethylbenzene to styrene. The steady state catalytic activity was obtained after 20 h time on stream reaction. Reaction conditions: 150 mg of catalysts, 550 °C, 2.8 % EB in helium, 30 mL·min^{-1}, atmospheric pressure.

3.5 Characterization and catalytic reaction of macroscopic shaped ND@NMC/SiC composite

The SEM morphologies showed in figure 86. A, B and C, it reveals the highly porous structures, where the nitrogen mesoporous active site are well anchored.The Brunauer-Emmett-Teller (BET) surface area and pore size characterization of ND/SiC and ND@NMC/SiC were performed under nitrogen adsorption/desorption experiments was presented in figure 86. The BET value was increased from 52 m^2/g for ND/SiC to 104 m^2/g ND@NMC/SiC, this increase especially attributed to the high intrinsic surface area of the NMC. And these isotherms with hysteresis shape, indicates that the composite consists essentially of a large network of meso and macropores.

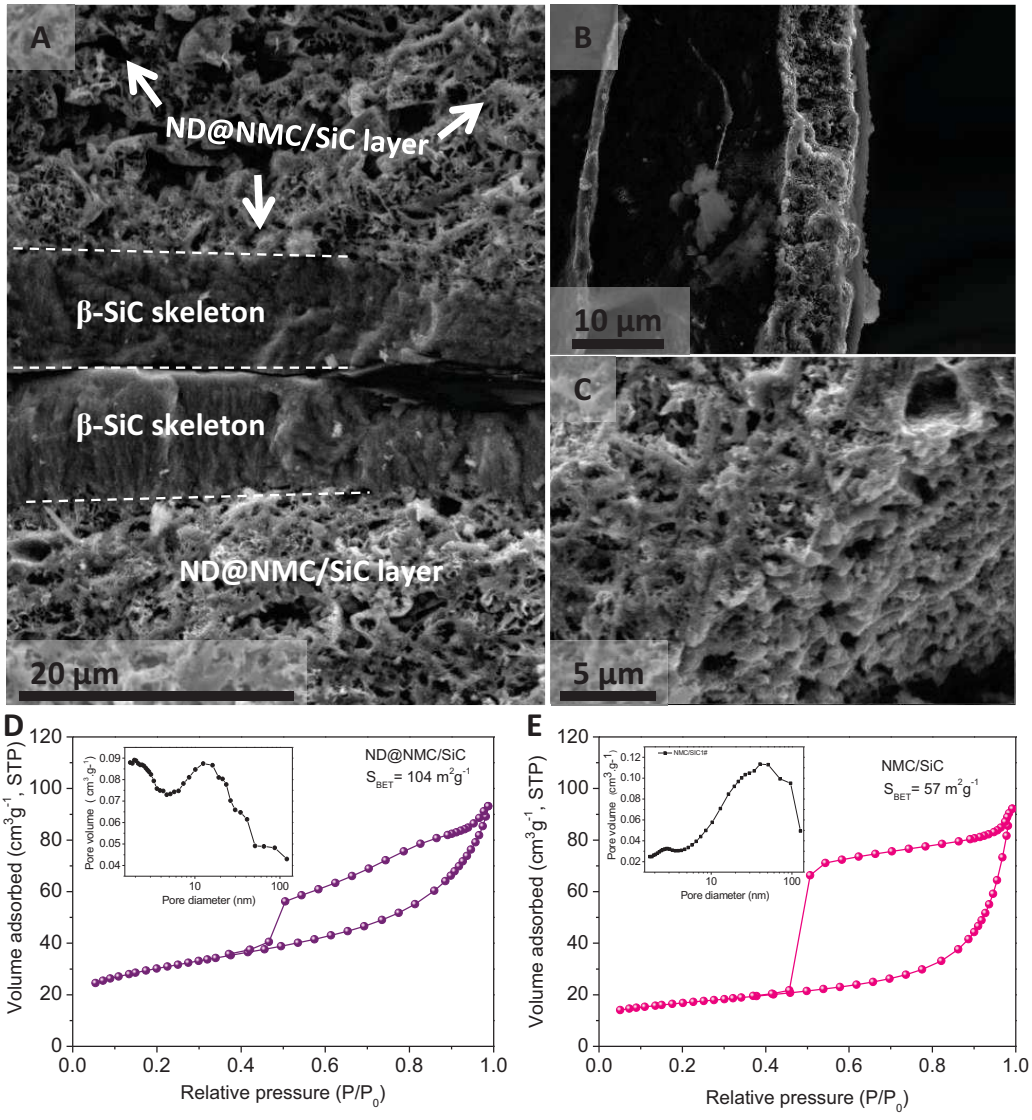

Figure 86. (A,B,C) SEM images and (D, E) the corresponding nitrogen adsorption isotherms

of macroscopic nitrogen-enriched carbon nanospheres on β-SiC foam.

The microstructure of ND@NMC/SiC composite was also investigated by EDX analysis, Figure 87. B, C, D and E, in order to get more details on the heteroatoms distribution on the surface, and the result showed that nitrogen loading are homogeneously coated on the topmost surface of the β-SiC foam support, this factor plays an important role in improvement of catalyst reactivity.

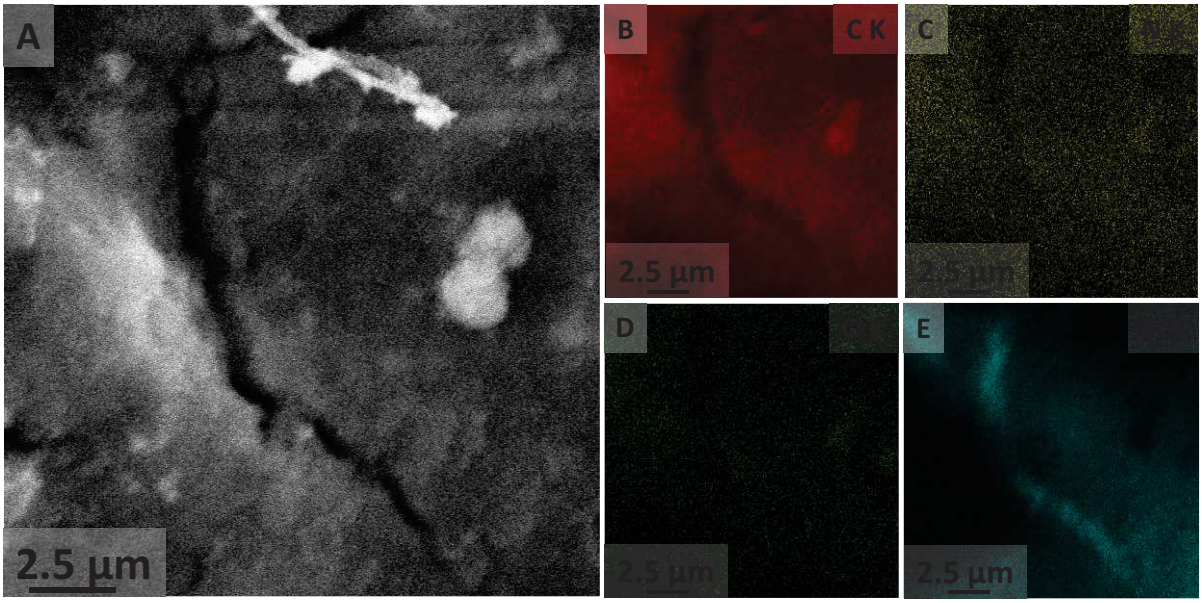

Figure 87. SEM picture of (A) NMC-ND supported on silicon carbide foam morphology and (B,C,D,E) the corresponding carbon, nitrogen, oxygen and silica map showing that the heteroatoms are homogeneously dispersed throughout the catalyst surface

The chemical compositions of ND@NMC/SiC composite were monitored by XPS as showed in Fig. 88. The survey spectrum of the NDs sample (Fig. 3a) clearly indicates the presence of C (61.25 At.%), N (10 At.%) , O (15.22 At.%) and Si(13.53), those result compared to pristine β-SiC indicate an increase in both C and N confirming that the nitrogen mesoporous active carbon are well anchored on the β-SiC surface.

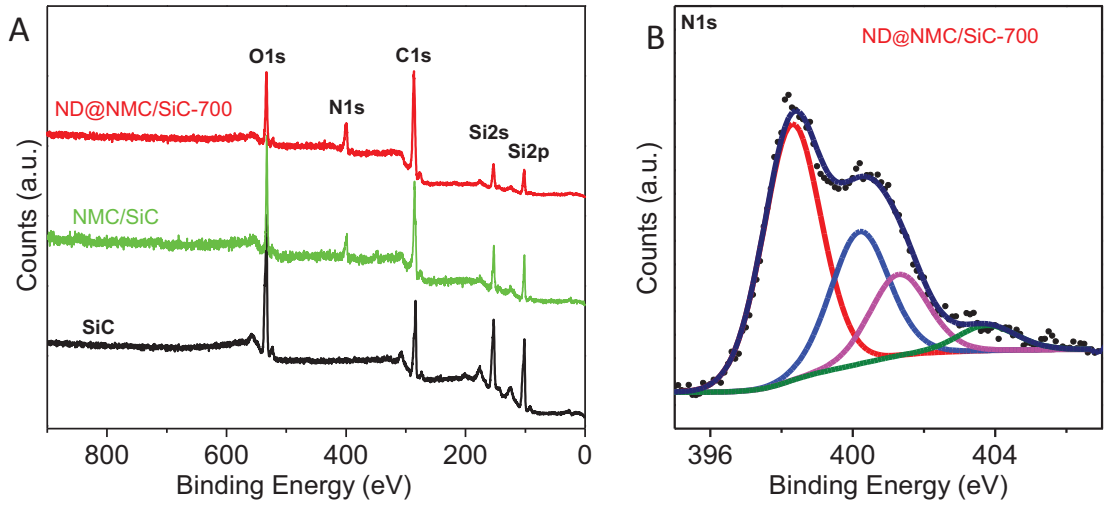

Figure 88. XPS spectra of the ND@NMC/SiC material: (A) Survey spectra (NMC/SiC and SiC were included for comparison), (C-D) high resolution N1s spectrum.

The DH performance of the ND@NMC/SiC was also compared with that of the commercial bulk Fe-K/Al_2O_3 catalyst under similar reaction conditions (Fig. 89A).[9] The Fe-K/Al_2O_3 catalyst shows a high DH activity at the beginning of the test followed by a sharp deactivation down to 2 $mmol_{ST}g_{ND}^{-1}h^{-1}$ (Fig. S2.B) followed by a steady-state. Such deactivation was attributed to the rapid coverage of the iron-based catalyst sites by a layer of carbonaceous leading to a drastic loss of the active site density per catalyst unit weight. The specific reaction rate, expressed in terms of molecules of EB converted per gram of active phase per hour, obtained on the different catalysts is presented in Fig. 89B and confirms again the superior DH activity of the ND@NMC/SiC catalyst.[19,20]

The high catalytic performance of the nitrogen-doped porous carbon studied in the present work could be attributed to the electronic modification of the carbon atoms by the adjacent nitrogen ones according to the pioneer work by Lai and co-workers.[21]

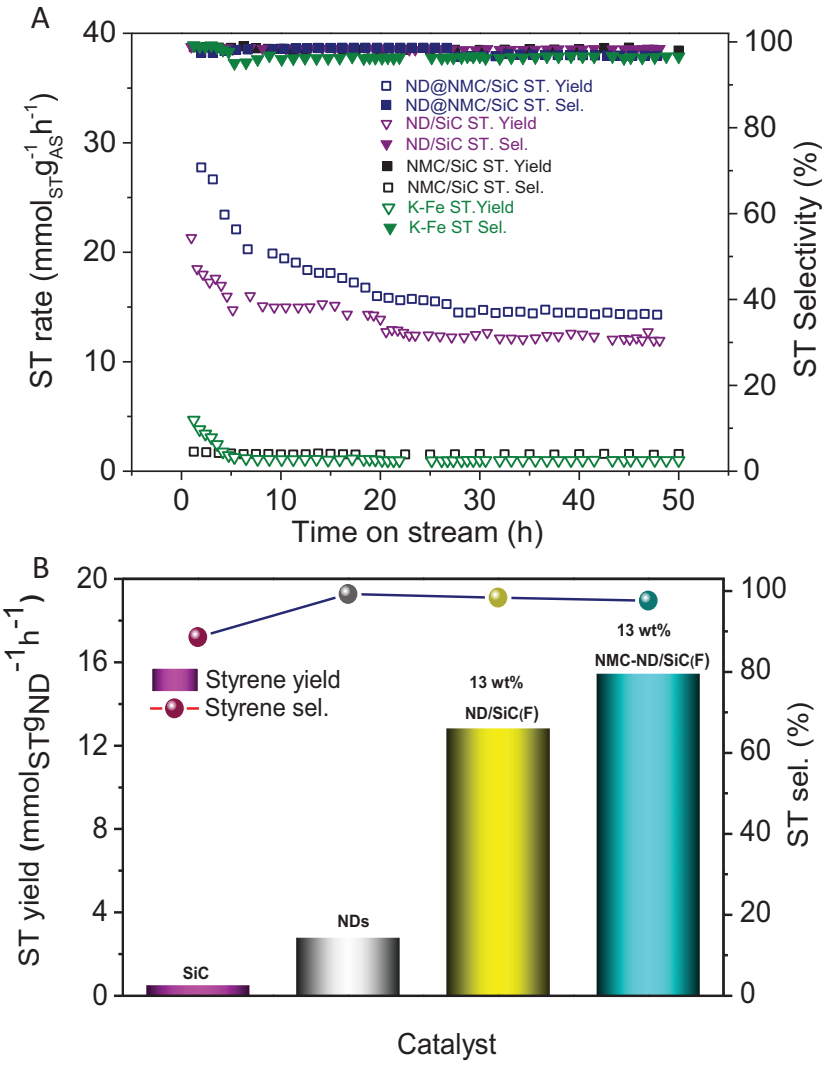

Figure 89. (A) Ethylbenzene (EB) dehydrogenation activity on of the ND-NMC and pristine ND unsupported and supported on silicon carbide foam (SiC-foam). **(B)** Benchmarking of various carbon based catalyst and the industrial promoted catalyst under steady-state (Reaction conditions: 300 mg, 550 °C, 2.8 % EB in helium, 30 mL·min^{-1}). The ST yield of ND-free catalysts is expressed as styrene formation rate per weight of catalysts per hour (mmol$_{ST}$ g$_{cat}^{-1}$ h^{-1}). Reaction conditions: 550 °C, 2.8 % EB in helium, 30 mL·min^{-1}, atmospheric pressure.

3.6 Macroscopic ND@NMC/SiC catalyst under severe dehydrogenation conditions

The comparison between the ND-NMC/SiC and ND/SiC are also evaluated under reaction conditions close to those operated in the industrial process, i.e. high temperature, i.e. 600°C, and high EB feed per catalyst weight. The catalytic performances obtained on the ND-NMC/SiC and ND/SiC catalysts at 600°C and under different EB concentration are presented in the Figure 90. The ND@NMC/SiC shows a higher DH performance, expressed as EB conversion, compared to the ND/SiC catalyst which confirms the better dispersion of the ND active sites on the former catalyst thanks to the presence of a NMC surrounding layer. The ND-NMC/SiC displays a steady-state EB conversion of about 40 % under the highest EB feed, i.e. 880 g/h, which is close to the industrial performance required. A deactivation was observed during the first 30 h under the high EB feeding before reaching a steady-state for additional 20 h on stream. The ND-NMC/SiC catalyst also displays a slightly higher ST selectivity compared to that of the ND/SiC, i.e. 97 instead of 95 %. Such difference in terms of ST selectivity could be attributed to the higher dispersion of the ND which reduces the re-adsorption process and secondary reactions leading to low weight by-products.

It can be seen that increasing the EB concentration in the flow rate also leads to a significant increase of the DH activity on both catalysts (Figure 90B). Such phenomenon could be attributed to the better saturation of the available catalytic sites present on the catalyst surface which in turn, leads to the full use of the available active sites per catalyst unit weight.

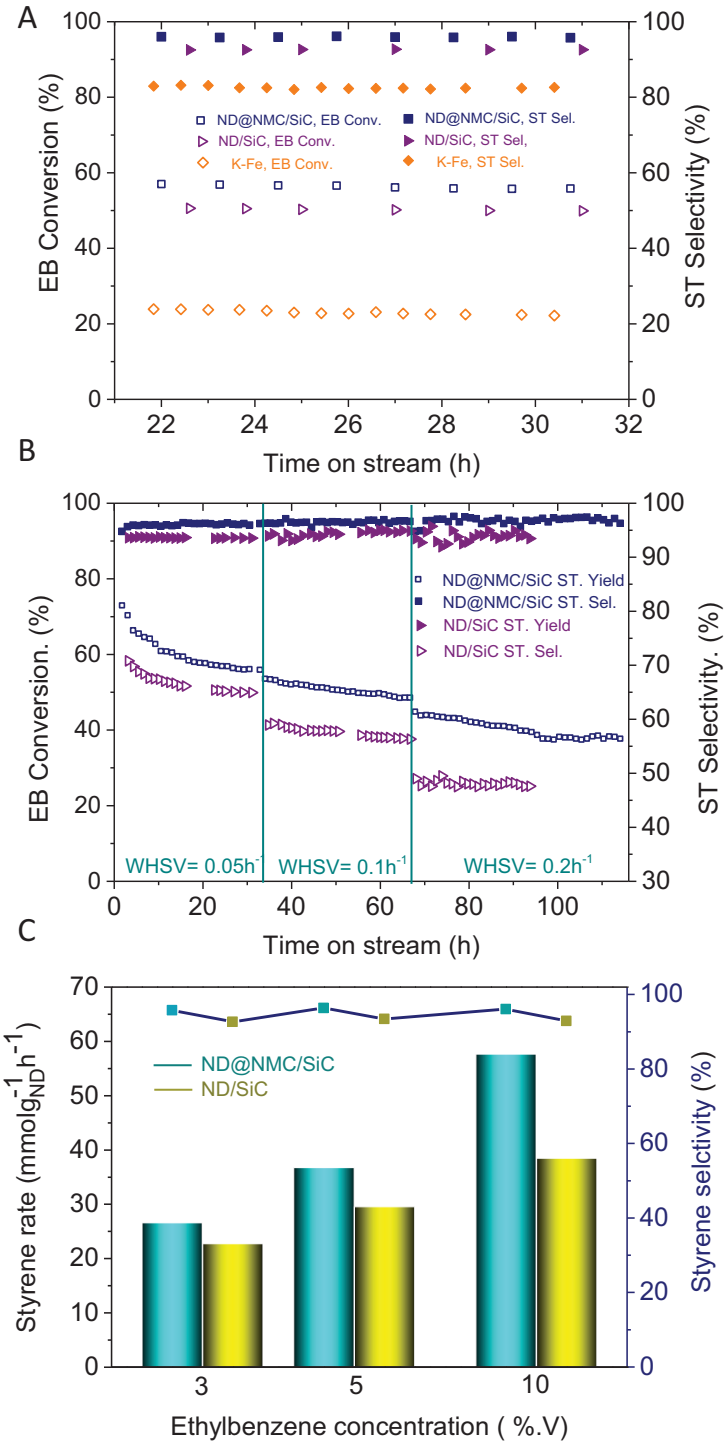

Figure 90. (A) Ethylbenzene (EB) conversion and styrene selectivity of the ND@NMC, ND@NMC/SiC and the industrial K-Fe catalyst. (Reaction conditions: 300 mg, 600 °C, 2.8 % EB in helium, 30 mL.min^{-1}) **(B)** Influence of the ethylbenzene concentration (A) the DH performance of the NMC-ND/SiC catalyst, **(C)** compare to the ND/SiC under the same reaction condition. Reaction conditions: catalyst weight = 300 mg, 600 °C, 2.8 - 5 - 10% EB in helium 30 mL.min^{-1}, corresponding respectively to 250, 435 and 881gh^{-1} EB feed rate.

Table 8. Physico-chemical characterization of different investigated materials.

Samples	BET_{SSA} ($m^2.g^{-1}$)	D_{BJH} (nm)	V_{TOTAL} ($cm^3.g^{-1}$)	C (at%)	O (at%)	Si (at%)	N (at%)	Nitrogen species (at.%)			
								Pyridinic	Pyrrolic	Graphitic	Oxidized
SiC	28	20	0.15	33.6	25.3	40.99	-	-	-	-	-
ND	258	16	1.27	92.8	7.2	-	-	-	-	-	-
ND-700	271	17	1.4	93.2	6.8	-	-	-	-	-	-
ND-900	525	13.8	2.04	94.6	5.4	-	-	-	-	-	-
ND@NMC-700	320	6.7	0.5	88.23	2.94	-	8.83	4.01	2.94	1.26	0.62
ND@NMC-900	333	6.8	0.6	92.51	2.68	-	4.82	1.48	1.9	1.05	0.38
ND/SiC	73	14	0.26	81.4	13.0	5.70	-	-	-	-	-
NMC/SiC-700	57	12.8	0.13	53.58	21.43	16.88	8.11	4.16	0.32	2.89	0.74
ND@NMC/SiC-700	104	6.5	0.13	61.25	15.22	13.53	10	5.17	2.67	1.65	0.51

4. Conclusion

In summary, we have successfully prepared a hybrid metal-free catalyst consisting of dispersing nanodiamonds within a nitrogen-doped mesoporous carbon (NMC) phase with

catalysis. The catalyst displays a high and stable dehydrogenation activity in the conversion of ethylbenzene into styrene under steam-free conditions. The high dehydrogenation performance could be attributed to the high dispersion of the metal-free nanodiamond centers within the NMC layer which provides a high surface contact for the reactant. The high stability was attributed to the ability of the catalyst to prevent cracking reactions leading to the formation of carbonaceous on the surface.

The catalyst was also evaluated under severe reaction conditions, i.e. high temperature and high ethylbenzene feeding, close to those used in the industrial process. Under these industrial conditions the catalyst exhibits a dehydrogenation performance extremely promising with a conversion approaching 40 % per pass while keeping the styrene selectivity at around 97 %. Again, no deactivation was observed as a function of time on stream for hundred hours indicating the high resistance of the catalyst towards carbonaceous encapsulation as encountered with the commercial iron-based catalyst.

Acknowledgements

The present project is part of the FREECATS project financed by the European Union within the 7FP research program through a contract number NMP3-SL-2012-280658. The authors would like to acknowledge T. Romero (ICPEES) for performing SEM analysis. The TEM experiments were carried out at the facilities of the IPCMS (UMR 7504 of the CNRS).

References

(1) Wong, W. Y.; Daud, W. R. W.; Mohamad, A. B.; Kadhum, A. A. H.; Loh, K. S.; Majlan, E. H. Recent Progress in Nitrogen-Doped Carbon and Its Composites as Electrocatalysts for Fuel Cell Applications. *Int. J. Hydrog. Energy* **2013**, *38*, 9370–9386.

(2) Gong, K.; Du, F.; Xia, Z.; Durstock, M.; Dai, L. Nitrogen-Doped Carbon Nanotube Arrays with High Electrocatalytic Activity for Oxygen Reduction. *Science* **2009**, *323*, 760–764.

(3) Chizari, K.; Deneuve, A.; Ersen, O.; Florea, I.; Liu, Y.; Edouard, D.; Janowska, I.; Begin, D.; Pham-Huu, C. Nitrogen-Doped Carbon Nanotubes as a Highly Active Metal-Free Catalyst for Selective Oxidation. *ChemSusChem* **2012**, *5*, 102–108.

(4) Zhao, Y.; Nakamura, R.; Kamiya, K.; Nakanishi, S.; Hashimoto, K. Nitrogen-Doped Carbon Nanomaterials as Non-Metal Electrocatalysts for Water Oxidation. *Nat. Commun.* **2013**, *4*, 2390.

(5) Liu, Y.; Yu, H.; Quan, X.; Chen, S.; Zhao, H.; Zhang, Y. Efficient and Durable Hydrogen Evolution Electrocatalyst Based on Nonmetallic Nitrogen Doped Hexagonal Carbon. *Sci. Rep.* **2014**, *4*.

(6) Atanda, L. A.; Balasamy, R. J.; Khurshid, A.; Al-Ali, A. A. S.; Sagata, K.; Asamoto, M.; Yahiro, H.; Nomura, K.; Sano, T.; Takehira, K.; *et al.* Ethylbenzene Dehydrogenation over Mg3Fe0.5−xCoxAl0.5 Catalysts Derived from Hydrotalcites: Comparison with Mg3Fe0.5−yNiyAl0.5 Catalysts. *Appl. Catal. Gen.* **2011**, *396*, 107–115.

(7) Balasamy, R. J.; Khurshid, A.; Al-Ali, A. A. S.; Atanda, L. A.; Sagata, K.; Asamoto, M.; Yahiro, H.; Nomura, K.; Sano, T.; Takehira, K.; *et al.* Ethylbenzene Dehydrogenation over Binary FeOx–MeOy/Mg(Al)O Catalysts Derived from Hydrotalcites. *Appl. Catal. Gen.* **2010**, *390*, 225–234.

(8) Mimura, N.; Takahara, I.; Saito, M.; Hattori, T.; Ohkuma, K.; Ando, M. Dehydrogenation of Ethylbenzene over Iron Oxide-Based Catalyst in the Presence of Carbon Dioxide. *Catal. Today* **1998**, *45*, 61–64.

(9) Zhang, J.; Su, D. S.; Blume, R.; Schlögl, R.; Wang, R.; Yang, X.; Gajović, A. Surface Chemistry and Catalytic Reactivity of a Nanodiamond in the Steam-Free Dehydrogenation of Ethylbenzene. *Angew. Chem. Int. Ed.* **2010**, *49*, 8640–8644.

(10) Schmidt, W. Solid Catalysts on the Nanoscale: Design of Complex Morphologies and Pore Structures. *ChemCatChem* **2009**, *1*, 53–67.

(11) Thanh, T. T.; Ba, H.; Truong-Phuoc, L.; Nhut, J.-M.; Ersen, O.; Begin, D.; Janowska, I.; Nguyen, D. L.; Granger, P.; Pham-Huu, C. A Few-Layer Graphene–graphene Oxide Composite Containing Nanodiamonds as Metal-Free Catalysts. *J. Mater. Chem. A* **2014**, *2*, 11349–11357.

(12) Li, H.; Liu, H.; Jong, Z.; Qu, W.; Geng, D.; Sun, X.; Wang, H. Nitrogen-Doped Carbon Nanotubes with High Activity for Oxygen Reduction in Alkaline Media. *Int. J. Hydrog. Energy* **2011**, *36*, 2258–2265.

(13) Hibino, T.; Kobayashi, K.; Heo, P. Oxygen Reduction Reaction over Nitrogen-Doped Graphene Oxide Cathodes in Acid and Alkaline Fuel Cells at Intermediate Temperatures. *Electrochimica Acta* **2013**, *112*, 82–89.

(14) Chen, C.; Zhang, J.; Zhang, B.; Yu, C.; Peng, F.; Su, D. Revealing the Enhanced Catalytic Activity of Nitrogen-Doped Carbon Nanotubes for Oxidative Dehydrogenation of Propane. *Chem. Commun.* **2013**, *49*, 8151.

(15) Chai, G.-L.; Hou, Z.; Shu, D.-J.; Ikeda, T.; Terakura, K. Active Sites and Mechanisms for Oxygen Reduction Reaction on Nitrogen-Doped Carbon Alloy Catalysts: Stone–Wales Defect and Curvature Effect. *J. Am. Chem. Soc.* **2014**, *136*, 13629–13640.
(16) Abdalla, B. K.; Elnashaie, S. S. E. H.; Alkhowaiter, S.; Elshishini, S. S. Intrinsic Kinetics and Industrial Reactors Modelling for the Dehydrogenation of Ethylbenzene to Styrene on Promoted Iron Oxide Catalysts. *Appl. Catal. Gen.* **1994**, *113*, 89–102.
(17) Zhao, Q.; Fellinger, T.-P.; Antonietti, M.; Yuan, J. Nitrogen-Doped Carbon Capsules via Poly(ionic Liquid)-Based Layer-by-Layer Assembly. *Macromol. Rapid Commun.* **2012**, *33*, 1149–1153.
(18) Liu, Y.; Ba, H.; Nguyen, D.-L.; Ersen, O.; Romero, T.; Zafeiratos, S.; Begin, D.; Janowska, I.; Pham-Huu, C. Synthesis of Porous Carbon Nanotubes Foam Composites with a High Accessible Surface Area and Tunable Porosity. *J. Mater. Chem. A* **2013**, *1*, 9508–9516.
(19) Ba, H.; Liu, Y.; Mu, X.; Doh, W.-H.; Nhut, J.-M.; Granger, P.; Pham-Huu, C. Macroscopic Nanodiamonds/β-SiC Composite as Metal-Free Catalysts for the Steam-Free Dehydrogenation of Ethylbenzene to Styrene. *Appl. Catal. Gen.*
(20) Ba, H.; Podila, S.; Liu, Y.; Mu, X.; Nhut, J.-M.; Papaefthimiou, V.; Zafeiratos, S.; Granger, P.; Pham-Huu, C. Nanodiamond Decorated Few-Layer Graphene Composite as an Efficient Metal-Free Dehydrogenation Catalyst for Styrene Production. *Catal. Today*.
(21) Truong-Phuoc, L.; Duong-Viet, C.; Doh, W.-H.; Bonnefont, A.; Janowska, I.; Begin, D.; Savinova, E. R.; Granger, P.; Pham-Huu, C. Influence of the Reaction Temperature on the Oxygen Reduction Reaction on Nitrogen-Doped Carbon Nanotube Catalysts. *Catal. Today* **2015**, *249*, 236–243.

Supporting Information

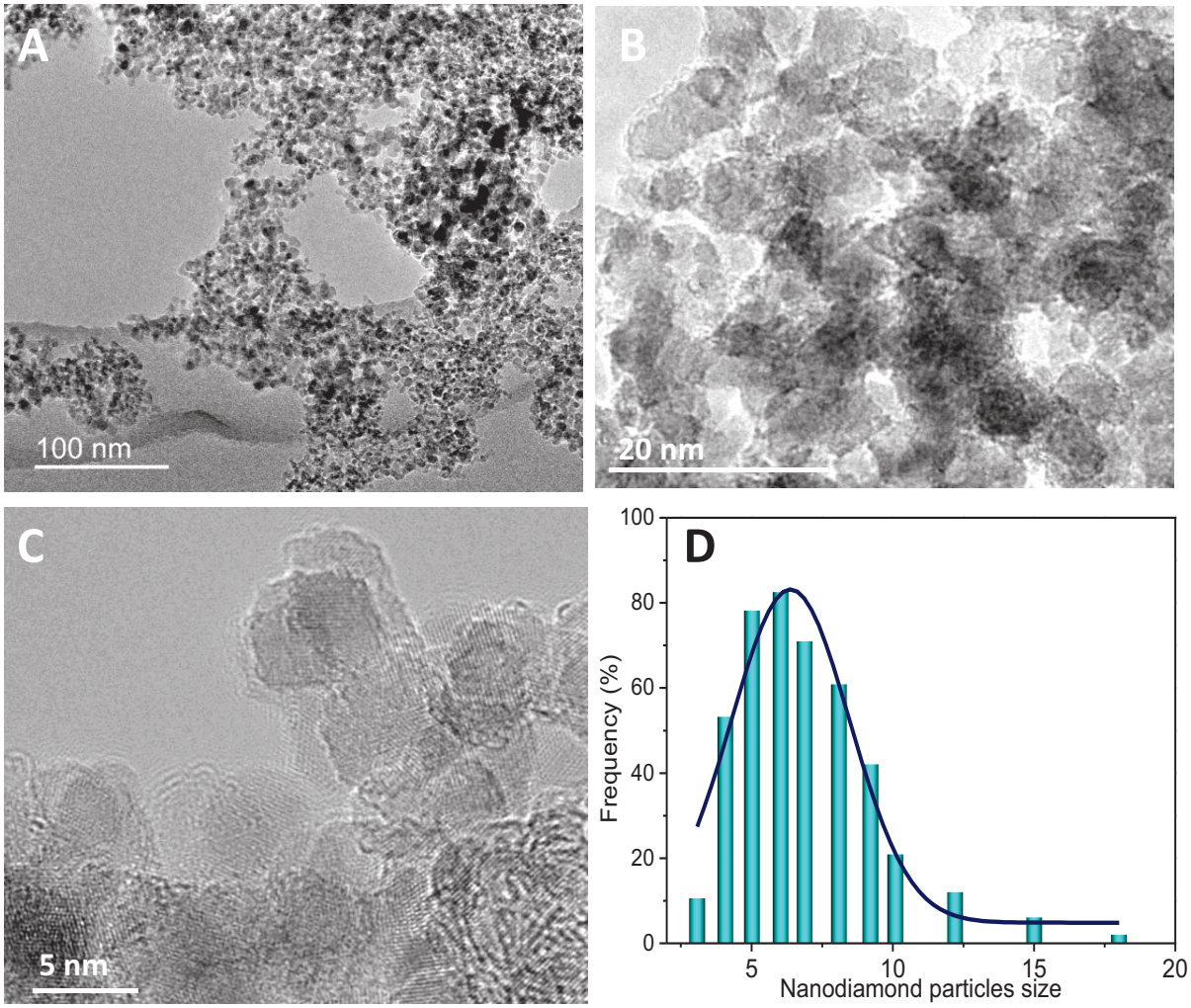

Figure S1. TEM micrographs of the pristine NDs powder.

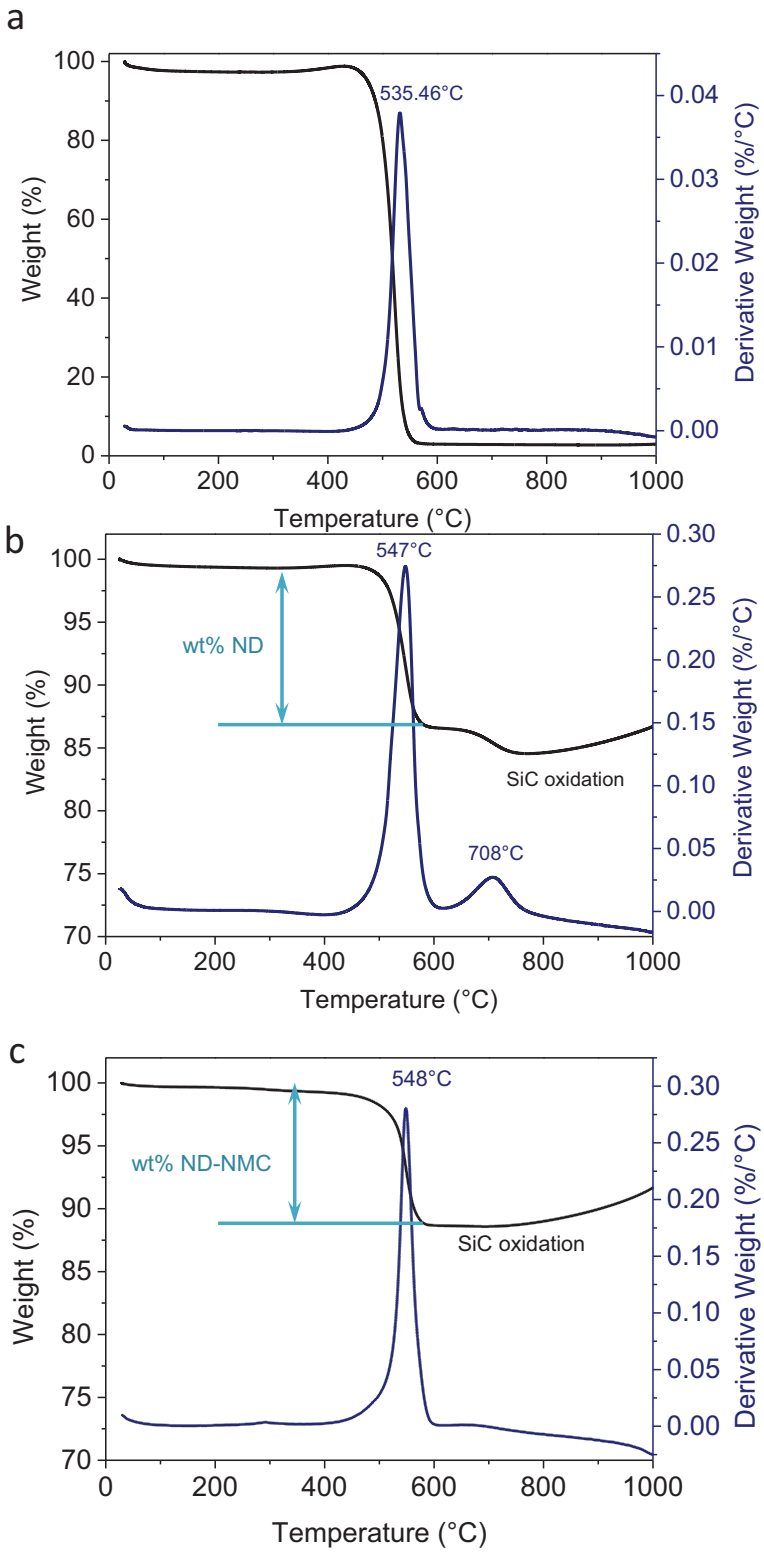

Figure S2. Thermogravimetric analysis (TGA) of the pristine ND, ND/SiC and ND@NMC/SiC foam composite. The mass loading of ND and ND-NMC is around 13 wt % on the as-prepared catalysts.

Chapter 7

Conclusion & Perspectives

Summary

The graphitic carbon-based materials, i.e. carbon nanotubes/nanofibers and graphene, nanodiamond have received an ever increasing scientific and industrial interest during the last decades[1,2,3] for several potential fields of application such as electronic,[4] energy conversion and storage,[5] nanomedicine,[6] waste water treatment,[7] and especially in the field of catalysis.[8] The scientific and industrial interests also rely on the possibility of shaping of these nanomaterials for concrete industrial applications.[9,10] The objective of the thesis deals with the preparation of supported nanodiamonds catalysts with higher exposed active sites per catalyst weight unit for improving the dehydrogenation catalytic performance. The supports will be consisted by few-layer graphene (FLG), graphene oxide/few-layer graphene (GO/FLG), carbon nanofibers decorated few-layer graphene (CNFs/FLG), and macroscopic silicon carbide foam. The best catalyst with appropriate shape will be further evaluated under the reaction conditions similar to which operated in the industrial plants in order to assess its industrial potential for future development.

This Chapter reports on the different conclusions from the results obtained within the framework of the Ph.D. followed by a short description of the different perspectives issued from the results obtained.

General conclusions

According to the results obtained one can stated that nanodiamonds is steadily dispersed on carbon-based supports, i.e. GO/FLG, CNFs/FLG, which allows the breakdown of the nanodiamonds aggregates into dispersed clusters evenly decorated the carbon host structure. The improved dispersion of the nanodiamonds phase on these carbon-based supports leads to a significant improvement of the dehydrogenation catalytic performance compared to the unsupported nanodiamonds (Fig. 91). The introduction of the carbon nanofibers onto the few-layer graphene surface leads to the formation of a hierarchical structure provide not only a higher accessibility of the reactant to the whole catalytic system but also to improve the nanodiamonds dispersion thanks to the high reactivity of the prismatic planes in the carbon nanofibers for anchoring the nanodiamonds particles. The dehydrogenation catalytic performance obtained on these supported nanodiamonds is several higher compared to that obtained on the industrial iron-based catalyst under steam-free conditions. Such better catalytic performance was attributed to the high desorption rate of the styrene intermediate product from the catalytic site before polymerization and also to

the high exposed active sites per unit weight of the catalyst. The temperature-programmed oxidation analysis carried out on the spent catalysts clearly evidences the much lower carbonaceous residue concentration on the nanodiamonds-based catalysts than on the iron-based catalyst. Finally, the nanodiamonds-based catalysts display a relatively stability as a function of time on stream and the spent catalyst can be easily regenerated by a simple oxidative process at low temperature for a short period.

The improvement of the dehydrogenation catalytic performance of the supported nanodiamonds allows us to settle a base for new optimization process regarding the future industrial development of this promising metal-free catalyst. It is worthy to note that for industrial development the carbon supports deveoped above cannot be efficiently used due to their nanoscopic dimension which generate high pressure drop across the catalyst bed and thus, new support with better physical properties is needed. The support of choice is the silicon carbide foam with random struts and interconnected structure which significantly improve the back mixing of the processing feed and the maintaining of the homogeneous temperature within the catalyst bed. The silicon carbide foam containing nanodiamonds catalyst indeed shows a great improvement of the dehydrogenation activity compared to the other carbon-based catalysts. The styrene selectivity remains high at around 99% and after an induction period no further deactivation was observed on the catalyst during a long-term test. The ND/SiC foam catalyst was also evaluated under relevant industrial reaction conditions, i.e. high ethylbenzene concentration (250 g/h) and high reaction temperature (600°C), in order to confirm the possibility of replacing the industrial iron-based catalyst by the metal-free one.

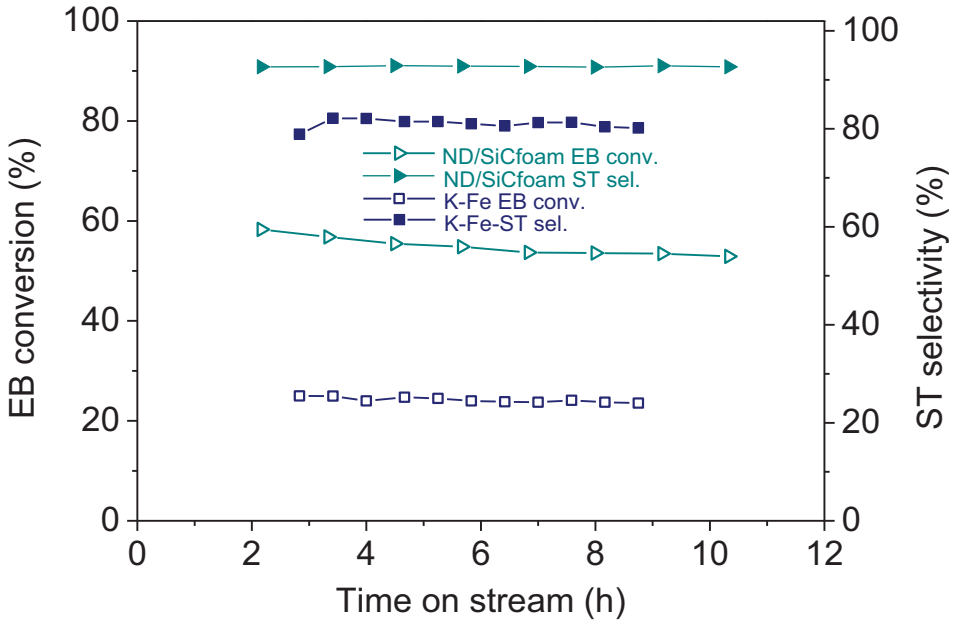

Figure 91 Comparison of EB conversion and ST selectivity over 13 wt% ND/SiC(F) and K-Fe catalysts at reaction temperature of 600 °C. Reaction conditions: 2.8 % EB in helium, 30 mL·min^{-1}, 300 mg of catalyst, atmospheric pressure.

The ND/SiC foam catalyst displays an extremely high dehydrogenation activity comparable to that reported for the industrial iron-based catalyst along with a high stability during the long-term test (Fig. 92).

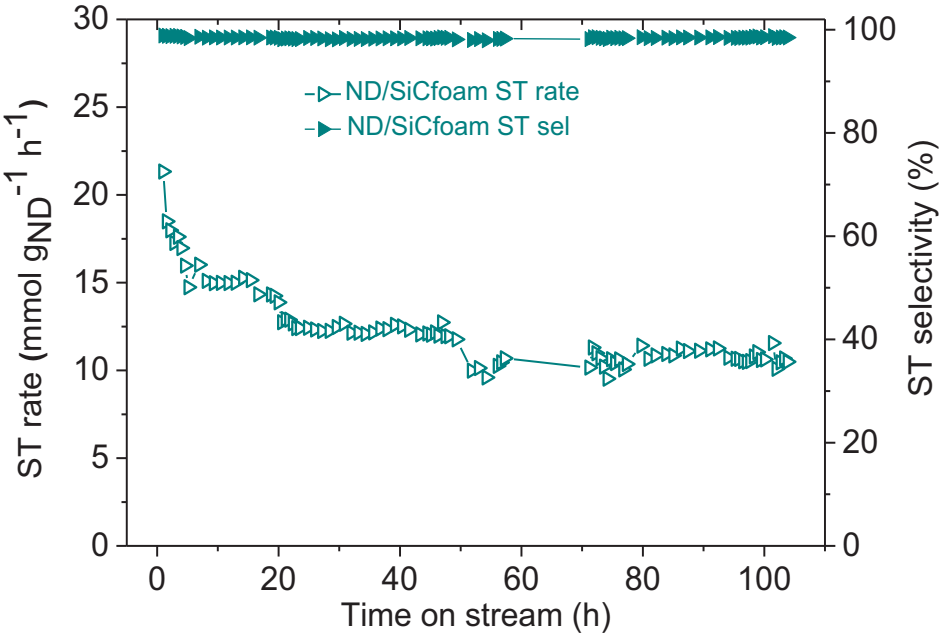

Figure 92. Catalytic performance of stream-free ethylbenzene dehydrogenation under long-term test at 550°C over 13 wt% ND/SiC(F) catalyst. Reaction conditions: 300 mg, 550°C, 2.8 % EB in helium, 30 mL·min^{-1}.

The spent catalyst can be easily regenerated through a simple air calcination process at low temperature. It is also noted that the regenerated catalyst exhibits an improved resistance towards deactivation for the subsequence long-term test. According to the catalytic results one can stated that metal-free catalyst based on the nanodiamonds supported on SiC foam could represent a viable alternative for the iron-based catalyst with lower environmental impact.

In an attempt to prepare a metal-free catalyst with lower environmental impact we have also developed a new synthesis route based on the use of food stuffs raw materials which allow the separate nucleation from the nanodiamond center. Such synthesis route was further implemented to prepare nanodiamonds coated by a layer of nitrogen-doped mesoporous carbon supported on the SiC foam. The as-synthesized catalyst exhibits a high and stable dehydrogenation catalytic performance for the direct conversion of ethylbenzene into styrene under relevant industrial conditions.

In summary, we have succeeded to prepare a high and stable metal-free catalyst, for the selective dehydrogenation process to convert ethylbenzene into styrene, with controlled macroscopic shape for replacing the industrial iron-based catalyst with weaker catalytic

performance and cost incentive. The synthesis methods developed allow one to prepare this metal-free catalyst in a simple way for mass production which is one of the most demanded prerequisite for the implementation of new catalyst in the field of heterogeneous catalysis field.

Perspectives

Numerous perspectives can be derived from the results obtained within the framework of this Ph.D. thesis and some of them are summarized below.

The developed nanodiamonds metal-free catalyst can be used in other catalytic applications such as liquid-phase aromatic hydrogenation process where the high adsorption properties of the active phase could be put in advance. The foam host structure could also play an important role by providing a high back mixing degree of the reactant along with microturbulences which could improve the contact surface and thus, the overall catalytic activity. In regard to this additional chemical engineering work is highly needed in order to rule out the direct influence of the above mentioned parameters on the final catalytic performance.

During the reaction, the catalyst is maintain under an unstable state by the external energy input and thus, it is expected that the way to target the energy into a tiny active regions is of great interest for maintaining the system in operation with a minimum energy input. In the case of the energy supply failure part of the system turns out to its stable state which resulted to an irreversible deactivation of the all system. The perspective which is aimed to be developed further is based on the selective heating of the active phase while using the support as a heat regulator. Indeed, the nanodiamonds are inductively active and thus, can be heated inside a magnetic inductive heater while the SiC is not. In such configuration one should expected to have an active center with high temperature for boosting the whole reaction process whereas the support will play a role of heat exchanger to prevent excessive temperature runaway within the catalyst bed. Up until now, no such hybrid system has been developed so far in the heterogeneous catalysis field and could represent an interesting catalytic system for fast reaction process which will going far beyond the framework of metal-free catalyst.

Finally, the nitrogen-doped mesoporous carbon developed within this Ph.D. thesis to separate the nanodiamonds centers could be also applied as metal-free catalyst in other catalytic processes such as partial oxidation or reduction processes where the catalytic performance improvement is of great interest. Preliminary work done on this system has confirmed it superiority catalytic performance in the above mentioned catalytic processes. However, the full exploitation of such metal-free hybrid system is still far from being fully

exploited and thus, additional characterization and catalytic application are still needed. Future work will be done to assess such high catalytic performance of this metal-free catalyst in these relevant catalytic processes reported above and also in other reactions where the use of metal-free catalyst could provide better catalytic systems compared to the traditional ones. Attention will be focused on the influence of the acid-base properties of these systems on their catalytic performance.

References

(1) Serp, P.; Corrias, M.; Kalck, P. Carbon Nanotubes and Nanofibers in Catalysis. *Appl. Catal. Gen.* **2003**, *253*, 337–358.

(2) Carrasco, P. M.; Montes, S.; García, I.; Borghei, M.; Jiang, H.; Odriozola, I.; Cabañero, G.; Ruiz, V. High-Concentration Aqueous Dispersions of Graphene Produced by Exfoliation of Graphite Using Cellulose Nanocrystals. *Carbon* **2014**, *70*, 157–163.

(3) Boudou, J.-P.; Curmi, P. A.; Jelezko, F.; Wrachtrup, J.; Aubert, P.; Sennour, M.; Balasubramanian, G.; Reuter, R.; Thorel, A.; Gaffet, E. High Yield Fabrication of Fluorescent Nanodiamonds. *Nanotechnology* **2009**, *20*, 235602.

(4) Miao, M. 3 - Carbon Nanotube Yarns for Electronic Textiles. In *Electronic Textiles*; Dias, T., Ed.; Woodhead Publishing: Oxford, 2015; pp. 55–72.

(5) Deng, J.-H.; Wang, F.-J.; Cheng, L.; Yu, B.; Li, G.-Z.; Hou, X.-G.; Li, D.-J.; Cheng, G.-A. Improved Field Emission of Few-Layer Graphene–carbon Nanotube Composites by High-Temperature Processing. *Mater. Lett.* **2014**, *124*, 15–17.

(6) Man, H. B.; Zhang, K.; Robinson, E.; Chow, E. K.; Ho, D. Chapter 15 - Engineering Nanoparticulate Diamond for Applications in Nanomedicine and Biology. In *Ultananocrystalline Diamond (Second Edition)*; Gruen, O. A. S. M., Ed.; William Andrew Publishing: Oxford, 2012; pp. 493–518.

(7) Choi, J.; Chung, J. Evaluation of Potential for Reuse of Industrial Wastewater Using Metal-Immobilized Catalysts and Reverse Osmosis. *Chemosphere* **2015**, *125*, 139–146.

(8) Schlögl, R. Chapter Two - Carbon in Catalysis. In *Advances in Catalysis*; Jentoft, B. C. G. and F. C., Ed.; Academic Press, 2013; Vol. 56, pp. 103–185.

(9) Tahri, N.; Jedidi, I.; Cerneaux, S.; Cretin, M.; Ben Amar, R. Development of an Asymmetric Carbon Microfiltration Membrane: Application to the Treatment of Industrial Textile Wastewater. *Sep. Purif. Technol.* **2013**, *118*, 179–187.

(10) Paradise, M.; Goswami, T. Carbon Nanotubes – Production and Industrial Applications. *Mater. Des.* **2007**, *28*, 1477–1489.

Annex

I. Publications

1. Synthesis of porous carbon nanotubes foam composites with a high accessible surface area and tunable porosity
   Y. Liu, **H. Ba**, D. L.Nguyen, O. Ersen, T. Romero, S. Zafeiratos, D. Begin, I. Janowska , C. Pham-Huu,
   Journal of Materials Chemistry A, 1, 9508-9516, 2013

2. Nitrogen-doped carbon nanotubes decorated silicon carbide as metal-free catalyst
   C. Duong-Viet, **H. Ba**, Y. Liu, L. Truong-Phuoc, J-M. Nhut, C. Pham-Huu,
   Chinese Journal of Catalysis, 35, 906-913 2014

3. Few-layer graphene-graphene oxide composite containing nanodiamonds as metal-free catalyst in the dehydrogenation of ethylbenzene
   T. Tran-Thanh, **H. Ba**, L. Truong-Phuoc, J-M. Nhut, O. Ersen, D. Begin, I. Janowska, D. L. Nguyen, P. Granger, C. Pham-Huu,
   Journal of Materials Chemistry A.2 11349-11357, 2014

4. Nanodiamonds decorated few-layer graphene composite as an efficient metal-free dehydrogenation catalyst for styrene production
   H. Ba, S. Podila, Y. Liu , J-M. Nhut, X. Mu, T. Tran-Thanh, V. Papaefthimiou, S. Zafeiratos, P. Granger, C. Pham-Huu,
   Catalysis Today, DOI *: 10.1016/j.cattod.2014.10.029* , 2015

5. Macroscopic nanodiamonds/β-SiC composite as an efficient metal-free catalyst for the steam-free dehydrogenation of ethylbenzene to styrene
   H. Ba, Y. Liu, X. Mu, W.H. Doh, J-M. Nhut, P. Granger, C. Pham-Huu,
   Applied Catalysis A, 10.1016/j.apcata.2015.04.022, 2015

6. Activation of few layer graphene by μW-assisted oxidation in water via formation of nanoballs - support for Pt nanoparticles

A. A Pirzado; L. Truong-Phuoc.; V. Papaefthimiou; C. Matei Ghimbeu; F. Le Normand; **H. Ba**; C. Pham-Huu,; T. Tran-Thanh; I. Janowska,
Journal of Colloid and Interface Science, DOI: 10.1016/j.jcis.2015.03.063, 2015

7. Microwave assisted growth of sapo-34 on β-SiC foams for methanol dehydration to dimethyl ether
M. M. Elamin, Z. Malaibari, **H.Ba**, J-M. Nhut, C. Pham-Huu, Oki Muraza
Chemical Engineering Journal, doi:10.1016/j.cej.2015.03.118, 2015

8. "Dressing" macroscopic shape catalyst supports with a highly N-enriched and metal-free active phase
H. Ba, Y. Liu, L. Truong-Phuoc, C. Duong-Viet, X. Mu, W. Hui Doh, T. Tran-Thanh, W. Baaziz, D. L. Nguyen, J-M. Nhut, I. Janowska, D. Begin, P. Granger, G. Tuci, G. Giambastiani, M. J. Ledoux, C. Pham-Huu,
Chemical Communication, Doi: 10.1039/C5CC05259A

9. Self-sustained nitrogen-doped carbon nanotubes as-metal-free catalyst for selective oxidation
H. Ba, C. Duong-Viet, Y. Liu, J-M. Nhut[a], P. Granger[b], M. J. ledoux, C. Pham-Huu[a],*
Compte Rendu de Chimie, Accepted 2015

10. Nanodiamonds decorated graphene-carbon nanofibers 3D architecture as a metal-Free catalyst for styrene production
H. Ba, L. Truong-Phuoc, Y. Liu, C. Duong-Viet, J-M Nhut, L. Nguyen-Dinh, P. Granger, O. Ersen, C. Pham-Huu
Carbon, Submitted, 2015

11. Nitrogen-enriched carbon nanospheres decorated silicon carbide as a superior metal-free catalyst for styrene production
H. Ba, Y. Liu, C. Duong-Viet, M. Iltis, J. Luo, L. Truong-Phuoc, J-M. Nhut, P. Granger, C. Pham-Huu.
ACS Catalysis, Submitted, 2015

12. Green Chemical Route to Produce Hierarchical Carbon Nanotubes Coated with Nitrogen-Doped Porous Carbon as Metal-free Catalyst

H. Ba, Y. Liu, L. Truong-Phuoc, J-M. Nhut, L-D Nguyen, O. Ersen, P. Granger,

G.Tuci, G. Giambastiani, C. Pham-Huu

Nature communication, Submitted, 2015

13. Carbon nanotubes containing oxygenated decorating defects as metal-free catalyst for partial oxidation of H_2S

C. Duong-Viet, L. **H. Ba,** Truong-Phuoc, J-M. Nhuta, P. Granger, M. J. ledoux, C. Pham-Huu

Journal of catalysis, Submitted, 2015

14. Minute made of N-S co-doped Carbon Metal-Free Active Phase.

H. Ba, J-M. Nhut, C. D-Viet, L. Truong-Phuoc, C. Pham-Huu,

Under preparation, 2015

15. Improvement of the Dehydrogenation of Ethyl-benzene by Nitrogen-doped Carbon hybridized Nanodiamonds and Graphitization level

T.T. Tung, **H. Ba**,Y. Liu, L. Truong-Phuoc, J-M Nhut, P. Granger, C. Pham-Huu

Under preparation, 2015

III. Book's chapter

Nitrgen-doped carbon nanotubes s as metal-free catalyst

C. Duong-Viet, **H. Ba,** L. Truong-Phuoc, J-M. Nhut[a], P. Granger, M. J. ledoux, C. Pham-Huu

Nanocarbon for catalysis, Elesevier Book series, submitted

III. Patents

1. Method for preparing highly nitrogen-doped mesoporous carbon composites
   C. Pham-Huu, G. Giambastiani, Y. Liu, **H. Ba**, L. Nguyen-Dinh, J-M. Nhut.
   Déposée par le CNRS, l'Université de Strasbourg et le CNR le 21 Janvier 2015.
   Demande de brevet Européen No. EP 15-152038, 2015.

2. Use of highly nitrogen-doped mesoporous carbon composites for catalytic advanced oxidation processes (AOP) for water and wastewater treatment.
   Liu Y., Nguyen-Dinh L., **Ba H**., Nhut J-M., Giambastiani G., Pham-Huu C.
   Déposée par le CNRS, l'Université de Strasbourg et le CNR le 21 Janvier 2015.
   Demande de brevet Européen No. EP 15-152039, 2015.

3. Procédé pour la mise en œuvre des structures mésoporeuses à base de composites de carbure de silicium recouvert par une couche de carbone pour l'échantillonnage passif des composés organiques semi-volatils.
   Levi M., **Ba H**., Millet M, Pham-Huu C.
   Demande de brevet Européen en cours.

4. Synthèse et fonctionnalisation de nanomatériaux graphitiques par désintégration
   Troung-Phuoc L., **Ba H**., Janowska I.
   Demande de brevet Européen en cours.

III. Orales presentation and poster

Orales

1. Exploring new routes for 1D and 2D carbon synthesis (*Keynote lecture*)
   Tran-Thanh T., **Ba H.**, Duong-Viet C., Melinte G., Ersen O., Liu Y., Schlatter G., Hebraud A., Begin D., Janowska I., Pham-Huu C.

Carbocat VI, June 22-25, Trondheim, Norway, 2014

2. Low-temperature synthesis of macroscopic porous nitrogen-doped carbon composite with high doping content and exclusive localization
   H. Ba, Y. Liu, C. Duong-Viet, J-M. Nhut, O. Ersen, D. Begin, I. Janowska, C. Pham-Huu,
   Carbocat VI, June 22-25, Trondheim, Norway 2014

3. Carbon nanotubes containing defects as metal-free catalyst
   C. Duong-Viet, **H. Ba**, L. Truong-Phuoc, W.H. Doh, Y. Liu, J-M. Nhut, S. Zafeiratos, D. Begin, I. Janowska, P. Granger, C. Pham-Huu
   6th International Worshop on Advanced Materials Science and Nanotechnology, November 2-6, Ha-Long, Viet-Nam, 2014

4. Nitrogen-doped carbon naotubes as metal-free catalyst
   C. Duong-Viet, L. Truong-Phuoc, T.Tran-Thanh, **H. Ba**, J-M. Nhut, C. Pham-Huu
   Scientific Conference on Oil and Petrochemical Engineering, October 8-10, Ha-Noi, Viet-Nam, 2014

5. Microwave assisted growth of SAPO-34 on SiC foams and its application in methanol dehydration to dimethyl ether
   M. M. Elamin, O. Muraza, Z. Malibari, **H. Ba**, J-M. Nhut, C. Pham-Huu
   FEZA conference, June 22-25, Lepziz, Germany, 2014

6. Catalyseurs sans métaux à base de nanodiamants pour la production de styrène
   Ba H., Liu Y., Ersen O., Nguyen-Dinh L., Nhut J-M., Begin D., Janowska I., Pham-Huu C.
   Symposium Franco-vietnamien. Chimie et matériaux pour un environnement durable, June 12-14, Da-Nang, Viet-Nam, 2013

Poster

1. Graphene containing nanodiamonds composite as metal-free dehydrogenation catalyst for styrene production
   H. Ba, Y. Liu, T. Tran-Thanh, L. Truong Phuoc, J-M. Nhut, I. Janowska, D. Begin, P. Granger, C. Pham-Huu.
   Carbocat VI, June 22-25, Trondheim, Norway, 2014

2. Nanomatériaux à base de carbone pour la production de Styrène
   H. Ba, Y. Liu, L. Truong Phuoc, J-M. Nhut, I. Janowska, D. Begin, P. Granger, C.Pham-Huu,
   Les Doctoriales d'Alsace, Strasbourg, 9-12 juin**, 2014**

3. High surface area composite made by α-Al2O3 support decorated with a network of carbon nanotubes for catalytic applications
   Y.Liu, **H.Ba**, T.Dintzer, F.Vigneron, I.Janowska, D.Begin, C.Pham-huu
   Carbocat V, June 21-23, Bressanon, Italy, 2012

4. Synthesis of porous carbon nanotubes foam composites with a high accessible surface area and tunable porosity
   H. Ba, Y. Liu, , L. Nguyen-Dinh, O. Ersen, T. Romero, S. Zafeiratos, D. Begin, I. Janowska, C. Pham-Huu,
   Carbocat V, June 21-23, Bressanon, Italy, 2012

IV. awards

1. Prix du projet innovant - Les Doctoriales d'Alsace 2014

2. Prix d'encouragement AMOPA 2014

Housseinou BA

Manufacturing of metal-free carbon-based catalysts for styrene production

Résumé

Le styrène (ST) est l'un des monomères aromatiques insaturés les plus importants dans l'industrie pétrochimique moderne. Le procédé de déshydrogénation (DH) de l'éthylbenzène (EB) en ST, représentant actuellement 90% de la production de ST, nécessite l'utilisation de catalyseurs hautement actifs et stables, et permettant un grand transfert de masse. Dans ce travail, nous avons développé de nouveaux matériaux sans métaux à base de carbone, utilisant les nanodiamants (NDs) comme phase active pour la production de ST. Les NDs ont été déposés sur différents supports 2D et 3D à base de carbure de silicium et de carbone, permettant d'améliorer leur dispersion, et conduisant ainsi à un catalyseur exempt de métal très stable avec des performances en DH élevées. Nous avons également réussi à synthétiser des matériaux carbonés dopés à l'azote (N@C) présentant une activité élevée et stable en DH comparée à celle obtenue sur NDs. Cette phase active N@C a été obtenue à partir de produits alimentaires (le D-glucose, l'acide citrique et le carbonate d'ammonium) par un procédé facile à mettre en œuvre, et peut aussi très bien être déposée sur d'autres supports macroscopiques.

Abstract

Styrene (ST) is one of the most important unsaturated aromatic monomers in modern petrochemical industry. The catalytic dehydrogenation reaction (DH) of ethylbenzene (EB) into styrene, which accounts for 90% of the ST production, demands highly activated and stabilized catalysts, as well as easily handing and efficient mass diffusion. In this work, we developed novel metal-free carbon-based materials using nanodiamonds (NDs) as an active phase for potential industrial catalysts for the direct dehydrogenation route to produce ST. The NDs were successfully immobilized on different 2D and 3D carbon-based and silicon carbide supports which could help to improve their dispersion, leading to metal-free catalyst with high catalytic performance and stability. We have also succeeded in synthesizing nitrogen-doped carbon materials (N@C) displaying a high and stable dehydrogenation activity for the ST production in place of NDs. These active N@C catalysts were produced from food processing materials, i.e. D-glucose, citric acid and ammonium carbonate, and could be also easily dressed on macroscopic supports by a facile and scalable method.